



Universidade Federal de São Carlos  
Centro de Ciências Exatas e de Tecnologia  
Programa de Pós-Graduação em Física  
Departamento de Física  
Grupo de Supercondutividade e Magnetismo

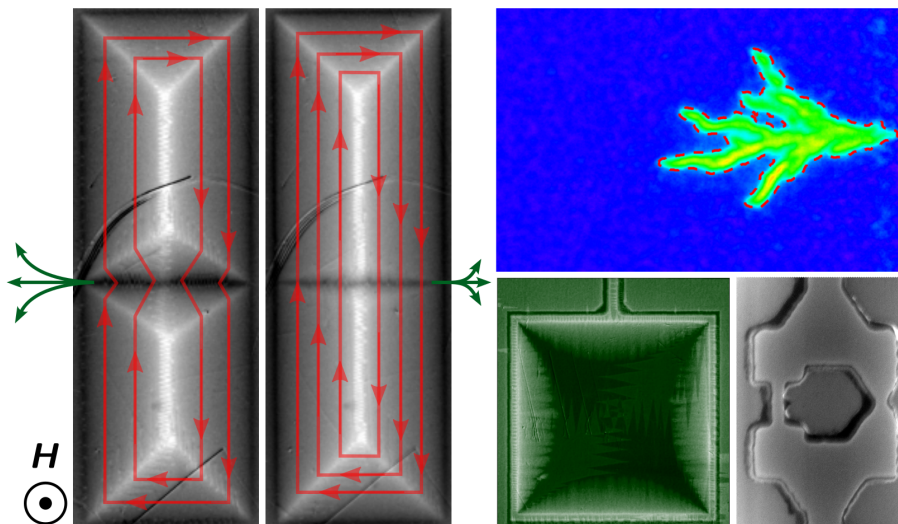
## Magnetic fields as a tool to control superconducting devices

Campos magnéticos como ferramenta para controlar  
dispositivos supercondutores

Davi Araujo Dalbuquerque Chaves

Ph.D. Thesis presented to the Graduate Program  
in Physics of Universidade Federal de São Carlos –  
UFSCar, as part of the requirements for obtaining  
the title of Doctor in Science (Physics).

**Advisor:** Maycon Motta  
**Co-advisors:** Wilson Aires Ortiz &  
Joris Van de Vondel



São Carlos – SP, Brazil  
October 2023



---

**Folha de Aprovação**

---

Defesa de Tese de Doutorado do candidato Davi Araujo Dalbuquerque Chaves, realizada em 16/10/2023.

**Comissão Julgadora:**

Prof. Dr. Maycon Motta (UFSCar)

Prof. Dr. Anna Maria Masoliver Palau (ICMAB)

Prof. Dr. Milorad Milosevic (UAntwerp)

Prof. Dr. Narcizo Marques de Souza Neto (CNPEM)

Prof. Dr. João Paulo Sinnecker (CBPF)

Araujo Dalbuquerque Chaves, Davi

Magnetic fields as a tool to control superconducting devices / Davi Araujo Dalbuquerque Chaves -- 2023. 183f.

Tese de Doutorado - Universidade Federal de São Carlos, campus São Carlos, São Carlos

Orientador (a): Maycon Motta

Banca Examinadora: Maycon Motta, Anna Palau

Masoliver, Milorad V. Milošević, Narcizo Marques de Souza Neto, João Paulo Sinnecker

Bibliografia

1. Supercondutividade. 2. Campos magnéticos. 3. Imageamento magneto-ótico. I. Araujo Dalbuquerque Chaves, Davi. II. Título.

Ficha catalográfica desenvolvida pela Secretaria Geral de Informática (SIn)

DADOS FORNECIDOS PELO AUTOR

Bibliotecário responsável: Ronildo Santos Prado - CRB/8 7325

# Abstract

## Magnetic fields as a tool to control superconducting devices

Davi Araujo Dalbuquerque Chaves

The quantum nature and dissipation-free flow of electric currents in superconducting materials have taken a central role as technological developments push forward the necessity of new methods for processing and dealing with the amount of information generated by modern consumption patterns. To enable such superconducting technologies, it is necessary to understand the underlying Physics dictating the behavior of superconductors, unveiling or allowing to control phenomena useful for applications. Due to its intrinsic relationship with the superconducting state, applied magnetic fields emerge as natural candidates for manipulating the properties of superconducting materials.

These ideas motivated the research conducted in the context of this thesis, which is structured as a collection of studies in which different superconducting systems are subjected to magnetic fields, aiming to investigate and control their behavior. In the first set of results presented, the temperature of a plain Nb thin film is reduced under different magnetic field cooling conditions. Then, flux penetration patterns are studied by magneto-optical imaging (MOI). The results demonstrate how the applied field spatial distribution and direction influence the ability of a superconducting device to transport electrical currents without dissipation, without the need for any complex nanofabrication steps. Such influence is due to the emergence of different trapped flux configurations in the superconductor, either facilitating or hampering further magnetic flux penetration, effectively reducing or increasing the effective maximum current the film can carry in the superconducting state.

It is true, however, that for most applications in superconducting technology, nanofabrication is required, in some cases demanding the creation of regions of suppressed superconductivity called weak-links. A different study investigates normal and superconducting

---

state properties of Nb films patterned with a single weak-link fabricated by focused ion beam (FIB) milling. The investigation quantifies the suppression of superconducting properties and the modification of the normal flow of electrons, finding that these are linked by the degree of impurities introduced by the nanofabrication. One interesting effect is the emergence of a local peak in the magnetic field-dependent magnetization of the patterned samples. In a separate work, we employ MOI to investigate these specimens under applied fields near such local peak. This study reveals that the patterned films undergo a behavior transformation from a weak-link to a strong-link, enabling more current to flow between the unpatterned Nb regions. Quantifying the MOI data allows us to understand the flux dynamics responsible for the peak effect.

In a different study, the properties of a dc superconducting quantum interference device (SQUID) presenting two parallel weak-links comprised of asymmetric constrictions of a superconducting amorphous MoGe film were investigated. It is possible to influence the behavior of such devices by modifying their geometry. The study demonstrates how understanding the relationship between the device and applied magnetic fields and currents allows preparing the SQUID in multiple energy states, readable at the same field value, thus allowing its use as a multilevel memory element. Finally, we aim to consolidate MOI as a reliable tool to quantitatively study the behavior of superconducting films under ac magnetic fields. For that, we investigate the independence of the thermomagnetic history on the ac magnetic susceptibility response of an amorphous MoSi film. This study relies on the possibility of emulating ac effects by cycling an applied dc field. The results are successfully compared with standard SQUID-based magnetometry while taking advantage of the local spatial resolution of MOI to reveal the quantitative behavior of individual flux avalanche events and the presence of zones of flux annihilation at interfaces between positive and negative flux regions.

**Keywords:** 1. superconductivity. 2. magnetic field. 3. superconducting technology. 4. magneto-optical imaging.

# Resumo

## Campos magnéticos como ferramenta para controlar dispositivos supercondutores

Davi Araujo Dalbuquerque Chaves

A natureza quântica e o transporte de correntes elétricas sem dissipação em materiais supercondutores assumiram papel central à medida que desenvolvimentos tecnológicos impulsionaram a necessidade de novos métodos para processar a grande quantidade de informação gerada pelos padrões de consumo atuais. Para fomentar tais tecnologias supercondutoras, é necessário entender a Física por trás do comportamento de supercondutores, revelando e permitindo controlar fenômenos úteis para aplicações. Devido à sua relação intrínseca com o estado supercondutor, campos magnéticos são candidatos naturais para manipular as propriedades de materiais supercondutores.

Essas ideias motivaram a pesquisa conduzida no contexto desta tese, a qual é estruturada na forma de uma coletânea de estudos nos quais diferentes sistemas supercondutores são submetidos a campos magnéticos visando investigar e controlar suas propriedades. No primeiro conjunto de resultados apresentados, a temperatura de um filme fino de Nb prístino é reduzida sob diferentes configurações de campo magnético aplicado. Então, os padrões de penetração de fluxo são estudados por imageamento magneto-ótico (MOI). Os resultados demonstram como a distribuição espacial e a direção do campo aplicado influenciam a habilidade de um dispositivo supercondutor de transportar correntes elétricas sem dissipação, removendo a necessidade de processos complexos de nanofabricação. Tal influência é devida à diferentes configurações de fluxo aprisionado no supercondutor, que facilitam ou dificultam mais penetração de fluxo, efetivamente reduzindo ou aumentando a máxima corrente efetiva que o filme pode transportar no estado supercondutor.

É verdade, contudo, que a maior parte das aplicações em tecnologia supercondutora necessita de nanofabricação e, em alguns casos, da criação de regiões de propriedades

---

supercondutoras suprimidas chamadas de elos-fracos. Um segundo estudo investiga as propriedades dos estados normal e supercondutor de filmes de Nb contendo um único elo-fraco fabricado pela técnica de escavação por feixe de íons focado. A investigação quantifica a supressão das propriedades supercondutoras e a modificação no fluxo de elétrons no estado normal, demonstrando que estes são conectados pelo grau de impurezas introduzido pela nanofabricação. Um efeito interessante é o aparecimento de um pico local na magnetização em função do campo magnético aplicado para as amostras que contêm o elo-fraco. Em um trabalho separado, nós empregamos MOI para investigar tais amostras sob campos aplicados próximos a esse pico. O estudo revela que os filmes que contêm o elo-fraco experienciam uma transformação, com a área nanofabricada passando a se comportar como um elo-forte que possibilita uma maior passagem de corrente entre as regiões inalteradas do filme de Nb. Quantificando os dados de MOI, fomos capazes de entender a dinâmica de fluxo magnética responsável por tal efeito.

Em um diferente estudo, investigamos as propriedades de um dispositivo supercondutor de interferência quântica dc (SQUID) contendo dois elos-fracos em paralelo constituídos por constrições de um filme supercondutor de MoGe amorfo. O comportamento de tais dispositivos pode ser alterado por modificações em sua geometria. Nessa investigação, buscou-se entender a relação entre o dispositivo e campos magnéticos e correntes, que permite preparar o SQUID em múltiplos estados de energia que podem ser lidos no mesmo valor de campo, permitindo, assim, seu uso como um elemento de memória multinível. Finalmente, demonstrou-se que a técnica de MOI é uma ferramenta confiável para estudar quantitativamente o comportamento de filmes supercondutores sob a influência de campos magnéticos ac. Para isso, investigamos a independência da susceptibilidade magnética ac de filmes de MoSi amorfos com sua história termomagnética. Esse estudo depende da possibilidade de emular efeitos ac variando um campo aplicado dc. Os resultados são comparados com outros obtidos por magnetometria SQUID padrão, enquanto tomamos vantagem da resolução espacial local do MOI para revelar o comportamento quantitativo

---

de eventos de avalanche de fluxo individuais e a presença de zonas de aniquilação na interface entre regiões de penetração de fluxo positivo e negativo.

**Palavras-chave:** 1. supercondutividade. 2. campo magnético. 3. tecnologia supercondutora. 4. imageamento magneto-ótico.



# Agradecimentos / Acknowledgments

*A translation of these Acknowledgments can be found after the following text.*

Todos aqueles que passaram pela experiência de produzir uma tese de doutorado têm boas e más histórias para contar. Eu também. Mas eu gostaria de começar esses curtos agradecimentos deixando registrado um fato. Iniciei o doutorado na UFSCar em agosto de 2019. Por si só, aos que estão cientes do momento político ao qual a ciência brasileira estaria subjugada nos anos seguintes, é claro que esses seriam tempos desafiadores. Contudo, depois de um intenso primeiro semestre de aulas e aprendizado científico, fomos forçados a interromper repentina e duradouramente nossas atividades no laboratório. A perspectiva de concluir com sucesso uma tese focada em atividades experimentais dentro do prazo não era boa. Certamente, houve a necessidade de uma grade dose de jogo de cintura para fazer as coisas funcionarem. E aqui deixo o meu primeiro e mais importante agradecimento. Ao vir fazer o doutorado em São Carlos, tive o prazer de fazer a feliz escolha de trabalhar com o Maycon. A parceria que desenvolvemos no começo das atividades em 2019 e nas incontáveis horas que trabalhamos juntos sentados à frente do computador, cada um em sua casa, se refletem não só no que eu julgo serem quatro anos com uma bem-sucedida produção científica, mas numa amizade que transcendeu a rotina do laboratório.

Agradeço também ao Ortiz, que abriu as portas do seu grupo para minha chegada, me orientou e foi, sem sombra de dúvidas, a pessoa mais importante no meu aprendizado sobre supercondutividade que hoje emprego diariamente em minhas atividades de pesquisa. Ao Caio, agradeço a oportunidade de me deixar transmitir o que aprendi nesses anos e pela

---

parceria de todos os dias. Obrigado ao Léo por me levar pra almoçar no RU e aos amigos que fiz em São Carlos por me fazerem sentir-me em casa na nova cidade.

Preciso também agradecer aos amigos que fiz na Bélgica. É difícil para mim dizer como a recepção que tive em Leuven foi substancialmente melhor do que aquilo que fui preparado para encontrar. Ao Joris, agradeço pela confiança, por acreditar em meu trabalho e por sempre estar presente para me ajudar. O que aprendi sobre como pensar e executar pesquisas científicas no tempo que passei sob sua orientação será valiosíssimo para o restante de minha carreira. Gostaria de agradecer ao Bart por sempre estar disponível para me ensinar. Seu conhecimento é verdadeiramente inspirador. Por fim, ao Lukas, Heleen e Donghua, muito obrigado por estarem sempre comigo durante meses nos quais eu podia ter estado muito sozinho. A parceria de vocês dentro e fora do laboratório foi fundamental para que meu período em Leuven tenha sido bem-sucedido e prazeroso. Suas amizades, que hoje transcendem barreiras continentais, são os maiores bens que trouxe desse período.

Quero também agradecer à minha família. Minha esposa Patrícia esteve o tempo inteiro ao meu lado me apoiando e agraciando meus dias com seu companheirismo e carinho. Minha mãe, que entende e sempre apoia minhas decisões de carreira, ainda que me levem para longe. O suporte que tenho de vocês é essencial para que eu venha conseguindo trilhar minha caminhada.

Por fim, gostaria de agradecer ao povo brasileiro, representado especialmente pela Capes e pelo CNPq, pelo apoio na minha formação científica e profissional. Toda minha trajetória acadêmica foi traçada em Universidades federais e já há dez anos recebo auxílio financeiro ininterrupto para perseguir essa formação, da iniciação científica ao mestrado e ao doutorado, incluindo a possibilidade da realização do estágio no exterior. O valor desse investimento não está perdido em mim e é minha missão como futuro cientista retornar à sociedade aquilo que ela me proporcionou.

O presente trabalho foi realizado com apoio da Coordenação de Aperfeiçoamento de

---

---

Pessoal de Nível Superior – Brasil (CAPES) – Código de Financiamento 001.

---

All those who had the experience of producing a Ph.D. thesis have good and bad stories to share. So do I. But I would like to begin these short acknowledgments by registering a fact. I began to pursue my Ph.D. at UFSCar in August 2019. In itself, for those who are aware of the political climate that Brazilian science was subjected to in the following years, it is evident that those were going to be challenging times. On top of that, after an intense first semester of classes and scientific learning, we were forced to abruptly stop our lab activities for a long period of time. The perspective of successfully finishing an experimental thesis in due time was not good. And here, I share my first and most important acknowledgment. By coming to São Carlos for my Ph.D. studies, I had the pleasure of making the choice to work with Maycon. The partnership we developed at the beginning of my activities in 2019 and through the uncountable hours shared in front of the computer, each one in their own house, is reflected not only in what I judge as a successful four-year scientific output but in a friendship that goes beyond our lab routine.

I also thank Ortiz, who opened the doors of his group for my arrival and was, without a shadow of a doubt, the most important person in my continuous learning about superconductivity, which I employ in my research activities on a daily basis. To Caio, I thank you for the opportunity of allowing me to transfer what I've learned in these years and for the everyday partnership. Thank you Léo for letting me join you for lunch and to the friends I made in São Carlos, thank you for making me feel at home in this new city.

I also want to thank the friends I made in Belgium. It is hard for me to properly state how much more welcomed I was in Leuven than I anticipated. To Joris, thank you for the trust, for believing in my work, and for always being there to help me. What I've learned about thinking and executing scientific research during the time I spent under your supervision will be extremely valuable for the remainder of my career. I want to thank Bart for always being available to teach me. Your knowledge is truly inspiring. At last, to Lukas, Heleen, and Donghua, thank you for being there with me during months I could've been really alone. Your partnership inside and outside the lab was essential to

---

make my time in Leuven successful and pleasant. These friendships that today overcome continental barriers are the greatest gifts I brought home from my time with you.

To my family. My wife Patrícia was always there for me, giving me the support I needed and gracing my days with her care and partnership. My mom, who understands and always supports my career choices, even when they take me far away. This support is essential for me to keep moving forward in my journey.

Lastly, I would like to thank the Brazilian people, specially represented by Capes and CNPq, for their support during my professional and scientific qualification. My whole academic experience was spent in federal Universities and for the last ten years, I have received continuous financial support to pursue this qualification—from bachelor research scholarships through my master's and Ph.D., including the chance to go abroad for an international internship. The value of this investment is not lost with me and it is my mission as a future scientist to give back to society what it has given me.

This study was financed in part by the Coordenação de Aperfeiçoamento de Pessoal de Nível Superior – Brasil (CAPES) – Finance Code 001

# Contents

<b>List of Figures</b>	<b>xvi</b>
<b>List of Abbreviations</b>	<b>xxi</b>
<b>Introduction</b>	<b>1</b>
<b>1 Superconductivity</b>	<b>6</b>
1.1 On the development of gas liquefaction . . . . .	6
1.2 The discovery of superconductivity . . . . .	9
1.3 A perfect diamagnet . . . . .	12
1.4 The London equations . . . . .	15
1.5 The Ginzburg-Landau theory . . . . .	17
1.6 Type-I and Type-II superconductors . . . . .	23
1.7 Macroscopic flux penetration . . . . .	30
1.7.1 Critical state models . . . . .	31
1.7.2 Flux avalanches . . . . .	37
1.8 The BCS theory . . . . .	41
1.9 The Josephson Effect and the SQUID . . . . .	53
1.10 An interlude . . . . .	62
<b>2 Methods</b>	<b>66</b>
2.1 Thin film deposition and patterning . . . . .	66

---

2.2	Magnetic measurements . . . . .	69
2.3	Electrical measurements . . . . .	75
<b>3</b>	<b>Cooling a superconductor under inhomogeneous magnetic fields</b>	<b>78</b>
<b>4</b>	<b>Transforming the behavior of a superconducting weak-link using magnetic fields</b>	<b>85</b>
<b>5</b>	<b>A magnetic-field-assisted superconducting multilevel memory</b>	<b>114</b>
<b>6</b>	<b>The interaction of a superconducting film and ac magnetic fields visualized by magneto-optical imaging</b>	<b>123</b>
	<b>Final remarks and outlook</b>	<b>139</b>
	<b>List of Publications</b>	<b>142</b>
	<b>Bibliography</b>	<b>144</b>

# List of Figures

- 1.1 The discovery of superconductivity. Measurements of the resistance of a pure mercury wire at low temperatures demonstrate a sudden drop in  $R$  when the sample is cooled down below a characteristic critical temperature  $T_c$ , equal to 4.2 K for Hg. Image extracted from Ref. [8]. . . . . 11
- 1.2 Temperature-dependent measurements of the specific heat of thallium showing discontinuity at  $T_c$  under constant magnetic field. The results provided evidence for the presence of latent heat in the transition. Image extracted from Ref. [12]. . . . . 13
- 1.3 The difference between the magnetic flux inside a superconductor and a perfect conductor in which the conductivity becomes infinite below a given temperature  $T_c$ . The samples are solid cylinders and are subjected to a field cooling procedure, meaning that a magnetic field is applied prior to entering the perfectly conductive state. . . . . 15
- 1.4 Gibbs free energy difference between the superconducting and normal states without an applied magnetic field as a function of  $|\psi|$ . The graphs are plotted according to Eq. (1.4) and using the definitions of Eq. (1.5) with  $\alpha_0 = \beta_0 = 1$ . . . . . 19
- 1.5 Schematic representation of  $H$ -vs- $T$  phase diagram and  $M(H)$  behavior with  $T < T_c$  for (a) a type-I superconductor and (b) a type-II superconductor. The graphs depict the existence of a mixed state for type-IIs, in



which the superconducting state coexists with magnetic flux penetrated in the form of vortices. . . . . 25

1.6 (a) Structure of a vortex. The top panel shows  $B_z$  as a function of position around the core of a vortex (green line) together with the behavior of  $|\Psi|^2$  (red). The bottom panel shows the shielding currents distribution. The right panel shows selected examples of visualization of vortices in superconductors: (b) first observation of the Abrikosov lattice, captured by Bitter decoration in a Pb-In alloy [40]; vortices in (c) amorphous  $\text{Mo}_{2.7}\text{Ge}$  thin film revealed by scanning-tunneling microscopy [41]; (d) Nb thin film revealed by magnetic-force microscopy [42]; and (e)  $\text{NbSe}_2$  single crystal revealed by magneto-optical imaging [43]. The Abrikosov lattice distortions evident in panels (d) and (e) result from vortex pinning. Adapted from [44]. 27

1.7 (a) A long bulk superconductor under a perpendicularly applied magnetic field  $\mathbf{H}$ , showing a pictorial representation of the flux distribution and shielding currents.  $B(x)$  is depicted according to the Bean model while  $H$  is (b) increased and (c) decreased. Panel (d) represents the  $J_y(x)$  distribution for the applied field labeled as 1. (e)  $B(x_0)$  as indicated in panels (a) and (b), evidencing the observed magnetic flux hysteresis in type-II superconductors. Adapted from [52]. . . . . 33

1.8 (a) Schematic representation of a long superconducting film subjected to a magnetic field applied perpendicularly to its surface. The film's thickness is  $d$  and its width is  $2w$ . The induced magnetic flux lines  $\mathbf{B}$  bend around the film due to the presence of circulating shielding currents  $\mathbf{J}$ . The (b)  $B_z(x)$  and (c)  $J_y(x)$  profiles after ZFC are obtained for different applied magnetic fields  $H$  according to the Bean model along the  $x$ -axis, as represented by the dashed gray line in panel (a) [57, 58]. . . . . 34

1.9 (a) Magneto-optical image of a long YBCO thin film under a perpendicular

magnetic field showing partial flux penetration up to a depth  $a$  into the sample. (b) The magnetic flux density perpendicular to the film's surface and (c) the shielding current density flowing in the film as measured along the vertical line in panel (a). Solid lines are calculated using the Bean model. Images are adapted from [60]. Other MOI results showing smooth flux penetration in superconducting films, clearly distinguishing the flux front from the Meissner state region: (d) YBCO [61]; (e) Nb [62]; and (f) Nb [49]. . . . . 35

1.10 Comparison between the (a) current density and (b) magnetic flux density for a superconducting thin film after ZFC obtained according to the Bean and Kim critical state models for different applied fields. Adapted from [58]. Magnetization hysteresis loops for a thin disk in the (c) Bean and (d) Kim models. The different loop sizes represent different maximum applied field amplitudes. Adapted from [65]. . . . . 36

1.11 (a) Positive feedback loop initiated by a thermomagnetic instability. Adapted from [49]. The dendritic flux pattern imprints on different superconducting films after avalanche events take place captured by MOI: (b) MgB<sub>2</sub> [68]; (c) Nb [49]; and (d) amorphous MoSi. . . . . 38

1.12 (a) Comparison between thermomagnetic model (TM) simulations (top) and magneto-optical images (bottom) obtained for a MgB<sub>2</sub> thin film, reproducing the observed dendritic patterns at different temperatures [80]. (b) TM simulations (bottom) [81] reproduce the reuse of previously established positive (bright) flux channels by negative (dark) flux avalanches in Nb films (top) [76]. (c) TM simulations (right) [61] reproduce the suppression of flux penetration during an avalanche event caused by the existence of a metallic capping layer over the right side of the superconducting film [77]. 41

1.13 Comparison between the experimentally measured superconducting gap

for several elemental superconductors and the BCS prediction. Adapted from [99]. . . . .	52
1.14 Electron tunneling between a normal metal and a superconductor. (a) Representation of the energy levels of two normal metals (N) separated by an insulating barrier (I) under an applied voltage $V_{\text{app}}$ . (b) Similar to the previous panel, but now one of the materials is a superconductor (S). (c) The expected tunneling current-voltage relationship for the situations in panels (a) and (b). (d) Giaever measurements for an Al/A <sub>2</sub> O <sub>3</sub> /Pb tunnel junction at different temperatures demonstrate the tunneling of electrons between the normal and superconducting materials. Adapted from [100]. . . . .	53
1.15 Schematic representation of a typical SIS Josephson junction. . . . .	56
1.16 Schematic representation of a dc SQUID. This circuit element is comprised of two parallel Josephson junctions, represented by $a$ and $b$ . Currents flow through the superconducting loop as indicated. A magnetic field is applied perpendicular to the SQUID. . . . .	58
1.17 Schematic representation of a typical SIS Josephson junction. . . . .	61
1.18 The highest known $T_c$ for different classes of superconductors through the years. Different symbols indicate different classes. Conventional BCS superconductors are shown as green circles, whereas high- $T_c$ cuprates appear as blue diamonds. Adapted from [120]. See [121] for more information. . . . .	63
1.19 The ratio between the energy gap and $k_B T_c$ as a function of the gap-to-Fermi energy ratio for different BCS and high-temperature superconductors. Adapted from [123]. . . . .	64
2.1 Standard lithography procedure. In step 1, a bare substrate is coated with a sensitive resist layer, which can be either of the positive or negative kind. Then, in step 2, the resist is exposed to an external agent to form the	

desired pattern, altering the properties of the exposed areas (in red). In step 3, a developing agent will remove either the exposed areas (positive resist) or the unexposed areas (negative resist), thus forming the mask onto which the thin film material is evaporated in step 4. Finally, in step 5, the remaining resist is lifted off from the substrate by a solvent solution, revealing the final sample. . . . . 68

2.2 (a) Schematic diagram of a typical magneto-optical imaging experimental setup. (b) An enlargement of the sample and MOL region. (c) A representation of the field-induced rotation of the Faraday-active layer's spontaneous magnetization. The panel also shows the rotation of the polarization angle of the light beam as it passes through the indicator. Features appear out of scale. . . . . 71

2.3 Representation of the Heliox  $^3\text{He}$  Cryostat system used for sub-Kelvin electrical transport measurements. The  $^3\text{He}$  refrigerator stick is highlighted in the main panel by the red contour. The details on the right show pictures from the inside of the inner vacuum chamber at the bottom of the refrigerator stick and the sample holder. Adapted from [119]. . . . . 76

# List of Abbreviations

◆ This list contains definitions for the notation used through different Sections of Chapters 1 and 2. The notation used in Chapters 3 through 6 is presented in the respective articles;

◆ Bold italic letters (e.g.,  $\mathbf{X}$  or  $\mathbf{x}$ ) refer to vector quantities. If the same letter appears in non-bold italic, it refers to the absolute value of the vector (i.e.,  $x = |\mathbf{x}|$ );

◆ A superscript  $*$  refers to the superconducting charge carriers (later identified as the Cooper pairs); a subscript  $F$  refers to the Fermi level; a subscript  $c$  refers to the superconducting critical value; a subscript  $s$  refers to the superconducting state, whereas  $n$  refers to the normal state.

$\mu_0$  – vacuum magnetic permeability

$h$  – Planck constant;  $\hbar = h/2\pi$

$k_B$  – Boltzmann constant

$\omega_D$  – Debye frequency

$\mathbf{r}$  – position

$\mathbf{k}$  – momentum

$t$  – time

$T$  – temperature

$\mathbf{H}$  – applied magnetic field

$\mathbf{B}$  – magnetic flux density

$\mathbf{M}$  – magnetization

$\mathbf{E}$  – electric field

$\mathbf{J}$  – electric current density

$\mathbf{A}$  – magnetic vector potential

$\mathcal{E}$  – energy

$\Delta$  – energy gap

$I$  – electric current

$V$  – voltage

$\rho$  – resistivity

$U$  – potential energy

$G$  – Gibbs free energy

$m$  – mass

## LIST OF ABBREVIATIONS

---

$e$  – electron charge

$\mathbf{v}$  – velocity

$\Phi$  – magnetic flux

$\Phi_0 = h/2e$  – magnetic flux quantum

GL – Ginzburg and Landau

BCS – Bardeen, Cooper, and Schrieffer

$H_{c1}$  – lower critical field

$H_{c2}$  – upper critical field

$\lambda$  – penetration depth

$\xi$  – coherence length

$\kappa = \lambda/\xi$  – GL parameter

FC – field cooling

ZFC – zero-field cooling

# Introduction

*Nature sometimes behaves unexpectedly. It is usually an opportunity.*

For centuries, our species gathered the power of fire to warm and protect ourselves, cook our food, and eventually light our houses and streets. Mastering this natural element was fundamental in allowing us to develop into civilizations. But, since the 19th century, understanding electricity has transformed our daily lives. Modern society depends on it to power houses, vehicles, farms, and industries. Electronic components have become entangled with our lifestyle, much like the device at which you are reading this thesis or the printer you used to put it on paper. The advent of the internet and the increased processing power of modern computers have enabled unprecedented access to information and services, reshaping our social patterns.

In a nutshell, these advancements depend on our understanding of how electrons and photons, the elementary particles of charge and light, act and interact with matter, respectively. However, we are facing a bottleneck in increasing computational power and storing the tremendous amount of data generated by our current information consumption rates. It may be necessary to move away from the “traditional” technology that has brought us this far to circumvent this, delving into the quantum aspects of nature to develop devices that can actively create and manipulate quantum states of matter. Superconductivity, a century-old physical phenomenon, takes a prestigious role in this endeavor.

In “normal” conducting metals, an electric current faces a characteristic resistance counteracting the flow of electrons, quantified by a material-dependent property called

resistivity. In such materials, resistivity decreases with decreasing temperatures, tending to a finite value related to the scattering of electrons with imperfections in the metal microstructure. At the beginning of the 20th century, Heike Kamerlingh Onnes and his collaborators at Leiden University were investigating the behavior of these materials at extremely low temperatures when they observed a rather unexpected effect. At temperatures greater than absolute zero, the resistivity of a metal could abruptly vanish, which is equivalent to saying it presented infinite conductivity.

This event marked the discovery of a phenomenon known as superconductivity. Today, we know this supposedly exotic behavior is not exclusive to metallic materials and is, in fact, relatively common in nature. Over fifty elements are known to be superconductors at adequate temperature and pressure conditions. There are numerous more alloys and compounds in this list. However, a theoretical understanding of superconductivity only came about a few decades after its first observation, partially because it was only in 1933 that Walther Meissner and Robert Ochsenfeld provided experimental evidence that infinite conductivity could not define the superconducting state by itself. These materials also have a characteristic interaction with magnetic fields, expelling magnetic flux from their interior, as they behave as perfect diamagnets. In 1957, John Bardeen, Leon Cooper, and Robert Schrieffer developed a theory fully capable of explaining the quantum origin of this macroscopically observable phenomenon. It turns out that, in the conventional superconductors described by the BCS theory, individual electrons are not responsible for carrying charge like in a normal metal. Instead, bound electron pairs form the stable condensed quantum state giving rise to superconductivity. Overall, studies on superconductivity have directly awarded five Nobel Prizes in Physics to ten different scientists. Some argue that there should have been more.

The technological implications of a material able to transport electrical currents without dissipation while simultaneously expelling magnetic flux are fascinating. Through the years, efforts to understand and develop these materials made superconducting tech-



nologies a reality more intertwined in our lives than we might expect. There are natural applications in electricity transmission lines, power generation, and constructing powerful magnets used in levitation passenger trains and medical magnetic resonance imaging. But superconductors are also present in numerous scientific laboratories, where they are used for high-sensitivity detection of magnetic fields in physical, biological, and geophysical sciences. Meanwhile, particle accelerators, detectors, and some fusion reactors also explore the remarkable properties of superconductors. In communication technology, mobile phone base transceiver stations already employ superconducting filters on a small scale to increase the signal coverage area.

If we return to the forthcoming stagnation of processing power development, we can more clearly highlight the potential of superconductors. In the earlier development stages of computer science, improvements in fabrication techniques increased the density of transistors per chip, enhancing energy efficiency. One key factor that has halted such development is that we are approaching the physical limits of transistor miniaturization. As sizes decrease, problems with current leakage heating these circuits arise, making it expensive to cool down large server rooms or data centers that deal with processing and storing information. Although not the only option, superconductors offer a dissipation-free alternative to traditional processor architectures. Today, superconducting electronics is flourishing with diodes, transistors, and memories. More than that, there are whole new families of superconducting logic harnessing the particular properties of superconductors to astonishingly lower the power required to move information within the processors. Such advancements in superconducting computing are fuelled by the development of quantum computers. These devices can exponentially reduce the computational steps required to perform some tasks by employing cleverly designed quantum algorithms, exploring the superposition in two-level quantum mechanical systems to build their basic units of information, the qubits. In principle, any two-level system can work as a qubit, but most of the existing quantum computers have found success employing superconducting qubits

in their quantum processor architecture.

Superconductors do not come all in the same shape and form. Superconducting technology is enabled by understanding the particularities and fundamental behaviors of these materials. The interaction of superconductors with magnetic fields is at the core of the phenomenon, as also evidenced by the works of Lev Landau and Vitaly Ginzburg and later Alexei Abrikosov. Given the right conditions, superconductors may allow magnetic flux to penetrate their interior while sustaining the superconducting behavior. Such penetration occurs by the admission of vortices carrying a single magnetic flux quantum and tends to organize in periodic triangular configurations. Those, however, can be manipulated to alter the overall response of superconducting materials.

These are the main ideas and concepts behind the research I will present in this thesis. In its simplest form, our motivation was to explore the fundamental interactions of superconducting samples and applied magnetic fields to reveal or understand phenomena useful for implementations in superconducting technology. We have focused on thin, low-temperature, conventional superconducting films as those are the most common choice for fabricating superconducting devices used in quantum technology.

This thesis is structured as a collection of studies, following the rules of the Physics Graduate Program of Universidade Federal de São Carlos. Taking advantage of this format, Chapter 1 presents a historical overview of the scientific developments that built the basic understanding of the superconducting phenomenon. Chapter 2 introduces the experimental techniques employed to fabricate and investigate the magnetic and electric properties of our superconducting films and devices. Specific references to more recent implications and achievements in superconducting technology and experimental techniques are given in the papers and manuscripts that constitute the core of this thesis, presented in Chapters 3 through 6. In Chapter 3, I present results demonstrating that cooling a film down to the superconducting state under spatially inhomogeneous magnetic fields can increase the device's ability to transport currents without dissipation. Chapter 4

presents two studies. The first is dedicated to investigating the effects of focused ion beam nanofabrication on a thin film's superconducting and normal state properties. The second one reveals how magnetic fields can be used to tune the behavior of these samples, allowing for a modulation of the superconducting current able to flow across regions of suppressed superconductivity. Chapter 5 presents a superconducting device capable of working as a multilevel memory element. Understanding how such a device interacts with magnetic fields and currents is paramount to operating it at different energy levels. The manuscript presented in Chapter 6 aims to solidify magneto-optical imaging—a technique that enables visualizing magnetic flux penetration on the micrometric scale—as a reliable quantitative way of investigating the interactions of superconducting films with ac magnetic fields. As such, it is used to explain why the ac response of superconducting films is independent of their thermomagnetic history, even in the presence of abrupt flux penetration events.

The results presented in this thesis reflect the research I conducted during my Ph.D. studies at the Superconductivity and Magnetism Group under the supervision of Professors Maycon Motta and Wilson Aires Ortiz at UFSCar in Brazil and at the Quantum Solid-State Physics group under the supervision of Professor Joris Van de Vondel during a six-month international internship period at KU Leuven in Belgium. They also count on the fundamental contributions of several Brazilian and international collaborators with whom I have coauthored the papers and manuscripts.

# Chapter 1

## Superconductivity

In short, superconductivity is a quantum many-body phenomenon manifested macroscopically. It is characterized by the simultaneous existence of two independent properties: infinite conductivity and perfect diamagnetism. These two short sentences carry an unutterable weight and hinge on the combined efforts of countless scientists who have advanced our knowledge about superconducting materials since their discovery in 1911 at the laboratory of Heike Kamerlingh Onnes. The process that has allowed us to enjoy the benefits of superconducting technology in everyday applications such as medical imaging and high-speed trains is the same that propels an ongoing quantum revolution powering superconducting computers. This centenary history is as beautiful as it is long. It is not my intention to explore all aspects of superconductivity but to present its roots along with some major developments that provide the scientific basis on which the investigations presented in this thesis stand.

### 1.1 On the development of gas liquefaction

A few moments may be viewed as the beginning of the history of superconductors. Here<sup>1</sup>, I will follow events from 1813—one hundred years before Onnes received his Nobel Prize. That was the year in which Micheal Faraday began working as a chemical assistant

---

<sup>1</sup>This Section is largely based on Refs. [1–4]. It also benefits from a lot of online research, mostly traced back to Ref. [5].

of Sir Humphry Davy at the Royal Institution in London. Mr. Faraday would become a prolific investigator and discoverer and live on as one of the most influential scientists ever. Among his revolutionary feats, in 1823, Faraday developed a mechanism that enabled the liquefaction of chlorine (among other gases) by applying high pressures and relatively low temperatures. By 1844, his method had allowed Faraday to liquefy almost every known gas<sup>2</sup>, but three elements remained elusive: oxygen, nitrogen, and hydrogen.

In 1852, James Prescott Joule and William Thomson (also known as Lord Kelvin) described the temperature variation experienced by an insulated gaseous or liquid substance when it passes through a constriction: a process that would become known as the Joule-Thomson effect. Depending on its properties and initial and final states, a fluid subjected to a Joule-Thomson process may be caused to cool down. In 1857, Carl Wilhelm Siemens developed the concept of regenerative cooling, a cycle in which expanded gas cools down incoming compressed gas. These ideas would become prominent techniques in refrigeration processes. Nonetheless, it was still impossible at that time to liquefy either of the above-mentioned elusive gases.

During the next few years, the field of thermodynamics experienced remarkable breakthroughs. In 1857, Rudolf Julius Emanuel Clausius published his seminal work on heat, introducing a theory of gases considering all degrees of freedom. Then, in 1859, James Clerk Maxwell postulated the first law of statistical mechanics. In the following decades, he, Ludwig Eduard Boltzmann, and Josiah Willard Gibbs would come to define the field of statistical mechanics, providing powerful tools to characterize thermodynamic systems. It was in this fertile environment that Thomas Andrews, in 1869, discovered the existence of critical points in fluids, at which its gaseous and liquid phases are indistinguishable. Soon after, in 1873, Johannes Diderik van der Waals proposed a model to describe the behavior of real gases. His equation of state, now known as the van der Waals equation,

---

<sup>2</sup>The noble gases would only become known in 1895 when Lord Rayleigh and Sir William Ramsay communicated they had successfully isolated a new element, argon, from atmospheric nitrogen.

accurately describes the behavior of gases above their critical temperature. It was then possible to correctly predict the position of critical points at the phase diagram of a given substance based on existing measurements carried out at higher temperatures.

It did not take long for the first of the elusive gases to be liquefied afterward. In 1877, Raoul-Pierre Pictet and Louis-Paul Cailletet independently managed to liquefy small quantities of oxygen. In 1883, Karol Stanisław Olszewski and Zygmunt Florenty Wróblewski liquefied oxygen and nitrogen from the atmosphere in a stable state. However, ten years after van der Waals derived his equation of state and sixty years after Faraday first liquefied gases, it was still not possible to obtain liquid hydrogen. The necessary ingredients were all known, but the experimentally available temperatures of around 80 K were far superior to hydrogen's critical temperature of 33 K.

This endeavor would shape a fascinating, years-long competition between Sir James Dewar, a successor of Faraday at the Royal Institution, and Heike Kamerlingh Onnes of Leiden University in the Netherlands. The details of this race are beyond the scope of this thesis. As it turned out, Dewar would conceive the necessary technical breakthrough enabling hydrogen liquefaction. In 1892, Dewar invented a double-wall cryogenic vessel that efficiently insulated the inner part from the external temperatures by pumping the air out of the space between the walls. The Dewar vessel, as it is still called in cryogenic laboratories, was a remarkable invention. Its concept was quickly applied in more mundane applications than gas liquefaction, such as for keeping coffee hot inside a thermos bottle. Equipped with his cryogenic vessel, Dewar liquefied hydrogen for the first time in 1898, employing a regenerative cooling procedure.

Different factors influenced the defeat of Onnes in the liquid hydrogen race, but as fate would have it, the finish line was moved just before the end of the competition. In 1895, Sir William Ramsay (among others) isolated helium from cleveite, a uranite variety. Helium was previously only found in the spectral lines from Sun radiation. It condensates below 4.2 K, considerably colder than hydrogen. Onnes then laid his sights on the new

goal, which he would be the first to accomplish—after thirteen years in 1908. By reducing helium’s boiling pressure, Onnes achieved temperatures as low as 1.04 K by 1910.

The fact that we can liquefy helium is a tale about people’s ingenuity and hard work. Overall, it took eighty-five years of technical and theoretical contributions from some of our brightest minds. After it was achieved, it took another fifteen years before helium could be liquefied anywhere on Earth outside of Onnes’ laboratory. We can now look back at those years with the benefit of perspective. Today, we enjoy not only hot coffees but also cold drinks from our refrigerators as we sit comfortably in air-conditioned spaces during hot summer days. We can transport perishable goods across continents. But then, we can also use the low temperatures provided by liquid helium to investigate aspects of nature previously hidden from us.

### 1.2 The discovery of superconductivity

In 1900, Paul Drude proposed his famous model describing the resistivity of a conducting metal by the scattering of electrons with ions within the material [6]. Although largely successful, it left some lingering questions. In particular, it was still unknown how resistivity should behave at extremely low temperatures. At the time, conflicting ideas permeated the scientific community, but there were already some established experimental facts. At moderate temperatures, the resistivity of metals decreased linearly with temperature. However, early studies conducted by Dewar showed that, at liquid hydrogen temperatures, the resistivity tended to a constant, non-zero value which depended on the degree of impurities in the material [1, 3].

Onnes had his own convictions, believing that Einstein’s description of the specific heat in solids based on quantum oscillations could be extended to explain why resistance diminished at low temperatures [1, 7]. Following this idea, Onnes expected that resistivity would drop to zero at zero temperature. A different hypothesis predicted that resistance would increase at low temperatures due to a recondensation of free electrons to their

parent atoms, reducing the number of available charge carriers in the metal.

Onnes then set up his helium cryostats to investigate this issue, handing the experimental responsibilities to Cornelis Dorsman, Gilles Holst, and chief technician Gerrit Jan Flim. What they found was rather astonishing and it is represented in Fig. 1.1—probably one of the most reproduced graphs in Physics history. By cooling down pure mercury wires, they observed an abrupt transition in the resistance when the sample reached a critical temperature ( $T_c$ ) of 4.2 K. Below  $T_c$ , the mercury sample did not appear to provide any resistance to electrical currents [8]. To put it differently, the sample resistance  $R$  drops to zero for temperatures  $T$  lower than  $T_c$ , or  $R(T < T_c) = 0$ . Gilles and Flim were at first skeptical of their finding, but repeating the experiment, rewiring the electrical contacts, and improving their experimental setup to produce results three orders of magnitude more precise only confirmed their initial observations. In 1911, Onnes communicated their findings at the first Solvay Conference (omitting the names of his collaborators, as was customary, although Gilles and Dorsman are credited in Onnes written communications [8]).

This was the first observation of the superconducting state, which receives its name from the infinite conductivity presented by materials below  $T_c$ . In the next two years, Onnes and his team had already identified the superconducting behavior in lead and tin samples, but could not observe it for gold and platinum [9, 10]. In 1913, Onnes was laureated with the Nobel Prize in Physics “for his investigations on the properties of matter at low temperatures which led, inter alia, to the production of liquid helium”. By 1914, they had experimentally demonstrated the persistent current property of superconductors, meaning that an applied current will flow essentially undisturbed through a material in the superconducting state with an extremely large decay time [11]. Their experiments also demonstrated two extremely important concepts in superconductivity: the existence of a critical current ( $I_c$ ) and a critical magnetic field ( $H_c$ ), meaning that if either the applied current through the superconductor or the applied magnetic field exceeds a characteristic

---



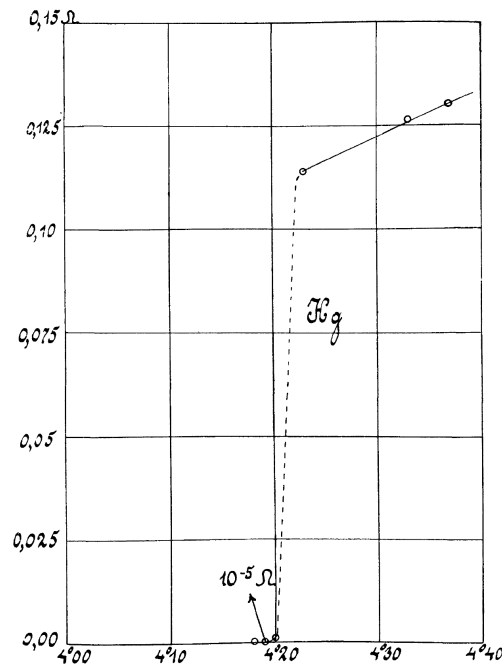


**Figure 1.1.** The discovery of superconductivity. Measurements of the resistance of a pure mercury wire at low temperatures demonstrate a sudden drop in  $R$  when the sample is cooled down below a characteristic critical temperature  $T_c$ , equal to 4.2 K for Hg. Image extracted from Ref. [8].

value, superconductivity is lost<sup>3</sup> [3]. That same year, however, saw the beginning of the Great War, halting experiments in Leiden until 1919.

By 1923, the list of known superconducting materials had been extended with the addition of thallium, uranium-lead, and indium. In 1925, a group led by Walther Meissner at the Physikalisch Technische Reichsanstalt in Berlin was the third to successfully liquefy helium. Their initial research focused on the question of whether all metals were superconductors [17]. By 1930, tantalum, titanium, thorium, gallium, and niobium were added to the list, while the Berlin team also discovered that chemical compounds and alloys could present the effect. At such time, the enticing possibilities of the superconducting

<sup>3</sup>It was only in 1926 that Onnes team experimentally determined that these two quantities express the same phenomenon, confirming a hypothesis from Francis Silsbee that critical currents derive from the critical field [12–14]—for type-I superconductors (Section 1.6). The extent of the Leiden team’s work in the first decades of the 20th century is indeed phenomenal. A great part of what is taught in fundamental superconductivity courses today was unveiled by his and his team’s findings. I would not be able to cover it in this thesis, but I do invite the reading of Refs. [3, 12] for a great historical and scientific perspective. For the full scope of superconductivity, I believe Refs. [15, 16] will be a great reading.

state were already evident. It evermore seemed like a prominent property among different materials, hence, considerable effort would begin to be exerted in trying to provide an explanation for the rapidly developing experimental observations. Beyond Onnes himself, names like Bohr, Pauli, Heisenberg, Bloch, Landau, and Brillouin all employed the newly developed and extremely successful quantum theory of metals to try to correctly describe the phenomenon. They all failed [17]. The common line of thought for all these researchers was that the fundamental aspect of superconductivity was its infinite conductivity. All other properties would follow from that. However, a series of experimental breakthroughs would soon change this panorama.

### 1.3 A perfect diamagnet

When investigating the temperature dependency of the thermal conductivity of superconducting lead, tin, and indium, Wander Johannes de Haas and H. Bremmer observed clearly different behaviors below  $T_c$  if the measurements were conducted with or without an applied magnetic field. These experiments, conducted between 1931 and 1932 constituted, probably for the first time, concrete evidence that the superconducting state was not merely an extreme case of the normal state electronic dynamics, and highlighted the determinant role played by magnetic fields in superconductors [12]. Parallel to these findings, in 1932, different studies conducted by Willem Hendrik Keesom, J. N. van den Ende, and J. A. Kok discovered that the specific heat of tin experiences a sharp discontinuity at  $T_c$ , what does not occur if the experiments are conducted under an applied field greater than  $H_c$ , impeding the superconducting transition.

The same discontinuity in the specific heat was observed two years later for thallium, this time clearly showing the presence of latent heat when the transition occurs under a magnetic field, see Fig. 1.2. This observation bears enormous implications. Ever since Onnes first presented his results at the first Solvay Conference, questions arose on whether the superconducting transition was accompanied by any structural change or phase tran-

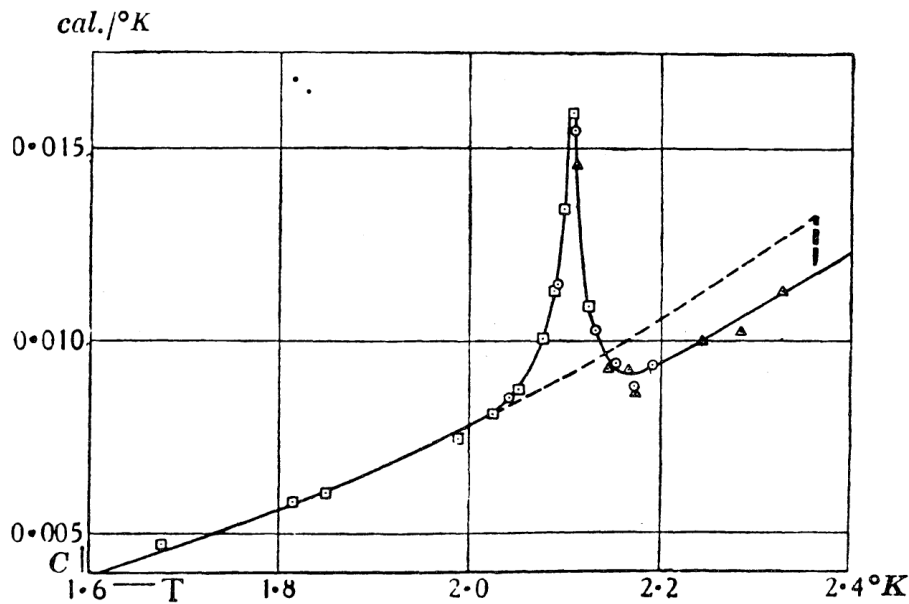


**Figure 1.2.** Temperature-dependent measurements of the specific heat of thallium showing discontinuity at  $T_c$  under constant magnetic field. The results provided evidence for the presence of latent heat in the transition. Image extracted from Ref. [12].

sition [1, 12]. At that time, it was not possible to give a satisfactory answer, but later x-ray diffraction experiments showed no evidence of changes in the lead crystal lattice at the superconducting and normal states. If a phase transition were to occur, earlier theoretical predictions indicated that a latent heat directly proportional to the magnetic field would reflect a change in the magnetic permeability between two distinct thermodynamic phases [18]. Therefore, the thallium's specific heat measurements revealed that the superconducting transition is a reversible thermodynamic phase transition. Hence, the superconducting state is revealed as a particular electronic state, with likely particular electromagnetic properties, that, once and for all, could not be understood simply as an extreme case of the electronic properties of "normal conducting" metals.

During the same period, in 1933, a famous experiment would explicitly demonstrate an undeniable difference between the properties of a hypothetical perfect conductor (with infinite conductivity) and those of a superconductor. For a number of years, there was a debate on how currents flow inside the superconductor, a question which was for already

some time of interest to Meissner. Max von Laue, who at the time had already been awarded his Nobel Prize, was a Professor at the University of Berlin and acted as a consultant at the Physikalisch Technische Reichsanstalt. He suggested to Meissner an experiment that was originally intended to finally determine whether currents were flowing in the bulk or on the surface of a superconductor. Meissner and Robert Ochsenfeld were to carry out the experiments to find a different and unexpected result [19,20]. Their main observation was that tin and lead cylinders would expel magnetic flux from their interior independent of their thermomagnetic history, meaning that either if the samples were first cooled down below  $T_c$  and then a magnetic field was applied (zero-field-cooled or ZFC), or if a magnetic field was applied and then the samples were cooled below  $T_c$  (field-cooled or FC), experiments did not find magnetic flux in the interior of the superconductors, i.e., the induced magnetic flux density  $\mathbf{B} = 0$ . Therefore, a superconductor presents perfect diamagnetism, expelling magnetic flux from its interior. This phenomenon came to be known as the Meissner-Ochsenfeld effect. It cannot be explained solely by considering the dynamical effects arising from infinite conductivity. To wit, within a perfect conductor, the magnetic flux inside any closed loop is constant [21]. This implies that, if magnetic fields are applied to a perfect conductor, shielding currents will emerge prohibiting flux penetration. However, if a material is already filled by magnetic flux and, only then, it becomes purely a perfect conductor, no differences should be found in the magnetic flux distribution on its interior (it does not expel flux). Furthermore, once the magnetic field is removed, the perfect conductor should trap magnetic flux, so it satisfies the condition of flux invariability. Figure 1.3 schematically highlights the differences in the resulting magnetic flux inside a superconductor and a perfect conductor after an FC procedure.

These remarkable findings implied that one needs to account for its perfect diamagnetism to describe the superconducting state. That knowledge, coupled with the applicability of thermodynamics to explain the superconducting transition, would soon pave the way for a series of phenomenological descriptions of superconductivity. Following, I will

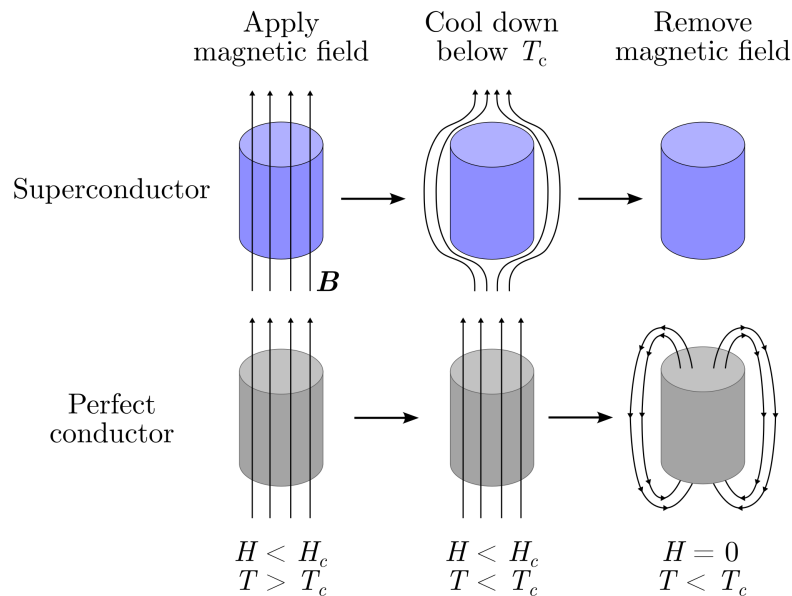


**Figure 1.3.** The difference between the magnetic flux inside a superconductor and a perfect conductor in which the conductivity becomes infinite below a given temperature  $T_c$ . The samples are solid cylinders and are subjected to a field cooling procedure, meaning that a magnetic field is applied prior to entering the perfectly conductive state.

highlight important aspects of the two most influential of these, providing further insight into fundamental aspects of superconducting behavior.

## 1.4 The London equations

In the early and mid-1930s Germany, as Hitler and the Nazi Party rose to power, a flurry of scientific minds fled west escaping their racial policies. Among them, a Jew scientist who previously held a junior position at the University of Berlin named Fritz London would be welcome at Oxford. There, he would be joined by his brother, Heinz London, who had just and abruptly defended his Ph.D. thesis in 1934, one of the last Jews to do so in Germany during Hitler’s regime. They lived together at Oxford for two years, where they could freely pursue science. I point to “Fritz”, Chapter 6 of Ref. [16], for details of this delicate period of their lives.

At Oxford, the London brothers would focus a lot of their efforts on the matter of a macroscopic theory of superconductivity, which was already pursued by Fritz for some

years. However, Meissner and Ochsenfeld’s new experimental findings put the matter into a new perspective. Fritz and Heinz would need to describe a perfect diamagnet. Already in 1934, Cornelis J. Gorter and Hendrik Casimir proposed an intriguing phenomenological two-fluid model for superconductors, assuming that a fraction of the electrons would condense into a ground state, as a superfluid, which was immersed in the normal electron fluid [12, 22].

The London brothers now understood that the typical Ohm’s law for metals was not suited to describe the superconducting condensate within Maxwell’s theory for electrodynamics. Then, they proposed a relationship to supplant Ohm’s law while considering  $\mathbf{B} = 0$  inside the superconductor as a fundamental law, not just a particular case, arriving at what is now referred to as **the second London equation** [15, 21, 23]:

$$\nabla \times \frac{m^*}{n_s e^{*2}} \mathbf{J}_s = -\mathbf{B} \quad \Rightarrow \quad \nabla^2 \mathbf{B} = \frac{\mu_0 n_s e^{*2}}{m^*} \mathbf{B} = \frac{1}{\lambda_L^2} \mathbf{B}. \quad (1.1)$$

Here,  $\mu_0$  is the vacuum magnetic permeability,  $\mathbf{J}_s$  is the superconducting current density,  $m^*$  and  $e^*$  respectively reflect the effective mass and charge of the superconducting charge carriers, and  $n_s$  is the density of such entities, i.e., non-scattering electrons. The above equation is in SI units, as I shall adopt in this Chapter.

There are two solutions for Equation (1.1). The first is the trivial case, which gives  $\mathbf{B} = 0$ . The other solution states that  $\mathbf{B}$  inside the superconductor exponentially decays from its value at the surface— $\mu_0 \mathbf{H}$ , where  $\mathbf{H}$  is the applied magnetic field—to zero over a characteristic length  $\lambda_L$  of the order of hundreds of nanometers [23]. Therefore, Equation (1.1) correctly captures the Meissner-Ochsenfeld effect. As  $\nabla \times \mathbf{B} = \mu_0 \mathbf{J}_s$ , it also implies that supercurrents flow in the superconductor shielding it from magnetic flux, generating a magnetization field opposite to  $\mathbf{H}$ . The shielding currents are confined to the same thin surface defined by  $\lambda_L$ .

As the London brothers note in their original paper, although Equation (1.1) allows the description of the Meissner-Ochsenfeld effect, it does not capture the infinite conductivity

aspect of the superconducting state. That, they achieved by considering that an electric field  $\mathbf{E}$  accelerates the superfluid according to the equation of motion  $m^*\partial\mathbf{v}_s/\partial t = -e^*\mathbf{E}$ , where  $\mathbf{v}_s$  is the velocity of the superconducting charge carriers. As  $\mathbf{J}_s = n_s e^* \mathbf{v}_s$ , they stated that

$$\mathbf{E} = \frac{m^*}{n_s e^{*2}} \frac{\partial \mathbf{J}_s}{\partial t} = \mu_0 \lambda_L^2 \frac{\partial \mathbf{J}_s}{\partial t}, \quad (1.2)$$

which is known as **the first London equation**. It captures the infinite conductivity of the superconducting state, given that the superfluid electrons flow in a steady state.

Given the above considerations,  $\lambda_L$  is known as the London **penetration depth**. It is the first of the superconducting characteristic length scales. Although phenomenological descriptions, the previous work by Gorter and Casimir and the London equations are regarded as the first fundamental building blocks toward a microscopic description of superconductivity. In fact, already in 1935, F. London suggested that the London equations had a quantum mechanical interpretation as the diamagnetism would result from the coherence of the ground state electronic wave function [12]. However, as the War again abruptly interrupted the progress of our understanding of superconductivity, it would take over a decade before another milestone was achieved in the field. This would come in 1948, when Fritz proposed that the London equations characterized superconductivity as the condensation of a quantum state in the momentum space, leading to long-range order of the momentum vector in real space [24]. In other words, he understood that superconductivity is a macroscopic quantum coherent state [15].

## 1.5 The Ginzburg-Landau theory

Parallel to the scientific development in the West, brilliant minds tackled the problem of superconductivity in the Soviet Union. The task of finding a complete phenomenological theory for the phenomenon was particularly of great interest to Lev Davidovich Landau, who even before the discovery of the Meissner-Ochsenfeld effect thought it would be

implausible to explain superconductivity simply as an extension of Drude's formalism for conducting electrons [15]. During the early 1930s, Landau would already experiment with descriptions of the superconducting state's free energy that contained features that would become a mark of his seminal theory of the second-order phase transition [25].

It should be noted that, although the London equations successfully described the Meissner-Ochsenfeld effect, they had relevant shortcomings. To wit, they do not describe the transition from the normal to the superconducting state by applied currents and magnetic fields, nor the surface energy at the normal-superconducting interface. Hence, in 1950, Landau and Vitaly Lazarevich Ginzburg published a phenomenological theory of superconductivity aiming to solve these problems [26]. The Ginzburg-Landau (GL) theory was based on Landau's second-order phase transition theory. This was supported by the previous experimental observation that a superconducting transition under zero magnetic field resulted in a specific heat discontinuity at  $T_c$  and no latent heat.

The GL theory postulates the existence of a spatially-varying complex order parameter [15, 21, 27]

$$\psi(\mathbf{r}) = |\psi(\mathbf{r})| \exp^{-i\phi(\mathbf{r})} \quad (1.3)$$

with modulus  $|\psi(\mathbf{r})|$  and phase  $\phi(\mathbf{r})$ . It relates to the effective density of superconducting charge carriers as  $|\psi(\mathbf{r})|^2 = |\psi|^2 = n_s$ . Hence, above  $T_c$ ,  $\psi$  equals zero, whereas it is finite in the superconducting state, below  $T_c$ . Near the second-order phase transition,  $\psi$  is small. Following Landau's theory, the Gibbs free energy difference per unit volume between the normal and superconducting phases can then be written as a power expansion of  $|\psi|^2$

$$G_s(T) - G_n(T) = \alpha(T)|\psi|^2 + \frac{1}{2}\beta(T)|\psi|^4, \quad (1.4)$$

where  $\alpha(T)$  and  $\beta(T)$  are phenomenological parameters that depend only on  $T$ . For the free energy to have a minimum and Eq. (1.4) to have physical meaning,  $\beta(T)$  should be positive. Then, above  $T_c$ ,  $\alpha(T)$  should be positive, such as the free energy of the superconducting state is higher than that of the normal state. Below  $T_c$ ,  $\alpha(T)$  is negative and the



system's minimum free energy is given by the condition  $|\psi|^2 = |\psi_0|^2 = |\alpha(T)|/\beta(T)$ , at which the superconducting state is at equilibrium. Therefore, in the absence of an applied magnetic field, the condensation energy of the superconducting phase can be written in terms of the thermodynamic critical field  $H_c$  as

$$\frac{\alpha^2(T)}{2\beta(T)} = \frac{\alpha_0^2(T/T_c - 1)^2}{2\beta_0} = \frac{H_c^2}{2\mu_0}, \quad (1.5)$$

where  $\beta(T) = \beta_0 > 0$  and  $\alpha(T) = \alpha_0(T/T_c - 1)$ , with  $\alpha_0 > 0$ . The temperature dependencies of  $\alpha(T)$  and  $\beta(T)$  are simplifying hypotheses that enable the problem to be treated analytically. In principle, they limit the validity of the GL theory for temperatures close to  $T_c$ , where the linear  $H_c(T)$  behavior expressed by Eq. (1.5) is a reasonable approximation.<sup>4</sup> Figure 1.4 schematically depicts the Gibbs free energy difference showing minima for  $T < T_c$ , highlighting the  $|\psi|$  equilibrium value and the condensation energy.

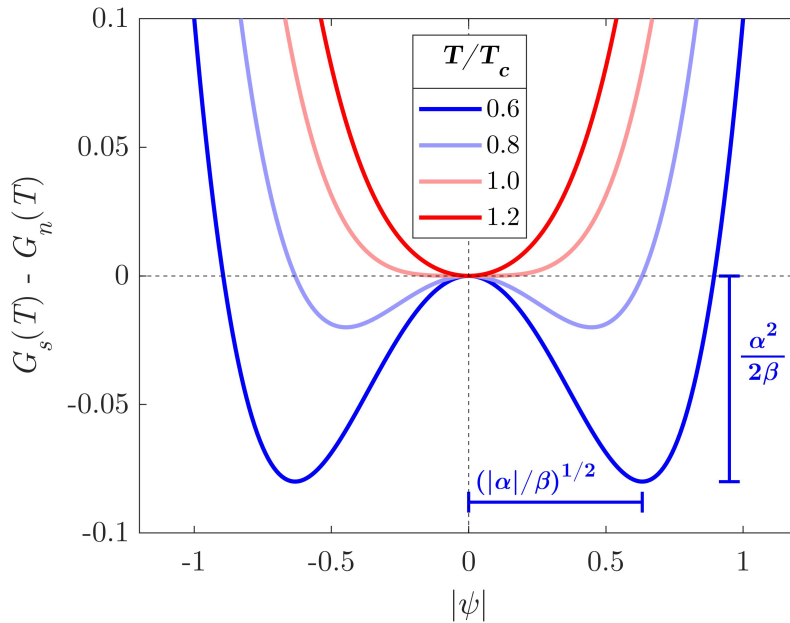


**Figure 1.4.** Gibbs free energy difference between the superconducting and normal states without an applied magnetic field as a function of  $|\psi|$ . The graphs are plotted according to Eq. (1.4) and using the definitions of Eq. (1.5) with  $\alpha_0 = \beta_0 = 1$ .

Taking into account the slow spatial variation of  $\psi(\mathbf{r})$  near the normal-superconducting

---

<sup>4</sup>One can overcome this limitation by choosing  $\alpha(T)$  and  $\beta(T)$  such that  $H_c \propto (1 - T^2/T_c^2)$  [28], by extending the functional to higher orders in  $(1 - T/T_c)$  [29], or by assuming a local electrodynamics [30].

transition and the existence of an applied magnetic field, the Gibbs free energy difference in Eq. (1.4) can be written as

$$G_s - G_n = \alpha(T)|\psi|^2 + \frac{1}{2}\beta(T)|\psi|^4 + \frac{1}{2m^*}|(-i\hbar\nabla + e^*\mathbf{A}(\mathbf{r}))\psi|^2 + \frac{\mathbf{B}^2}{2\mu_0}, \quad (1.6)$$

where the added terms represent, respectively, the kinetic energy of the superconducting charge carriers and the energy density stored due to the magnetic field. The vector potential  $\mathbf{A}$  is related to the induced magnetic field as  $\mathbf{B}(\mathbf{r}) = \nabla \times \mathbf{A}(\mathbf{r})$ .

Then, minimizing the total Gibbs free energy of the superconducting state,  $\int d^3\mathbf{r}G_s$ , with respect to variations in  $\psi(\mathbf{r})$ , we obtain

$$\alpha(T)\psi(\mathbf{r}) + \beta|\psi|^2\psi(\mathbf{r}) + \frac{1}{2m^*}(-i\hbar\nabla + e^*\mathbf{A}(\mathbf{r}))^2\psi(\mathbf{r}) = 0, \quad (1.7)$$

which is known as **the first Ginzburg-Landau equation** and allows for the description of the spatial variation of the order parameter. Although Eq. (1.7) resembles the Schrödinger equation and we are aware of the quantum nature of superconductivity, one should not take the order parameter as a wave function for the superconducting charge carriers, but rather as a representation of some averaged quantity that enables currents to flow [15].

According to Eq. (1.6),  $\int d^3\mathbf{r}G_s$  is also a functional of  $\mathbf{A}(\mathbf{r})$ . Then, minimizing the free energy with respect to variations in  $\mathbf{A}(\mathbf{r})$ , selecting the gauge where  $\nabla \cdot \mathbf{A}(\mathbf{r}) = 0$ , and using  $\nabla \times \mathbf{B} = \mu_0\mathbf{J}_s$  and Eq. (1.3), we arrive at **the second Ginzburg-Landau equation**

$$\mathbf{J}_s = -\frac{ie^*\hbar}{2m^*}(\psi^*(\mathbf{r})\nabla\psi(\mathbf{r}) - \psi(\mathbf{r})\nabla\psi^*(\mathbf{r})) - \frac{e^{*2}}{m^*}\mathbf{A}(\mathbf{r})|\psi|^2 = \frac{e^{*2}}{m^*}\left(\frac{\hbar}{e^*}\nabla\phi - \mathbf{A}(\mathbf{r})\right)|\psi|^2, \quad (1.8)$$

which reveals the distribution of the superconducting currents flowing inside a material in the superconducting state.

Therefore, the GL equations are a set of coupled differential equations that spatially resolve the behavior of a superconductor near the superconducting-normal state transition,

i.e., as  $T \rightarrow T_c$ . Considering appropriate boundary conditions<sup>5</sup> near the interface between a semi-infinite superconductor ( $x > 0$ ) and a non-superconducting material ( $x < 0$ ) and the absence of applied magnetic fields, i.e.,  $\mathbf{A}(\mathbf{r}) = 0$ , the first GL equation can be rewritten as

$$\frac{\hbar^2}{2m^*} \frac{d^2\psi(x)}{dx^2} + \alpha(T)\psi(x) + \beta(T)|\psi|^2\psi(x) = 0 \Rightarrow \xi^2(T) \frac{d^2f(x)}{dx^2} + f(1 - f^2) = 0, \quad (1.9)$$

where  $f = \psi/\psi_0$  and

$$\xi(T) = \sqrt{\frac{\hbar}{2m^*|\alpha(T)|}} \propto \sqrt{\frac{1}{1 - T/T_c}}. \quad (1.10)$$

Then, solving the modified first GL equation leads to

$$\psi(x) = \psi_0 \tanh\left(\frac{x}{\sqrt{2}\xi}\right). \quad (1.11)$$

The parameter  $\xi$  then receives the name of **coherence length** and it is the second characteristic length of superconductors. Equation (1.11) describes how the order parameter increases inside superconducting materials at the interface with a normal region. This way,  $\xi$  can be described as the length scale in which the order parameter will recover from variations of its equilibrium value.

Looking now at the second GL equation, in the absence of an applied field, hence with no circulating currents, we realize that  $\psi^*(\mathbf{r})\nabla\psi(\mathbf{r}) = \psi(\mathbf{r})\nabla\psi^*(\mathbf{r})$ , which implies that the phase  $\phi(\mathbf{r}) = \phi$  is position independent. In the case of a weak magnetic field, the order parameter is approximately constant and  $|\psi| = |\psi_0|$ . Given that  $\nabla \times \mathbf{B} = \mu_0\mathbf{J}$ , Eq. (1.8) is written as

$$\nabla^2 \mathbf{B} = \frac{\mu_0 e^*{}^2 |\psi_0|^2}{m^*} \mathbf{B}, \quad (1.12)$$

which is analogous to the second London equation [Eq. (1.1)]. Therefore, the London equations are a particular case of the GL theory, which, in turn, describes the penetration

---

<sup>5</sup>In their original paper, Ginzburg and Landau provide what is referred to as a natural boundary condition choice [15],  $\hat{\mathbf{n}} \cdot (-i\hbar\nabla - e^*\mathbf{A}(\mathbf{r}))\psi(\mathbf{r}) = 0$ , valid only exactly at a superconductor-insulator interface, where  $\hat{\mathbf{n}}$  is the direction normal to the interface. Consider, for instance, the interface of a superconducting material and vacuum. In 1964, Pierre-Gilles de Gennes proposed a more general boundary condition, valid in the interface between a superconductor and a normal metal [31].

depth as

$$\lambda(T) = \sqrt{\frac{m^* \beta}{\mu_0 e^{*2} |\alpha(T)|}} \propto \sqrt{\frac{1}{1 - T/T_c}}. \quad (1.13)$$

Importantly, although strictly only valid as  $T \rightarrow T_c$ , the obtained GL equations work well at low temperatures, provided that  $\xi$  and  $\lambda$  are known at those temperatures. They also provide a clear look into the quantum nature of superconductivity. Consider now a superconductor under a given applied magnetic field, so that a shielding current density flows as described by the second GL equation [Eq. (1.8)]. By taking the line integral of  $\mathbf{J}_s$  around an arbitrarily closed contour and employing the Stokes theorem (as  $\mathbf{B} = \nabla \times \mathbf{A}$ ), we find that

$$\frac{m^*}{e^{*2}} \oint \frac{\mathbf{J}_s}{|\psi(\mathbf{r})|^2} \cdot d\mathbf{l} + \int \mathbf{B} \cdot d\mathbf{s} = \frac{\hbar}{e^*} \oint \nabla \phi \cdot d\mathbf{l}, \quad (1.14)$$

where we identify  $\Phi = \int \mathbf{B} \cdot d\mathbf{s}$  as the flux through the superconductor. As the order parameter is a single-valued function, the integral over the phase  $\phi$  around any closed contour must be a multiple of  $2\pi$ , which implies that

$$\Phi' = \frac{m^*}{e^{*2}} \oint \frac{\mathbf{J}_s}{|\psi(\mathbf{r})|^2} \cdot d\mathbf{l} + \Phi = \frac{\hbar}{e^*} 2\pi n = n\Phi_0, \quad (1.15)$$

where  $n$  is an integer winding number. This is a powerful result, valid for any superconductor as described by the GL theory. It defines  $\Phi'$  (called a “fluxoid”) as the sum of the enclosed flux and the line integral involving the current density. More importantly, Eq. (1.15) shows that the fluxoid is quantized, defining the magnetic flux quantum  $\Phi_0 = h/e^*$ .<sup>6</sup>

The quantization of the magnetic flux enclosed by a superconductor had just been predicted by F. London [32] and would later be confirmed by experiments independently conducted by Deaver and Fairbank [33] and by Doll and Nábauer [34] in 1961 in papers submitted to Physical Review Letters within a three-day interval. It was one of many suc-

---

<sup>6</sup>*Spoilers for Section I.7:* In 1950, the superconducting charge carriers were still unknown. After the BCS theory applied the concept of Cooper pairs to describe superconductivity in 1957, the flux quanta could be correctly identified as  $\Phi_0 = h/2e \approx 2.068 \times 10^{-15}$  Wb.

cesses of the GL theory, which is to this day the preferred description of superconductivity for many physicists worldwide.

## 1.6 Type-I and Type-II superconductors

Another fundamental feature of Ginzburg and Landau's theory is the prediction of type-II superconductivity. To achieve that, let us define the ratio

$$\kappa = \frac{\lambda(T)}{\xi(T)} \tag{1.16}$$

known as the **Ginzburg-Landau parameter**. The fact that  $\kappa$  appears to be independent of temperature is a product of the simplifying assumptions for the temperature dependencies of  $\alpha(T)$  and  $\beta(T)$ . In practice, however,  $\kappa$  decreases with increasing temperatures [28, 35]. Writing  $\kappa$  as a function of  $H_c$  allows one to write down dimensionless GL equations that depend on this unique material parameter.<sup>7</sup> As I will discuss,  $\kappa$  is associated with a fundamental property of superconducting materials, the surface energy of the interface between the normal and superconducting phases [15].

Let's again think about the interface between a non-superconducting and a superconducting phase, both homogeneous. As demonstrated by the GL equations, the order parameter has a given equilibrium value with modulus  $|\psi_0|$  deep inside the superconductor and vanishes as it approaches the interface with a characteristic length scale  $\xi$ . Meanwhile, shielding currents circulating within a surface layer with thickness  $\lambda$  exponentially restrict magnetic flux penetration into the superconductor. This interplay gives rise to a surface tension between the homogeneous phases, leading to a "mixed phase" region, in which superconductivity is not fully established [21].

Such a surface tension,  $\sigma_{ns}$ , is defined by the free energy difference between a given homogeneous phase (either normal or superconducting) and the mixed phase. Considering the Gibbs free energy in Eq. (1.6) and the first GL equation (1.7), at the thermodynamic

---

<sup>7</sup>For a step-by-step derivation, see Chapter 6, Section XI of Ref. [21].

critical field  $H_c$ <sup>8</sup>

$$\sigma_{ns} \approx \frac{H_c^2}{2\mu_0}(\xi - \lambda). \quad (1.17)$$

Therefore,  $\sigma_{ns}$  may be either positive or negative, depending on the relationship between  $\xi$  and  $\lambda$  or, alternatively, on the value of  $\kappa$ . In their original work, GL showed that  $\sigma_{ns} > 0$  if  $\kappa < 1/\sqrt{2}$ . They argued that this was the most relevant solution, as the experimental data available at the time indicated that most superconductors followed the relationship  $\kappa \ll 1$  [15].

If  $\sigma_{ns}$  is positive, the homogeneous phase has lower free energy than the mixed phase. In this case, the superconducting material will completely expel magnetic flux from its interior (Meissner state) until the applied magnetic field reaches  $H_c$ . At such a point, superconductivity can no longer be sustained and the material undergoes an abrupt transition to the normal state. These materials are called **type-I superconductors**.

It would be a couple of works published in the 1950s by Alexei Alexeyevich Abrikosov that revealed striking results on the behavior of materials with  $\kappa > 1/\sqrt{2}$ , known as **type-II superconductors** [36–38]. In the case of a negative  $\sigma_{ns}$ , it is energetically favorable for a superconductor to develop normal regions containing magnetic flux. As expected, they present some remarkably different properties than their type-I counterparts. As the applied magnetic field is increased, a type-II will remain in the Meissner state until  $H$  reaches a value  $H_{c1}$  known as the **lower critical field**. At such a field, the material allows the entrance of magnetic flux, of which the density grows as  $H$  is further increased. This is called the **mixed state**. When the applied field reaches a value

$$H_{c2} = \frac{\Phi_0}{2\pi\mu_0\xi^2} = \sqrt{2}\kappa H_c, \quad (1.18)$$

known as the **upper critical field**, the superconductor transitions to the normal state.  $H_{c2}$  can be obtained from the first GL equation and expresses the limit in which the

---

<sup>8</sup>For a derivation of the expression for  $\sigma_{ns}$  and more in-depth discussion, I refer to Chapter 6, Section XII of Ref. [21].

distance between magnetic flux regions is of the order of  $\xi$ . A schematic comparison of the characteristic  $H$ -vs- $T$  phase diagram and the field-dependent magnetization  $M(H)$  of both types of superconductors is presented in Fig. 1.5. As, in the Meissner state,  $\mathbf{B} = \mu_0(\mathbf{H} + \mathbf{M}) = 0 \Rightarrow \mathbf{H} = -\mathbf{M}$ .

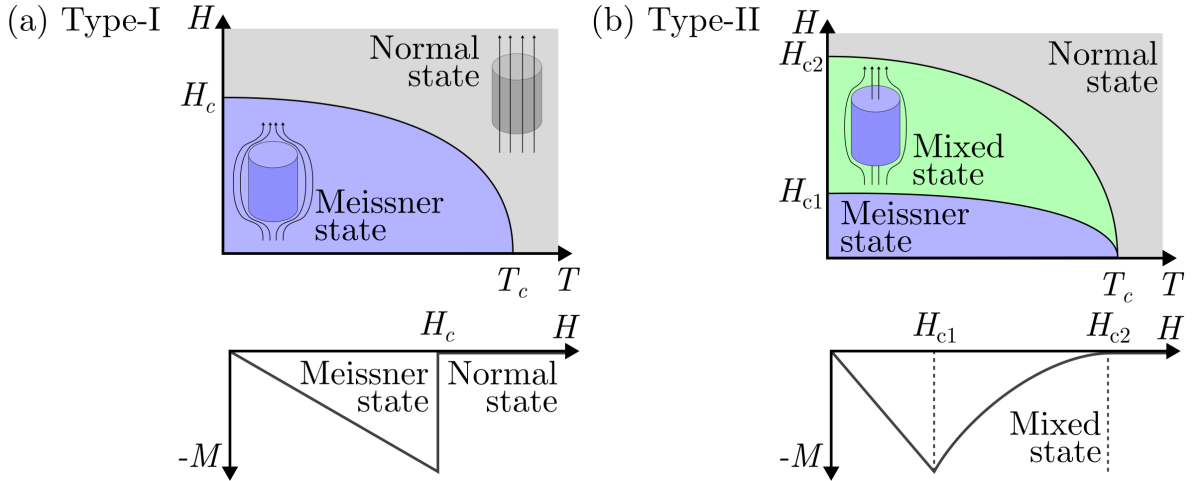


**Figure 1.5.** Schematic representation of  $H$ -vs- $T$  phase diagram and  $M(H)$  behavior with  $T < T_c$  for (a) a type-I superconductor and (b) a type-II superconductor. The graphs depict the existence of a mixed state for type-IIs, in which the superconducting state coexists with magnetic flux penetrated in the form of vortices.

For the mixed state energy to be minimal, the ratio between the surface area of flux-field regions and the magnetic flux needs to be maximum, meaning the regions should be as small as possible. This condition is consistent with the fluxoid quantization discussed in Section 1.5. Thus, as shown by Abrikosov, magnetic flux penetrates superconductors as fluxoids or **vortices** carrying a single flux quantum and separated from the superconducting phase by circulating shielding currents. From the previous discussions on the physical meanings of  $\xi$  and  $\lambda$ , it is possible to grasp the fact that the radius of the normal vortex core, in which the order parameter is approximately null, is equal to  $\xi$ , whilst the shielding currents flow within a radius  $\lambda$ , stopping flux penetration. This can be demonstrated considering the London approximation, in which  $\kappa \gg 1$  and vortices can be treated as isolated entities as the order parameter is constant everywhere but at the vortex core. If

the applied field is perpendicular to the superconductor's surface (let's say along the  $\hat{z}$  direction), the problem is two-dimensional. Hence, assuming that a vortex is located at the origin of the coordinate system, the second London equation [Eq. (1.1)] is modified to

$$\lambda^2 \nabla^2 \mathbf{B} - \mathbf{B} = \Phi_0 \delta(\mathbf{r}) \hat{z}, \quad (1.19)$$

where  $\delta(\mathbf{r})$  is the bidimensional Dirac delta function. Solving the above equation reveals that the perpendicular component of the magnetic flux density  $B_z$  around a vortex behaves as

$$B_z(r) = \frac{\Phi_0}{2\pi\lambda^2} K_0\left(\frac{r}{\lambda}\right) \propto \begin{cases} \ln(r/\lambda), & \text{if } r \rightarrow 0 \\ \exp(-r/\lambda), & \text{if } r \rightarrow \infty \end{cases}, \quad (1.20)$$

where  $K_n$  is a  $n$ th-order Bessel function. Accordingly, the absolute value of the shielding current density is given as a function of the distance to the vortex as

$$J_s(r) = \frac{\Phi_0}{2\pi\lambda^3} K_1\left(\frac{r}{\lambda}\right). \quad (1.21)$$

Equations (1.20) and (1.21) are plotted in Fig. 1.6(a) together with the spatial distribution of the order parameter around an isolated vortex.

To understand what happens in the presence of multiple vortices, we can investigate the interaction between two of them. First, we realize that the energy required to create a single vortex,  $\mathcal{E}_v$ , is a combination of contributions arising from the magnetic field energy, the circulating shielding currents, and suppression of the condensation energy at the vortex core, leading to

$$\mathcal{E}_v = \frac{\Phi_0^2}{4\pi\mu_0\lambda^2} \ln(\kappa + c), \quad (1.22)$$

where  $c$  accounts for the condensation energy loss. Inspecting Eq. (1.22), we see that  $\mathcal{E}_v$  depends quadratically on the vortex flux. Therefore, the energy required to create one vortex bearing a magnetic flux  $n\Phi_0$  is higher than that required to create  $n$  vortices with flux  $\Phi_0$ . This is why I have been neglecting  $n > 0$  solutions in previous equations. It should be said, however, that such multiquanta vortices do exist in nature, particularly at mesoscopic systems [39].



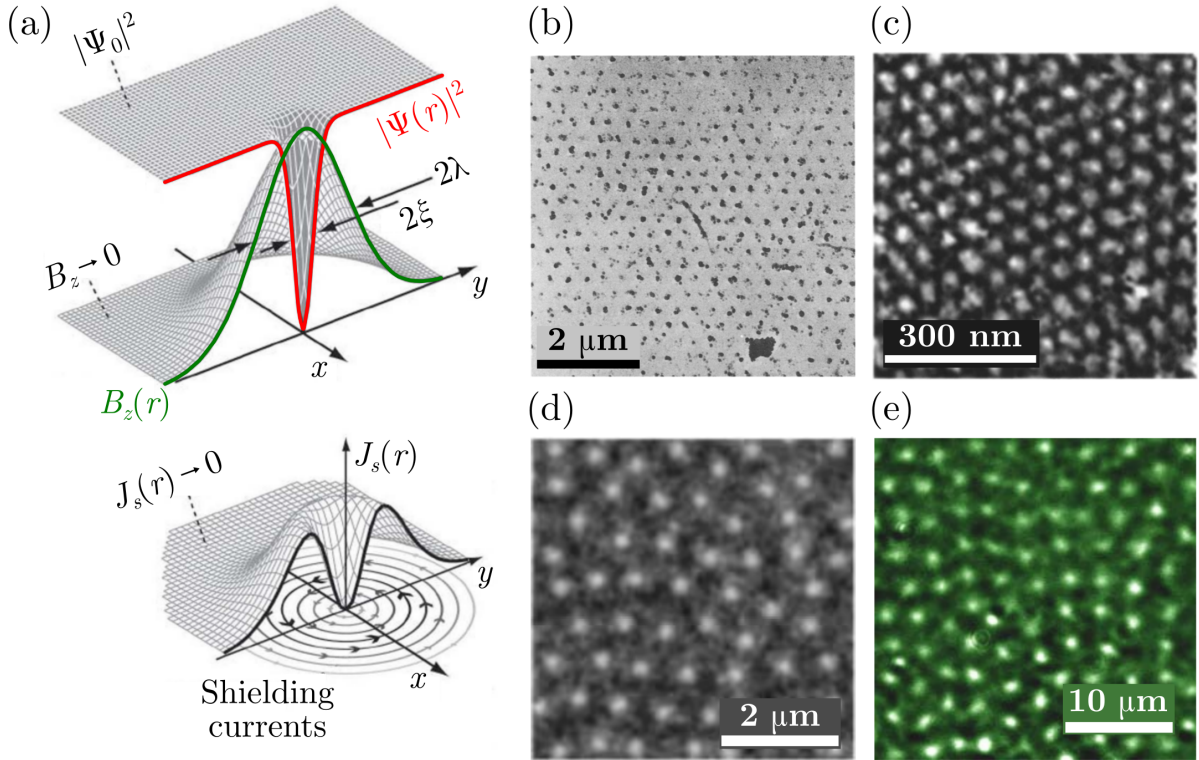


**Figure 1.6.** (a) Structure of a vortex. The top panel shows  $B_z$  as a function of position around the core of a vortex (green line) together with the behavior of  $|\Psi|^2$  (red). The bottom panel shows the shielding currents distribution. The right panel shows selected examples of visualization of vortices in superconductors: (b) first observation of the Abrikosov lattice, captured by Bitter decoration in a Pb-In alloy [40]; vortices in (c) amorphous  $\text{Mo}_{2.7}\text{Ge}$  thin film revealed by scanning-tunneling microscopy [41]; (d) Nb thin film revealed by magnetic-force microscopy [42]; and (e)  $\text{NbSe}_2$  single crystal revealed by magneto-optical imaging [43]. The Abrikosov lattice distortions evident in panels (d) and (e) result from vortex pinning. Adapted from [44].

If multiple vortices permeate the superconductor, within the London approximation, the induced magnetic flux density is a superposition of the flux carried by each vortex, then

$$B_z = \sum_i \frac{\Phi_0}{2\pi\lambda^2} K_0\left(\frac{r_i}{\lambda}\right). \quad (1.23)$$

For simplicity, considering a system containing two vortices located at  $\mathbf{r}_i$  and  $\mathbf{r}_j$  and separated by a distance  $r_{ij}$ , as Eq. (1.22) is position-independent, the system energy is

given by

$$\mathcal{E}_v^{ij} = \mathcal{E}_v^i + \mathcal{E}_v^j + \Phi_0 U_{ij}(r_{ij}) = 2\mathcal{E}_v + \frac{\Phi_0^2}{2\pi\mu_0\lambda^2} K_0 \left( \frac{r_{ij}}{\lambda} \right), \quad (1.24)$$

where the interaction term  $U_{ij}$  is determined by the magnetic field at vortex  $i$  due to the presence of vortex  $j$  or vice-versa. Hence, vortices with magnetic flux pointing in the same direction interact repulsively. It is also possible, depending on how they are nucleated, that vortices exist in the superconducting material with opposite flux directions, forming a vortex-antivortex pair. In this case, we find that the interaction is attractive and will lead to a mutual annihilation when the pair comes in close proximity [45, 46].

Considering a superconductor permeated only by vortices with the same flux direction, the repulsive interaction implies that there is an equilibrium periodic configuration rather than a random distribution of vortices that minimizes the system's energy. This problem was tackled by Abrikosov in 1957 [37]. In the limit in which  $\Psi(\mathbf{r}) \rightarrow 0$  and considering that  $\Psi(\mathbf{r})$  depends only on  $x$ , choosing a gauge in which  $A_y = Hx$ , where  $A_y$  is the  $y$ -direction component of  $\mathbf{A}$  and  $H \rightarrow H_{c2}$  is a constant applied magnetic field, he found that, neglecting non-linear terms, the first GL equation in normalized units<sup>9</sup> took the form of a quantum oscillator equation

$$\frac{d^2\Psi(\mathbf{r})}{dx^2} + \kappa^2 H^2 x^2 \Psi(\mathbf{r}) = \kappa^2 \Psi(\mathbf{r}) \quad (1.25)$$

for which the solution is

$$\Psi(\mathbf{r}) = \sum_i C_i \exp \left[ iqny - \frac{\kappa^2}{2} \left( x^2 - \frac{qn}{\kappa^2} \right)^2 \right], \quad (1.26)$$

with  $C_i$  and  $q$  being arbitrary coefficients. Inserting this result into the second GL equation, Abrikosov showed that

$$B = H - \frac{q - H}{\beta_A(2\kappa^2 - 1)}, \quad \text{where } \beta_A = \frac{|\Psi|^4}{(|\Phi|^2)^2}. \quad (1.27)$$

---

<sup>9</sup>The unit transformation is  $\Phi \rightarrow \Phi/\Phi_0$ ,  $\mathbf{B} \rightarrow \mathbf{B}/(\sqrt{2}H_c)$ , and  $\mathbf{r} \rightarrow \mathbf{r}/\lambda$ .

Returning to the Gibbs free energy per unit volume proposed by GL, Abrikosov used the above reasoning to write down that

$$G_s - G_n \propto B^2 - \frac{\kappa - B}{1 + \beta_A(2\kappa^2 - 1)}. \quad (1.28)$$

Therefore, to minimize the free energy means to minimize the parameter  $\beta_A$ , for which he obtained a value of

$$\frac{\partial \beta_A}{\partial C_i^*} = 0 \Rightarrow \beta_A = \frac{q}{\kappa\sqrt{2}} \left[ \sum_i \exp\left(-n^2 \frac{q^2}{2\kappa^2}\right) \right]^2, \quad (1.29)$$

while imposing the periodicity of  $\Psi(\mathbf{r})$  in  $x$  from the recursion relationship  $C_i = C_{i+1}$ , meaning that the vortex would arrange in the form of a square lattice. In this case, Abrikosov found that  $\beta_A^{\min} = 1.18$ . In 1964, W. H. Kleiner, L. M. Roth, and S. H. Autler revisited Abrikosov's formalism and proved that a recursion relationship of the type  $C_i = C_{i+2}$ , corresponding to a triangular lattice, would actually result in lower free energy, with  $\beta_A^{\min} = 1.16$  and, therefore, would be the preferred vortex arrangement in the mixed state [47].<sup>10</sup>

The periodic arrangement of vortices as a triangular lattice in type-II superconductors has become known as the **Abrikosov lattice**. Its prediction is one of the major theoretical achievements in superconductivity. The existence of the Abrikosov lattice was experimentally confirmed in 1967 using the Bitter decoration technique to map the magnetic flux on the surface of a Pb-In alloy [40]. Since then, a number of different techniques have been employed to visualize and study vortices in superconductors, from which I have selected some images to show in Fig. 1.6(b-e). It would take too many years, but in 2003, Ginzburg and Abrikosov, together with Anthony James Leggett, were awarded the Nobel Prize in Physics “for pioneering contributions to the theory of superconductors and superfluids”. Unfortunately, Landau had passed away thirty-five years earlier, but in 1962

---

<sup>10</sup>In Abrikosov's paper from 1957, he states that he also investigated the case of a triangular lattice. There, however, he found by numerical integration that  $\beta_A^{\min} = 1.32$ , slightly off from the correct result.

he too was awarded the Nobel Prize in Physics “for his pioneering theories for condensed matter, especially liquid helium”.

## 1.7 Macroscopic flux penetration

The triangular vortex lattice is an equilibrium configuration. It follows from Eq. (1.24) that the force per unit length vortex  $i$  exerts in vortex  $j$  is [21, 48, 49]

$$\mathbf{F}_{ij} = \mathbf{J}_i \times \Phi_j = \mathbf{J}_i \times \Phi_0 \hat{\mathbf{z}}. \quad (1.30)$$

Such force induces vortices to move with a velocity  $\mathbf{v}$  perpendicular to the current direction during the penetration process, pushing them into the interior of the sample. This leads to opposing damping and Magnus forces acting on the vortices. Such dynamics give rise to an electric field  $\mathbf{E}$ , which, in turn, may lead to power dissipation. An analogous process occurs in the presence of an applied transport current. In light of this picture, one might be tempted to say that vortices are unwanted for applications of superconductivity, as the dissipated energy would eliminate one of the most enticing characteristics of the phenomenon. However, it is actually vortex movement that should be avoided, which leads to the concept of **vortex** or **flux pinning**.

Let us consider a superconductor with  $n$  vortices, such as the total flux density is  $\mathbf{B} = n\Phi_0\hat{\mathbf{z}}$ , experiencing a total current density  $\mathbf{J}$ . From the above discussion, the vortex lattice will move subject to an average Lorentz force density

$$\mathbf{f}_L = \mathbf{J} \times \mathbf{B}. \quad (1.31)$$

To pin the magnetic flux, i.e., stop vortices from moving, an opposing force must act on the material. This is known as the pinning force  $\mathbf{F}_p$ . As it should balance out  $\mathbf{f}_L$ , the pinning force density defines the maximum current density a superconductor can carry without triggering a dissipative process, i.e., remaining superconducting, as  $\mathbf{f}_p = -\mathbf{J}_c(T, B) \times \mathbf{B}$ , where the critical current density  $\mathbf{J}_c$  generally depends on both temperature and the induced flux density in the superconductor.

The origin and description of pinning forces is an interesting and complex matter explored by several models, which will not be discussed in depth in this thesis.<sup>11</sup> Essentially, to pin vortices, the material must present some inhomogeneity that locally suppresses the superconducting properties. Thus, this point has a lower condensation energy facilitating vortex nucleation as per Eq. (1.22). These **pinning centers** also act as attractive potentials for vortices nucleated somewhere else in the material effectively trapping them until a Lorentz force greater than  $F_p$  acts on the flux entities. These reduced free energy regions cause distortions in the Abrikosov lattice, as evidenced by Fig. 1.6(d-e).

Pinning centers trap vortices more effectively if their size is of the order of  $\xi$ , i.e., similar to the vortex core size. They may be intrinsic to the material, arising from the presence of any kind of impurities and defects such as vacancies or dislocations, or due to grain boundaries and non-superconducting regions in granular superconductors. Moreover, as trapping vortices is essential to increase the amount of current able to flow in the superconducting state (more pinning means higher  $J_c$ ), the introduction of artificial pinning centers has been an important strategy in the development of superconducting technology. There are different means to achieve that, but the idea is always to create “defective” regions of suppressed superconducting properties. As examples pertinent to this thesis, I can point to the creation of columnar defects by ion beam irradiation [50] and the introduction of nanofabricated arrays of through holes, called antidots [49, 51].

### 1.7.1 Critical state models

Flux penetration in the mixed state can also be treated from a macroscopic perspective. This approach disregards the presence of individual vortices and treats all flux within a superconductor as a continuous flux front with density  $\mathbf{B}$ , which decreases from the surface toward the center of the specimen. As shielding currents arise to counteract the presence of magnetic flux, the overall current density  $\mathbf{J}$  flowing in a type-II is coupled to

---

<sup>11</sup>For further reading on this topic, I suggest the seminal review article by Blatter et al. [48]. Also, Chapter 9, Section V.B of Ref. [21] offers a list of more specific references.

$\mathbf{B}$  by Ampère’s law  $\nabla \times \mathbf{B} = \mu_0 \mathbf{J}$ . This is the main notion explored by **critical state models** [21, 52–54].

The critical state is defined as that in which all current flows with its critical value where there is penetrated magnetic flux in the superconductor, such as

$$\nabla \times \mathbf{B} = \mu_0 \mathbf{J}_c(T, \mathbf{B}) = \mu_0 \frac{J_0(T)}{f(\mathbf{B})} \hat{\mathbf{J}}, \quad (1.32)$$

where  $J_0(T)$  depends only on temperature,  $f(\mathbf{B})$  is some dimensionless function of the flux density, and  $\hat{\mathbf{J}}$  is the current density direction. The exact shape of the flux density profiles depends on the sample geometry. Moreover, different critical state models adopt different  $f(\mathbf{B})$  to try to emulate the behavior presented by real superconducting samples.

The simplest critical state model was introduced by Charles Bean in 1962 [53, 55]. Known as the **Bean model**, it assumes the critical current density to be independent of  $\mathbf{B}$ , i.e.,  $J_c^{\text{Bean}}(T, \mathbf{B}) = J_0(T)$ . For a long rectangular bulk superconductor, the Bean model describes flux penetration and shielding currents distribution as exemplified in Fig. 1.7(a–d). If the sample is zero-field cooled and then a perpendicularly applied magnetic field is progressively increased, the flux density decreases linearly from the edges toward the center of the superconductor, as described by Eq. (1.32) using  $J_c^{\text{Bean}}$ . For sufficiently low applied fields, there will be an inner, zero-flux Meissner state region within a distance  $a$  from the center of the sample. The distribution of the perpendicular component of  $\mathbf{B}$  is hysteretic and will continue to change in accordance with the magnetic field history, as shown in Fig. 1.7(e).

In the studies discussed in this thesis, we did not deal with bulk samples but rather thin films—samples with thicknesses in the nanometer range supported by a substrate. This change in geometry has severe implications for the interaction between the superconductor and an external magnetic field. For instance, if the film’s thickness  $d$  is smaller than the material’s penetration depth  $\lambda$ , the circulating currents will be restricted by this geometric factor. As was demonstrated by J. Pearl in 1964, this constriction modifies the

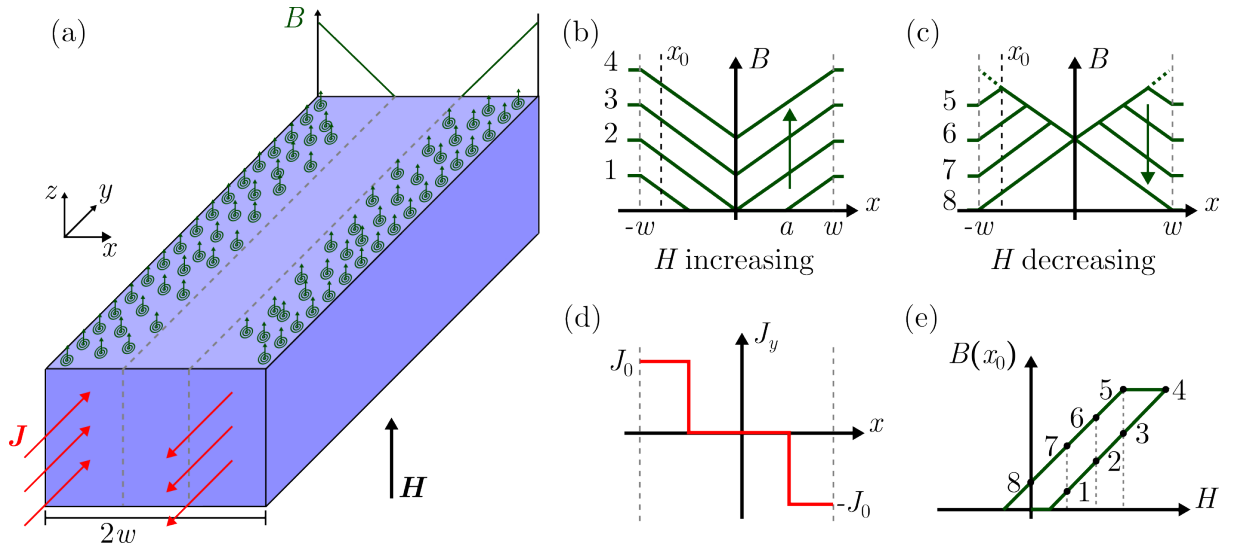


**Figure 1.7.** (a) A long bulk superconductor under a perpendicularly applied magnetic field  $\mathbf{H}$ , showing a pictorial representation of the flux distribution and shielding currents.  $B(x)$  is depicted according to the Bean model while  $H$  is (b) increased and (c) decreased. Panel (d) represents the  $J_y(x)$  distribution for the applied field labeled as 1. (e)  $B(x_0)$  as indicated in panels (a) and (b), evidencing the observed magnetic flux hysteresis in type-II superconductors. Adapted from [52].

characteristic length scale for flux penetration into the thin superconductor, giving rise to an effective penetration depth  $\Lambda(T) = 2\lambda^2(T)/d$  [56].

When treating flux penetration macroscopically, it is necessary to consider the emergence of non-negligible demagnetizing effects due to the reduction of the sample thickness [57, 59]. In the Bean model framework, this will lead to distinctively different flux and shielding current distributions for a thin specimen in comparison to a bulk sample. Figure 1.8 depicts the expected profiles for a long rectangular thin film as the external field is increased after ZFC. There are some important aspects to notice. As schematically represented in Fig. 1.8(a), the reduced thickness causes the induced field to tightly wrap around the film, leading to the accumulation of magnetic flux at the edges of the specimen. This also leads to a discontinuity in the  $\mathbf{B}$  component parallel to the film's surface, which dictates that currents flow in the whole sample instead of being confined to the flux front penetration depth.

The magneto-optical imaging (MOI) technique is a powerful tool to visualize such

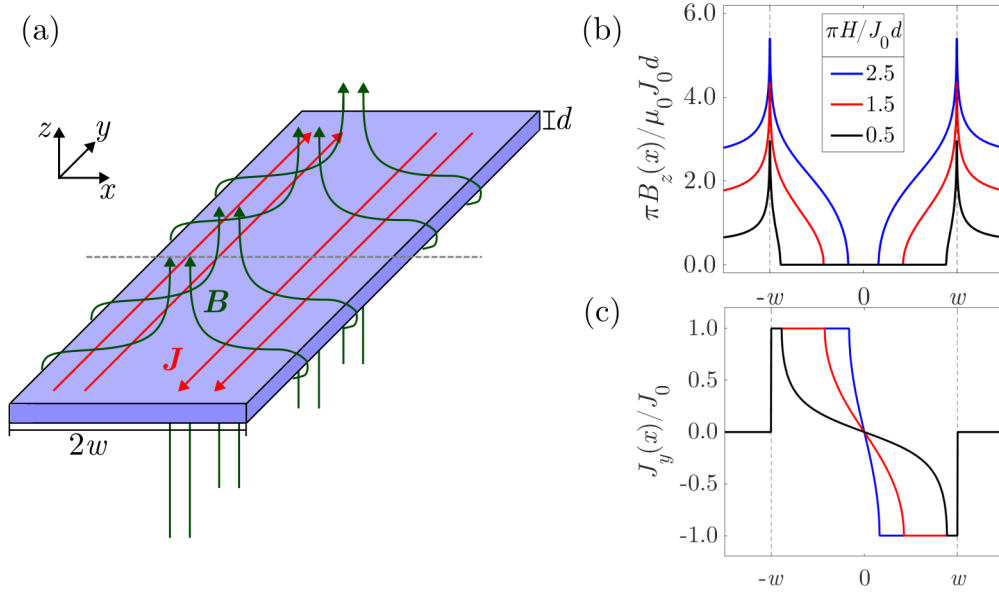


**Figure 1.8.** (a) Schematic representation of a long superconducting film subjected to a magnetic field applied perpendicularly to its surface. The film's thickness is  $d$  and its width is  $2w$ . The induced magnetic flux lines  $\mathbf{B}$  bend around the film due to the presence of circulating shielding currents  $\mathbf{J}$ . The (b)  $B_z(x)$  and (c)  $J_y(x)$  profiles after ZFC are obtained for different applied magnetic fields  $H$  according to the Bean model along the  $x$ -axis, as represented by the dashed gray line in panel (a) [57, 58].

macroscopic flux configurations, as it allows to resolve magnetic flux with a typical scale in the micrometer range [63]. Figure 1.9(a-c) shows quantitative MOI results obtained for a long  $\text{YBa}_2\text{Cu}_3\text{O}_{7-\delta}$  (YBCO) thin film, highlighting the observed flux density and shielding current profiles [60]. The solid lines are the Bean model predictions. This is a pristine example to demonstrate the effectiveness of the apparently oversimplified Bean model to describe commonly observed experimental results. Such a critical-state-like flux penetration is often referred to as **smooth flux penetration**. Figure 1.9(d-f) shows other examples of smooth penetration captured by MOI in different superconducting films.

There are, however, instances in which the Bean model does not capture important features of the flux penetration into type-II specimens, as will be exemplified in Chapter 4 of this thesis. In these cases, it is necessary to account for the  $\mathbf{B}$  dependency in Eq. (1.32). Several  $f(\mathbf{B})$  have empirically been adopted, leading to distinct critical state models [21]. Among these, a model proposed by Y. B. Kim, C. F. Hempstead, and A. R. Strnad is



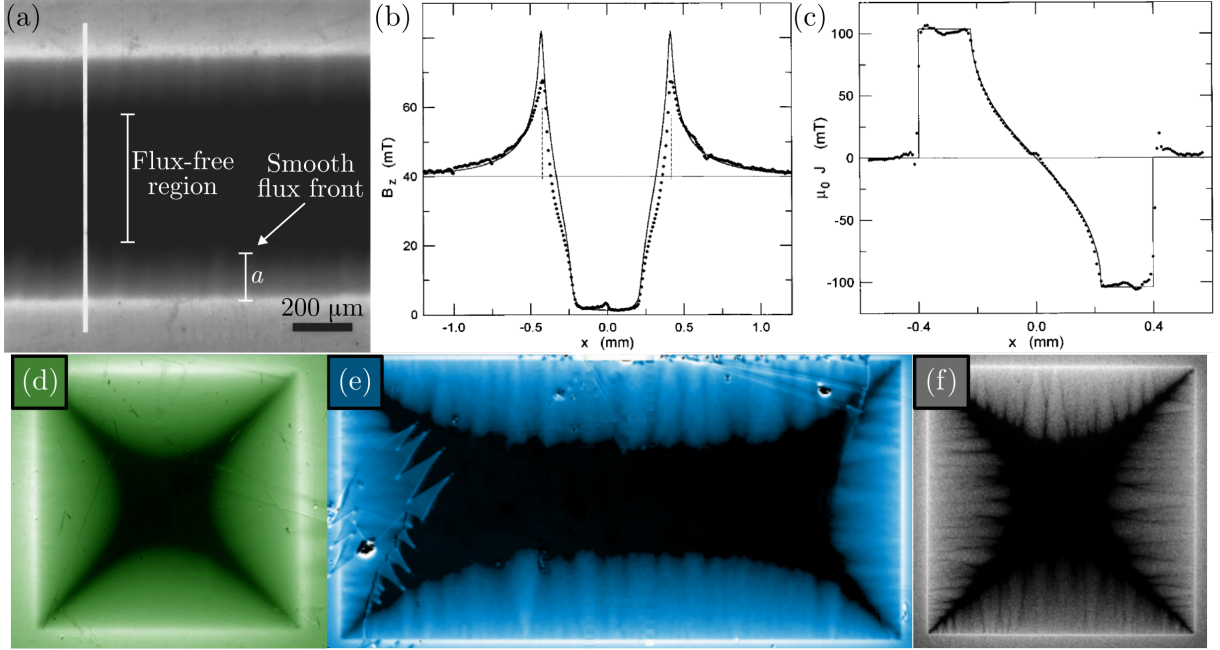


**Figure 1.9.** (a) Magneto-optical image of a long YBCO thin film under a perpendicular magnetic field showing partial flux penetration up to a depth  $a$  into the sample. (b) The magnetic flux density perpendicular to the film's surface and (c) the shielding current density flowing in the film as measured along the vertical line in panel (a). Solid lines are calculated using the Bean model. Images are adapted from [60]. Other MOI results showing smooth flux penetration in superconducting films, clearly distinguishing the flux front from the Meissner state region: (d) YBCO [61]; (e) Nb [62]; and (f) Nb [49].

the most frequently successfully employed [54, 64]. The **Kim model** assumes the critical current density as  $J_c^{\text{Kim}}(T, B) = J_0(T)/(1 + B/B_0(T))$ . For a  $2w$ -wide long film presenting a generic flux-dependent critical current density, the shielding current and flux density profiles at a given temperature can be written as [58]

$$J_y(x) = \begin{cases} -\frac{2}{\pi}x\sqrt{a^2 - x^2} \int_a^w dx' \frac{J_c(B_z(x'))}{(x'^2 - x^2)\sqrt{x'^2 - a^2}}, & |x| < a, \\ -\frac{x}{|x|}J_c(B_z(x)), & a < |x| < w, \end{cases} \quad (1.33)$$

$$B_z(x) = B_f|x|\sqrt{x^2 - a^2} \int_a^w dx' \frac{J_c(B_z(x'))}{J_0(x^2 - x'^2)\sqrt{x'^2 - a^2}}, \quad a < |x| \neq w, \quad (1.34)$$

$$\mu_0 H = B_f \int_a^w dx' \frac{J_c(B_z(x'))}{J_0\sqrt{x'^2 - a^2}}, \quad (1.35)$$

$$B_f = \frac{\mu_0 J_0 d}{\pi}. \quad (1.36)$$

Solving these equations considering  $J_c^{\text{Bean}}(T, B)$  recovers the behavior depicted in Fig. 1.8.

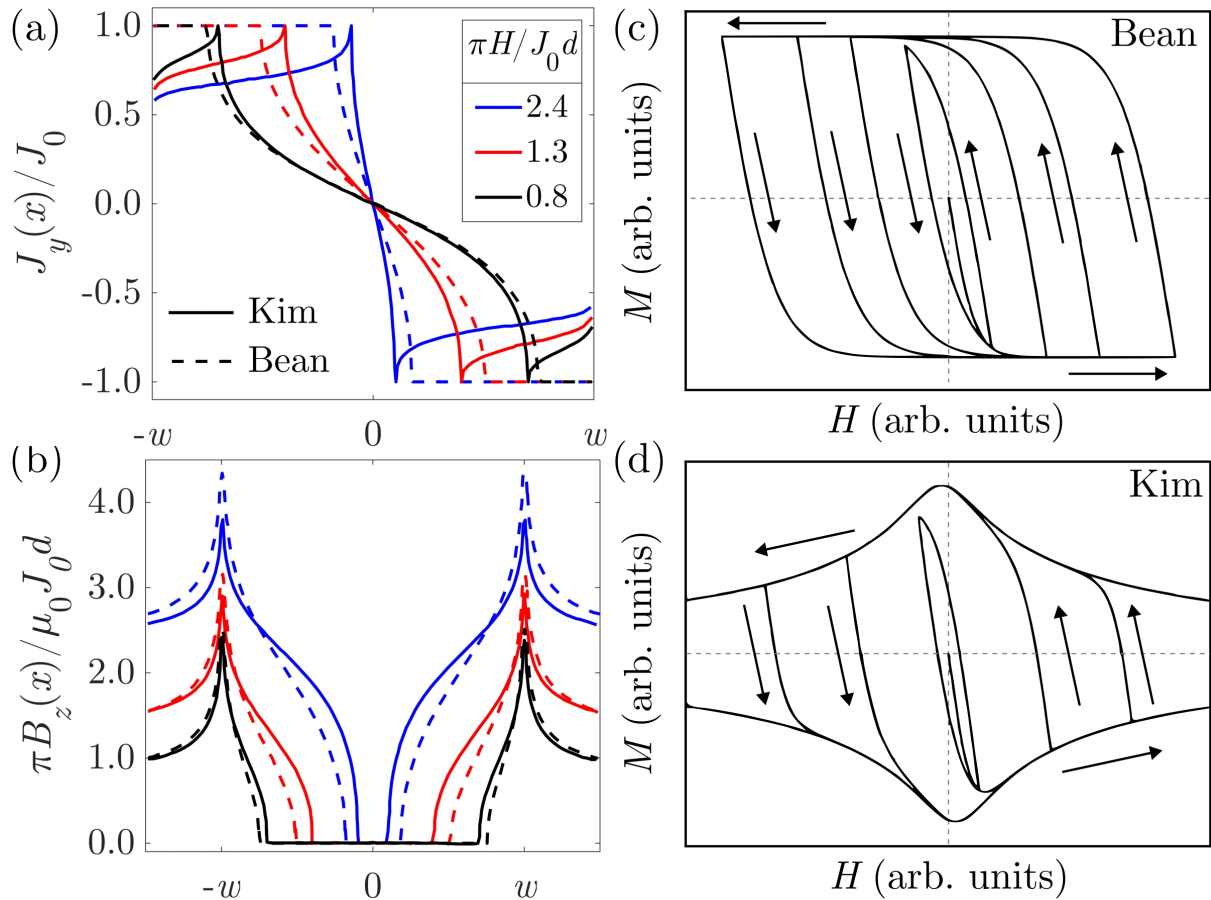


**Figure 1.10.** Comparison between the (a) current density and (b) magnetic flux density for a superconducting thin film after ZFC obtained according to the Bean and Kim critical state models for different applied fields. Adapted from [58]. Magnetization hysteresis loops for a thin disk in the (c) Bean and (d) Kim models. The different loop sizes represent different maximum applied field amplitudes. Adapted from [65].

If  $J_c^{\text{Kim}}(T, B)$  is used instead, different profiles are obtained, as demonstrated by Fig. 1.10(a-b)—highlighting the potential impact of the choice of  $f(\mathbf{B})$  on the interpretation of the macroscopic flux distribution in type-II superconductors.

As critical state models describe both  $\mathbf{B}$  and  $\mathbf{J}$  under some particular applied field  $\mathbf{H}$ , they can also be employed to calculate the magnetization  $\mathbf{M}$  of superconducting specimens, given that

$$\mathbf{M} = \frac{\mathbf{B}}{\mu_0} - \mathbf{H} = \frac{1}{2V} \int_V d^3\mathbf{r} (\mathbf{r} \times \mathbf{J}). \quad (1.37)$$

The exact shape of the magnetization hysteresis loop  $M(H)$  will depend on the critical

state model adopted and the magnitude of the applied field, as exemplified for a thin superconducting disk in Fig. 1.10(c-d). For the Bean model, depending on the sample geometry, there is a relationship between the flux-independent  $J_c^{\text{Bean}}$  and the height of the magnetization hysteresis, i.e., the difference in the saturated magnetization for a sample fully penetrated by magnetic flux while the field is increased or decreased,  $\Delta M$ . It is also possible to establish a relationship between  $J_c^{\text{Bean}}$  and the depth of the flux penetration front  $a$  into the sample. For a thin film, this is given by

$$J_c^{\text{Bean}} = \frac{\pi H}{d \cosh^{-1} \left( \frac{w}{a} \right)}. \quad (1.38)$$

Critical state models are a great tool to extract meaningful information about a material's superconducting properties. They rely on the existence of a smooth flux front that gradually penetrates a given sample when an applied magnetic field is ramped up or down. However, under some circumstances, such flux movement may lead to breakdowns of the critical state.

### 1.7.2 Flux avalanches

Although disregarded by the critical state interpretation, it is essential to remember that all flux that penetrates a superconductor in the mixed state does so in the form of vortices. Therefore, the dynamics of flux penetration are defined by the movement of vortices that nucleate at the edges of the sample and move toward its center pushed inward by the magnetic pressure exerted by further incoming vortices as the field is changed. As previously discussed, such vortex movement is a dissipative process, and the stability of the critical state will depend on the material's ability to assimilate the dissipated heat [49, 66, 67].

In that regard, there are two important material parameters: the **thermal diffusion coefficient**,  $D_t$ , and the **magnetic diffusion coefficient**,  $D_m$ , which are given by

$$D_t = \frac{\kappa_t}{C} \quad \text{and} \quad D_m = \frac{\rho}{\mu_0}, \quad (1.39)$$

where  $\kappa_t$  is the thermal conductivity,  $C$  the heat capacity, and  $\rho$  the electrical resistivity of the material. If the superconductor can assimilate the heat dissipated by vortex movement faster than the characteristic time vortices take to move through the material, i.e.,  $D_t \gg D_m$ , then a critical-state-like penetration takes place as the heat dissipates through the sample. However, if  $D_m \gg D_t$ , a rapid variation of magnetic flux heats the sample in a quasi-adiabatic process, meaning that it is confined to the neighborhood of the vortex movement, transferring a determined amount of heat  $\delta Q$  to that part of the sample. Such **thermomagnetic instability** is the onset of a thermally induced breakdown of the critical state.

The heat  $\delta Q$  generated locally increases the temperature by  $\delta T$ . As the critical current flowing in the superconductor depends both on  $T$  and  $\mathbf{B}$ , the increase in temperature will lead to a reduction in  $J_c$  and, consequently, of the pinning force, thus allowing for further magnetic flux penetration. By Faraday's induction law, the increase in  $\mathbf{B}$  induces an electric field  $\mathbf{E}$ . As there are circulating currents in the superconductor, such an electric field will give rise to further heat dissipation by Joule's law. This leads to the positive feedback loop represented in Fig. 1.11(a), which will stop when  $\delta Q$  is no longer large enough to locally increase the temperature of the superconductor.

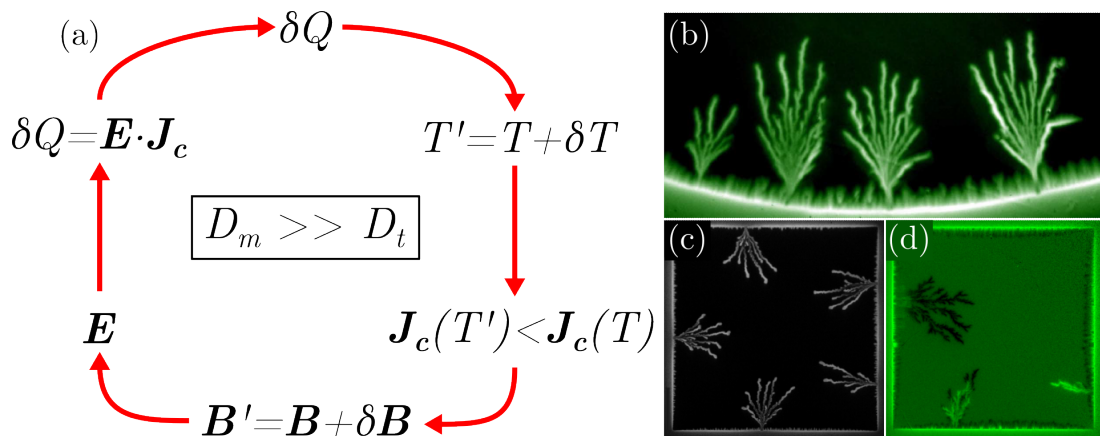


**Figure 1.11.** (a) Positive feedback loop initiated by a thermomagnetic instability. Adapted from [49]. The dendritic flux pattern imprints on different superconducting films after avalanche events take place captured by MOI: (b)  $\text{MgB}_2$  [68]; (c) Nb [49]; and (d) amorphous MoSi.

These thermomagnetic instabilities can then lead to abrupt, large flux penetration events, known as **flux avalanches**. They may occur in bulk samples and were first experimentally reported in 1956 by Schawlow using Bitter decoration [69]. In global measurements, flux avalanches are characteristically observed as sudden jumps in the sample's magnetization [49, 64].<sup>12</sup> However, the most amazing observations of magnetic flux avalanches are made by exploring the spatial aspects of flux penetration using MOI to study superconducting thin films. In such specimens, avalanches take remarkable dendritic patterns as those exemplified in Fig. 1.11(b-d). There is vast and rich scientific literature exploring the characteristics of flux avalanches. They are stochastic events in which flux penetration may occur on the scale of hundreds of km/s [70, 71]. Avalanches are triggered depending on the sample's critical current density, occurring, in general, at low temperatures and moderate magnetic fields [72]. Avalanche morphology also depends on temperature and applied magnetic field, as well as on the penetrated flux landscape [73] and sample geometry [70]. They can also be to some extent affected by the inclusion of nanostructured defects [74–76] or capping layers [77, 78]. As this thesis' results will not be specifically focused on these aspects, I will encourage the interested reader to explore the above-referenced works as well as specialized review papers on the topic [49, 61, 79].

Due to avalanches' extreme velocities, it is experimentally challenging to study the dynamics of their propagation into superconducting films. Furthermore, the stochastic and localized nature of the phenomenon introduces complications to the quantitative characterization of the sample's features after an avalanche event—although these can be overcome as will be discussed in Chapter 6 of this thesis. Therefore, it is paramount that a theoretical approach can describe flux avalanches and corroborate experimental findings.

The **thermomagnetic model** sets out to do just that [80]. It accounts for the swift flux motion in a superconducting thin film by assuming a highly nonlinear current-voltage

---

<sup>12</sup>A global measurement provides results that consider the evaluated specimen as a whole, therefore not providing insight into particularities of spatially localized events. In contrast, local measurements spatially resolve the analyzed behavior.

relationship, yielding

$$\mathbf{E} = \begin{cases} \mathbf{J}\rho_0 \left(\frac{J}{J_c}\right)^n, & T \leq T_c \text{ and } J \leq J_c, \\ \mathbf{J}\rho_0, & T \leq T_c \text{ and } J > J_c, \\ \mathbf{J}\rho_n, & T > T_c, \end{cases} \quad (1.40)$$

where  $\rho_0$  is a resistivity constant,  $\rho_n$  is the normal state resistivity, and  $n = n_0 T_c / T$  is the flux creep exponent where  $n_0$  is a constant. Then, the temperature distribution in the studied material can be obtained by substituting Eq. (1.40) into the heat diffusion equation

$$dc\dot{T} = d\nabla \cdot (\kappa_t \nabla T) - h(T - T_0) + d\mathbf{J} \cdot \mathbf{E}, \quad (1.41)$$

where  $c$  is the specific heat,  $\dot{T}$  is the time-derivative of  $T$ , and  $h$  is the coefficient of heat transfer between the superconductor and the substrate kept at temperature  $T_0$ . Both  $\kappa_t$ ,  $c$ , and  $h$  are assumed to be proportional to  $T^3$ .

To describe the magnetic dynamics of the superconducting film, it is interesting to define a local magnetization  $g(\mathbf{r})$  such as

$$\mathbf{J} = \nabla \times g(\mathbf{r})\hat{\mathbf{z}}, \quad (1.42)$$

where  $\mathbf{r}$  lies on the film plane and is perpendicular to  $\hat{\mathbf{z}}$ . Then, inverting Biot-Savart's law under the condition that  $g(\mathbf{r}) = 0$  outside the film, it is possible to show that the time-evolution of the local magnetization is given by

$$\dot{g}(\mathbf{r}, t) = 2\mathcal{F}^{-1} \left\{ \frac{1}{k} \mathcal{F} \left[ \frac{\dot{B}_z(\mathbf{r}, t)}{\mu_0} - \dot{H}(\mathbf{r}, t) \right] \right\}, \quad (1.43)$$

where  $\mathcal{F}$  denotes the Fourier transform and  $k$  the momentum. A discrete numerical approach can be implemented to efficiently solve Eqs. (1.41) and (1.43), revealing the dynamics of flux avalanche propagation [80]. It has been very successfully employed in several studies, reproducing with remarkable accuracy different characteristics of avalanche behavior, as exemplified by the comparisons shown in Fig. 1.12. Thermomagnetic model simulations can also go beyond our experimental capacities and have, for instance, found

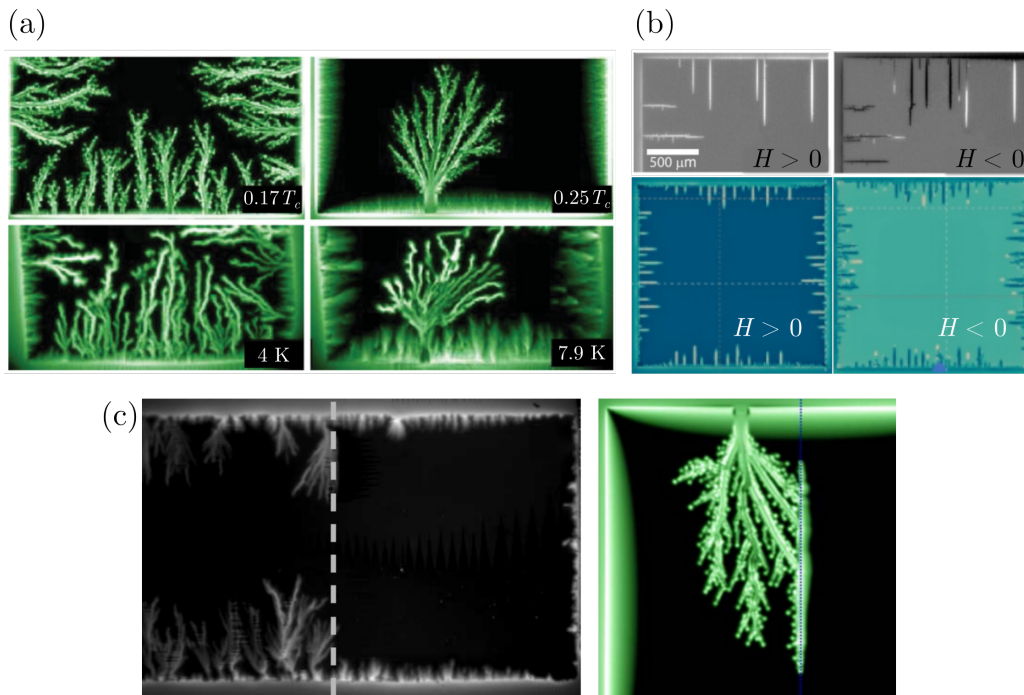


**Figure 1.12.** (a) Comparison between thermomagnetic model (TM) simulations (top) and magneto-optical images (bottom) obtained for a  $\text{MgB}_2$  thin film, reproducing the observed dendritic patterns at different temperatures [80]. (b) TM simulations (bottom) [81] reproduce the reuse of previously established positive (bright) flux channels by negative (dark) flux avalanches in Nb films (top) [76]. (c) TM simulations (right) [61] reproduce the suppression of flux penetration during an avalanche event caused by the existence of a metallic capping layer over the right side of the superconducting film [77].

that temperatures can increase beyond  $T_c$  as avalanches propagate through the superconductor so that superconductivity is likely to be fully suppressed at these hot spots [68]. Such numerical results provide a reliable means to study magnetic flux avalanche dynamics.

## 1.8 The BCS theory

Up to this point, this thesis has dealt with superconductivity from a phenomenological perspective. It has covered many of the fundamental characteristics of superconducting behavior and even showed how we can use different models to quantify important properties of these materials. It has not, however, posed a simple and fundamental question:

*why do superconductors superconduct?* The experimental discovery of several important characteristics of the phenomenon suggested that the “facts of superconductivity were simple”, as put by Brian Pippard [82]. But for decades after the Leiden’s group discovery, this very question would elude (and outright frustrate) great scientific minds. Paraphrasing a famous warning issued by Richard Feynman, one of a few Nobel laureates to fail to develop a successful microscopic theory for superconductivity: to work on this problem would lead to the terrible realization that you are too stupid to solve it.<sup>13</sup>

Fortunately, when John Bardeen invited a then twenty-five years-old Leon Neil Cooper to join him as a postdoc at the University of Illinois in 1955, he was unaware of such an encouraging perspective. As a matter of fact, as he recalls [82], he was not aware of superconductivity at all. Bardeen was looking for someone well-versed in the then-modern tools of quantum field theory, and Cooper was personally recommended by Chen-Ning “Frank” Yang. Around the same time, then twenty-four years old Ph.D. student John Robert Schrieffer wanted to work on a “real problem” for his thesis and joined Bardeen’s efforts to tackle the matter of superconductivity. That was it. A man who in two years would receive the Nobel Prize in Physics for the discovery of the transistor and two talented and highly motivated twenty-something years old, B, C, and S. That was the team that would finally pen down a theory capable of explaining all known features of superconductivity—at least at the time, anyway. The path they took to get there was far from linear and I will not follow its every turn in this thesis, leaving it to the indicated literature. But to grasp the core concepts that enabled the development of the BCS theory, let us first recall what were the “facts of superconductivity” by 1955.

At that time, it was known that below a characteristic critical temperature  $T_c$ , the superconductor experienced a sharp transition to a zero-resistance state. If a strong enough

---

<sup>13</sup>There are many historical texts covering the eventful period of the 1950s and the quest for a microscopic theory for superconductivity. There are also many texts, interviews, and seminars presented by those directly involved in the effort. I can recommend Chapter 2.2 of Ref. [15] and the absolutely delightful first chapters of Ref. [82] for a first-hand perspective of the events as they transpired at the University of Illinois, where the BSC theory was born.



magnetic field was applied to the material in the superconducting state, it would transition back to the normal state. The magnitude of such a critical field  $H_c$  decreased with increasing temperatures. Moreover, below  $T_c$ , the superconductor would expel magnetic flux lines from its interior. The transition was a second-order phase transition if there was no applied magnetic field, whereas it was a first-order phase transition under applied fields, as evidenced by the presence of latent heat in specific heat measurements only in the second case. There is also a sharp discontinuity in the electronic specific heat at  $T_c$ , which then exponentially decays to 0 at  $T = 0$  in the absence of an applied field. This observation implies one extremely important characteristic of superconductors. The specific heat may be written as proportional to the temperature-derivative of the entropy or, alternatively, to the temperature-derivative of the expected energy value of the system. Suppose now that the system has an energy gap  $\Delta$ . If the temperature is such that  $k_B T \ll \Delta$ , system particles will be mainly found in the ground state and the system is not able to absorb any energy until the temperature is increased to  $k_B T \sim \Delta$ . Here,  $k_B$  is the Boltzmann constant. Therefore, in the temperature range  $0 < k_B T < \Delta \sim k_B T_c$ , there is no variation of the system energy, and the specific heat is exponentially suppressed, strongly indicating that there is a gap in the energy spectrum of superconductors.

Moreover, there was a variety of different metals, compounds, and alloys which were known to be superconductors, so the phenomenon was thought to be fairly common and the specific structure of the material should not affect qualitative aspects of the superconducting state. It was also pretty evident at the time that the superconducting transition had to be associated with some change in the nature of the electronic wave function. As Fritz London had shown in 1948, superconductivity was associated with the condensation of a quantum state in the momentum space. Electrons, however, are fermions and thus subjected to Pauli's exclusion principle and are unable to form condensates. Hence, superconductivity should arise from some electronic interaction. Coulomb repulsion however yielded an average energy per atom  $10^8$  times greater than that estimated from  $T_c$ , so it

was necessary to figure out how electrons interacted in the superconducting state.

There is still one important fact, maybe the final piece of the puzzle, that has not yet been mentioned in this thesis. Two independent letters published in the same volume of *Physical Review* on March 24, 1950, demonstrated what is known as the **isotope effect** in superconductors. The works by Emanuel Maxwell [83] and C. A. Reynolds, B. Serin, W. H. Wright, and L. B. Nesbitt [84] clearly showed that the transition temperature of different mercury isotopes depended on the mass of the ionic lattice  $M_{\text{ion}}$ . This can be put as

$$T_c \propto \sqrt{M_{\text{ion}}} \propto \omega_D, \quad (1.44)$$

where  $\omega_D$  represents the Debye frequency for the phonons in the lattice. In essence, phonons are quasiparticles that describe the vibration modes in an elastic structure.<sup>14</sup> Therefore, phonons, or more specifically electron-phonon interactions, should play a key role in the superconducting transition.

John Bardeen moved from the Bell Laboratories to the University of Illinois in 1951. There, he would be able to freely direct his efforts, dedicating himself to establishing a laboratory to study semiconductors and to trying to solve the problem of finding a theory for superconductivity, absorbing all experimental and theoretical advances and bottlenecks in the process. So, he was fully aware of all the above-mentioned facts. One such advancement was made by Herbert Fröhlich in 1952 [85]. Studying the interaction between electrons and lattice vibrations, he noticed that the electron-phonon interaction could give rise to an apparently weak yet attractive force between electrons. He imagined this could be the mechanism by which phonons allowed for the superconducting transition. However, his method did not account for modifications that would come by the consideration of the repulsive Coulomb forces between electrons and was not suited to calculate the details

---

<sup>14</sup>It is customary and to some extent fair to define phonons as quantized sound waves in the same way that photons are quantized light waves. But it is important to have in mind that phonons are an emergent phenomenon, i.e., you cannot detect a phonon in the same way you can detect a photon, which is an elementary particle.

of the energy spectrum and electromagnetic properties of superconductors. In Fröhlich's words, those would have to wait for the development of new theoretical methods.

Before Cooper arrived, Bardeen had another celebrated postdoc, David Pines, who obtained his Ph.D. under David Bohm at Princeton, where they developed a procedure called random phase approximation in their collective description of electron interactions [86–89]. Bardeen and Pines would work together from 1952 to the beginning of 1955. Among their successes, one was paramount to the later BCS theory: their work on the electron-phonon interaction in metals [90]. By extending the random phase approximation to account for ionic motion, they could fully consider how the Coulomb interaction modified the coupling between electrons and electrons and phonons. The results were very similar to those Fröhlich had found three years before. For two electrons near the Fermi surface with energies differing by less than a characteristic phonon energy, a phonon-mediated electron-electron interaction would win out the Coulomb repulsion and there would be a net attractive interaction between the electrons.

Having absorbed all of these developments after his arrival in Illinois, Cooper was convinced that the essential point to solving the problem of superconductivity was the energy gap—a common view, as he recalled. He then directed his complex theoretical tools, so esteemed by Bardeen, to the task of understanding the many-electron system and unveiling the origin of such a gap. He would say [82], paralleling the words of Feynman: “I attempted to sum various sets of diagrams: ladders, bubbles, and many others. I tried low-energy theorems, Breuckner's method, functional integrals, and so on. After more attempts than I care to mention, during the fall of 1955, I was no longer feeling so clever”. It was then that Cooper changed his approach to the problem, instead trying to solve the most simple question he did not know the answer to.

Let us assume a normal metal in the ground state such that all electronic orbitals with momentum below the Fermi surface,  $k < k_F$ , are occupied and all others are empty [21, 91, 92]. For two electrons, with positions  $\mathbf{r}_1$  and  $\mathbf{r}_2$ , interacting via an attractive potential

$U(r_1 - r_2)$ , the Schrödinger equation can be written in the coordinates of the center of mass of the two-body system as

$$\left\{ -\frac{\hbar^2 \nabla_{\mathbf{R}}^2}{4m_e} - \frac{\hbar^2 \nabla_{\mathbf{r}}^2}{m_e} + U(\mathbf{r}) \right\} \Psi(\mathbf{r}, \mathbf{R}) = \mathcal{E} \Psi(\mathbf{r}, \mathbf{R}), \quad (1.45)$$

where  $m_e$  is the electron mass,  $\mathbf{r} = \mathbf{r}_1 - \mathbf{r}_2$  and  $\mathbf{R} = (\mathbf{r}_1 + \mathbf{r}_2)/2$ . As the potential does not depend on  $\mathbf{R}$ , the wave function can be written as  $\Psi(\mathbf{r}, \mathbf{R}) = \psi(\mathbf{r}) \exp(i\mathbf{K} \cdot \mathbf{R})$ , where  $\mathbf{K}$  is the momentum of the center of mass. Thus we arrive at

$$\left\{ -\frac{\hbar^2 \nabla_{\mathbf{r}}^2}{m_e} + U(\mathbf{r}) \right\} \psi(\mathbf{r}) = \left( \mathcal{E} - \frac{\hbar^2 K^2}{4m_e} \right) \psi(\mathbf{r}). \quad (1.46)$$

If  $\mathbf{k}_1 = -\mathbf{k}_2$ , such as  $K = 0$ , the spins of the electrons will form either singlet or triplet states to ensure the anti-symmetry of  $\Psi(\mathbf{r}, \mathbf{R})$ . Taking the Fourier transform of the above equation for such a system leads to [21, 91]

$$\int \frac{d^3 k'}{(2\pi)^3} U(\mathbf{k} - \mathbf{k}') \psi(\mathbf{k}') = \left( \mathcal{E} - \frac{\hbar^2 k^2}{m_e} \right) \psi(\mathbf{k}) = (\mathcal{E} - 2\mathcal{E}_{\mathbf{k}}) \psi(\mathbf{k}), \quad (1.47)$$

where  $\mathcal{E}_{\mathbf{k}}$  is the free electron energy. This equation also shows that, if  $\mathcal{E} < 2\mathcal{E}_{\mathbf{k}}$ , a bound state is formed, as the energy of the electron pair is lower than the energy of the two individual electrons. In the following steps, we shall determine this energy.

Defining  $\tilde{\psi}(\mathbf{k}) = (\mathcal{E} - 2\mathcal{E}_{\mathbf{k}}) \psi(\mathbf{k})$ , we can rewrite the equation above as

$$\tilde{\psi}(\mathbf{k}) = - \int \frac{d^3 k'}{(2\pi)^3} \frac{U(\mathbf{k} - \mathbf{k}')}{2\mathcal{E}_{\mathbf{k}'} - \mathcal{E}} \tilde{\psi}(\mathbf{k}'). \quad (1.48)$$

We now recall the previous results by Pines and Bardeen. They stated that an attractive potential such as the one we imagined in the above Schrödinger equation only occurs for electrons near the Fermi level for which the energy difference lies below a characteristic phonon energy. Then, we are prompted to select a potential  $U(\mathbf{k} - \mathbf{k}') = -U_0$  for  $\mathcal{E}_{\mathbf{k}} - \mathcal{E}_F \sim \mathcal{E}_{\mathbf{k}'} - \mathcal{E}_F < \hbar\omega_D$  and 0 otherwise. For a singlet state, as is the general case for superconductors [21], we have  $\tilde{\psi}(\mathbf{k})$  independent of  $\mathbf{k}$ . Furthermore, as the typical phonon energy  $\hbar\omega_D$  is much smaller than  $\mathcal{E}_F$ , we can approximate the density of states

of the two-electron system by its value at the Fermi level  $N(\mathcal{E}_F)$ . Then, by changing the integration variable using the definition of  $\mathcal{E}_k$ , it is possible to show that

$$1 = U_0 N(\mathcal{E}_F) \int_{\mathcal{E}_F}^{\mathcal{E}_F + \hbar\omega_D} \frac{d\mathcal{E}'}{2\mathcal{E}' - \mathcal{E}} = \frac{U_0 N(\mathcal{E}_F)}{2} \ln \left( \frac{2\mathcal{E}_F - \mathcal{E} + 2\hbar\omega_D}{2\mathcal{E}_F - \mathcal{E}} \right) \quad (1.49)$$

$$\Rightarrow \mathcal{E}_b = 2\mathcal{E}_F - \mathcal{E} = \frac{2\hbar\omega_D}{\exp(2/U_0 N(\mathcal{E}_F)) - 1}, \quad (1.50)$$

where  $\mathcal{E}_b$  is the binding energy of the electron pair. If we had considered a **weak coupling** limit, such as  $U_0 N(\mathcal{E}_F) \ll 1$  and  $2\mathcal{E}_F - \mathcal{E} + 2\hbar\omega_D \rightarrow 2\hbar\omega_D$ , the binding energy would be given by

$$\mathcal{E}_b = 2\hbar\omega_D \exp \left( -\frac{2}{U_0 N(\mathcal{E}_F)} \right). \quad (1.51)$$

This is the core idea of Cooper's famous work [93]. No matter how small the attraction between two electrons is, they will form a bound state, which is today called a **Cooper pair**. Two electrons near the Fermi level are then unstable with respect to the formation of a Cooper pair. It was evident to Cooper and his collaborators at Illinois that if the ground state was composed of such pairs, it would explain the emergence of the energy gap and the superconducting state. In other words, the many-body electronic system would be unstable with respect to the formation of a new ground state. But as Cooper found out, extending the results from two electrons to the actual many-body system was a troublesome task [82].

This part of the puzzle was to be cracked by Schrieffer. After Cooper had found the bound states, the Ph.D. student joined the efforts of trying to solve the many-body problem. As the months passed, Schrieffer became worried he would not be able to finish his work in time to write his thesis, so much so that he began working on ferromagnetism on the side [82]. This was the setting for a famous piece of superconducting lore. Shortly after Cooper's publication at the end of 1956, Bardeen had to travel to Stockholm for the burdensome task of receiving his (first) Nobel Prize. Prior to his advisor's departure, Schrieffer shared his worries with Bardeen, who told him to "give it another month" and wait until he returned from Sweden: "maybe something will happen".

Well, something happened. One key point preventing the successful expansion of Cooper's ideas to the general many-body solution was that it was not evident how to build a many-body wave function that satisfied Pauli's exclusion principle and led to a single quantum state to describe the non-dissipative flow of Cooper pairs. More specifically, as had previously been worked out by Bardeen and Pines, consider the electron-electron interaction term of the electronic system Hamiltonian given by

$$\mathcal{H}_{\text{el-el}} = \sum_{\mathbf{k}\mathbf{k}'\sigma\sigma'} \frac{\hbar\omega|M_{\mathbf{k}_p}|^2}{(\mathcal{E}_{\mathbf{k}} - \mathcal{E}_{\mathbf{k}'})^2 - (\hbar\omega)^2} c_{\mathbf{k}'-\mathbf{k}_p,\sigma'}^\dagger c_{\mathbf{k}',\sigma'} c_{\mathbf{k}+\mathbf{k}_p,\sigma}^\dagger c_{\mathbf{k},\sigma} + \mathcal{H}_{\text{Coul}}, \quad (1.52)$$

where  $|M_{\mathbf{k}_p}|$  is the electron-phonon interaction matrix element for a phonon with wave vector  $\mathbf{k}_p$  and  $c^\dagger$  and  $c$  are, respectively, the creation and annihilation operators for electrons in states defined by a wave vector  $\mathbf{k}$  and spin  $\sigma$ .  $\mathcal{H}_{\text{Coul}}$  accounts for a screened Coulomb interaction. Then, due to Pauli's exclusion principle, the matrix elements of the operators in Eq. (1.52) for an arbitrary many-electron configuration alternate in sign, yielding a very small net interaction energy.

While attending a pair of scientific meetings in New York, what Schrieffer realized was that he could arrive at a configuration in which all matrix elements were negative by occupying the individual electronic states in pairs—meaning that if one of the pair states is occupied, the other would also be. Then, it was a matter of identifying the pair configuration that better favored the formation of a ground state. To respect the conservation of momentum, all pairs should have the same momentum  $\mathbf{k}_1 + \mathbf{k}_2 = \mathbf{q}$ . Also, terms of parallel spin states would reduce the interaction, so the pair constituents should have opposite spins. Then, focusing on the  $\mathbf{q} = 0$  case, the ground state would be composed of pairs such that if the state  $\mathbf{k}_\uparrow$  was occupied, so was state  $-\mathbf{k}_\downarrow$ , where  $\uparrow$  and  $\downarrow$  respectively represent the up and down spin states.

These were the breakthroughs that allowed Bardeen, Cooper, and Schrieffer to postulate their famous theory in 1957 [94,95]. In their seminal works, they employ a variational approach to show that, similar to the Cooper pair formation, an attractive interaction be-

tween electrons will lead to the formation of a condensed state with an energy lower than that of the normal state—no matter how weak this interaction is. The theory also yields the Meissner-Ochsenfeld effect, a critical magnetic field, the isotope effect, an energy gap, and a second-order phase transition with penetration depths and specific heat values with respect to the temperature immediately being shown to agree with experiments. The BCS theory was a resounding and immediate success, being met with almost universal approval. A few years later, in 1972, the men responsible for its inception were awarded the Nobel Prize in Physics “for their jointly developed theory of superconductivity, usually called the BCS-theory”. Following, the reader will excuse me for some anachronism as I will give a hint of how the BCS ideas can be used to demonstrate important aspects of superconductivity. In that, I will make use of a couple of “tricks” [91,92] not used in the BCS papers. I will most certainly not provide in-depth coverage of the issue, nor claim that I will present a formal deduction of the equations. The BCS theory has a much more profound impact on Physics than what I would be able to cover and, for that, I refer to references such as [82].

So, following Schrieffer’s insight, we can write an effective Hamiltonian

$$\mathcal{H} = \sum_{\mathbf{k}\sigma} \xi_{\mathbf{k}} c_{\mathbf{k}\sigma}^\dagger c_{\mathbf{k}\sigma} + \frac{1}{n} \sum_{\mathbf{k}\mathbf{k}'} U_{\mathbf{k}\mathbf{k}'} c_{\mathbf{k}\uparrow}^\dagger c_{-\mathbf{k}\downarrow}^\dagger c_{-\mathbf{k}'\downarrow} c_{\mathbf{k}'\uparrow}, \quad (1.53)$$

where  $\xi_{\mathbf{k}} = \mathcal{E}_{\mathbf{k}} - \mu$ ,  $\mu$  is the chemical potential, and  $n$  is the number of paired electrons. The second term of the right-hand side of the equation accounts for the destruction and creation of Cooper pairs following the idea of the occupation of the electronic states in pairs. To decouple this quadratic term, we can use a mean-field approximation, such that

$$\left\langle c_{\mathbf{k}\uparrow}^\dagger c_{-\mathbf{k}\downarrow}^\dagger c_{-\mathbf{k}'\downarrow} c_{\mathbf{k}'\uparrow} \right\rangle \approx \left\langle c_{\mathbf{k}\uparrow}^\dagger c_{-\mathbf{k}\downarrow}^\dagger \right\rangle c_{-\mathbf{k}'\downarrow} c_{\mathbf{k}'\uparrow} + c_{\mathbf{k}\uparrow}^\dagger c_{-\mathbf{k}\downarrow}^\dagger \left\langle c_{-\mathbf{k}'\downarrow} c_{\mathbf{k}'\uparrow} \right\rangle - \left\langle c_{\mathbf{k}\uparrow}^\dagger c_{-\mathbf{k}\downarrow}^\dagger \right\rangle \left\langle c_{-\mathbf{k}'\downarrow} c_{\mathbf{k}'\uparrow} \right\rangle. \quad (1.54)$$

Then, defining a function

$$\Delta_{\mathbf{k}} = -\frac{1}{n} \sum_{\mathbf{k}'} U_{\mathbf{k}\mathbf{k}'} \left\langle c_{-\mathbf{k}'\downarrow} c_{\mathbf{k}'\uparrow} \right\rangle \quad (1.55)$$

the effective Hamiltonian can be written as

$$\mathcal{H} = \sum_{\mathbf{k}\sigma} \xi_{\mathbf{k}} c_{\mathbf{k}\sigma}^\dagger c_{\mathbf{k}\sigma} - \sum_{\mathbf{k}} \left( \Delta_{\mathbf{k}} c_{\mathbf{k}\uparrow}^\dagger c_{-\mathbf{k}\downarrow}^\dagger + \Delta_{\mathbf{k}}^* c_{-\mathbf{k}\downarrow} c_{\mathbf{k}\uparrow} \right) + \sum_{\mathbf{k}} \Delta_{\mathbf{k}} \left\langle c_{\mathbf{k}\uparrow}^\dagger c_{-\mathbf{k}\downarrow}^\dagger \right\rangle. \quad (1.56)$$

To solve this Hamiltonian without resorting to a variational approach, we can introduce the following Bogoliubov transformation<sup>15</sup>

$$c_{\mathbf{k}\uparrow} = u_{\mathbf{k}}^* \gamma_{\mathbf{k}\uparrow} + v_{\mathbf{k}} \gamma_{-\mathbf{k}\downarrow}^\dagger \quad (1.57)$$

$$c_{-\mathbf{k}\downarrow}^\dagger = u_{\mathbf{k}} \gamma_{-\mathbf{k}\downarrow}^\dagger - v_{\mathbf{k}}^* \gamma_{\mathbf{k}\uparrow} \quad (1.58)$$

$$1 = |u_{\mathbf{k}}|^2 + |v_{\mathbf{k}}|^2, \quad (1.59)$$

leading to the effective BCS Hamiltonian and wave function [91]

$$\mathcal{H}_{\text{BCS}} = \sum_{\mathbf{k}\sigma} \gamma_{\mathbf{k}\sigma}^\dagger \gamma_{\mathbf{k}\sigma} \sqrt{\xi_{\mathbf{k}}^2 + |\Delta_{\mathbf{k}}|^2} + \sum_{\mathbf{k}} \left( \xi_{\mathbf{k}} - \sqrt{\xi_{\mathbf{k}}^2 + |\Delta_{\mathbf{k}}|^2} + \Delta_{\mathbf{k}} \left\langle c_{\mathbf{k}\uparrow}^\dagger c_{-\mathbf{k}\downarrow}^\dagger \right\rangle \right) \quad (1.60)$$

$$|\Psi_{\text{BCS}}\rangle = \prod_{\mathbf{k}} \left( u_{\mathbf{k}} + v_{\mathbf{k}} c_{\mathbf{k}\uparrow}^\dagger c_{-\mathbf{k}\downarrow}^\dagger \right) |0\rangle, \quad (1.61)$$

where  $|0\rangle$  is the wave function for the vacuum of electrons. Equation (1.60) evidences that, even at the Fermi level, an energy equal to  $2|\Delta_{\mathbf{k}}|$  is necessary to excite the system's quasiparticles from the ground state. Therefore, the superconductor described by the BCS theory has an energy gap given by the gap function defined in Eq. (1.55). However, we still need to determine for what conditions such a gap is different from zero.

Using the Bogoliubov transformation and the fact that the Bogoliubov operators follow Fermi-Dirac statistics, it is possible to rewrite Eq. (1.55) as

$$\Delta_{\mathbf{k}} = -\frac{1}{n} \sum_{\mathbf{k}'} \frac{U_{\mathbf{k}\mathbf{k}'} \Delta_{\mathbf{k}'}}{2\sqrt{\xi_{\mathbf{k}'}^2 + |\Delta_{\mathbf{k}'}|^2}} \tanh \left( \frac{\sqrt{\xi_{\mathbf{k}'}^2 + |\Delta_{\mathbf{k}'}|^2}}{2k_B T} \right), \quad (1.62)$$

which allows us to investigate  $\Delta_{\mathbf{k}}$  for different  $U_{\mathbf{k}\mathbf{k}'}$  and  $T$ . Based on the Cooper pair solution, we may select a constant attractive potential  $U_{\mathbf{k}\mathbf{k}'} = -U_0$  that acts on electrons

---

<sup>15</sup>In a sense, this transformation defines new quasiparticles comprised of the superposition of electrons and holes of opposite spin and momentum. They are commonly called *Bogoliubons*. It is unfair to Nikolai Bogoliubov that he is reserved only a footnote in this Chapter, which I have done for the sake of conciseness. His work on superconductivity paralleled, and in some aspects surpassed, that of BCS. For more context on that, I invite the reader to check out Chapter 7 of [82], Chapter 2.3 of [15], and [96].



within a shell around the Fermi surface with thickness  $\hbar\omega_D$ , such as  $\Delta_{\mathbf{k}} = \Delta$ . Since it is independent of  $\mathbf{k}$ , this implies an s-wave gap. Thus, using that  $\hbar\omega_D \ll \mu$  to again approximate the density of states of the system by  $N(\mathcal{E}_F)$ , we find that [91]

$$1 = U_0 N(\mathcal{E}_F) \int_0^{\hbar\omega_D} \frac{d\mathcal{E}'}{\sqrt{\mathcal{E}'^2 + \Delta^2(T)}} \tanh\left(\frac{\sqrt{\mathcal{E}'^2 + \Delta^2(T)}}{2k_B T}\right). \quad (1.63)$$

The above gap equation is obtained for an arbitrary  $T$ . Analyzing it in the limit that  $T \rightarrow 0$ , such that  $\Delta(T) \rightarrow \Delta(0)$ , yields

$$1 = U_0 N(\mathcal{E}_F) \ln\left(\frac{2\hbar\omega_D}{\Delta(0)}\right) \Rightarrow \Delta(0) = 2\hbar\omega_D \exp\left(-\frac{1}{U_0 N(\mathcal{E}_F)}\right), \quad (1.64)$$

where we have used the experimental observation that  $\Delta(0) \ll \hbar\omega_D$ . This result is similar to that of Eq. (1.51) for the binding energy of a Cooper pair. It shows that, no matter how weak an attractive interaction between electrons is, it will lead to the formation of a stable condensed state with a non-zero energy gap at  $T = 0$ . In other words, as was the suspicion of BCS after Cooper demonstrated the existence of the bound states, the normal state is indeed unstable toward the formation of the superconducting state.

Let us now return to Eq. (1.63) and take the other limiting case, meaning that in which  $\Delta(T) \rightarrow 0$  or  $T \rightarrow T_c$ . Using that  $\hbar\omega_D \gg k_B T_c$  and Euler's constant  $\gamma_E \approx 0.577$ , we arrive at

$$1 = U_0 N(\mathcal{E}_F) \int_0^{\hbar\omega_D} \frac{d\mathcal{E}'}{\mathcal{E}'} \tanh\left(\frac{\mathcal{E}'}{2k_B T_c}\right) \approx U_0 N(\mathcal{E}_F) \ln\left(\frac{2 \exp(\gamma_E) \hbar\omega_D}{\pi k_B T_c}\right) \quad (1.65)$$

$$T_c = \frac{2 \exp(\gamma_E) \hbar\omega_D}{\pi k_B} \exp\left(-\frac{1}{U_0 N(\mathcal{E}_F)}\right), \quad (1.66)$$

which shows that  $T_c \neq 0$  for an arbitrarily small  $U_0$ . Additionally, we note that  $T_c \propto \omega_D$ , recovering the isotope effect [Eq. (1.44)]. From Eqs. (1.64) and (1.66), we obtain the universal BCS relationship

$$\frac{2\Delta(0)}{k_B T_c} \approx 3.52. \quad (1.67)$$

Such a ratio between  $\Delta(0)$  and  $T_c$  could be experimentally obtained with great accuracy for most known superconductors at the time, as demonstrated in Figure 1.13. Its

prediction was one of the early successes of BCS. There were others, as I previously mentioned. There was also a series of rapidly obtained theoretical results that improved on, unveiled new aspects of, and reinforced the validity of BCS [82]. Among those, especially in the context of this thesis, the work of Lev Petrovich Gor'kov deserves a highlight [97]. In 1959, he demonstrated that the Ginzburg-Landau equations could be obtained from the BCS theory [97]. By employing a thermodynamic Green function formalism, he showed that under the strict consideration that  $T \rightarrow T_c$  (similar to GL), implying that the gap and superconducting parameters had a slow spatial variation [97,98], BCS yielded equations in complete analogy to the GL equations, where the gap function took the part of the order parameter (or a pair wave function) and the effective charge of the superconducting charge carrier is correctly identified as the Cooper pair charge ( $e^* = 2e$ ). This achievement was of utmost importance as it consolidated the highly successful GL phenomenological description of superconductivity, which is still largely employed to explain experimental observations. It also helped to advance our understanding of the GL theory by providing a microscopic interpretation of its parameters.

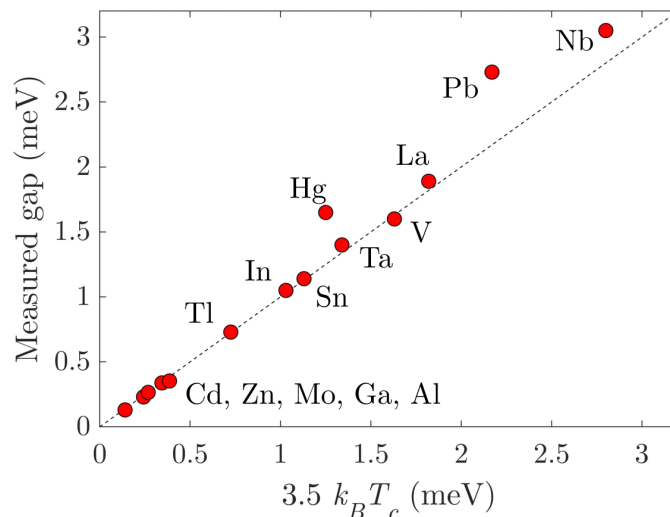


**Figure 1.13.** Comparison between the experimentally measured superconducting gap for several elemental superconductors and the BCS prediction. Adapted from [99].

## 1.9 The Josephson Effect and the SQUID

In 1958, a Norwegian engineer named Ivar Giaever moved to New York, where he was assigned to work on thin films together with John Fischer at the General Electric Research Laboratory [15, 100]. Together, they were performing electron tunneling experiments in metal films separated by a thin insulating layer, inspired by Leo Esaki's earlier work on semiconductors [101]. Soon after, Giaever began pursuing a formal Physics education, eventually earning his Ph.D. from Rensselaer Polytechnic Institute. There, he was introduced to superconductivity and, during a lecture about the BCS theory, was captivated by the concept of the energy gap.

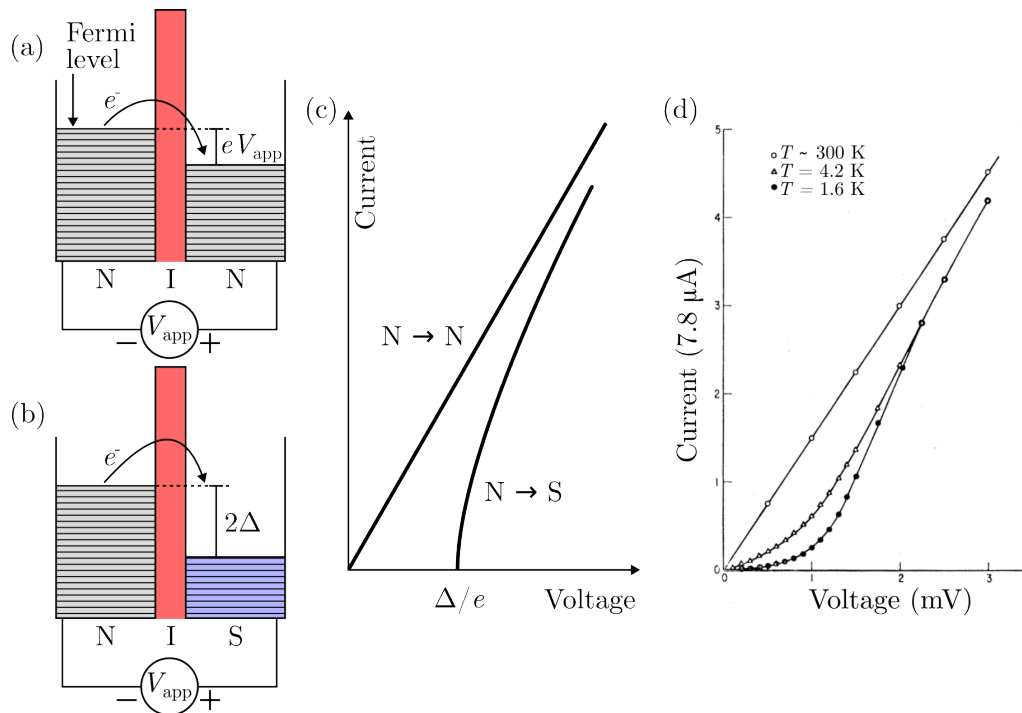


**Figure 1.14.** Electron tunneling between a normal metal and a superconductor. (a) Representation of the energy levels of two normal metals (N) separated by an insulating barrier (I) under an applied voltage  $V_{app}$ . (b) Similar to the previous panel, but now one of the materials is a superconductor (S). (c) The expected tunneling current-voltage relationship for the situations in panels (a) and (b). (d) Giaever measurements for an Al/A<sub>2</sub>O<sub>3</sub>/Pb tunnel junction at different temperatures demonstrate the tunneling of electrons between the normal and superconducting materials. Adapted from [100].

What Giaever realized was that their tunneling experiments could be used to gauge the

superconducting gap. As represented in Fig. 1.14(a), if two normal metals are separated by some insulating barrier, an applied voltage  $V_{\text{app}}$  will lead to different Fermi energies for each metal. Then, only electrons with energy  $eV_{\text{app}}$  can leave from the left side of the barrier to the right side, as lower energy states are occupied. This process results in a measurable linear current-voltage relationship (or  $I$ - $V$ ). Now, suppose the material on the right is a superconductor and thus presents an energy gap, as in Fig. 1.14(b). Electrons now can only tunnel through the barrier if their energy is greater than the gap, i.e., for an applied voltage greater than  $\Delta/e$ , resulting in a modified  $I$ - $V$ , as represented in Fig. 1.14(c).

To test this hypothesis, in 1960, Giaever conceived a rather simple and elegant experiment [102]. He fabricated Al/Al<sub>2</sub>O<sub>3</sub>/Pb multilayered thin films. The insulating oxide layer was only a few Angstroms thick. This is known as a tunnel junction. By cooling the samples down to 4.2 K, he ensured the Pb layer was superconducting ( $T_c = 7.2$  K at zero magnetic field), while Al remained in the normal state ( $T_c = 1.2$  K at zero field). However, if a sufficiently large magnetic field was applied, both layers would behave as normal metals. Then, he measured  $I$ - $V$  in both cases, identifying the expected suppression of the tunnel current within the superconductor for low voltages. Figure 1.14(d) shows analogous results Giaever obtained when conducting his experiments without an applied field at different temperatures. At room temperature, both layers behave as normal metals, while at 4.2 K and 1.6 K only Pb is superconductive. The curves reproduce the  $I$ - $V$  curve depicted in Fig. 1.14(c) with some electrons flowing for voltages lower than  $\Delta/V_{\text{app}}$  due to thermal excitation. Furthermore, if tunneling currents could be considered proportional to the density of states (in the low  $N(\mathcal{E})$  regime), Giaever's results confirmed those obtained by BCS. Therefore, it was demonstrated that single electrons could tunnel through a barrier between a normal metal and a superconductor, respecting the energy gap described by the BCS theory. Today, with the benefit of hindsight, I can claim that a natural following question was "what about the tunneling of Cooper pairs through a

barrier between two superconductors?”

As Sir Brian Pippard recalled [15], around the time of Giaever’s experiments, people believed that the joint tunneling of two electrons would be an extremely unlikely event, as its probability was the square of that of the single electron tunneling. Thus, this phenomenon would be too rare to result in a measurable *supercurrent* through a barrier between two superconductors. It is true, though, that two separate works, published on following pages of the same issue of Physical Review Letters, showed evidence of supercurrent tunneling already in 1960, one by James Nicol, Sidney Shapiro, and Paul H. Smith [103] and the other by Giaever [104]. However, none related the observations to the tunneling of Cooper pairs.

The mention of Pippard in this context is intentional. Although it was not he who solved the puzzle, he is intertwined in the history of it. In 1961, Pippard was a Professor of Physics at Cambridge where he agreed to supervise the Ph.D. studies of one twenty-one years old Brian David Josephson. According to Pippard, Josephson had a “brilliant undergraduate career” in Mathematics and Physics but wanted to write an experimental thesis to balance up his expertise [15]. Although he would do just that, Josephson couldn’t help but pursue his independent theoretical work during those years. He was much aided by one happy coincidence. From 1961 through 1962, Philip W. Anderson spent a sabbatical year as a lecturer at Cambridge, later recalling that having Josephson as his student on a solid-state and many-body course was “a disconcerting experience because everything had to be right or he would come up and explain it to me after class” [105]. The interaction between these three men would shape Josephson’s famous publication on the possible tunneling of Cooper pairs through a barrier between superconductors in 1962 [106]. Since then, this phenomenon has become known as the **Josephson effect**. Anderson made a point of letting it be clear that the work was Josephson’s own, from start to finish [105], but Pippard and Josephson seemed more willing to give Anderson his share of merit as well [15, 107].

In his work, Josephson used a perturbational approach to expand on a newly developed description of the tunneling of electrons by a coupling transfer Hamiltonian [108] and the already known Bogoliubov formalism for the superconducting theory. In essence, what he showed was that the macroscopic nature of the condensed quantum state is reflected in the tunneling of Cooper pairs. Because in superconductors the electronic wave functions are phase-coherent, electrons would not tunnel individually but rather it is the wave function that describes the coherent behavior of the ground state that dictates tunneling. In other words, the probability of Cooper pair tunneling is proportional to that of a single electron. This bears remarkable implications, some already realized by Josephson in his original paper. We can grasp the basic understanding of the phenomenon by considering the system depicted in Fig. 1.15.

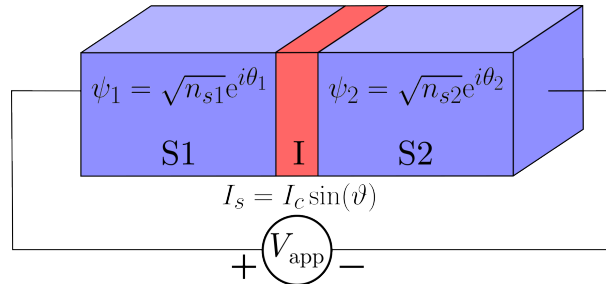


**Figure 1.15.** Schematic representation of a typical SIS Josephson junction.

Imagine two superconductors with macroscopic wave functions  $\psi_1$  and  $\psi_2$  separated by a thin insulating barrier such as they are coupled by an effective potential  $U_c$  [21]—an SIS junction. The barrier between the superconductors is known as a **weak-link**. If a voltage is applied across the superconductors and we take the zero potential in the center of the barrier, the Cooper pair potential energies for each side are  $eV_{app}$  and  $-eV_{app}$ . Thus, we can write down a set of coupled Schrödinger equations for the system,

$$i\hbar \frac{d\psi_1}{dt} = eV_{app}\psi_1 + U_c\psi_2 \quad (1.68)$$

$$i\hbar \frac{d\psi_2}{dt} = -eV_{app}\psi_2 + U_c\psi_1. \quad (1.69)$$

As  $|\psi_{1,2}|^2$  represents the probability density that Cooper pairs are found at each super-

conductor, we can take

$$\psi_1 = \sqrt{n_{s1}} \exp(i\theta_1), \quad \psi_2 = \sqrt{n_{s2}} \exp(i\theta_2) \quad \text{and} \quad \vartheta = \theta_2 - \theta_1, \quad (1.70)$$

where  $\vartheta$  is the phase difference across the barrier. Both the Cooper pair densities and the phases depend on time. Substituting the wave functions in Eq. (1.68) and taking the imaginary and real parts yields, respectively

$$\frac{\hbar \cos(\theta_1)}{2\sqrt{n_{s1}}} \frac{dn_{s1}}{dt} - \hbar\sqrt{n_{s1}} \sin(\theta_1) \frac{d\theta_1}{dt} = eV_{\text{app}}\sqrt{n_{s1}} \sin(\theta_1) + U_c\sqrt{n_{s2}} \sin(\theta_2) \quad (1.71)$$

$$-\frac{\hbar \sin(\theta_1)}{2\sqrt{n_{s1}}} \frac{dn_{s1}}{dt} - \hbar\sqrt{n_{s1}} \cos(\theta_1) \frac{d\theta_1}{dt} = eV_{\text{app}}\sqrt{n_{s1}} \cos(\theta_1) + U_c\sqrt{n_{s2}} \cos(\theta_2). \quad (1.72)$$

Multiplying Eq. (1.71) by  $\cos(\theta_1)$  and Eq. (1.72) by  $\sin(\theta_1)$  then subtracting the equations gives

$$\frac{dn_{s1}}{dt} = \frac{2U_c}{\hbar} \sqrt{n_{s1}n_{s2}} \sin(\vartheta), \quad (1.73)$$

where we used the trigonometric relationship  $\sin(a - b) = \sin(a) \cos(b) - \sin(b) \cos(a)$ .

Following the same procedure for Eq. (1.69), we find

$$\frac{dn_{s2}}{dt} = -\frac{2U_c}{\hbar} \sqrt{n_{s1}n_{s2}} \sin(\vartheta). \quad (1.74)$$

The tunneling supercurrent across the barrier is nothing more than the flow of Cooper pairs from one superconductor to the other. Therefore, the tunneling current density is linked to the variation of the Cooper pair density in the superconductors. From the equations obtained above, we note that

$$J_s = J_c \sin(\vartheta), \quad (1.75)$$

where  $J_c$  is the maximum current able to flow through the barrier, proportional to the coupling constant. Equation (1.75) is known as **the first Josephson relation** and expresses the current-phase relationship of the junction. It states that, even if there is no voltage difference between the superconductors, a phase difference across the barrier will spontaneously induce a tunneling superconducting current that varies periodically with

$\vartheta$ . This is known as the dc Josephson effect. It was first confirmed experimentally by J. M Rowell and Anderson (already back at the Bell Labs) in 1963 [109]. A tunnel junction comprised of two superconducting electrodes that presents the Josephson effect, such as the one in Fig. 1.15, is more commonly called a **Josephson junction**.

If, instead, we multiply Eq. (1.71) by  $\sin(\theta_1)$  and Eq. (1.72) by  $\cos(\theta_1)$  [and analogously for Eq. (1.69)], by adding the equations and assuming  $n_{s1} \approx n_{s2}$  we find **the second Josephson relation**

$$\frac{d\vartheta}{dt} = \frac{2e}{\hbar} V_{\text{app}} = \frac{2\pi}{\Phi_0} V_{\text{app}}, \quad (1.76)$$

which predicts the temporal evolution of  $\vartheta$  under an applied dc voltage. Integrating Eq. (1.76) and substituting it in Eq. (1.75), we find that, if a dc voltage is applied across the barrier between two superconductors, an oscillating tunneling current will flow with a frequency  $f_J$  proportional to the applied voltage

$$\frac{f_J}{V_{\text{app}}} = \frac{2e}{h} = \frac{1}{\Phi_0} = 483.6 \times 10^{12} \text{ Hz/V}, \quad (1.77)$$

known as the **Josephson frequency**. This phenomenon is known as the ac Josephson effect. The first experimental evidence of its existence was found by Sidney Shapiro in 1963 [110] and the effect was confirmed by Giaever in 1965 [111].

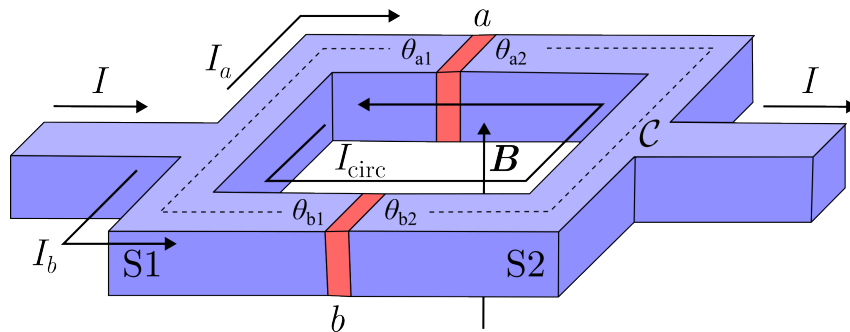


**Figure 1.16.** Schematic representation of a dc SQUID. This circuit element is comprised of two parallel Josephson junctions, represented by  $a$  and  $b$ . Currents flow through the superconducting loop as indicated. A magnetic field is applied perpendicular to the SQUID.

In the general case of an SIS junction subjected to an applied magnetic field, Eq. (1.14) tells us that the phase across the junction is related to the total magnetic flux through



the barrier. Furthermore, the current density term can be neglected if the integration path is chosen as such  $\mathbf{J}_s = 0$  or does not contribute to the integral [15]. This leads us to one of the most remarkable applications of Josephson junctions.

Consider a superconducting loop comprised of two parallel SIS junctions ( $a$  and  $b$ ) subjected to a perpendicular magnetic field and an applied transport current  $I$ , as represented in Fig. 1.16. The applied current separates into  $I_a$  and  $I_b$ , flowing on each side of the loop. As these currents have the same direction, they generate opposing magnetic fields, which give rise to an opposing circulating current  $I_{\text{circ}} = (I_a - I_b)/2$  contributing to the total flux inside the loop. If we take the integration path  $\mathcal{C}$  represented by the dashed line in Fig. 1.16, the fact that the system's macroscopic wave function has to be single-valued requires that the total acquired phase difference is an integer multiple of  $2\pi$ , i.e.,

$$\oint \nabla\phi \cdot d\mathbf{l} = 2\pi n_v = (\theta_{a2} - \theta_{a1}) + (\theta_{b2} - \theta_{a2}) + (\theta_{b1} - \theta_{b2}) + (\theta_{a1} - \theta_{b1}), \quad (1.78)$$

where  $n_v$  is a winding number and we can identify  $\theta_{a2} - \theta_{a1} = \vartheta_a$  and  $\theta_{b1} - \theta_{b2} = -\vartheta_b$ . Thus, using Eq. (1.14), we can show that

$$2\pi n_v = \vartheta_a - \vartheta_b + \frac{2\pi}{\Phi_0} \int_{\mathcal{C}} \mathbf{B} \cdot d\mathbf{s} + \frac{2\pi}{\Phi_0} \mu_0 \lambda^2 \left\{ \int_{a2}^{b2} \mathbf{J}_s \cdot d\mathbf{l} + \int_{b1}^{a1} \mathbf{J}_s \cdot d\mathbf{l} \right\}. \quad (1.79)$$

For dissipationless currents flowing in a closed loop, the self-induced flux is proportional to the total kinetic inductance of the system  $L_k$  [21]. Hence, the fourth term on the right-hand side of Eq. (1.79) can be rewritten in terms of the kinetic inductance of the junctions. If  $\Phi$  is the total flux enclosed by  $\mathcal{C}$ , the total phase difference between junctions  $b$  and  $a$  is thus given by

$$\vartheta_b - \vartheta_a = 2\pi n_v + \frac{2\pi}{\Phi_0} (\Phi + I_a L_k^a + I_b L_k^b). \quad (1.80)$$

This equation evidences the quantization of the flux density through the superconducting loop. As one vortex carries one flux quantum,  $n_v$  is commonly called the **vorticity**

---

**number.** For simplicity, let's assume  $n_v = 0$  and that the kinetic inductance of the junctions is negligible. Furthermore, the junctions' critical current densities are the same, i.e.,  $J_c = J_c^a = J_c^b$ . Substituting Eq. (1.80) in the first Josephson relation yields

$$J_s = J_c \sin(\vartheta_1) + J_c \sin(\vartheta_2) = 2J_c \sin\left(\frac{\vartheta_1 + \vartheta_2}{2}\right) \cos\left(\frac{\vartheta_1 - \vartheta_2}{2}\right) \quad (1.81)$$

$$J_s = 2J_c \sin\left(\vartheta_1 + \pi \frac{\Phi}{\Phi_0}\right) \cos\left(\pi \frac{\Phi}{\Phi_0}\right), \quad (1.82)$$

thus, the maximum current density that can flow in the superconducting loop for a given  $\Phi$  is

$$J_s^{\max} = 2J_c \left| \cos\left(\pi \frac{\Phi}{\Phi_0}\right) \right|. \quad (1.83)$$

Therefore, the current flowing through the loop is periodically modulated by an applied magnetic field, reaching maximum values when  $\Phi$  takes values of integer multiples of the flux quantum  $\Phi_0$ . Such an oscillating feature arises from the interference between the supercurrents flowing on each side of the loop, with the junctions playing an analogous role to that of the double slits on Young's light interference experiment [21]. For this reason, the circuit element depicted in Fig. 1.16 is known as a dc superconductor quantum interference device, or **dc SQUID**. It was first realized by Robert C. Jaklevic, John Lambe, Arnold H. Silver, and James E. Mercereau in 1964 [112] and its technological appeal became immediately evident as a powerful magneto- and voltmeter. By 1966, John Clarke (another of Pippard's famous graduate students) developed a SQUID-based device capable of measuring voltages of about  $10^{-14}$  V in one second [113]. Over time, SQUIDs have evolved and they are today one of the main electrical components enabling quantum technology [15, 114]. The sheer impact of Josephson's discovery is truly overwhelming. He was awarded the 1973 Nobel Prize in Physics "for his theoretical predictions of the properties of a supercurrent through a tunnel barrier, in particular those phenomena which are generally known as the Josephson effects". The prize was shared with Leo Esaki and Giaever "for their experimental discoveries regarding tunneling phenomena in semiconductors and superconductors, respectively". Although not recognized by the

Nobel Committee for his contributions to the development of the Josephson effect, Philip Anderson’s career was filled with an unmatched array of contributions to the field of Condensed Matter. In 1977, he shared the Nobel Prize in Physics with Sir Nevill Francis Mott and John Hasbrouck Van Vleck “for their fundamental theoretical investigations of the electronic structure of magnetic and disordered systems”.

The Josephson effect is not exclusive to SIS junctions as the one we have imagined thus far. In fact, two weakly coupled superconductors may allow for the tunneling of Cooper pairs irrespective of the nature of the weak-link, which, for instance, can be a normal metal (SNS junctions) or even a geometrical constriction of the superconducting material (ScS junctions) [114, 115]. In Chapter 5 of this thesis, I will present results obtained for a SQUID device in which the Josephson junctions are of the ScS type, as the one represented in Fig. 1.17.

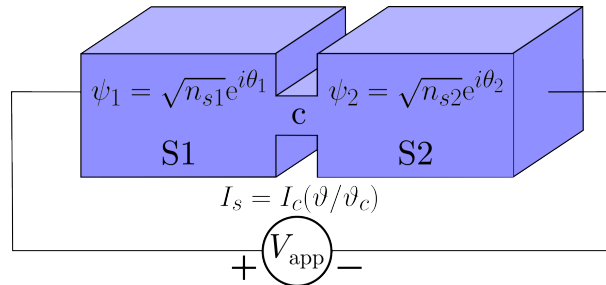


**Figure 1.17.** Schematic representation of a typical SIS Josephson junction.

In this case, given that the length of the constriction is much greater than the coherence length, the first Josephson relation is modified as the current-phase relationship becomes linear [116–119]. Writing Eq (1.75) for the current that flows over the ScS junction, we have that

$$I_s = I_c \frac{\vartheta}{\vartheta_c}, \quad (1.84)$$

where  $\vartheta_c$  is a critical phase difference over the junction which destroys the superconducting behavior. Taking the time-derivative of the above equation and using the second Josephson relation [Eq. (1.76)], it is possible to show that for the long weak-link the

kinetic inductance dominates the dynamics of current variation such that

$$I_s = \frac{\Phi_0}{2\pi} \frac{1}{L_k} \vartheta. \quad (1.85)$$

If a SQUID is comprised of two such ScS junctions with different critical currents, we can rewrite Eq. (1.81) as

$$I_s = \frac{I_c^a \Phi_0}{2\pi L_k^a} \vartheta_a + \frac{I_c^b \Phi_0}{2\pi L_k^b} \vartheta_b. \quad (1.86)$$

Furthermore, similarly to the SQUID with SIS junctions,

$$\vartheta_b - \vartheta_a = 2\pi \left( n_v + \frac{\Phi}{\Phi_0} \right) = 2\pi \left( n_v + \frac{B}{\Delta B} \right), \quad (1.87)$$

where  $\Delta B = \Phi_0 A_{\text{loop}}$  and  $A_{\text{loop}}$  is the area of the superconducting loop. From Eqs. (1.86) and (1.87) and enforcing that the superconducting state is lost if  $|\vartheta_{a,b}| \geq \vartheta_c^{a,b}$ , it is possible to obtain a relationship for the ScS SQUID critical current for any given  $n_v$  and  $B$  across the loop, where  $I_c$  is defined as the lowest current for which any of the SQUID's arms transitions to the normal state. These  $I_c(B, n_v)$  relationships display characteristic polygonal shapes, periodically distributed with respect to  $B$ , known as **vorticity diamonds**. Each vorticity diamond differs from its nearest neighbor by the admission or exclusion of one flux quantum in the loop, i.e., by  $\pm n_v$ .

## 1.10 An interlude

Before I move on to focus on the results obtained by the research conducted in the context of this thesis, I wanted to say a few words about some things I will not talk about. If this text happens to be your first contact with superconductivity and I have made a good job describing the advancements in the understanding of this phenomenon until the mid-1960s, you may think that we completely understand what is happening and, by now, are only exploring the possibilities that arise from this remarkable natural behavior. This is far from the truth. In fact, in the Introduction to the text, I have mentioned that there are five Nobel Prizes directly awarded to advancements in superconductivity, but

you may have noticed that I have so far only accounted for four. I think an informative way of communicating this for newcomers in the field is by looking at what we can call a “race for room-temperature superconductors”.

One aspect that is paramount to our ability to explore superconductivity in everyday life is the critical temperature. At the time of the BCS theory, in all known superconducting materials, the dissipationless state only came about in extremely low-temperature conditions, requiring the use of liquid helium as a refrigerant. Therefore, the cost of cooling something down to the superconducting state was considerably high. This has motivated a quest to find materials with ever-higher  $T_c$  values essentially since superconductivity was discovered. However, until the mid-1980s, the superconductor with the highest known  $T_c$  was  $\text{Nb}_3\text{Ge}$  at around 23 K. There is a famous plot that tracks the evolution of the highest superconducting  $T_c$  by year of discovery.

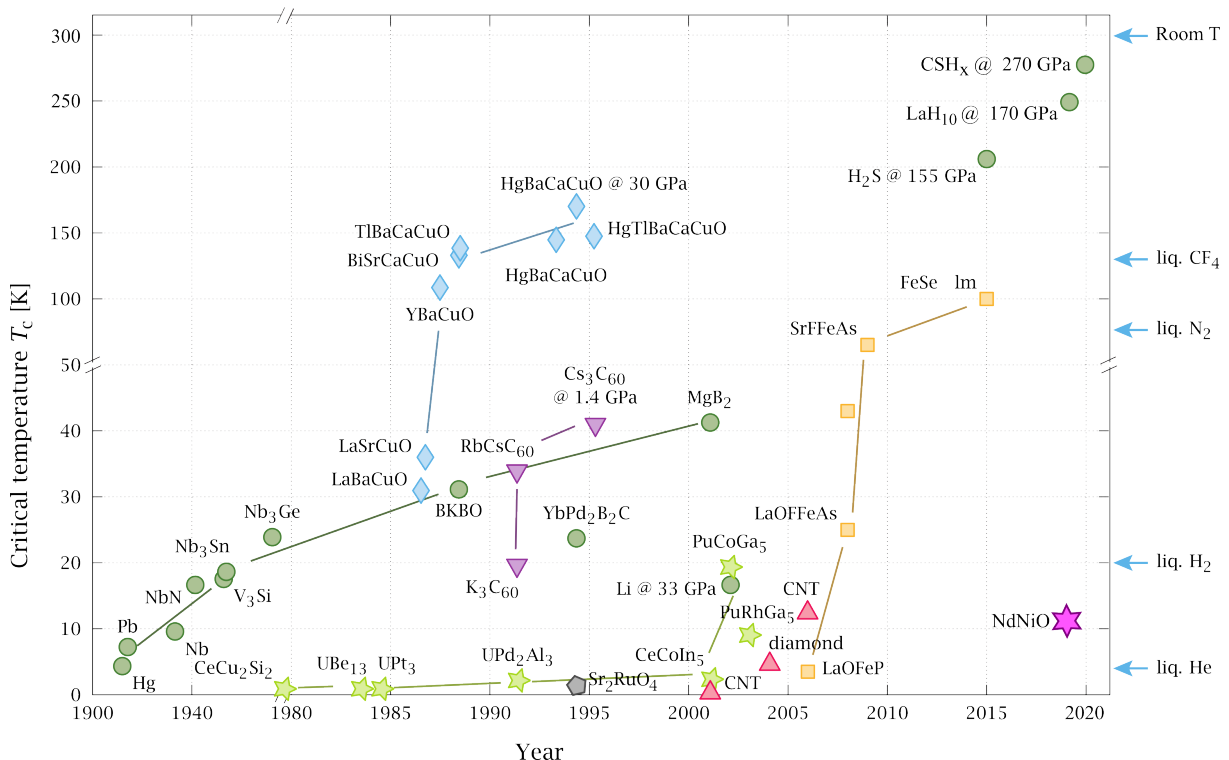


**Figure 1.18.** The highest known  $T_c$  for different classes of superconductors through the years. Different symbols indicate different classes. Conventional BCS superconductors are shown as green circles, whereas high- $T_c$  cuprates appear as blue diamonds. Adapted from [120]. See [121] for more information.

Then, in 1986, something happened. Figure 1.18 presents blue-shaped diamonds that skyrocketed the highest known  $T_c$  to over 130 K at ambient pressure in a matter of a couple of years. This exciting development was the result of a breakthrough by Johannes Georg Bednorz and Karl Alexander Müller [122]. They had discovered a new class of superconductors! These were not metallic in the normal state, but ceramic materials that combined rare earth elements with copper oxide and are usually referred to as cuprates, high-temperature superconductors, or high- $T_c$ s. But that is not all that is exciting. It was soon figured out that such materials do not follow the BCS theory. They do not present an s-wave gap and the coupling mechanism is not the same as that described by BCS. For instance, this can be seen in Fig. 1.19 in which the measured gap of high- $T_c$ s clearly deviates from the BCS prediction. The impact of their discovery was so big that just one year later, in 1987, Bednorz and Müller were awarded the Nobel Prize in Physics “for their important breakthrough in the discovery of superconductivity in ceramic materials”.

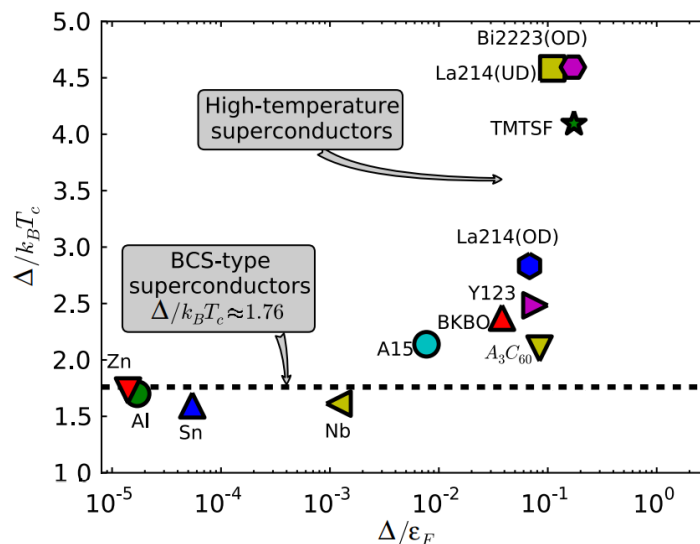


**Figure 1.19.** The ratio between the energy gap and  $k_B T_c$  as a function of the gap-to-Fermi energy ratio for different BCS and high-temperature superconductors. Adapted from [123].

To this day, a complete microscopic description of superconductivity in these high-temperature superconductors is missing. Moreover, new classes of superconducting ma-

---

materials have been discovered through the years. In a very informative review paper from 2017 [124], G. R. Stewart enumerates nine classes of superconductors with particular sets of behaviors not described by the BCS theory, which have become known as **unconventional superconductors**. In this thesis' results, I will deal directly only with BCS-type, or **conventional superconductors**, although we believe and point out that some of the observed effects should also be observed for high- $T_c$ s.

Furthermore, a plethora of new phenomena (and new implications of previously-known phenomena) in superconductors continue to be discovered regularly, as I hope this thesis will demonstrate. So, if you are indeed new to the study of superconductivity, there is plenty to be excited about. Of course, Bardeen, Cooper, and Schrieffer could not have known about all this in 1957 and, as Cooper said sometime later [82], had they known it, they would probably never have built their beautiful theory to describe conventional superconductors. Instead, their success came about by focusing on one “simple” issue: to explain the emergence of the superconducting gap. Maybe the contributions of the young researchers involved in this endeavor, as well as several others made by graduate students to the development of superconductivity, will serve as inspiration that good ideas and hard work may pay off big time.

# Chapter 2

## Methods

This thesis is structured as a collection of papers and manuscripts. As such, each particular study made use of an appropriate collection of experimental techniques to enable the presented research. In this Chapter, I will briefly introduce the methods explored to fabricate and study the superconducting thin film samples and devices investigated in these different works. The important details of the techniques and materials that are particular to each work are provided in the texts of the following Chapters.

### 2.1 Thin film deposition and patterning

All samples studied in the context of this thesis were thin films deposited by physical vapor deposition (PVD). Such a method relies on the decomposition of a particular condensed target material, which is then vaporized and transported through a high vacuum environment to a substrate, at which it recondenses in the form of a thin film [125]. Different PVD techniques present particular advantages and two were used in the works in this thesis.

**Dc magnetron sputtering.** Sputtering is the physical process by which atoms on the surface of a target material are ejected by the momentum transferred by incident ions [125]. In sputter deposition techniques, these atoms constitute the vapor phase which is transported to the substrate. One key advantage of sputtering is that it allows



the deposition of materials with high melting points, which are harder or more expensive to deposit by techniques that rely on the thermal evaporation of the target material. In dc magnetron sputtering [126], after a base pressure is reached, argon gas is inserted into the high vacuum environment and a controllable working pressure is achieved. Then, a voltage is applied between the substrate and the target, and a glow discharge process results in the formation of an  $\text{Ar}^+$ -rich plasma. The positive ions are attracted by the negative potential on the target, bombarding its surface and leading to the sputtering of the material. Meanwhile, a set of magnets creates a magnetic field that keeps electrons on trajectories contained in the neighborhood of the target. This serves two purposes: it increases the probability of ionizing the argon gas, leading to higher deposition rates; and prevents such electrons from interfering with the deposition at the substrate.

**Pulsed laser deposition.** In this technique, a high-power pulsed laser beam is used to provide the necessary energy to vaporize the surface of a target material in a high vacuum environment [127]. The strong electric field of the laser beam excites electrons in the target, which then collide with atoms, transferring the necessary energy to evaporate the material in an out-of-equilibrium process that typically takes place in tens of nanoseconds. The evaporated material forms a plasma plume comprised of a mixture of atoms, ions, electrons, molecules, clusters, and particulates. These characteristics make pulsed laser deposition an ideal technique to fabricate thin films closely matching the stoichiometry of the target materials, ideal for the deposition of complex oxides or amorphous structures. The plume rapidly expands in the vacuum chamber, creating a jet of material that is propelled perpendicularly to the target surface and recondenses at the substrate, forming the desired thin film.

In the different studies, the investigated thin film samples needed to be patterned into particularly desired structures, with feature scales ranging from nanometers to millimeters. To prepare the patterns enabling such fabrication control, we used either **optical lithography** (OL) or **electron-beam lithography** (EBL) [128,129]. Although the latter

presents a higher resolution, enabling the fabrication of structures with details typically in the range of tens of nanometers, the working principle of both techniques is very similar, as illustrated in Fig. 2.1.

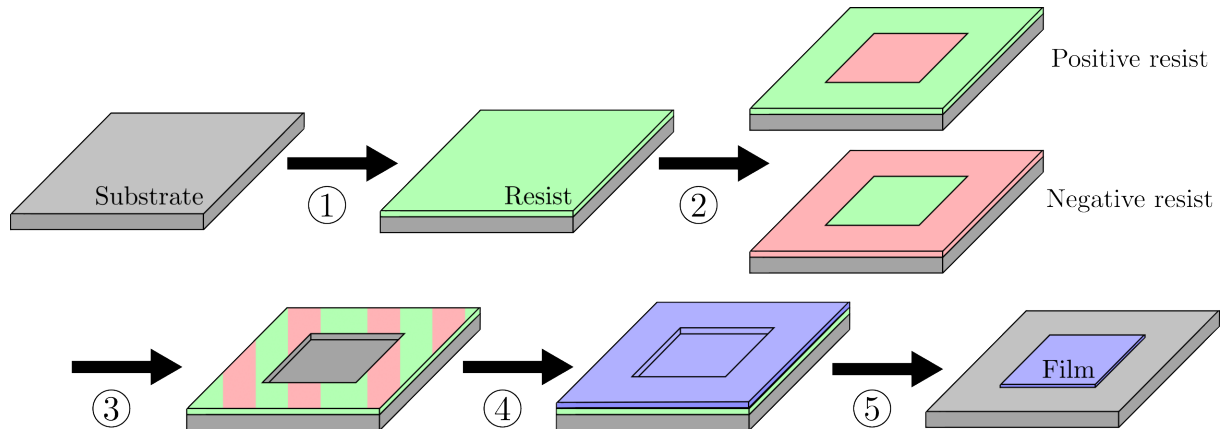


**Figure 2.1.** Standard lithography procedure. In step 1, a bare substrate is coated with a sensitive resist layer, which can be either of the positive or negative kind. Then, in step 2, the resist is exposed to an external agent to form the desired pattern, altering the properties of the exposed areas (in red). In step 3, a developing agent will remove either the exposed areas (positive resist) or the unexposed areas (negative resist), thus forming the mask onto which the thin film material is evaporated in step 4. Finally, in step 5, the remaining resist is lifted off from the substrate by a solvent solution, revealing the final sample.

In step 1, thin resist layers are applied to the substrate by spin coating. After each coating step, the temperature is increased to remove excess resist solvents. In EBL, resists are electron-sensitive materials, of which the solubility can be modified by exposure to an electron beam. In OL, resists are sensitive to light exposure. Then, in step 2, the desired patterns are written to the resist-coated substrate by either an electron beam or a light source. In step 3, a substance known as a developer is applied to the previously exposed coated substrate. The resist may either be of the positive type, which will lead to the removal of all exposed areas of the resist by the developer, or negative, in which case the unexposed areas are removed. This creates a mask for the deposition of the samples, which takes place in step 4. Finally, any excess resist is removed in step 5, known as lift-off, with the aid of a solvent solution, such as hot acetone.

After the initial deposition, in two of the studies presented in this thesis, the samples were subjected to an additional patterning step. In **focused ion beam** (FIB) milling, a finely-focused high-energy ion beam interacts with the surface of the material, sputtering atoms with maximum resolution typically in the range of units of nanometers [130, 131]. The depth of the milled regions can be controlled by the applied FIB dose and exposure, whereas ions are typically provided by a liquid-metal gallium ion source at which high electric fields cause the emission of  $\text{Ga}^+$ . An inherent advantage of this patterning method is that it does not require the development of a mask such as the ones I just described. However, it is unavoidable that FIB milling introduces impurities in the form of disorder and  $\text{Ga}^+$  implantation into the structure of the irradiated material.

## 2.2 Magnetic measurements

The research in this thesis deals with the interaction of magnetic fields with superconducting specimens. In all but one of the following studies, different techniques were used to gauge the sample magnetic response, with particular emphasis given to **magneto-optical imaging** [63, 132]. MOI allows for the visualization of the magnetic flux within superconductors combining high magnetic flux sensitivity with a temporal resolution as small as 10 ns and an unmatched field-of-view, ranging from several hundred nanometers to centimeters<sup>16</sup>. Regarding sensitivity, MOI setups can reach minimum detectable fields in the range of  $10^{-7} \text{ T}/\sqrt{\text{Hz}}$  [132]. These values outperform other magnetic imaging techniques, such as Lorentz microscopy and Bitter decoration, and are comparable to those in state-of-the-art scanning NV center magnetometry [132–134]. However, MOI field sensitivity does not match that of modern magnetic force microscopy ( $10^{-8} - 10^{-9} \text{ T}/\sqrt{\text{Hz}}$ ) and scanning SQUID sensors ( $10^{-11} \text{ T}/\sqrt{\text{Hz}}$ ) [133, 134].

To map the local magnetic response in a superconducting sample, MOI takes advantage

---

<sup>16</sup>In the configurations typically used in the MOI setup at UFSCar, the temporal resolution is of the order of 100 ms, whereas the maximum spatial resolution is of the order of a few units of micrometers.

of the Faraday magneto-optical effect [63]. This phenomenon consists of the rotation of the polarization plane of linearly polarized light beams as they pass through a Faraday-active medium in the presence of magnetic fields. Here, Faraday-active means that the material presents a large Faraday effect, which is gauged by a material and frequency-dependent parameter called Verdet constant,  $C_V(\omega)$ . The rotation angle  $\theta_F$  also depends both on the length of the Faraday-active region,  $l$ , and on the intensity of the magnetic field parallel to the light beam,  $H_z$ , such that

$$\theta_F = C_V(\omega)lH_z. \quad (2.1)$$

Importantly, superconducting materials have not been found to present large  $C_V(\omega)$  values. Therefore, visualizing the flux patterns in these materials by MOI requires the use of a Faraday-active sensing layer, also called a magneto-optical layer (MOL) or indicator. In other words, the images obtained in a MOI experiment reflect the magnetic flux line distribution in the sensing layer, which is modified by the presence of the nearby superconducting sample. MOLs are most frequently constituted of a bismuth-substituted yttrium iron garnet (Bi-YIG)—the Faraday-active material with an in-plane spontaneous magnetization—grown on gadolinium gallium garnet (GGG) substrates and capped by a reflective aluminum layer. A local magnetic field in the Bi-YIG layer results in a magnetization component parallel to the light beam, as represented in Fig. 2.2.

A typical MOI setup is sketched in Fig. 2.2. The sample to be studied is mounted on top of a cold finger inside an evacuated cryostat, just below an optical window. The MOL is then placed in direct contact with the sample to minimize its distance to the film. A visible light source emits a light beam that is linearly polarized by a polarization filter. A beam splitter then directs the polarized beam to the sample region, where it interacts with the MOL, first passing through the transparent GGG substrate, then the Bi-YIG Faraday-active layer, and then being reflected by the Al mirror. This ensures that light passes twice through the sensing layer, doubling the rotation angle. Finally, the rotated

light beam passes through an analyzing filter, set close to  $90^\circ$  relative to the polarizer, thus only allowing rotated light to pass through, which is then captured by a charge-coupled device (CCD) camera. The image obtained maps the intensity of the incoming light at the camera, which is proportional to the rotation angle and thus to the local  $H_z$ . As the magnetic field at the sample region is directly related to the sample's magnetization, such an image reveals how the perpendicular component of the magnetic flux is distributed throughout the sample.

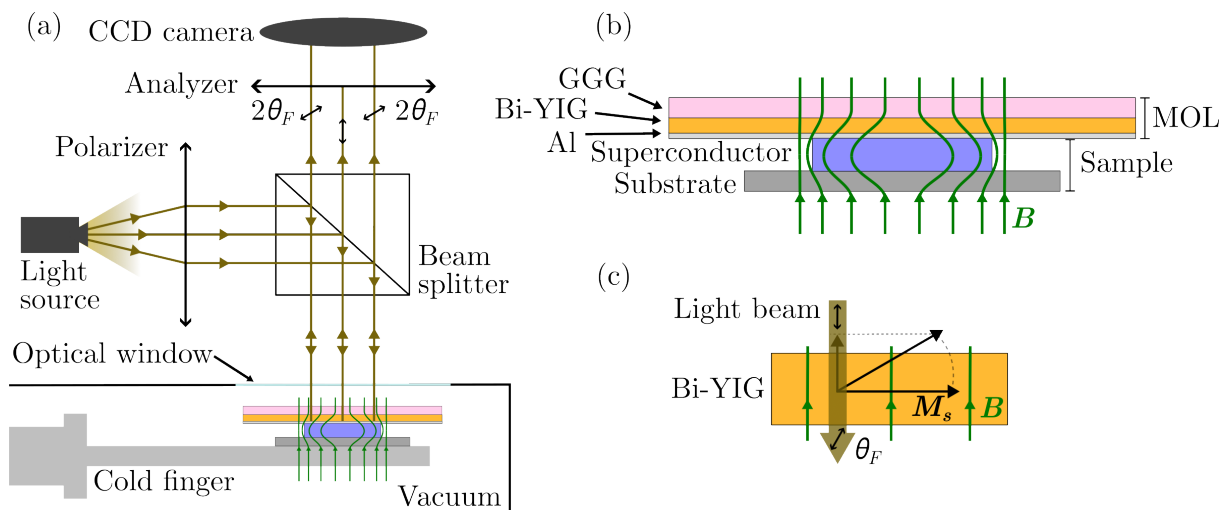


**Figure 2.2.** (a) Schematic diagram of a typical magneto-optical imaging experimental setup. (b) An enlargement of the sample and MOL region. (c) A representation of the field-induced rotation of the Faraday-active layer's spontaneous magnetization. The panel also shows the rotation of the polarization angle of the light beam as it passes through the indicator. Features appear out of scale.

Being an optical measurement, raw MOI results are not a quantitative representation of the magnetic properties of a superconductor. However, it is possible to perform a calibration allowing to quantify the magnetic flux density perpendicular to the sample surface,  $B_z$  [62, 63, 135]. As the light rotation occurs in the sensing layer, it is in principle necessary to account for its properties when calculating the relationship between  $B_z$  and the acquired intensity  $\mathcal{I}$ . For the described iron garnet MOLs, it can be shown that [63]

$$B_z(x, y) = B_k \tan \left\{ \arcsin \left( \frac{1}{cM_s} \arcsin \left( \sqrt{\frac{\mathcal{I}(x, y) - \mathcal{I}_{bkg}(x, y)}{\mathcal{I}'(x, y)}} \right) + \Delta\theta \right) \right\}, \quad (2.2)$$

where  $B_k$  and  $c$  are properties of the Faraday-active layer and  $M_s$  is its spontaneous in-plane magnetization. Additionally,  $\mathcal{I}(x, y)$  is the intensity of the light reflected by the mirror as it leaves the MOL,  $\mathcal{I}_{bkg}(x, y)$  is the measured background intensity, and  $\Delta\theta$  is an angular deviation between the polarizer and the analyzer from the  $90^\circ$  orientation. The coordinates  $(x, y)$  define the positions in the image. Inverting the equation above, one obtains

$$\mathcal{I}(x, y) - \mathcal{I}_{bkg}(x, y) = \mathcal{I}'(x, y) \sin^2 \left\{ cM_s \left[ \sin \left( \arctan \left( \frac{B_z(x, y)}{B_k} \right) \right) - \Delta\theta \right] \right\}. \quad (2.3)$$

Thus, by performing measurements varying the applied field intensity above  $T_c$ , such that the superconducting magnetization does not interfere with the results, it is possible to calibrate a  $\mathcal{I}(H)$  curve for each pixel of the CCD camera in the specific experimental assemble. However, for most practical applications, the magnetic fields are much lower than the ones necessary to saturate the MOL and the expression above can be approximated by the parabolic relationship [62, 135]

$$\mathcal{I}(x, y) - \mathcal{I}_{bkg}(x, y) = a(x, y)B_z^2(x, y) + b(x, y)B_z(x, y) + c(x, y), \quad (2.4)$$

where  $a$ ,  $b$ , and  $c$  are empirical calibration parameters.

Once the magnetic flux density is known, it should be possible to apply Ampère's law to obtain the current density flowing in the superconductor as

$$\mathbf{J} = \frac{1}{\mu_0} \nabla \times \mathbf{B}, \quad (2.5)$$

however, MOI only provides information on the perpendicular component of  $\mathbf{B}$ . Hence, it is necessary to turn to the Biot-Savart law to obtain a convenient relationship between  $B_z$  and the current density. As the superconducting samples investigated by MOI are usually thin films, it is possible to consider a flat geometry, where currents only flow along the film's  $xy$  plane, such that [63, 136]

$$B_z(\mathbf{r}) = \frac{\mu_0}{4\pi} \int_{\mathcal{V}} d^3\mathbf{r}' \frac{(y - y')J_x(x', y') - (x - x')J_y(x', y')}{|\mathbf{r} - \mathbf{r}'|^3}. \quad (2.6)$$

As there are two unknown quantities,  $J_x$  and  $J_y$ , we need an additional equation to solve the problem. If there are no transport currents applied or if the magneto-optical image contains the whole superconducting sample, then this is given by  $\nabla \cdot \mathbf{J} = 0$ .

As the current density lies on the  $xy$  plane, one possible approach to solving the problem is to introduce a perpendicular stream function  $\mathbf{g} = g(x, y)\hat{\mathbf{z}}$ , such that

$$\mathbf{J} = \nabla \times g(x, y)\hat{\mathbf{z}} \Rightarrow \begin{cases} J_x(x, y) = \frac{\partial g(x, y)}{\partial y} \\ J_y(x, y) = -\frac{\partial g(x, y)}{\partial x} \end{cases} . \quad (2.7)$$

This is the same procedure adopted by the thermomagnetic model described in Section 1.7.2. As before,  $g(x, y)$  has the physical meaning of a local magnetic moment [137].

We can then rewrite Eq. (2.6) using Eq. (2.7) as

$$B_z(\mathbf{r}) = \mu_0 \int_{\mathcal{V}} d^3\mathbf{r}' \frac{2(z - z')^2 - (x - x')^2 - (y - y')^2}{4\pi|\mathbf{r} - \mathbf{r}'|^5} g(x', y') \quad (2.8)$$

so that the problem becomes a matter of inverting this modified Biot-Savart equation. Then, assuming that the current density does not vary along the perpendicular component and extending the  $xy$  integration limits to an infinite plane, we can employ the convolution theorem to reduce the integrals to a product of two functions in momentum space, which, after integrating along the  $z'$  direction, results in [137]

$$\tilde{g} = \frac{\tilde{B}_z}{\mu_0 \exp(-kh) \sinh(kd/2)} . \quad (2.9)$$

Here,  $d$  is the thickness of the superconducting film and  $h$  is the height above the film's surface where the flux density distribution is measured, i.e., the distance between the top surface of the film and the sensing layer<sup>17</sup>.  $\tilde{B}_z$  and  $\tilde{g}$  are two-dimensional Fourier transformations of  $B_z$  and  $g$ , given by

$$\tilde{B}_z(k_x, k_y) = \int_{-\infty}^{\infty} dx \int_{-\infty}^{\infty} dy B_z(x, y) \exp[i(k_x x + k_y y)] \quad (2.10)$$

$$\tilde{g}(k_x, k_y) = \int_{-\infty}^{\infty} dx \int_{-\infty}^{\infty} dy g(x, y) \exp[i(k_x x + k_y y)] , \quad (2.11)$$

---

<sup>17</sup>In the typical configuration used at the MOI station at UFSCar,  $h \sim 5 \mu\text{m}$  [138].

which can be solved numerically and combined with Eq. (2.7) to obtain  $J_x$  and  $J_y$ . In the studies conducted in this thesis, we have employed the algorithms described in [136] to accomplish this task.

In addition to MOI, standard global magnetic characterization was performed on a Magnetic Property Measurement System model 5S (MPMS-5S) from Quantum Design [139]. The system is equipped with a high-sensitivity SQUID-based detector, allowing measurements of magnetic moments as small as  $10^{-11}$  Am<sup>2</sup> (or  $10^{-8}$  emu) with temperature control in the range of 1.8 K to 400 K and applied dc magnetic fields with intensities up to  $\sim 3979$  A/m (or 50 kOe). For dc measurements, the sample is moved through a second-order gradiometer consisting of a series of superconducting loops inductively coupled to the SQUID detector. Then, the magnetic flux variation caused by the sample movement changes the current in the superconducting loops. Such signal is transferred to the SQUID, which acts as a current-to-voltage converter and from which the output signal is a periodic function of the magnetic flux quantum. During a measurement scan, the sample is stopped at different positions and the SQUID voltage is averaged from several readings. Thus, it is possible to obtain the distribution of the voltage induced on the SQUID as a function of the sample position relative to the gradiometer. Considering the circuit geometry and that the currents induced in the loops can be approximated by those induced by a point-source magnetic dipole, the MPMS-5S software uses the induced voltage-per-position data to obtain the magnetic moment of the sample [140, 141]. The equipment can also employ the same detection mechanism to measure ac magnetic susceptibilities, which describe the field variation of the magnetic moment, with a sensitivity on the order of  $10^{-12}$  Am<sup>2</sup>. In this mode, an oscillating probe magnetic field is responsible for the variation of the sample's magnetic moment at fixed positions, giving rise to the change in current in the gradiometer. The setup then measures both an in-phase and an out-of-phase response, with respect to the applied ac field. The probe field can be applied in conjunction with dc fields and has a maximum amplitude of 3.8 Oe and frequencies



ranging from  $10^{-3}$  Hz to  $10^3$  Hz.

## 2.3 Electrical measurements

Except for Chapter 3<sup>18</sup>, all reported electrical measurements were carried out on a four-probe scheme to eliminate unwanted contributions from contact resistance. In essence, a constant electric current  $I$  is applied between two contact leads, inducing a voltage drop  $V$  across the sample. This is measured by a pair of sensing connections, or voltage leads, positioned between the current leads. In a conducting material, these quantities are related to the resistance by Ohm's law, which states that  $V = RI$ . Thus, at any given temperature and applied field, the sample resistivity can be measured as

$$\rho = \frac{RA_{cs}}{l} = \frac{VA_{cs}}{Il}, \quad (2.12)$$

where  $A_{cs}$  is the cross-sectional area of the sample and  $l$  is the distance between the voltage leads. If a sample is superconducting, there is no resistance, and, consequently, the measured voltage is also null. Then, increasing the applied current until the sample first registers a non-zero voltage allows the measurement of its critical current,  $I_c$ .

Resistance measurements for temperatures above 2 K were carried out on a Physical Property Measurement System model 6000 (PPMS-6000) from Quantum Design, equipped with a DC resistance module enabling measurements with a sensitivity of 15 nV [139]. The system allows temperature control from 1.9 K to 400 K and applied fields up to  $\sim 7162$  A/m (or 90 kOe). For measurements conducted below 1 K, we employed an Oxford Instruments' Heliox  $^3\text{He}$  Cryostat [142], with base temperatures of 300 mK and available magnetic fields up to  $\sim 3979$  A/m (or 50 kOe). The  $^3\text{He}$  isotope has a lower condensation point (3.2 K) in comparison to the more abundant  $^4\text{He}$  (4.2 K). The

---

<sup>18</sup>In this case, the sample geometry prevented us from using of a four-probe measurement scheme, and a two-probe method needed to be employed. As the electrical measurements in that work aimed only to detect the superconducting transition, precise information about the sample resistivity was not strictly necessary.

operational principle that enables the Heliox cryostat to achieve such low temperatures can be explained with the help of Fig. 2.3.

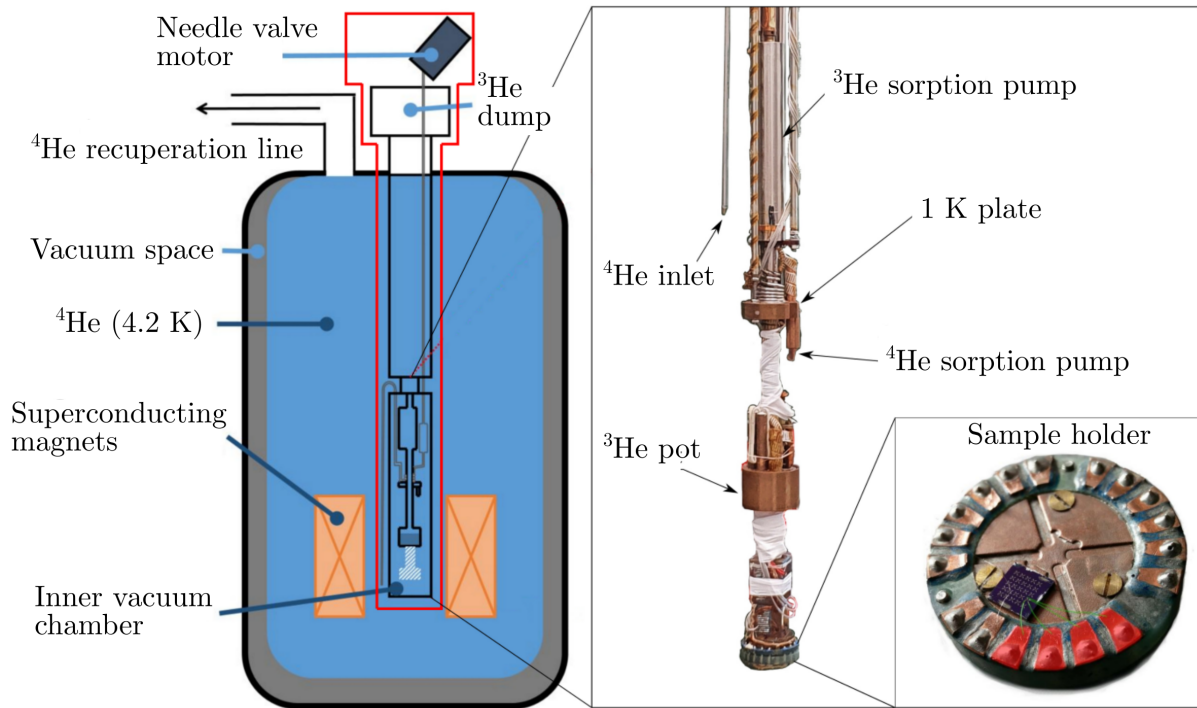


**Figure 2.3.** Representation of the Heliox  $^3\text{He}$  Cryostat system used for sub-Kelvin electrical transport measurements. The  $^3\text{He}$  refrigerator stick is highlighted in the main panel by the red contour. The details on the right show pictures from the inside of the inner vacuum chamber at the bottom of the refrigerator stick and the sample holder. Adapted from [119].

The cryostat contains a  $^3\text{He}$  refrigerator stick inserted on a conventional liquid  $^4\text{He}$  Dewar vessel, inside of which the temperature is kept at 4.2 K. At room temperature, the studied sample is mounted on the sample holder and placed at the bottom of the refrigerator stick. A cone is attached to the stick and the air is pumped out until the inner vacuum chamber reaches a pressure of around 0.1 Pa. The inner vacuum chamber is then filled with a small amount of  $^4\text{He}$  gas, which provides better thermal contact and accelerates the cooling time once the stick is inserted into the Dewar vessel. This gas will be absorbed by the charcoal  $^4\text{He}$  sorption pump once the temperature reaches 30 K at the chamber. When the inner vacuum chamber is in thermal equilibrium at 4.2 K,  $^4\text{He}$  is

pumped through the  $^4\text{He}$  inlet by an external rotational pump, cooling the 1 K plate to around 1.5 K, below the condensation temperature of  $^3\text{He}$ . At such point, a heater warms the  $^3\text{He}$  sorption pump to 30 K, releasing the trapped  $^3\text{He}$  gas, which condensates at the 1 K plate, with the resulting liquid  $^3\text{He}$  being collected at the  $^3\text{He}$  pot. Once most gas is liquefied, the heater at the  $^3\text{He}$  sorption pump is turned off, such as it will again absorb  $^3\text{He}$  gas. This lowers the vapor pressure above the liquid  $^3\text{He}$ , reducing its temperature to the base value of 300 mK. Then, the temperature at the  $^3\text{He}$  pot can be controlled by the sorption pump temperature.

## Chapter 3

# Cooling a superconductor under inhomogeneous magnetic fields

In this Chapter, I present a study on how cooling a superconducting film from its normal state to a temperature below  $T_c$  in the presence of spatially inhomogeneous magnetic fields affects the superconducting response of the sample. This was motivated by (i) the fact that a graded distribution of artificial pinning centers is able to increase the amount of current a superconductor can carry without dissipation and (ii) numerical results indicating how non-homogeneous field cooling procedures influenced the vortex arrangement in the superconductor [143,144]. In the results published as an Editor's Pick on Applied Physics Letters [145]<sup>19</sup>, we demonstrate and explain how the spatial distribution of the magnetic field applied during a field-cooling procedure directly affects the effective critical current density of a plain Nb film, i.e., without complex nanofabrication steps.

---

<sup>19</sup>Reproduced from D. A. D. Chaves et al., Applied Physics Letters, 119, 022602, 2021; licensed under a Creative Commons Attribution (CC BY) license, with the permission of AIP Publishing.

# Enhancing the effective critical current density in a Nb superconducting thin film by cooling in an inhomogeneous magnetic field

Cite as: Appl. Phys. Lett. **119**, 022602 (2021); doi: [10.1063/5.0058680](https://doi.org/10.1063/5.0058680)

Submitted: 1 June 2021 · Accepted: 26 June 2021 ·

Published Online: 12 July 2021



View Online



Export Citation



CrossMark

D. A. D. Chaves,<sup>1</sup> I. M. de Araújo,<sup>1</sup> D. Carmo,<sup>1,2</sup> F. Colauto,<sup>1</sup> A. A. M. de Oliveira,<sup>3</sup> A. M. H. de Andrade,<sup>4</sup> T. H. Johansen,<sup>5</sup> A. V. Silhanek,<sup>6</sup> W. A. Ortiz,<sup>1</sup> and M. Motta<sup>1,a)</sup>

## AFFILIATIONS

<sup>1</sup>Departamento de Física, Universidade Federal de São Carlos, 13565-905 São Carlos, SP, Brazil

<sup>2</sup>Laboratório Nacional de Luz Síncrotron, Centro Nacional de Pesquisa em Energia e Materiais, 13083-100 Campinas, SP, Brazil

<sup>3</sup>Instituto Federal de Educação, Ciência e Tecnologia de São Paulo, Campus São Carlos, 13565-905 São Carlos, SP, Brazil

<sup>4</sup>Instituto de Física, Universidade Federal do Rio Grande do Sul, 91501-970 Porto Alegre, RS, Brazil

<sup>5</sup>Department of Physics, University of Oslo, Blindern, P.O. Box 1048, 0316 Oslo, Norway

<sup>6</sup>Experimental Physics of Nanostructured Materials, Q-MAT, CESAM, Université de Liège, B-4000 Sart Tilman, Belgium

<sup>a)</sup>Author to whom correspondence should be addressed: [m.motta@df.ufscar.br](mailto:m.motta@df.ufscar.br)

## ABSTRACT

Quantitative magneto-optical imaging of a type-II superconductor thin film cooled under zero, homogeneous, and inhomogeneous applied magnetic fields indicates that the latter procedure leads to an enhancement of the screening capacity. Such an observation is corroborated by both  $B$ -independent and  $B$ -dependent critical state model analyses. Furthermore, repulsive (attractive) vortex-(anti)vortex interactions were found to have a decisive role in the shielding ability, with initial states prepared with vortices resulting in a shorter magnetic flux front penetration depth than those prepared with antivortices. The proposed strategy could be implemented to boost the performance of thin superconducting devices.

Published under an exclusive license by AIP Publishing. <https://doi.org/10.1063/5.0058680>

The ability of type-II superconductors to carry an electric current without dissipation is intrinsically related to how the material can effectively immobilize penetrated quantized flux lines—the superconducting vortices. In other words, the larger its vortex pinning capacity, the higher the critical current density  $J_c$ .<sup>1</sup> In the framework of the Bean critical state model,<sup>2,3</sup> in which the critical current is independent of the local magnetic flux density  $\mathbf{B}$ , the relationship between  $J_c$  and the amount of penetrated magnetic flux in a thin film with stripe geometry is<sup>4,5</sup>

$$J_c^{\text{Bean}} = \frac{\pi H}{d \cosh^{-1} \left( \frac{w}{w-p} \right)}, \quad (1)$$

where  $d$  and  $w$  are the thickness and the half-width of the film, respectively,  $H$  is the intensity of a perpendicularly applied magnetic field, and  $p$  is the flux front penetration depth measured from the edges.

Although very common and mostly successful, the application of Eq. (1) is limited by the strict hypothesis of the Bean model, which implicates a current density plateau wherever there is a penetrated flux in the superconductor. In practice, however, this is not always true, and a  $J_c(\mathbf{B})$  dependency was recently shown necessary to explain particular experimental observations on the flux penetration in Nb films.<sup>6–8</sup> In this regard, the Kim critical state model<sup>9,10</sup> shows that, indeed, differences in both flux penetration and current distribution patterns in superconducting films arise when taking such a dependency into account,<sup>11</sup> suggesting that a careful investigation of flux penetration in these samples should go beyond the Bean model.

The enhancement of the pinning capacity is an important quest in developing better superconducting devices for practical applications.<sup>12–14</sup> A successful strategy in this regard is to engineer superconducting specimens with artificial pinning center arrays, a series of nanofabricated indentations or inclusions of varied nature spread throughout the material.<sup>15–21</sup> It has been shown that a graded

distribution of holes, or antidots (ADs), emulating the actual vortex distribution in superconducting films can result in  $J_c$  values higher than those resulting from a uniform distribution.<sup>22,23</sup> In addition, an array of defects arising from the conformal transformation of an annular section of a hexagonal lattice, resembling the Abrikosov vortex lattice,<sup>24,25</sup> has been predicted to further enhance the pinning efficiency.<sup>26</sup> Such conformal crystal structures were achieved experimentally with ADs, confirming an increase in  $J_c$ .<sup>27,28</sup> This kind of defect array preserves features of the local sixfold symmetry of the initial lattice. Moreover, it averts the emergence of flux channeling effects,<sup>29,30</sup> ultimately hindering the occurrence of thermomagnetic flux avalanches, which may disrupt superconductivity and be detrimental to the operation of superconducting devices.<sup>31,32</sup> Alternatively, results have shown that Penrose tiling arrays,<sup>33–35</sup> randomly distributed ADs,<sup>36</sup> and disordered hyperuniform AD arrays<sup>37</sup> may enhance the critical currents over a broad range of applied fields.

Menezes and de Souza Silva<sup>38</sup> showed that a vortex system under a tailored external field spontaneously organizes in a highly inhomogeneous stable array that may be mapped into a hexagonal lattice by a conformal transformation. Later, Menezes *et al.*<sup>39</sup> theoretically investigated the vortex landscape of a thin superconducting disk under perpendicular inhomogeneous magnetic fields equivalent to that generated by a concentric current loop. These authors reported that regardless of the presence of an additional applied homogeneous magnetic field, vortices may self-organize into a variety of defect-free conformal configurations, depending on the thermomagnetic history. Although the behavior of superconducting films under inhomogeneous fields has been studied before, theoretically<sup>40</sup> and experimentally,<sup>41,42</sup> particularly in the context of superconductor/ferromagnetic hybrids,<sup>43–47</sup> an experimental investigation was still lacking, on how field cooling in homogeneous and inhomogeneous out-of-plane field configurations affects the screening capacity of a macroscopic superconducting film.

In this Letter, we demonstrate, studying a Nb thin film, that the flux front penetration is affected by different field cooling procedures, being more pronounced when cooling is performed under inhomogeneous fields. Moreover, comparing states prepared either with vortices or antivortices reveals that repulsive vortex–vortex interactions enhance the screening of incoming magnetic flux, while the attraction among vortices and antivortices results in a deeper penetration, indicating a hierarchy on the effective critical current dependent on these interactions and the distribution of previously trapped flux lines.

To conduct these investigations, we fabricated the Nb superconducting device presented in Fig. 1(a). The 200 nm-thick film was grown via dc magnetron sputtering on a Si substrate in a UHV system with a base pressure lower than  $2 \times 10^{-8}$  Torr. The device was patterned via optical lithography into a 2.48 mm-wide square film surrounded at a distance of 0.08 mm by a concentric 0.06 mm-wide Nb square ring connected to contact pads allowing for an electric current to pass through. The superconducting critical temperature ( $T_c$ ) at zero dc field and  $i = 10$  mA is 8.5 K.<sup>48</sup>

Measurements of both the temperature in the sample vicinity and the ring resistance showed that a 60 mA current will drive the ring to the normal state and disrupt the thermal equilibrium in the film, prompting the selection of 50 mA as the working current. At such a current and for an applied field of 70 Oe, which leads to a full penetration state in the film, the ring showed a superconducting critical

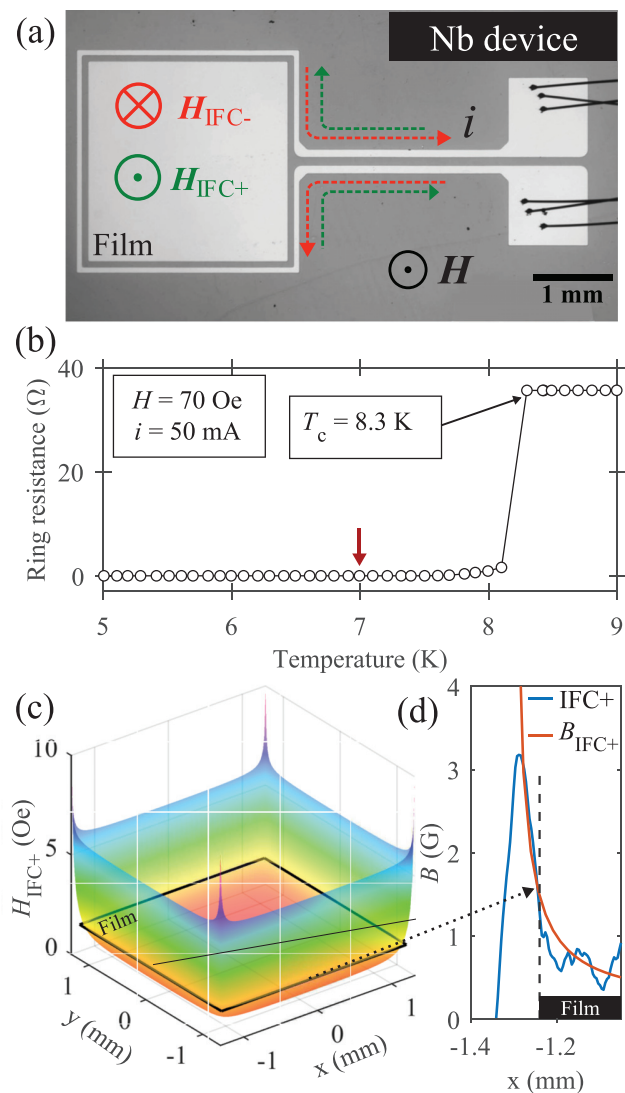


**FIG. 1.** (a) Optical image of the Nb device. Current directions and associated magnetic fields are indicated. (b) Temperature-dependent resistance of the ring for  $H = 70$  Oe and  $i = 50$  mA. (c) Calculated field distribution  $H_{\text{IFC}+}(x, y)$  generated by a counterclockwise 50 mA current applied to the ring. Black square represents the film edges. (d)  $B(x)$  profile in the film after IFC+ procedure obtained from quantitative MOI (blue) plotted alongside calculated  $B_{\text{IFC}+}$  profile.

temperature  $T_c = 8.3$  K, as demonstrated in Fig. 1(b). Accordingly, it was found that a temperature of  $T = 7$  K was suitable for these measurements to ensure reproducibility.

The magneto-optical imaging (MOI) technique,<sup>31</sup> based on the Faraday effect, was used to investigate the flux penetration patterns in the Nb device. The experimental station was equipped with Helmholtz coils to generate a highly uniform magnetic field up to 150 Oe perpendicular to the film. A Bi-substituted yttrium iron garnet film (Bi:YIG) presenting a mostly in-plane spontaneous magnetization was used as a Faraday-active indicator.<sup>49</sup> Domain walls separating regions

presenting different magnetization orientations are known to appear in such magneto-optical (MO) materials. These walls are seen as saw-tooth-like lines that are easily displaced, leaving an undesired but unavoidable imprint in the MO image. Nonetheless, these domains have negligible influence on the overall flux distribution in the superconducting film.

Moreover, immediate analysis of MO images allows for a qualitative investigation of the flux distribution, as the local brightness is related to the magnitude of the perpendicular flux density. To obtain a quantitative picture, a pixel-by-pixel calibration algorithm<sup>50</sup> implemented on MATLAB was used to recover the  $B(x, y)$  distribution. We also use the plugin StackReg<sup>51</sup> together with ImageJ software<sup>52</sup> to correct for sample drift within a precision of  $\pm 2$  pixels (or  $\pm 8 \mu\text{m}$ ) in the position of any given image throughout the measurements.

Our main goal was to investigate the effect of different cooling routes on the flux front penetration depth in the Nb film. To achieve that, we prepared the specimen with five different initial states characterized by the cooling: (i) in the absence of a magnetic field, or zero-field cooling (ZFC); (ii) with either a positive or negative uniformly applied magnetic field, or cooling in a homogeneous field (HFC $\pm$ ); and (iii) using currents flowing through the ring to generate inhomogeneous fields before cooling down the device (IFC $\pm$ ), as exemplified in Fig. 1(a). Then, a positive out-of-plane uniform field  $H$  was applied to probe the flux penetration in the film. The different field orientations during cooling prepared the film either with a distribution of flux lines in the same direction as the applied magnetic field (vortices, HFC+ and IFC+) or in the opposite direction (antivortices, HFC- and IFC-). This is an important distinction since interactions between vortices are repulsive,<sup>53</sup> but vortex-antivortex interactions are attractive and may lead to the annihilation of the flux entities.<sup>54</sup> These interactions have a decisive impact on the penetration dynamics of incoming vortices.<sup>55-58</sup>

Given the different field cooling procedures, one must make sure that images from different measurement runs are comparable. Since flux penetration occurs from the edges to the center of the superconducting films, we compare images, in which the effective applied field  $H_{\text{eff}}$  has the same magnitude at the middle point of the borders. For the ZFC and HFC cases,  $H_{\text{eff}} = H$ , however, as current flows through the ring throughout an entire IFC run, in this case,  $H_{\text{eff}}$  is a vectorial sum of the uniform field and the contribution arising from the ring,  $H_{\text{IFC}\pm}$ . Figure 1(c) presents  $H_{\text{IFC}\pm}(x, y)$  values inside the ring calculated from the Biot-Savart law and reveals that it has a magnitude of 1.5 Oe at the middle of the sample edges. As indicated in Fig. 1(d), the flux density in the film after the IFC+ procedure matches the behavior of the inhomogeneous field profile (apart from fluctuations due to garnet domains) as one moves away from the borders, confirming our assumption that  $H_{\text{eff}} = H + 1.5 \text{ Oe}$ .

One can further attest the validity of this protocol exploring the flux distribution in the film. Figure 2(a) is obtained by performing a pixel-by-pixel subtraction of the local flux density value in the HFC+ image from the corresponding point in the IFC+ one, both for  $H_{\text{eff}} = 1.5 \text{ Oe}$ , i.e., the same field at the edges. When comparing this image to Fig. 1(a), one can see that although the current ring is visible, the sample edges are not, indicating that the comparison protocol is valid. Mapping the  $B$  profile along one of the borders in Fig. 2(a) reinforces such fact by showing a  $B(x)$  distribution around 0 G within the restrictions of our experimental uncertainty that presents a standard

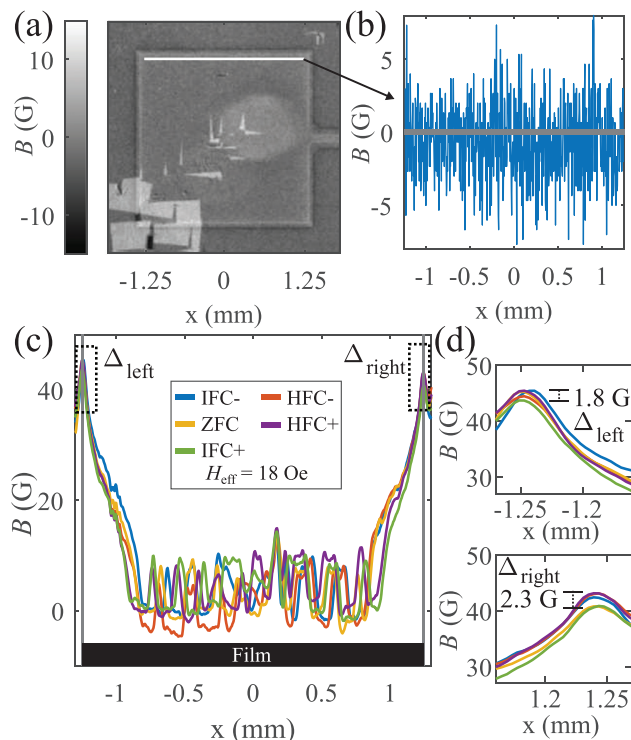


**FIG. 2.** (a) Subtraction of HFC+ and IFC+ field distributions with  $H_{\text{eff}} = 1.5 \text{ Oe}$ . (b) Flux distribution along the film edge indicated by white straight line for  $H_{\text{eff}} = 1.5 \text{ Oe}$  at 7 K. (c) Flux distribution along the direction indicated by short-dashed line in Fig. 3 for all cooling procedures with  $H_{\text{eff}} = 18 \text{ Oe}$  at 7 K. (d) Details showing  $\Delta_{\text{left}}$  and  $\Delta_{\text{right}}$  regions highlighted by dashed boxes in panel (c).

deviation of 2.6 G—see Fig. 2(b). Directing our attention to spatial profiles passing through the film center, indicated schematically by the short-dashed line at the ZFC MO image in Fig. 3, and investigating all cooling routes with  $H_{\text{eff}} = 18 \text{ Oe}$ , one can see in Figs. 2(c) and 2(d) that a 2D averaging interpolation of the images provides more representative quantitative information, showing that the maximum difference between the fields at the edges for different procedures [ $\Delta_{\text{left}} = 1.8 \text{ G}$  and  $\Delta_{\text{right}} = 2.3 \text{ G}$ , as defined in Fig. 2(d)] is again well within our experimental error. In practice,  $\Delta$  depends on both  $H_{\text{eff}}$  and the position chosen to map the field across the sample. Choosing other positions for mapping the field might cause a slight variation on the absolute values of  $B$  but, regardless where,  $\Delta$  is always within the experimental resolution for magnetic fields of our experimental setup. It is important to mention that the intense variations along the field-free central region in the profiles are due to magnetic domains in the indicator, also visible in Fig. 3. The magnetic flux scan direction has been chosen so as to minimize artifacts created by the spontaneous proliferation of magnetic domains along the edges of the film.

If, for example, we take the same  $H_{\text{eff}} = 18 \text{ Oe}$  to gauge the penetration patterns after different cooling procedures, the qualitative picture represented in Fig. 3 emerges. Going from the leftmost (IFC-) to the rightmost panel (IFC+), a decrease in the flux front penetration depth is observed. This trend is more apparent in the lower row of

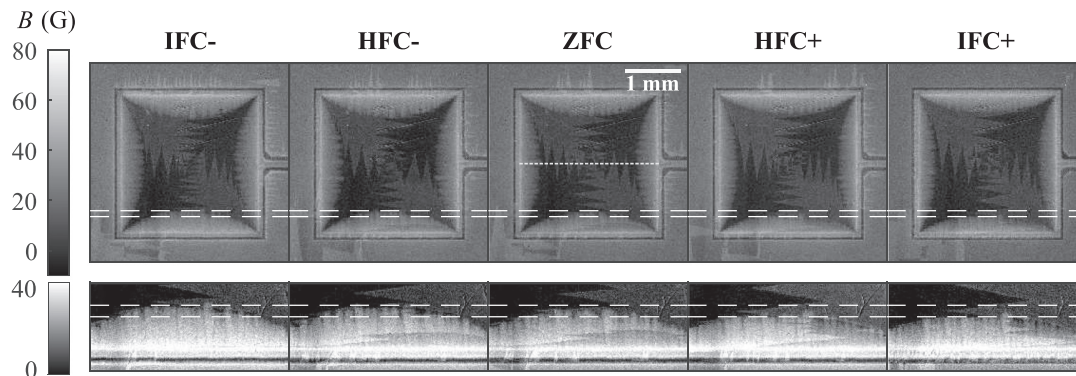


**FIG. 3.** Field distribution in the Nb film for  $H_{\text{eff}} = 18$  Oe at 7 K and all cooling routes. Bottom panels are zoomed up details of the bottom edges showing the flux front penetration depth for each case. Long-dashed lines are guides to the eye, and the short-dashed line in ZFC represents the region of the  $B$  profile in Fig. 2(c).

Fig. 3, which shows zooms of the bottom edge of the sample. This ordering reveals a hierarchy on the capacity to screen external magnetic fields related to the cooling route, since the left panels represent states prepared with antivortices, while the right ones are prepared with vortices. Although our measurements cannot resolve the dynamics of individual vortices, the results suggest that vortex–vortex interactions make it harder for the incoming vortices to penetrate the film as they need to overcome the barrier established by the repulsive potential. Therefore, the positive field cooling procedure may be interpreted as frozen pinned vortices acting as long-range pinning center-like landscapes or magnetic pinning-like distributions. In the HFC case, these frozen vortices are in a uniform distribution, whereas they are in a graded distribution in the IFC case. We could expect that a larger amount of vortices inside the sample would result in a shallower flux front; however, the graded distribution strongly suppresses vortex entry. When, in turn, incoming vortices are faced with antivortices, the attractive potential facilitates vortex penetration since annihilation processes may be allowing them to further penetrate the film, resulting in the overall effect observed in Fig. 3.

Moreover, one notices that the extreme cases in Fig. 3 are IFC (“–” on the left and “+” on the right extremity), indicating that the initial flux distribution arising from cooling under inhomogeneous fields has a more pronounced effect on the flux front penetration depth than the homogeneous counterparts. These observations are in line with previous results, showing that non-uniform pinning center distributions enhance the screening capacity of superconductors,<sup>23,27</sup> and that inhomogeneous magnetic fields can be used to create optimal vortex arrangements to improve pinning.<sup>39</sup> Such analysis is independent of any numerical data treatment and can be made directly from the raw intensity distribution obtained from MOI, dramatically diminishing the importance of the visible garnet domains in the results.

Turning to the Bean model, the shorter flux penetration depth observed as one moves toward the IFC+ case implies a higher effective current density, i.e., a higher screening current flowing through the film at the same effective field. This is shown in Table I where the values of  $p$  were measured directly from Fig. 3 within a six-pixel uncertainty. In addition to the absolute values estimated for  $J_{\text{eff}}^{\text{Bean}}$  from Eq. (1), the result is also presented in numbers relative to the ZFC case, indicating the percentage variation observed for each procedure.

The same behavior can also be observed for different effective applied fields. Subtracting IFC+ images from IFC– ones, in a procedure similar to that presented in Fig. 2(a), the resulting contrast highlights the difference in the flux penetration. For instance, if the flux penetration of image “A” is deeper than that of image “B,” subtracting B from A would result in a positive (bright) contrast at the flux front. This is precisely what is observed in Fig. 4 for  $H_{\text{eff}} = 12, 24, 36,$  and  $48$  Oe, fading out for higher effective fields. Therefore, the IFC+ case always presents the shortest flux front penetration depth and, consequently, the higher screening capacity.

It is desirable, however, to go beyond the Bean model to properly analyze flux penetration in Nb films. From average  $B(y)$  profiles considering five rows along the center of the film, current density distributions were obtained by means of numerical calculations in the framework of the Kim model, as described in Ref. 11. The results are normalized by the unknown critical current density at zero applied field  $J_{c0}$ . Then, despite the influence of garnet domains, defining the effective current density  $J_{\text{eff}}^{\text{Kim}}$  as the absolute current value in the maximum flux front penetration depth of the IFC+ case allows one to firmly state that, where there is flux penetrated,  $J_{\text{eff}}^{\text{Kim}}$  is higher as you move from left to right in Fig. 3, as represented in Table I for  $H_{\text{eff}} = 18$  Oe.

Evaluating  $J_{\text{eff}}^{\text{Kim}}$  for different  $H_{\text{eff}}$  allows us to reach the same conclusion, i.e., there is a consistent enhancement of the screening capacity in states prepared with vortices, that is maximized for a field cooling performed with inhomogeneous fields. Figure 5 summarizes

**TABLE I.** Comparison between current density variation obtained from the Bean and Kim models.

Procedure	Bean model		Kim model	
	$p \pm 0.024$ (mm)	$J_{\text{eff}}^{\text{Bean}}$ ( $10^5$ A/cm $^2$ )	$J_{\text{eff}}^{\text{Bean}}$ (%)	$J_{\text{eff}}^{\text{Kim}}$ (%)
IFC–	0.383	$24.6 \pm 1.0$	94.2	95.6
HFC–	0.375	$25.0 \pm 1.1$	95.6	97.5
ZFC	0.350	$26.2 \pm 1.2$	100	100
HFC+	0.300	$28.9 \pm 1.4$	110.3	103.4
IFC+	0.288	$29.6 \pm 1.5$	113.2	107.3



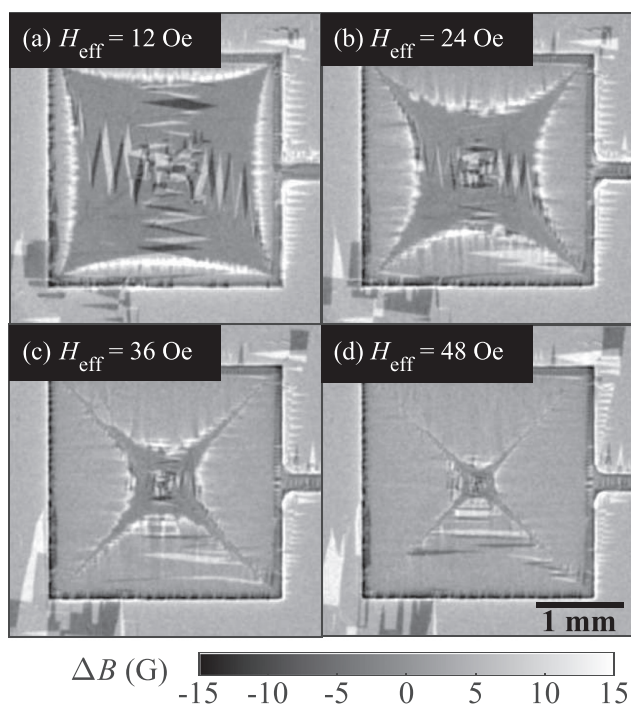


**FIG. 4.** Subtraction of the IFC+ image from the corresponding IFC− for different  $H_{\text{eff}}$ : (a) 12, (b) 24, (c) 36, and (d) 48 Oe. Brighter pixels indicate a positive contrast.

this observation, highlighting an upward trend in current variation from the left to the right side in both analyses. The inset shows the maximum current enhancement for different  $H_{\text{eff}}$ ; the decrease observed in  $J_{\text{eff}}^{\text{Bean}}$  matches the tendency in Fig. 4. Also, the apparent smaller enhancement for  $J_{\text{eff}}^{\text{Kim}}$  might result from the  $J_{c0}$  normalization, which must probably has different values for the different cooling routes.

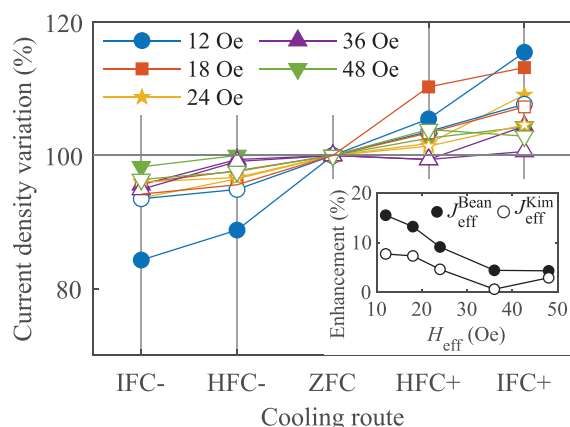


**FIG. 5.** Schematic representation of the current density variation for different field cooling procedures and  $H_{\text{eff}}$ . Inset shows the evolution of current density enhancement with  $H_{\text{eff}}$ . In both panels,  $J_{\text{eff}}^{\text{Bean}}$  (closed symbols) and  $J_{\text{eff}}^{\text{Kim}}$  (open symbols) analyses are represented.

In conclusion, we have fabricated a superconducting device that provides controllable applications of inhomogeneous magnetic fields in an Nb film. Quantitative MOI revealed the influence of different cooling routes on the flux front penetration depth. Both Bean and Kim models indicate that cooling procedures under inhomogeneous magnetic fields have the strongest impact on the effective shielding current flowing throughout the superconductor. Even though the spatial resolution of our MOI station does not allow for a statement to be made on the vortex arrangements in comparison to those predicted by Menezes *et al.*,<sup>39</sup> our findings indicate that cooling in an inhomogeneous field is a viable route to enhance its effective critical current. Moreover, the MO images show that when the film was initially prepared with states permeated by antivortices, the flux penetration was deeper. This fact hints at a hierarchy on the screening capacity dependent on the nature of the interactions of the incoming vortices with previously pinned flux lines, i.e., repulsive vortex–vortex interactions hamper flux penetration, which is translated into a higher effective screening current. Therefore, not only the interaction mechanism is recognized as an important ingredient to comprehend these results, but also the frozen vortex distribution throughout the material. Our findings may also be extended to bulky materials, as hinted by results described by Morita *et al.*<sup>39</sup> for a high- $T_c$  specimen cooled in a homogeneous field. Further examination using a different experimental approach that reaches individual vortex resolution is necessary to prove the conformal distribution of vortices. Additionally, we foresee that the initial state may also influence the threshold field to trigger flux avalanches.

The authors thank C. C. de Souza Silva and L. R. E. Cabral for the enlightening discussions, Laboratório de Conformação Nanométrica (LCN/IF/UFRGS) for the Nb film growth, and Laboratório de Microfabricação (LMF/LNNano/CNPEN) for the lithography. The authors also acknowledge financial support from Brazilian agencies: Coordenação de Aperfeiçoamento de Pessoal de Nível Superior–Brasil (CAPES)–Finance Code 001; National Council for Scientific and Technological Development (CNPq); and São Paulo Research Foundation (FAPESP). This work is also supported by the Fonds de la Recherche Scientifique - FNRS through Grant No. T.0204.21 and the COST Action CA16218 “NanoCoHybri” supported by COST (European Cooperation in Science and Technology), [www.cost.eu](http://www.cost.eu).

#### DATA AVAILABILITY

The data that support the findings of this study are available from the corresponding author upon reasonable request.

#### REFERENCES

- G. Blatter, M. V. Feigel'man, V. B. Geshkenbein, A. I. Larkin, and V. M. Vinokur, *Rev. Mod. Phys.* **66**, 1125 (1994).
- C. P. Bean, *Phys. Rev. Lett.* **8**, 250 (1962).
- C. P. Bean, *Rev. Mod. Phys.* **36**, 31 (1964).
- E. H. Brandt, M. V. Indenbom, and A. Forkl, *Europhys. Lett.* **22**, 735 (1993).
- E. Zeldov, J. R. Clem, M. McElfresh, and M. Darwin, *Phys. Rev. B* **49**, 9802 (1994).
- L. Jiang, C. Xue, L. Burger, B. Vanderheyden, A. V. Silhanek, and Y.-H. Zhou, *Phys. Rev. B* **101**, 224505 (2020).
- L. Burger, I. S. Veshchunov, T. Tamegai, A. Silhanek, S. Nagasawa, M. Hidaka, and B. Vanderheyden, *Supercond. Sci. Technol.* **32**, 125010 (2019).

- <sup>8</sup>M. Motta, L. Burger, L. Jiang, J. G. Acosta, Ž. Jelić, F. Colauto, W. Ortiz, T. Johansen, M. Milošević, C. Cirillo, C. Attanasio, C. Xue, A. V. Silhanek, and B. Vanderheyden, *Phys. Rev. B* **103**, 224514 (2021).
- <sup>9</sup>Y. B. Kim, C. F. Hempstead, and A. R. Strnad, *Phys. Rev. Lett.* **9**, 306 (1962).
- <sup>10</sup>D.-X. Chen and R. B. Goldfarb, *J. Appl. Phys.* **66**, 2489 (1989).
- <sup>11</sup>J. McDonald and J. R. Clem, *Phys. Rev. B* **53**, 8643 (1996).
- <sup>12</sup>S. R. Foltyn, L. Civale, J. L. MacManus-Driscoll, Q. X. Jia, B. Maiorov, H. Wang, and M. Maley, *Nat. Mater.* **6**, 631 (2007).
- <sup>13</sup>A. Gurevich, *Annu. Rev. Condens. Matter Phys.* **5**, 35 (2014).
- <sup>14</sup>X. Obradors and T. Puig, *Supercond. Sci. Technol.* **27**, 044003 (2014).
- <sup>15</sup>L. Civale, A. D. Marwick, T. K. Worthington, M. A. Kirk, J. R. Thompson, L. Krusin-Elbaum, Y. Sun, J. R. Clem, and F. Holtzberg, *Phys. Rev. Lett.* **67**, 648 (1991).
- <sup>16</sup>M. Baert, V. V. Metlushko, R. Jonckheere, V. V. Moshchalkov, and Y. Bruynseraede, *Phys. Rev. Lett.* **74**, 3269 (1995).
- <sup>17</sup>J. I. Martin, M. Vélez, J. Nogués, and I. K. Schuller, *Phys. Rev. Lett.* **79**, 1929 (1997).
- <sup>18</sup>B. Gautam, M. A. Sebastian, S. Chen, S. Misra, J. Huang, F. J. Baca, R. Emergo, T. Haugan, Z. Xing, H. Wang, and J. Z. Wu, *Appl. Phys. Lett.* **113**, 212602 (2018).
- <sup>19</sup>A.-L. Zhang, C. Xue, and J.-Y. Ge, *Appl. Phys. Lett.* **115**, 132601 (2019).
- <sup>20</sup>X. Xu, J. Rochester, X. Peng, M. Sumption, and M. Tomsic, *Supercond. Sci. Technol.* **32**, 02LT01 (2019).
- <sup>21</sup>L. B. S. Da Silva, A. Serquis, E. E. Hellstrom, and D. Rodrigues, *Supercond. Sci. Technol.* **33**, 045013 (2020).
- <sup>22</sup>V. R. Misko and F. Nori, *Phys. Rev. B* **85**, 184506 (2012).
- <sup>23</sup>M. Motta, F. Colauto, W. A. Ortiz, J. Fritzsche, J. Cuppens, W. Gillijns, V. V. Moshchalkov, T. H. Johansen, A. Sanchez, and A. V. Silhanek, *Appl. Phys. Lett.* **102**, 212601 (2013).
- <sup>24</sup>A. A. Abrikosov, *Sov. Phys. JETP* **5**, 1174 (1957).
- <sup>25</sup>W. H. Kleiner, L. M. Roth, and S. H. Autler, *Phys. Rev.* **133**, A1226 (1964).
- <sup>26</sup>D. Ray, C. J. O. Reichhardt, B. Janko, and C. Reichhardt, *Phys. Rev. Lett.* **110**, 267001 (2013).
- <sup>27</sup>Y.-L. Wang, M. L. Latimer, Z.-L. Xiao, R. Divan, L. E. Ocola, G. W. Crabtree, and W.-K. Kwok, *Phys. Rev. B* **87**, 220501 (2013).
- <sup>28</sup>S. Guénon, Y. J. Rosen, A. C. Basaran, and I. V. Schuller, *Appl. Phys. Lett.* **102**, 252602 (2013).
- <sup>29</sup>M. Menghini, R. J. Wijngaarden, A. V. Silhanek, S. Raedts, and V. V. Moshchalkov, *Phys. Rev. B* **71**, 104506 (2005).
- <sup>30</sup>M. Motta, F. Colauto, R. Zadorosny, T. H. Johansen, R. B. Dinner, M. G. Blamire, G. W. Ataklti, V. V. Moshchalkov, A. V. Silhanek, and W. A. Ortiz, *Phys. Rev. B* **84**, 214529 (2011).
- <sup>31</sup>J. I. Vestgård, T. H. Johansen, and Y. M. Galperin, *Low Temp. Phys.* **44**, 460 (2018).
- <sup>32</sup>F. Colauto, M. Motta, and W. A. Ortiz, *Supercond. Sci. Technol.* **34**, 013002 (2021).
- <sup>33</sup>V. Misko, S. Savel'ev, and F. Nori, *Phys. Rev. Lett.* **95**, 177007 (2005).
- <sup>34</sup>A. V. Silhanek, W. Gillijns, V. V. Moshchalkov, B. Y. Zhu, J. Moonens, and L. H. A. Leunissen, *Appl. Phys. Lett.* **89**, 152507 (2006).
- <sup>35</sup>M. Kemmler, C. Gürlich, A. Sterck, H. Pöhler, M. Neuhaus, M. Siegel, R. Kleiner, and D. Koelle, *Phys. Rev. Lett.* **97**, 147003 (2006).
- <sup>36</sup>Y. L. Wang, L. R. Thoutam, Z. L. Xiao, B. Shen, J. E. Pearson, R. Divan, L. E. Ocola, G. W. Crabtree, and W. K. Kwok, *Phys. Rev. B* **93**, 045111 (2016).
- <sup>37</sup>Q. Le Thien, D. McDermott, C. J. O. Reichhardt, and C. Reichhart, *Phys. Rev. B* **96**, 094516 (2017).
- <sup>38</sup>R. M. Menezes and C. C. de Souza Silva, *Sci. Rep.* **7**, 12766 (2017).
- <sup>39</sup>R. M. Menezes, E. Sardella, L. R. E. Cabral, and C. C. de Souza Silva, *J. Phys.* **31**, 175402 (2019).
- <sup>40</sup>M. V. Milošević, S. V. Yampolskii, and F. M. Peeters, *Phys. Rev. B* **66**, 024515 (2002).
- <sup>41</sup>S. A. Govorkov, A. F. Khapikov, B. Heinrich, J. C. Irwin, R. A. Cragg, and A. A. Fife, *Supercond. Sci. Technol.* **9**, 952 (1996).
- <sup>42</sup>A. Heinrich, M. Kuhn, B. Schey, W. Biegel, and B. Stritzker, *Physica C* **405**, 41 (2004).
- <sup>43</sup>A. Y. Aladyshev, A. K. Vorob'ev, P. P. Vysheslavtsev, E. B. Klyuenkov, A. S. Mel'nikov, Y. N. Nozdrin, and I. D. Tokman, *Sov. Phys. JETP* **89**, 940 (1999).
- <sup>44</sup>W. Gillijns, A. Y. Aladyshev, A. V. Silhanek, and V. V. Moshchalkov, *Phys. Rev. B* **76**, 060503 (2007).
- <sup>45</sup>A. Y. Aladyshev, A. V. Silhanek, W. Gillijns, and V. V. Moshchalkov, *Supercond. Sci. Technol.* **22**, 053001 (2009).
- <sup>46</sup>I. F. Lyuksyutov, D. G. Naugle, A. E. Ozmetin, M. K. Yapici, and J. Zou, *J. Supercond. Novel Magn.* **23**, 1079 (2010).
- <sup>47</sup>J. Brisbois, M. Motta, J. I. Avila, G. Shaw, T. Devillers, N. M. Dempsey, S. K. P. Veerapandian, P. Colson, B. Vanderheyden, P. Vanderbemden, W. A. Ortiz, N. D. Nguyen, R. B. G. Kramer, and A. V. Silhanek, *Sci. Rep.* **6**, 27159 (2016).
- <sup>48</sup>There is a difference between  $T_c$  obtained through measurements in a Quantum Design superconducting quantum interference device (SQUID) magnetometer ( $\sim 9$  K) and our MOI setup (8.5 K). It appears mainly as a consequence of a non-optimum thermal contact between the sample and the cold-finger type cryostat. Despite that, this difference does not affect the results shown here.
- <sup>49</sup>L. E. Helseth, A. G. Solov'yev, R. W. Hansen, E. I. Il'yashenko, M. Baziljevich, and T. H. Johansen, *Phys. Rev. B* **66**, 064405 (2002).
- <sup>50</sup>G. Shaw, J. Brisbois, L. B. G. L. Pinheiro, J. Müller, S. Blanco Alvarez, T. Devillers, N. M. Dempsey, J. E. Scheerder, J. Van de Vondel, S. Melinte, P. Vanderbemden, M. Motta, W. A. Ortiz, K. Hasselbach, R. B. G. Kramer, and A. V. Silhanek, *Rev. Sci. Instrum.* **89**, 023705 (2018).
- <sup>51</sup>P. Thévenaz, U. E. Ruttimann, and M. Unser, *IEEE Trans. Image Process.* **7**, 27 (1998).
- <sup>52</sup>C. A. Schneider, W. S. Rasband, and K. W. Eliceiri, *Nat. Methods* **9**, 671 (2012).
- <sup>53</sup>E. H. Brandt, *Phys. Rev. B* **79**, 134526 (2009).
- <sup>54</sup>E. Sardella, P. N. Lisboa Filho, C. C. de Souza Silva, L. R. E. Cabral, and W. A. Ortiz, *Phys. Rev. B* **80**, 012506 (2009).
- <sup>55</sup>F. Bass, B. Y. Shapiro, and M. Shvartsner, *Phys. Rev. Lett.* **80**, 2441 (1998).
- <sup>56</sup>F. Bass, B. Y. Shapiro, I. Shapiro, and M. Shvartsner, *Phys. Rev. B* **58**, 2878 (1998).
- <sup>57</sup>A. Schwarz, U. H. Pi, M. Liebmann, R. Wiesendanger, Z. G. Khim, and D. H. Kim, *Appl. Phys. Lett.* **88**, 012507 (2006).
- <sup>58</sup>R. B. G. Kramer, A. V. Silhanek, W. Gillijns, and V. V. Moshchalkov, *Phys. Rev. X* **1**, 021004 (2011).
- <sup>59</sup>M. Morita, M. Tanaka, T. Sasaki, M. Hashimoto, and K. Sawano, in *Advances in Superconductivity IV* (Springer, 1992), pp. 447–450.

## Chapter 4

# Transforming the behavior of a superconducting weak-link using magnetic fields







In developing superconducting devices for nanoscale applications, it is necessary to employ fabrication techniques with the required nanometric spatial resolution, where focused ion beam milling becomes a prominent tool. However, exposing pristine specimens to the ion beam introduces defects to the material, locally compromising superconductivity. To study the effects of FIB milling on a prototypical superconducting material, we fabricated high-quality Nb thin films which were then grooved by FIB milling, creating a single weak-link separating two pristine Nb regions. In the first paper presented in this Chapter, we investigate the normal and superconducting states' properties of pristine and grooved films, quantifying the effects of the nanofabrication. Among the results of this study, published as an Editor's Choice on Materials [146], we notice the emergence of a local peak in the magnetization hysteresis loop for the grooved films. We further investigate this effect in a second study, published on Physical Review B [147]<sup>20</sup>. By exploring quantitative magneto-optical imaging, we discuss how the presence of the weak-link influences the vortex dynamics in the films, leading to a tunable field-induced transformation of the weak-link behavior into a strong-link behavior.

---

<sup>20</sup>Copyright © 2023 by American Physical Society. All rights reserved.

## Article

# Superconducting Properties and Electron Scattering Mechanisms in a Nb Film with a Single Weak-Link Excavated by Focused Ion Beam

Marlon Ivan Valerio-Cuadros <sup>1,†,‡</sup> , Davi Araujo Dalbuquerque Chaves <sup>1,‡</sup> , Fabiano Colauto <sup>1</sup> , Ana Augusta Mendonça de Oliveira <sup>2</sup> , Antônio Marcos Helgueira de Andrade <sup>3</sup> , Tom Henning Johansen <sup>4</sup> , Wilson Aires Ortiz <sup>1</sup>  and Maycon Motta <sup>1,\*</sup> 

<sup>1</sup> Departamento de Física, Universidade Federal de São Carlos, São Carlos 13565-905, SP, Brazil; marlon190@gmail.com (M.I.V.-C.); davi@df.ufscar.br (D.A.D.C.); fcolauto@df.ufscar.br (F.C.); wortiz@df.ufscar.br (W.A.O.)

<sup>2</sup> Instituto Federal de Educação, Ciência e Tecnologia de São Paulo, Campus São Carlos, São Carlos 13565-905, SP, Brazil; oliveira.a.a.m@gmail.com

<sup>3</sup> Instituto de Física, Universidade Federal do Rio Grande do Sul, Porto Alegre 91501-970, RS, Brazil; antonio.andrade@ufrgs.br

<sup>4</sup> Department of Physics, University of Oslo, POB 1048, Blindern, NO-0316 Oslo, Norway; t.h.johansen@fys.uio.no

\* Correspondence: m.motta@df.ufscar.br; Tel.: +55-16-3509-1523

† Current address: Departamento de Física, Universidade Estadual de Maringá, Av. Colombo, 5790—Jardim Universitário, Maringá 87020-900, PR, Brazil.

‡ These authors contributed equally to this work.



**Citation:** Valerio-Cuadros, M.I.; Chaves, D.A.D.; Colauto, F.; Oliveira, A.A.M.d.; Andrade, A.M.H.d.; Johansen, T.H.; Ortiz, W.A.; Motta, M. Superconducting Properties and Electron Scattering Mechanisms in a Nb Film with a Single Weak-Link Excavated by Focused Ion Beam. *Materials* **2021**, *14*, 7274. <https://doi.org/10.3390/ma14237274>

Academic Editor: Antonio Leo, Gaia Grimaldi and Armando Galluzzi

Received: 24 October 2021

Accepted: 20 November 2021

Published: 28 November 2021

**Publisher's Note:** MDPI stays neutral with regard to jurisdictional claims in published maps and institutional affiliations.



**Copyright:** © 2021 by the authors. Licensee MDPI, Basel, Switzerland. This article is an open access article distributed under the terms and conditions of the Creative Commons Attribution (CC BY) license (<https://creativecommons.org/licenses/by/4.0/>).

**Abstract:** Granularity is one of the main features restricting the maximum current which a superconductor can carry without losses, persisting as an important research topic when applications are concerned. To directly observe its effects on a typical thin superconducting specimen, we have modeled the simplest possible granular system by fabricating a single artificial weak-link in the center of a high-quality Nb film using the focused ion beam technique. Then, its microstructural, magnetic, and electric properties in both normal and superconducting states were studied. AC susceptibility, DC magnetization, and magneto-transport measurements reveal well-known granularity signatures and how they negatively affect superconductivity. Moreover, we also investigate the normal state electron scattering mechanisms in the Boltzmann theory framework. The results clearly demonstrate the effect of the milling technique, giving rise to an additional quadratic-in-temperature contribution to the usual cubic-in-temperature *sd* band scattering for the Nb film. Finally, by analyzing samples with varying density of incorporated defects, the emergence of the additional contribution is correlated to a decrease in their critical temperature, in agreement with recent theoretical results.

**Keywords:** granular superconductivity; weak-link; thin film; ion implantation

## 1. Introduction

Structured thin films have shown promise for applications in different areas, including electronics and medicine. In particular, micro- and nanoscopic patterned superconducting films have received attention as their electric and magnetic properties may be optimized for technological purposes [1–13]. In this context, focused ion beam (FIB) milling is an extraordinary tool that allows to obtain structures not possible to design by other nanofabrication methods [14–16]. FIB can reach spatial accuracy of about 20 nm and has been used to control the superconducting properties of several materials, including niobium films [4,6,8,10,13,17–20]. A serious drawback, however, is an inevitable contamination due to ion implantation that may cause severe damage to the milled material, modifying its physical characteristics [15,21] and being detrimental to superconducting specimens [22,23]. It has been reported for Nb films [24] that FIB leads to gallium implantation resulting in a

systematic increase in their residual resistivity accompanied by a decrease in the superconducting critical temperature ( $T_c$ ). Such a behavior is also common to other ionic specimens, as well as implantation techniques [25–27].

It is well-known that the temperature-dependent resistivity  $\rho(T)$  of most metals can be modeled as a power law,  $\rho(T) \propto T^n$ , where the exponent  $n$  is governed by interactions between electrons and lattice vibrations [28]. In general terms, for temperatures above a material-dependent threshold that can usually be approximated by the Debye temperature  $\Theta_D$ ,  $\rho(T)$  increases linearly as the scattering mechanism is related only to fluctuations of the metallic ions about their equilibrium lattice sites [28]. For  $T < \Theta_D$ , it is important to account for lattice motion and electron-phonon interactions to properly describe the electronic scattering, whose probability to occur is greatly reduced. This, suitably, diminishes the electrical resistance leading to an  $n = 5$  behavior for regular metals according to the Bloch-Grüneisen description [29]. For transition metals, such as Nb, the picture is different due to an overlap between the upper filled  $s$ -band and the partially unfilled  $d$ -band with drastically different Fermi velocities that may act as traps, removing scattered electrons from the conduction band [30]. Between  $\Theta_D$  and a certain temperature proportional to the minimum phonon momentum required to scatter electrons from the  $s$ - to the  $d$ -band, Wilson [31] showed that such  $sd$  interband scattering leads to a cubic-in- $T$  ( $n = 3$ ) behavior of  $\rho(T)$ , which was also verified experimentally [32].

On the other hand, the inclusion of impurities in the crystalline structure, which occurs during FIB milling due to ionic implantation, is expected to influence the normal state transport properties of superconducting materials [33]. In this case, a new  $n = 2$  additive contribution to  $\rho(T)$  is present. Although somewhat different approaches have been used to explain such term—see, for instance, Refs. [34,35]—the main idea is that there is an enhancement in electron-electron scattering due to interactions with lattice defects [36]. A recent work sheds new light on the nature of the relationship between superconductivity and the emergence of this quadratic-in- $T$  normal state resistivity behavior for thin films [37]. By combining the analysis of several experimental data and different theoretical techniques, the authors unveiled the role of lattice distortion and softening in establishing a so-called pseudo-Umklapp electron-electron scattering channel. Their approach led to analytical expressions for  $T_c$  and the quadratic-in- $T$  coefficient dependency on the residual resistivity, depending on the electron-phonon coupling regime and a universal kinematic scaling relationship.

Concerning practical applications of type-II superconductors, an ingredient must be considered: the presence of weak-links (WLs) [38]. Many superconducting materials are inherently comprised by arrangements of two distinctive regions: grains, which present bulky superconductivity, and WLs, at which the superconducting properties are partially or completely suppressed. For instance, these weak-link regions can be junctions of conducting, insulating, or weaker superconducting materials between neighboring grains [38,39], misaligned grain boundaries in polycrystalline samples [40], areas penetrated by magnetic fields [41], and nonstoichiometric material among the grains – a prominent feature in ceramic specimens [42]. Although WLs are essential to some superconducting devices, most notably SQUIDS that take advantage of the Josephson Effect to measure magnetic fields with unmatched accuracy [43], their presence deteriorates the overall connectivity of the grains as a result of different inter- and intragrain critical current densities [42]. Effectively, they depreciate the maximum supercurrent which the superconductor is able to transport, representing a rather limiting consequence for certain applications. An important example is the natural occurrence of granularity in high-temperature cuprate superconductors, for which the improvement of transport properties has been a key topic of study along the last four decades [40,44–47]. For such materials, the decrease of the critical current in a single grain boundary has been demonstrated experimentally [48,49] by means of transport measurements and magneto-optical Imaging (MOI) of bicrystalline  $\text{YBa}_2\text{Cu}_3\text{O}_{7-\delta}$  thin films. In this case, single-crystalline superconducting grains are connected by an intergrain region or a single grain boundary. On the other hand, the presence of macroscopic defects

created artificially in low-temperature superconducting thin films, such as in patterned or ion-implanted Nb devices [18,50], may create areas of suppressed superconductivity which separates large superconducting regions. These regions behave approximately as extended macroscopic superconducting grains despite being composed of several interconnected single crystalline grains, i.e., a polycrystalline material. Therefore, we borrow the terminology *grain* for this extended superconducting grain hereafter. For the latter group of samples, the FIB technique stands out once more, since it does not only allow patterning samples with great precision, but the resulting ionic implantation is expected to degrade the superconducting properties.

In this work, we present a toy model aiming to investigate the influence of a single WL in both superconducting and normal state properties of a high-quality niobium thin film. Our sample is prepared by excavating a nanoscale-depth groove along the width of the rectangular film using FIB milling, resulting in a system comprising two superconducting grains connected by a WL, i.e., the groove. Magnetic responses are investigated via AC susceptibility and DC magnetization measurements for different applied magnetic field and temperature configurations, evidencing the granular signatures of the specimen. Additionally, we studied the normal state electronic transport in the sample using resistivity measurements for one grain, for the groove, and for the series association of the two grains and the groove. These results were analyzed in the framework of the Boltzmann theory, considering the Bloch-Grüneisen and Wilson regimes, and reveal the expected  $n = 3$  behavior for the niobium grains. In the impurity-rich groove region, resistivity data demonstrate the presence of an additional  $n = 2$  term in  $\rho(T)$ , which is directly connected to the milling process. Finally, it is possible to obtain the electronic mean free path from the transport data for both contributions and calculate two typical length scales related to the superconducting behavior, the coherence length and the penetration depth, once more displaying a deterioration of the superconductivity due to the presence of the weak-link.

## 2. Materials and Methods

A 180 nm thick Nb film was deposited onto a SiO<sub>2</sub> substrate by magnetron sputtering under base pressure lower than  $2 \times 10^{-8}$  Torr. Standard optical lithography was used to sharply define the borders of a rectangular film with  $3 \times 1$  mm<sup>2</sup>. The tailored WL was artificially created by the excavation of a micrometric-width groove prepared in a FIB apparatus by adjusting a dose of 1.2 nC/μm<sup>2</sup>. The groove crossed the entire extension of the central region of the film perpendicularly to the longer edges, creating thus two identical regions with the same superconducting properties (S) coupled by a less robust superconductor (S'), as exemplified in Figure 1a,b. For comparison, a non-patterned control sample, i.e., a pristine film, was also prepared. Additionally, to investigate the relationship between  $T_c$  and the disorder caused by the milling procedure, five different samples were prepared analogously by changing the beam dose to 0.1, 0.2, 0.3, 0.6, and 1.8 nC/μm<sup>2</sup>.

AC susceptibility measurements  $\chi_{AC}(T) = \chi'(T) + i\chi''(T)$  were carried out with a commercial Quantum Design MPMS-5S (Quantum Design, San Diego, USA). The real in-phase component  $\chi'$  is associated with the inductive response, i.e., the magnetic moment, whereas the imaginary out-of-phase part  $\chi''$  refers to the resistive response of the superconductor, i.e., its resistive losses caused by the oscillating excitation field [51–53].  $\chi_{AC}(T)$  was obtained for temperatures ranging from 2 K up to 10 K, using a fixed frequency  $f$  of 100 Hz, for values of the excitation field within the  $\pm 3.8$  Oe interval. Temperature-dependent DC magnetization curves were obtained using the same setup for  $T = 6.0, 6.5,$  and  $7.0$  K under applied DC magnetic fields in the range  $\pm 500$  Oe. Both AC and DC fields were always applied perpendicular to the plane of the film.

The topography of the film was investigated by atomic force microscopy (AFM) in a Digital Instruments Nanoscope V (Digital Instruments, Santa Barbara, CA, USA). The images were obtained in the peak-force tapping mode. The cantilevers used were Veeco Antimony(n)-doped Si model TAP150A and their tip was shaped like a polygon-based pyramid, with radius of 8 nm, height of 17.5 μm and tip set back of 15 μm. Besides that, the

sample composition was inspected using an Energy Dispersive X-ray Spectrometry (EDS) module coupled to a Philips XL-30 FEG Scanning Electron Microscope (FEI Company, Eindhoven, The Netherlands) (SEM), which was also employed to obtain complementary information on the film surface. The acceleration voltage used was 15 kV and the diameter of the probe was 500 nm. The estimated statistical error in the elemental composition is 3.5%.

To provide electric contacts, five aluminum wires with diameter of 20  $\mu\text{m}$  were inserted on the film by a TPT-HB05 Wirebonder (TPT, Munich, Germany) in the wedge mode. Figure 1b shows a scheme of the electric contacts placed in the plain region and in the excavated groove. An electric current was applied between the electrodes identified as 1 and 5, and the voltage was measured in two different channels, between the electrodes 2 and 3 for the plain region ( $V_G$ ) and, separately, between the electrodes 3 and 4 for the excavated region ( $V_{SS'S}$ ), resulting in the standard four-probe configuration for each contribution. Thus, it was possible to compare the transport properties of the unspoiled part of the film with the one etched by the FIB.

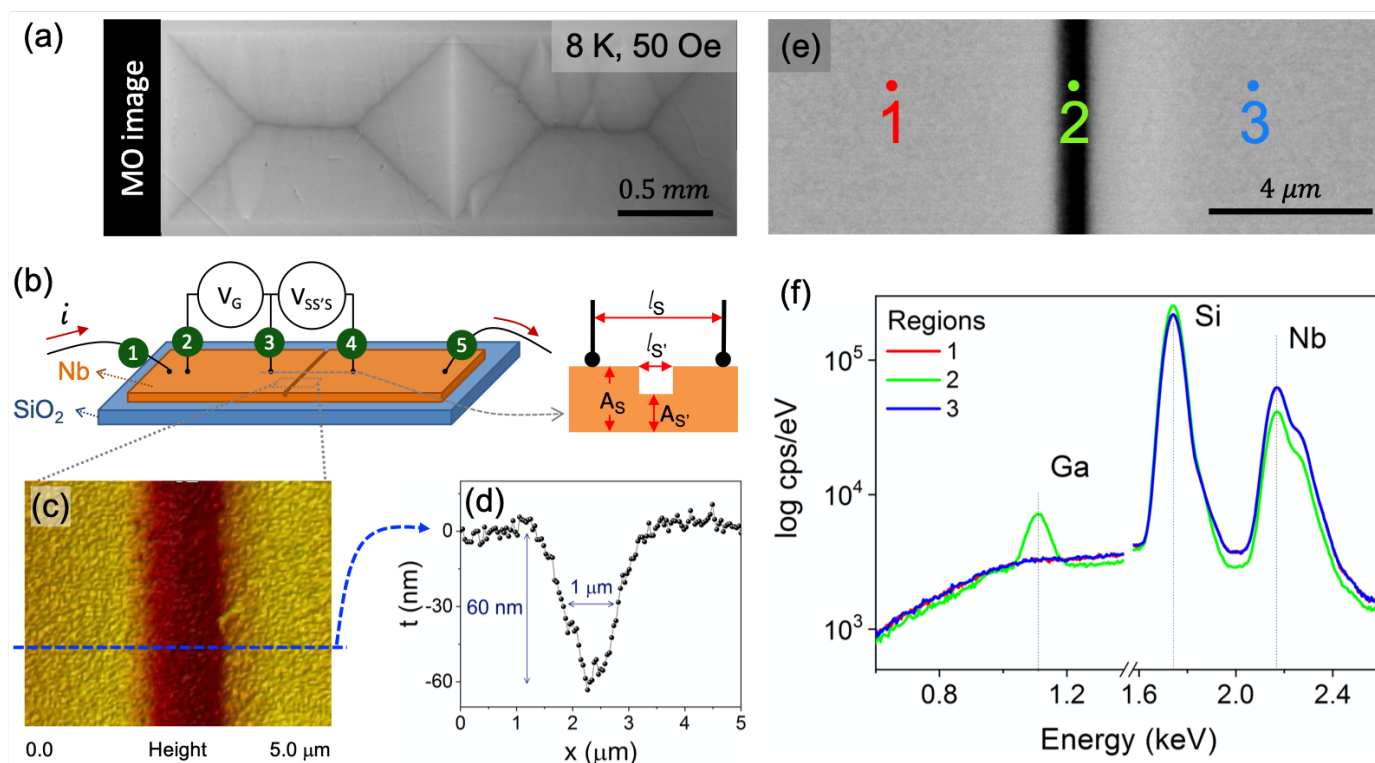


**Figure 1.** (Color online) (a) Magneto-optical (MO) image of the grooved Nb film taken at 8 K and 50 Oe after a ZFC procedure. (b) Schematic representation of the sample and details of the contact leads used in transport measurements. (c) AFM image and (d) profile for the SS'S region. (e) SEM image and the identification of three different points at which the EDS spectra were taken. (f) EDS spectra showing the  $K_{\alpha}$  line for gallium, which appears only in the region inside the groove (2).

Transport measurements were carried out in a Quantum Design PPMS-6000 (Quantum Design, San Diego, CA, USA) to determine the superconducting and normal state parameters associated with the grains and the weak-link. In order to obtain the WL resistivity, the different sections of the sample were treated as resistors in series. The resistance between the electrodes 3 and 4 is due to a plain region (S), summed to the grooved region (S'), and the second plain region (S). Thus, the resistivity due only to the groove  $\rho_{S'}$  is given by:

$$\rho_{S'} = \left( \frac{A_{S'}}{l_{S'}} \right) \cdot \left( R - \frac{\rho_G(l_S - l_{S'})}{A_S} \right) \quad (1)$$

where  $\rho_G$  is the grain resistivity, which is equivalent to the S contribution.  $A_S$ ,  $A_{S'}$ ,  $l_S$ , and  $l_{S'}$  are the cross-section areas and the lengths of the S and S' contributions, respectively. Although the groove presents a non-uniform width (see Figure 1d), the resistivity results were obtained by considering its profile as a right angle step, as sketched in Figure 1b.

### 3. Results

This section is divided into four parts: (i) Sample characterization; (ii) Superconducting properties; (iii) Normal state properties; and an analysis of (iv) The evolution of the critical temperature with disorder, which are described ahead.

#### 3.1. Sample Characterization

Concerning the terminology “grain” to define the polycrystalline unpatterned Nb film regions, one should be careful to inspect if, indeed, both areas behave uniformly as unique superconducting entities. A powerful technique to do so is MOI, which allows one to map the flux distribution [54,55]. Figure 1a shows a magneto-optical (MO) image for the grooved Nb specimen captured using MOI at 8 K for an applied field of 50 Oe after a zero field cooling (ZFC) procedure. The MO image demonstrates that the two large superconducting regions separated by the groove are independently filled by magnetic flux. Besides that, the groove presents a higher gray intensity, i.e., a higher intensity of magnetic flux penetrates the groove, as a consequence of weaker shielding currents. Thus, the flux penetration patterns are similar to those obtained by Palau et al. [56] and Polyanskii et al. [49] for YBCO films grown on bicrystal substrates, i.e., two grains separated by a grain boundary. Therefore, it is reasonable to treat our grooved sample as a system comprising two superconducting grains, separated by a single weak-link.

An important step to ensure that the studied specimen reproduces properly the proposed system is to inspect the quality of the notch along the sample width after patterning. For this, a careful analysis has been done throughout the groove and its surroundings using AFM, SEM, and EDS. A representative AFM image of this region is presented in Figure 1c, which shows a top view of the center of the specimen. A cross-section scan along the dashed line is shown in panel (c). The groove shows a V-shaped profile with full-width at half-height and depth of approximately 1.0  $\mu\text{m}$  and 60 nm, respectively. A SEM image, presented in Figure 1e, also confirms this width.

In order to determine its final composition and the existence of Ga implanted into the groove, three different sample regions were mapped using EDS spectra. Figure 1e shows schematically the position where the spectra were taken: one exactly at the notch, labeled as 2, and other two in the plain parts of the Nb film, on each side of the channel, labeled as 1 and 3. The spectra are presented in Figure 1f for those regions, exhibiting peaks related to Si and Nb from the substrate and the superconducting film, respectively. As expected, regions 1 and 3 show quite similar results. Nonetheless, an additional peak appears at 1.11 keV at the channel position, being identified as due to gallium implanted during excavation. The composition in position 2, considering only Nb and Ga elements, is Nb-5.3at%Ga. Another evidence of the thickness variation in the sample is given by the peak height of the different elements in the EDS spectra. The Nb peak is smaller for the groove, whereas the peak related to Si is larger in comparison to regions 1 and 3. It occurs due to the thinner thickness of Nb in the groove, resulting in a deeper interaction range with Si when compared to the plain Nb regions. The analysis confirms that, as designed, the sample is composed of two Nb superconducting grains connected by a region of expected depressed superconductivity, i.e., the WL.

#### 3.2. Superconducting Properties

The superconducting properties were investigated by using different techniques. AC susceptibility, DC magnetization, and magneto-transport measurements were employed to characterize the consequences of grooving the Nb film using FIB.



Temperature-dependent AC susceptibility measurements were performed for two different specimens: the structured film with the central groove, named Grooved Film (GF); and a sister sample without the channel, identified as Plain Film (PF). This allows us to compare directly both responses and identify the influence of the WL. Figure 2a shows both the  $\chi'$  (closed symbols) and  $\chi''$  (open symbols) components of  $\chi_{AC}$ . Data for the GF and PF samples are presented as colored and gray curves, respectively, for different excitation field amplitudes ( $h$ ),  $f = 100$  Hz, measured under the remnant DC magnetic field ( $H_{rem}$ ) of the superconducting magnet ( $\sim 1$  Oe). Calibration of both components of the susceptibility was performed through division of the acquired data by the value of the real component of the susceptibility at its most negative plateau,  $\chi'_0$ , at which the studied films are in the Meissner state.

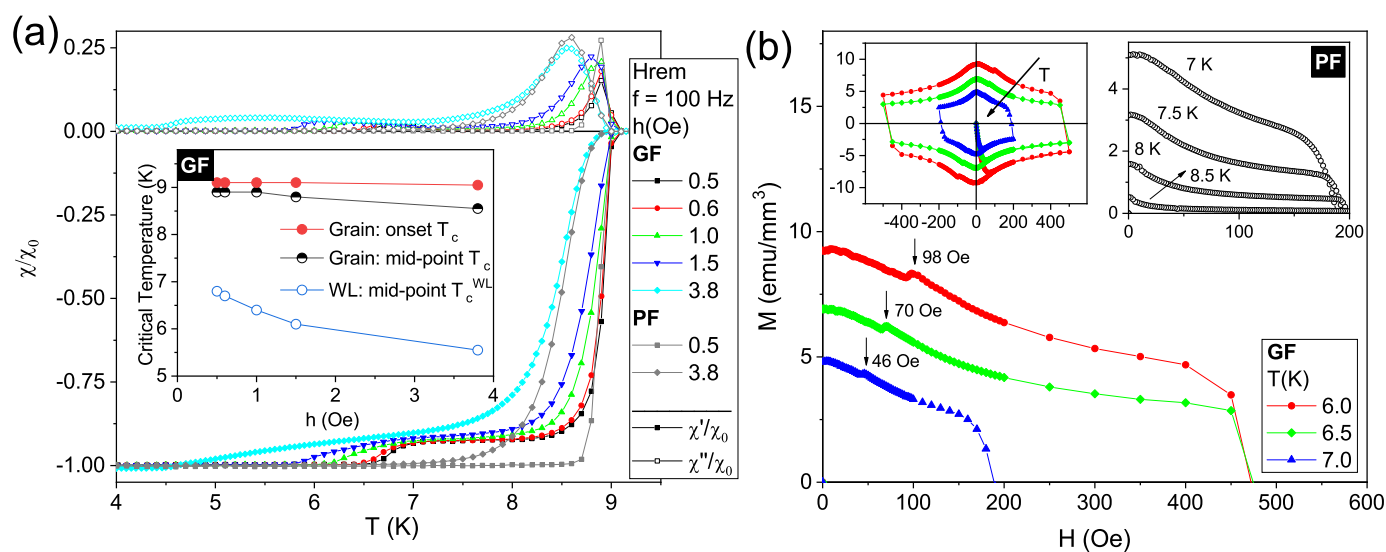


**Figure 2.** (Color online) (a) Temperature-dependent AC susceptibility for two different samples: a plain film (PF) and a structured film with a central groove (GF). The measurements were taken for 100 Hz and remnant DC field ( $H_{rem}$ ). Open symbols (above the line at  $\chi/\chi_0 = 0$ ) represent the  $\chi''$  component, while closed symbols (below  $\chi/\chi_0 = 0$ ) are  $\chi'$  values. The inset presents the critical temperatures versus AC field amplitude ( $h$ ) obtained for the GF specimen using different criteria. (b) Detail of magnetic moment versus DC applied field ( $H$ ) curves taken at different temperatures ( $T$ ) for the GF sample. The upper left inset presents the complete hysteresis loops for the GF sample, whereas the upper right inset shows the forth quadrant of the  $M(H)$  curves for the PF sample at different temperatures. The axis units are consistent throughout the panels.

For  $h = 0.5$  Oe (square symbols), both samples show a sharp transition at 9.1 K below which the  $\chi'$  and  $\chi''$  components separate from each other. For the GF film, the transition shows a characteristic signature of granular systems: a double drop in the in-phase component  $\chi'$  together with a couple of peaks in  $\chi''$  [52]. Differently, the PF specimen presents a single step accompanied by a single peak in  $\chi'$  and  $\chi''$ , respectively. For the structured sample the effective volume fraction of the pristine grains ( $f_g$ ) is 0.92 [57,58], with an estimated superconducting transition width  $\delta T_c = 1.0$  K. This quantity measures the difference between the onset of the transition and the point at which the curve reaches the Meissner plateau. On the other hand, the same transition is much narrower for the PF case with  $\delta T_c = 0.6$  K, defined when the  $\chi'$  reaches  $-0.995$ . For higher AC field amplitudes, the transition due to the pristine part of the sample becomes gradually broader as a consequence of a decreasing of its capacity to screen out the AC field. For instance, Figure 2a includes measurements for both films at  $h = 3.8$  Oe (diamond symbols): transitions are broader than those recorded at smaller values of  $h$ , being even wider for the GF as compared to that for the PF. A similar effect was shown by Navau et al. [58]. The authors have numerically calculated the effects on the AC susceptibility of a WL between two square grains in a film with different granular fractions. In that case, the first transition for the

specimen with two identical grains, i.e., when  $f_g < 1$ , is wider than for the plain sample ( $f_g = 1$ ), which is similar to our specimen PF. Besides that, the magnitude of the intrinsic peak in  $\chi''$  is also larger for the plain sample. These two features are in agreement with our experimental results. In other words, those effects are a consequence of the existence of a poorer superconductor between the grains, allowing the penetration of magnetic flux into their inner edges.

The inset in Figure 2a shows the dependence of  $T_c$ , due to the grains, on  $h$  evaluated at the first drop in  $\chi'(T)$  onset point and as it reaches half of its minimum value (mid-point). The weak-link critical temperature,  $T_c^{WL}(h)$ , defined by the second drop in  $\chi'(T)$  is also represented. The onset  $T_c$  obtained for the various  $h$  differs only within experimental error, in agreement with the PF data, as the drive field amplitude is not large enough to influence the stronger intragrain shielding capacity. On the other hand, by comparing the mid-point critical temperatures for both grain and WL, a stronger variation with  $h$  is observed for the latter. This fact can be attributed to structural inhomogeneities in the groove, i.e., the presence of WLS for which the intergranular magnetic response is strongly affected by  $h$ , being consistent with the expected damage caused by the gallium ion beam, which is confined to such region.

Turning our attention now to DC magnetic measurements, a maximum in the magnetization hysteresis loop,  $M(H)$ , is expected to occur in the decreasing field branch for negative near-zero applied fields as a consequence of the critical current density  $J_c$  dependence on  $H$  [59]. The actual peak position can be estimated using critical-state models for different  $J(H)$  relations considering specific geometries [59,60] and it is known to be shifted toward  $H = 0$  as the sample thickness is decreased, with thin films as an extreme example [61,62]. Figure 2b shows a detail of the magnetization curves,  $M(H)$ , for the GF and PF samples at different temperatures, while the upper left inset therein presents the complete hysteresis loop for the GF sample revealing the expected global maximum near  $H = 0$ , also visible in the upper right inset for the PF specimen. In the main panel, local maxima in  $M(H)$  can be observed for all curves with peak positions moving away from zero as the temperature is decreased for the GF sample. Those local maxima are absent on the corresponding curves for the PF sample, as shown in the upper right inset. This feature has been observed previously for granular samples [62,63] and can be understood considering the specimen morphology and magnetic history. As the field is increased from  $H = 0$ , flux penetrates and is pinned inside the grains. Once  $H$  is decreased from its maximum magnitude, the total magnetic field at a grain boundary is, therefore, a balance between opposite contributions, one from the applied field and the other resulting from the trapped flux lines inside neighboring grains. In thin films, a global peak in  $M(H)$  for  $H > 0$  is thus unambiguously related to granularity, resulting from a complex WL network, and appears as the field contributions cancel each other, leading to a null net magnetic field at the grain boundaries [63]. The fact that there is a local maximum for  $H > 0$  only in the grooved sample – besides a global one around zero field – is due to the presence of a single WL. A detailed investigation about this secondary maximum in  $M(H)$  will be reported elsewhere. Thus, based on all these evidences presented by its AC and DC magnetic responses, the structured film with the central groove behaves as two grains interconnected by a single WL. More recently, it has also been demonstrated that it is possible to actively control the vortex pinning potential between patterned insulating groove-like regions in Nb nanodevices by applying currents into the superconducting film from a normal metal [9].

Whereas the performed magnetic measurements, as a global technique, probe the volume-averaged magnetic moment, resistivity measurements detect the superconducting state in a more localized way, when one or more superconducting paths are established between the electrodes [64,65]. For this purpose, electric contacts were placed onto the GF sample, as illustrated in Figure 1, allowing us to detect the grain response, similar to a pristine specimen, as well as the SS'S contribution, at the vicinity of the groove.

Temperature-dependent resistance measurements,  $R(T)$ , show a sharp superconducting transition at 9.2 K at remnant field for the plain region, as illustrated in the inset of Figure 3a. Although no noticeable difference on the onset  $T_c$  was detected for applied currents ranging from  $i = 0.1$  mA to  $i = 5.0$  mA, the transition width  $\delta T_c$  increases from 0.15 K for 0.1 mA to 0.20 K for all the other values of the current. The same transition as measured for the SS'S contribution, i.e., including the groove, is presented in the main panel of Figure 3a. As before, there is no important dependence of the grain  $T_c$  on the applied current, but the data show an increase in  $\delta T_c$  up to 0.30 K. Furthermore, a second transition, related to the groove, can be observed below 8.75 K. The mid-point WL critical temperature is shown to depend on the current as values obtained from the temperature-derivative of  $R(T)$  reveal that  $T_c^{WL} = 8.70$  K, 8.65 K, 8.55 K, and 8.25 K for  $i = 0.1$  mA, 0.5 mA, 1.0 mA, 5.0 mA, respectively. The second transition width is as wide as 0.90 K for the highest value of applied current. At this point, one should be careful when comparing Figures 2a and 3a. In the AC susceptibility curves, the AC driving magnetic field acts to probe the magnetic response of the specimen and, therefore, has a different physical role in the measurements than the applied DC magnetic field. Thus, the only possible comparison is between the curves taken at remnant DC magnetic field, for the lowest values of excitation, i.e.,  $h = 0.5$  Oe and  $i = 0.1$  mA, respectively. In this case, the different values observed via magnetic and resistance measurements for the temperature of the WL transition are a consequence of the difference between the techniques. Particularly, a superconducting transition will be observed in an electrical transport measurement as soon as there is a percolative transport of supercurrent between the two electrodes. When decreasing the temperature from the normal state, this event tends to occur before the volume-average transition to superconductivity gauged in the magnetic measurements. It is also important to note that the resistance magnitude of the grain and SS'S contributions cannot be directly compared as the distances between the electrodes are different.

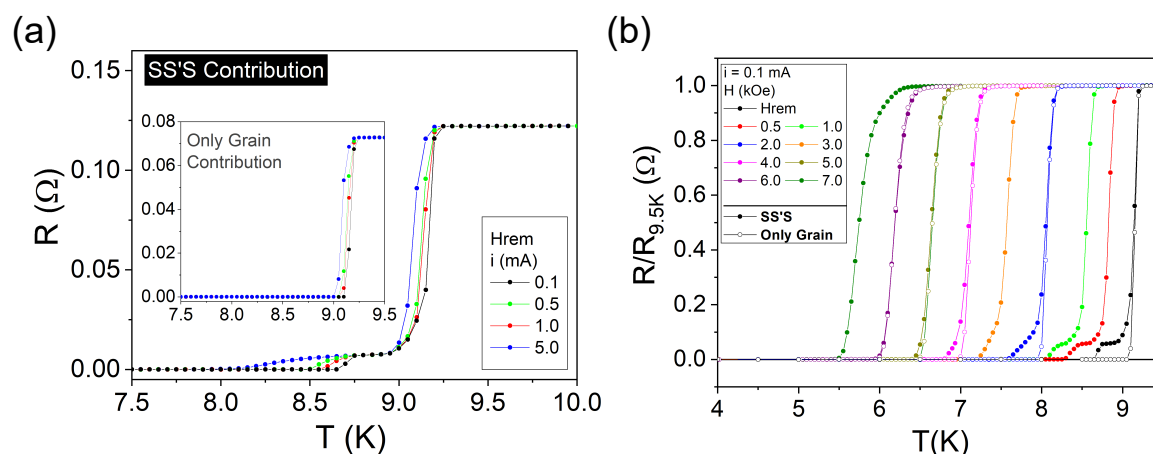


**Figure 3.** (Color online) (a) Temperature-dependent resistance curves for the SS'S contribution (main panel) and for the grain region (inset) for different applied currents ranging from 0.1 to 5.0 mA at  $H_{rem}$ . (b) Temperature-dependent resistance normalized by the resistance at 9.5 K for the SS'S contribution (closed symbols) at  $i = 0.1$  mA and different applied DC magnetic fields ranging from remnant field to 7 kOe, and for remnant field, 2 kOe, 4 kOe, 5 kOe, and 6 kOe for the grain region (open symbols).

The evolution of the superconducting transition for the SS'S contribution with different applied fields at a fixed current  $i = 0.1$  mA is shown in Figure 3b normalized by the resistance values at 9.5 K,  $R_{9.5K}$ , for each curve. The transition related to the grain contribution becomes wider and the onset  $T_c$  decreases down to 6.50 K at  $H = 7$  kOe. As the applied field increases and so does  $\delta T_c$ , it becomes difficult to differentiate between the first transition and the second one due to the groove. To visualize this trend, Figure 3b also presents the  $R(T)/R_{9.5K}$  evolution for the grain only, i.e., between the electrodes 2 and 3, as shown in Figure 1b. At  $H_{rem}$ , the second transition is well defined for the SS'S data, and

it does not appear for the grain, as expected. This difference progressively becomes more subtle until 6 kOe, when it is not possible to resolve any vestige of the second transition. It occurs due to the overall deterioration of superconductivity of each contribution which leads to similar critical temperatures at this DC applied field.

From Equation (1) and the magneto-transport measurements, several normal-state and superconducting parameters for the grain and WL contributions were determined. The overall crystal quality was estimated by the Residual Resistivity Ratio (RRR), which is the ratio of the room-temperature resistivity to the resistivity at 10 K ( $\rho_{300\text{K}}/\rho_{10\text{K}}$ ). RRR is a hallmark measurement of the degree of disorder in a given sample, as the residual resistivity is directly related to the concentration of defects. In this way, more defects lead to a higher  $\rho_{10\text{K}}$ , indicating a reduction of the electronic mean free path, and consequently a lower RRR. As expected, the value of RRR for the grain is higher than for the WL, as reported in Table 1. Moreover, although RRR for the grain may be comparable to other reported values for sputtered Nb films [66], it is considerably smaller than what is found for single-crystal Nb films [67]—this is an indication of the important role played by the polycrystalline morphology of the grain region in the resistivity response. It is also worth mentioning that for the SS'S contribution, i.e., the groove added to the neighbor grains, RRR = 6.47, similar to values reported by Dobrovolskiy et al. [18]. These values indicate a poorer quality for the WL due to the milling and implantation processes of gallium which lead to the increase of the concentration of defects on the grooved region. Furthermore, their onset critical temperatures, mean free paths,  $l$ , coherence lengths at 0 K,  $\zeta(0)$ , and penetration depth,  $\lambda(0)$ , are shown in Table 1. The effects of milling the Nb film in the normal state properties are analysed ahead.

Based on features of the Fermi level for Nb, Mayadas et al. [68] reported a material constant relationship given by  $\rho_0 l = 3.72 \times 10^{-6} \mu\Omega\text{cm}^2$ , where  $\rho_0$  is the sample residual resistivity. Using this equation and  $\rho_0$  values obtained from the best fits of our  $\rho(T)$  data, which will be discussed later and are reported in Table 2, we were able to estimate the mean free path for the grain and WL regions. In the case of the value of  $\rho_0$  obtained for the WL, it is important to keep in mind that the shape of the groove has been approximated in carrying out the resistivity calculations. This may lead to a slight misrepresentation of the actual value of  $\rho_0$ , which would impact the quantities to be obtained as follows. Nevertheless, the qualitative direct comparison between the grain and weak-link presently in study will hold true. As expected,  $l$  is much lower in the WL due to impurities introduced during the milling process, however, in both cases, it is reasonable [18] to consider that the sample is in the dirty limit, in which the mean electronic free path is smaller than the coherence length—a scale that defines the typical length within which the superconducting order parameter can vary appreciably. It is then possible to calculate the temperature dependent coherence length,  $\zeta(T)$ , in the dirty limit as [69]:

$$\zeta(T) = 0.855 \sqrt{\frac{\zeta_0 l}{1 - T/T_c}}, \quad (2)$$

where  $\zeta_0$  is the so-called Pippard's coherence length and is of the order of 39 nm for Nb [64]. The results presented in Table 1 evidence a significant suppression in  $\zeta(0)$  in the WL, highlighting the detrimental effect of its presence in the sample superconducting properties.

Another important length scale present in superconductors is the penetration depth  $\lambda(T)$ , which represents the typical distance magnetic fields are able to penetrate the material. Considering the dirty limit, it can be calculated in terms of the mean free path as [69]:

$$\lambda(T) = 0.613 \lambda_L(0) \sqrt{\frac{\zeta_0}{l(1 - T/T_c)}}, \quad (3)$$

where  $\lambda_L(0)$  is the London penetration depth at  $T = 0$ , also of the order of 39 nm [70]. The value obtained for  $\lambda(0)$  for the grain after this procedure is listed in Table 1. It is

somewhat smaller than other typical values found in the literature for Nb thin films of similar thickness [71]. Nevertheless, an increase in  $\lambda(0)$  is observed for the WL compared to the grain. This direct comparison indicates a lower ability of the WL to shield the magnetic field due to the suppression of superconductivity in this region.

**Table 1.** Resistivity at 300 K and 10 K; RRR; Superconducting critical temperature,  $T_c$ ; mean free path,  $l$ ; coherence length,  $\xi(0)$ ; penetration depth,  $\lambda(0)$ . All listed parameters were obtained for the grain and weak-link contributions.

Parameters	Grain	Weak-Link
$\rho_{300}$ [ $\mu\Omega\text{cm}$ ]	22.48	302.49
$\rho_{10}$ [ $\mu\Omega\text{cm}$ ]	3.11	114.62
RRR	7.23	2.64
$T_c^{\text{onset}}$ [K]	$9.25 \pm 0.05$	$8.75 \pm 0.05$
$l$ [nm]	$12.02 \pm 0.05$	$0.33 \pm 0.03$
$\xi(0)$ [nm]	$18.51 \pm 0.04$	$3.06 \pm 0.14$
$\lambda(0)$ [nm]	$43.06 \pm 0.09$	$259 \pm 12$

### 3.3. Normal State Properties

The resistivity curves were analyzed in the framework of the Boltzmann transport, Bloch-Grüneisen, and Wilson-Grüneisen theories [28,29,31,72,73]. The fundamental equation to describe the electron-phonon (e-ph) interaction in the temperature-dependent resistivity is presented as the second term on the right side of Equation (4),

$$\rho(T) = \rho_0 + \rho_{\text{e-ph}} = \rho_0 + K_0 \left( \frac{T}{\Theta_D} \right)^n \int_0^{\Theta_D} \frac{x^n}{(e^x - 1)(1 - e^{-x})} dx \quad (4)$$

where  $\rho_0$  is the residual resistivity due to defect scattering and  $\Theta_D = 275$  K for Nb [74].

The exponent  $n$  depends on the nature of the interaction and usually assumes the values 2, 3, or 5. When  $n = 3$ , the main mechanism is called *sd* interband scattering and the resistivity contribution is labelled  $\rho_{sd}$ . This mechanism is a known feature of transition metals where conduction band electrons with a high Fermi velocity (*s* band) can be scattered by lattice vibrations into an unfilled *d* band with a low Fermi velocity and vice-versa. For a single band metal, however, the most important mechanism arises from phonon-scattered electrons within the *s* shell, named *ss* intraband scattering. In this case,  $n = 5$  and this contribution is labelled  $\rho_{ss}$ .

Based on Ref. [18], an exponent  $n = 5$  was chosen for the plain grain contribution and an attempt to determine the upper limit of temperature ( $T_{\text{max}}$ ) for which  $T \ll \Theta_D$  was made. It is worth mentioning that for temperatures near  $\Theta_D$ , the contribution  $\rho_{\text{e-ph}}$  is proportional to  $T$  regardless of the value of  $n$  [75]. As the resistivity measurements were carried out up to room temperature, different curves were fitted by changing the maximum temperature in steps of 50 K, from 50 K up to 300 K, always considering the initial point at 10 K, i.e., above  $T_c$ . The upper inset of Figure 4a illustrates the R-square coefficient for the fitting curves against  $T_{\text{max}}$ . This analysis reveals a clear enhancement of R-square up to  $T_{\text{max}} = 150$  K, above which point it stays nearly constant, i.e., three decimal places are equal. Such behavior deviates from the expected  $T \ll \Theta_D$  criterion, which implicates that higher maximum temperatures would lead to a worst fit of Equation (4). Nevertheless, the main panel of Figure 4a exhibits the experimental data in blue and the fitting curve in red, obtained by setting  $T_{\text{max}}$  as 150 K to present an example. It fits reasonably well for intermediate temperatures, but clearly deviates for lower ones, as revealed by the bottom inset. One can observe the relative fit error, defined as  $[(\rho_{\text{measured}} - \rho_{\text{fit}})/\rho_{\text{measured}} \times 100\%]$ , which shows a minimum close to  $-10\%$  at lower temperatures, increasing up to a maximum value of  $\sim 3\%$  and decreasing gradually for higher temperatures. A similar behavior appears if we choose values for  $T_{\text{max}}$  larger than 150 K.

Although a substantial difference appears between the data below 30 K, a relatively high value of R-square is reached when taking  $n = 5$ , as given in Table 2. To find a solution for such a discrepancy, in the next step, the exponent  $n$  was left as a free parameter in the fitting procedure. Again, the R-square coefficient evolution with different  $T_{\max}$  values was investigated. The results in the upper inset of Figure 4b reveal an almost constant, close to 1, behavior up to 150 K, decreasing above it – as expected when  $T \rightarrow \Theta_D$ . As such,  $T_{\max} = 150$  K is found to be the highest value of maximum temperature satisfying the  $T \ll \Theta_D$  criterion. The fit of Equation (4) for such  $T_{\max}$  yields an exponent  $n = (3.000 \pm 0.013)$  and an R-square value considerably higher than those obtained for  $n = 5$ , as shown in Table 2. Furthermore, the main panel of Figure 4b shows both the measured and the new fitting curves, evidencing a greater agreement between them at low temperatures. The relative fit error, depicted in the lower inset, is less than  $\pm 0.4\%$  over the whole temperature range. Therefore, although there is an undeniably significant contribution to the electronic scattering due to the grain morphology, the previous analysis demonstrates that the temperature-dependent resistivity of the plain Nb film (grain) is governed by the *sd* interband scattering mechanism, instead of the *ss* intraband one. This behavior has also been previously observed for high-purity Nb bulk samples [32] and sputtered Nb films [66].

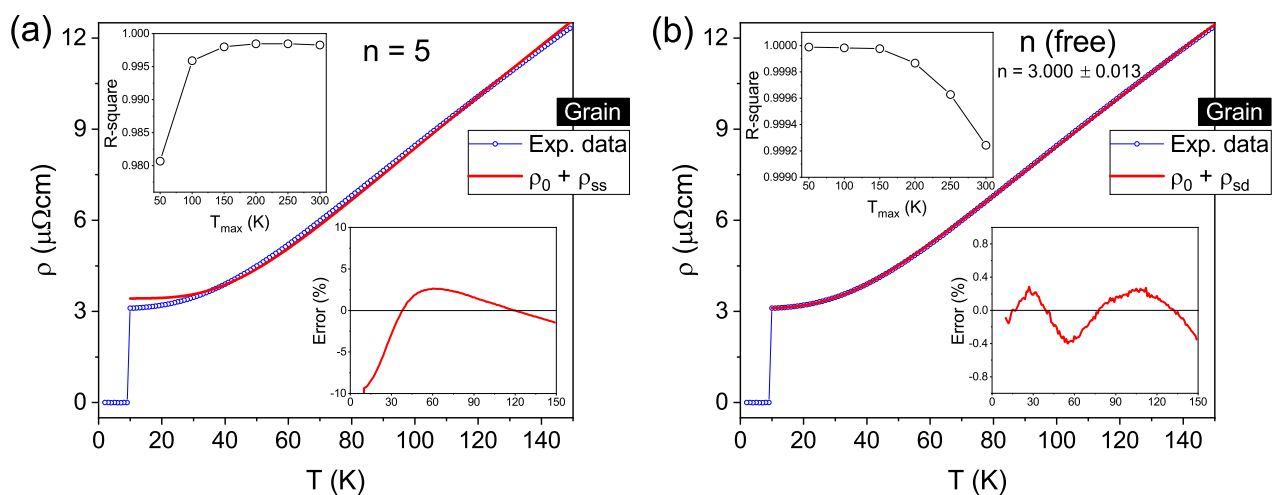


**Figure 4.** (Color online) Temperature-dependent resistivity for the grain contribution. In panel (a), the red line is the fitting for  $n = 5$  in Equation (4) up to 150 K, whereas (b) shows the fitting for  $n$  as a free parameter for same equation. The upper and lower insets for both panels show the R-square coefficient versus the upper limit of temperature  $T_{\max}$  and the relative fit error versus temperature, respectively.

**Table 2.**  $\rho(T)$  fittings for the grain and groove components.

Contribution	$\rho(T) =$	$n$	$\rho_0$ ( $\mu\Omega\text{cm}$ )	$B$ ( $10^{-5} \text{K}^{-2}$ )	$K_0$ ( $\mu\Omega\text{cm}$ )	Adj. R-Square
Grain	$\rho_0 + \rho_{ss}$	5	$3.426 \pm 0.018$	-	$80.5 \pm 0.3$	0.99799
Grain	$\rho_0 + \rho_{sd}$	$3.000 \pm 0.013$	$3.095 \pm 0.004$	-	$39.21 \pm 0.25$	0.99998
Groove	$\rho_0 + \rho_{sd}$	3	$117.8 \pm 0.3$	-	$437 \pm 2$	0.99601
Groove	$\rho_0 + \rho_{sd} + \rho_{epi}$	3	$113.30 \pm 0.09$	$3.93 \pm 0.06$	$307 \pm 2$	0.99988

Concerning the resistivity data for the grooved region, Equation (4) was used in the first fittings. We assumed the exponent  $n = 3$  based on the results discussed in the previous paragraph for the plain film region. Nonetheless, the fitting curve shows a significant deviation from the experimental data, which can be as high as 3%, over the whole temperature range, as presented in the main panel of Figure 5a and reinforced by the relative fit error in the bottom inset. The R-square coefficient versus  $T_{\max}$  curve in the top inset shows a maximum value at 100 K, which is still far from ideal fitting. It

should be pointed out that the previously mentioned possible misrepresentation of  $\rho_0$  due to the approximation of the groove shape would only contribute to the  $\rho(T)$  curve as a constant. Therefore, this is not the cause for the large error obtained as it does not influence the variation in  $\rho(T)$  as the temperature increases. In other words, the behavior of the temperature-dependent resistivity is correctly represented in Figure 5. In fact, an additional scattering mechanism must be considered, due to the gallium ions implanted during the notch excavation. For highly disordered metals, it is necessary to account for the quantum interference of all different possible sources of electron scattering, for which the overall effect may result in the presence of a  $T^2$  term in  $\rho(T)$  [35,76]. Doing so has led to the development of the so-called electron-phonon-impurity (epi) interference effect, which also considers the inelastic scattering of electrons by impurities. It has been shown experimentally that such a theory successfully describes the resistivity behavior of several metallic thin films, including Nb, over a large range of temperatures [77–79]. To account for the presence of the epi mechanism in the groove, an additional term, given by Equation (5), was added to Equation (4), in accordance with Matthiessen’s rule. It is noteworthy that at low temperatures ( $T < \Theta_D/5$ ), the integral in Equation (5) approaches  $\pi^2/6$ , and its temperature dependence is simplified to  $\rho_0 BT^2$  [76,77], however, this approximation is not used here.

$$\rho_{\text{epi}}(T) = \rho_0 BT^2 \left( \frac{6}{\pi^2} \right) \int_0^{\left(\frac{\Theta_D}{T}\right)} \left[ \frac{x^2 e^x}{(e^x - 1)^2} - \frac{x}{(e^x - 1)} \right] dx \quad (5)$$

where  $B$  is the epi coefficient.

Figure 5b illustrates the resistivity fit considering the terms  $T^3$  and  $T^2$ . The main panel shows a good agreement between the measured and fitting curves over the full range of temperature, which is confirmed by the bottom inset presenting a maximum fitting error value of 0.8%. Besides that, as shown in the top inset and listed in Table 2, the R-square coefficient goes through a maximum at 150 K, a value perfectly compatible with that arising from the previous analysis for plain Nb. Therefore, the effect of Ga impurities—implanted into the groove during the FIB excavation—on the temperature-dependent resistivity, manifests itself as an additional scattering term (epi), properly represented by the expression in Equation (5).

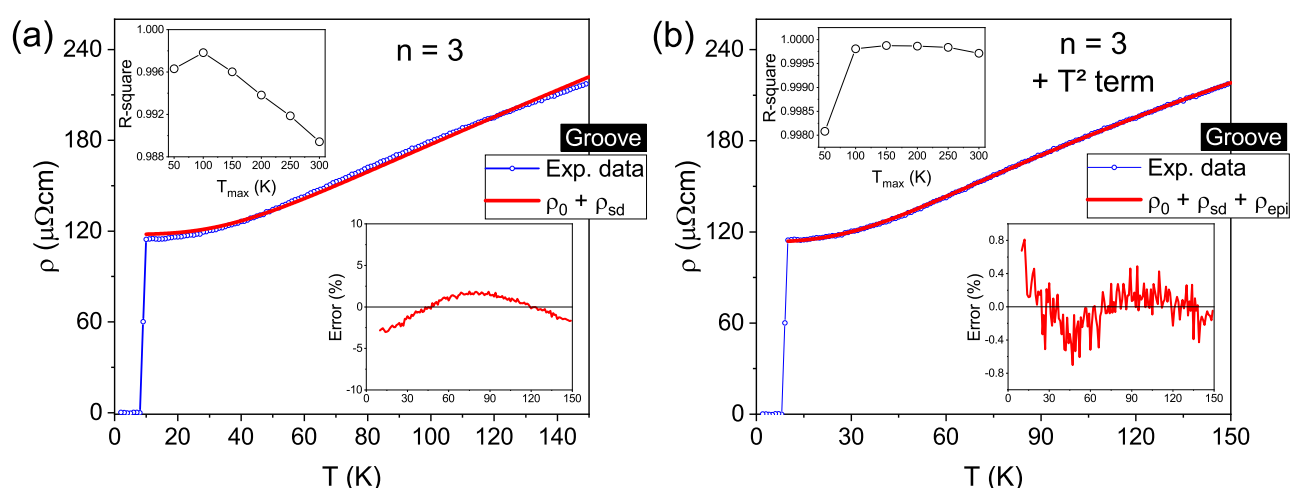


**Figure 5.** (Color online) Resistivity versus temperature (up to 150 K) curves for the groove. The fitting depicted by the red curve in (a) represents the  $sd$  band scattering ( $n = 3$ ), as described by Equation (4). In (b), the red curve represents the fitting considering an additional contribution given by Equation (5) in comparison to the fitting in (a). The lower inset in both panels represents the relative fit error and the upper insets shows the quality of the fit given by the R-square coefficient, which changes when the temperature upper limit is varied.

### 3.4. The Evolution of the Critical Temperature with Disorder

In the last sections, the effects of FIB milling on the superconducting and normal state properties of the tailored Nb film prepared using a dose of  $1.2 \text{ nC}/\mu\text{m}^2$  were demonstrated in detail. The changes in the critical temperature of the WL region,  $T_c^{WL}$ , and the emergence of the defect-driven quadratic-in- $T$  term in  $\rho(T)$  are both attributed to the presence of implanted Ga impurities in the groove region. Recently, the mechanism behind the simultaneous emergence of both effects in superconducting thin films has been elucidated as resulting from the distortion and softening of the lattice due to stabilized defects [37], as the ones due to the FIB milling process. The theory predicts that strong-coupled superconductors, such as Nb, present a decrease in  $T_c$  as the residual resistivity  $\rho_0$  is increased—which arises by increasing the density of defects in the specimen. An analytical expression that allows one to gauge the variation of  $T_c^{WL}$  for the grooved Nb samples has been derived as [37]:

$$\frac{\delta T_c^{WL}}{T_{c0}^{WL}} \approx -t_1 \left( \frac{\delta \rho_0}{\rho_{00}} \right) - t_2 \left( \frac{\delta \rho_0}{\rho_{00}} \right)^2, \quad (6)$$

where  $T_{c0}^{WL}$  and  $\rho_{00}$  are the values of  $T_c^{WL}$  and  $\rho_0$  for the lowest available concentration of defects,  $\delta \rho_0 = \rho_0 - \rho_{00}$ , and  $\delta T_c^{WL} = T_c^{WL} - T_{c0}^{WL}$ . The positive coefficients  $t_1$  and  $t_2$  are related to different electronic and phononic material characteristics as discussed in Ref. [37].

To investigate this trend for this kind of nanofabricated single WL samples, we varied the dose used during the FIB milling from  $0.1 \text{ nC}/\mu\text{m}^2$  to  $1.8 \text{ nC}/\mu\text{m}^2$ .  $T_c^{WL}$  values were then evaluated by the mid-point of the weak-link transition in  $T$ -dependent AC susceptibility curves, such as those presented in Figure 2a. Although our measurements do not allow access to  $\rho_0$  values, it is true that the residual resistivity is directly related to defect concentration, being thus reasonable [25,80–84] to use the dose as the relative control parameter gauging the amount of impurities introduced in the film by the incoming Ga atoms. In other words, we may assume the relationship  $\delta \rho_0 / \rho_{00} \sim \delta(\text{dose}) / \text{dose}_0 = \delta(\text{dose} - \text{dose}_0) / \text{dose}_0$ , with  $\text{dose}_0 = 0.1 \text{ nC}/\mu\text{m}^2$ . Accordingly,  $T_{c0}^{WL}$  represents the WL transition temperature for the sample with  $\text{dose}_0$ .

The evolution of the relative  $T_c^{WL}$  variation with the concentration of defects measured by the relative dose variation is presented in Figure 6. The first clear characteristic is the presence of the expected monotonous decrease of  $T_c^{WL}$  as the defect concentration is increased, reaching values as low as  $(3.5 \pm 0.1) \text{ K}$ . Furthermore, Equation (6) was fitted to the data only by replacing  $\rho_0$  by the values of the respective doses used in the fabrication process. The model agrees reasonably well with the experimental data, despite the values of  $T_c^{WL}$  being collected via volume-average magnetic measurements, and not from resistivity. The overall agreement seems to validate the relationship assumed to exist between  $\delta \rho_0$  and  $\delta(\text{dose})$ . This not only corroborates the findings of [37], but also indicates that the model is a rather robust description of the underlying mechanism leading to the simultaneous occurrence of a variation in  $T_c$  and the emergence of the quadratic-in- $T$  resistive contribution in defect-bearing specimens. The relationship between superconductivity and normal state properties in our single WL Nb samples is then demonstrated to arise from the inclusion of defects, evidencing once again the milling procedure as the cause of the deterioration of superconducting properties.



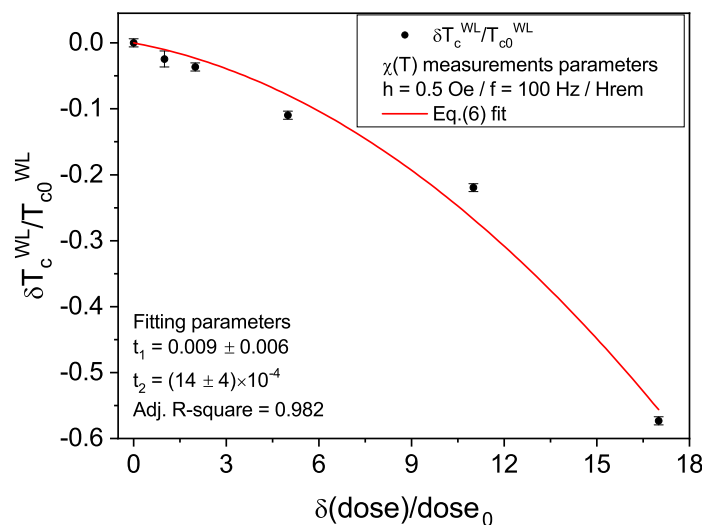


**Figure 6.** Relative change of the critical temperature as a function of the relative beam dose used during groove milling. Red solid curve is the fit of Equation (6) using the FIB dose as control parameter. This analysis demonstrates that the data follows the expected trend for strong-coupled superconductors.

#### 4. Conclusions

We have successfully fabricated a thin-film granular system, composed by two high-quality Nb grains separated by a single artificial weak-link excavated using the FIB technique. This sample allowed us to gauge the effects of granularity in the most simple system possible, considering materials and etching technique widely used to obtain nanopatterned superconducting devices. The analysis of the AC and DC magnetic responses evidenced a couple of features related to its granular morphology, namely a double-step transition as the sample is cooled down from the normal to the Meissner state and the existence of a local maximum in the hysteresis loop. Furthermore, transport measurements also revealed the existence of a double transition to the superconducting state, caused by the presence of the groove in the center of the film. By isolating the grain and groove contributions to the resistivity, we were able to determine several normal state and superconducting parameters related to each of them. These results demonstrate a slight worsening of the sample performance caused by the notch. Furthermore, we conducted a careful investigation of the normal state scattering mechanisms in the different parts of the sample by fitting the temperature-dependent resistivity curves based on the Wilson-Grüneisen model. Thus, it was shown that for the plain Nb thin film *sd* interband scattering is the main mechanism contributing to the resistivity. When studying the behavior for the groove region, however, an additional defect-driven quadratic-in-*T* term arising from the presence of Ga impurities implanted during the FIB excavation was shown necessary to describe properly the scattering process in the sample. This effect is shown to be correlated to a decrease in the superconducting critical temperature by analyzing different samples produced with varying degrees of disorder, being in a good agreement with a recent theoretical description.

**Author Contributions:** Conceptualization, M.I.V.-C. and M.M.; methodology, F.C., A.A.M.d.O., A.M.H.d.A. and M.M.; software, M.I.V.-C. and D.A.D.C.; validation, M.I.V.-C., F.C., D.A.D.C. and M.M.; formal analysis, M.I.V.-C., D.A.D.C., W.A.O. and M.M.; investigation, M.I.V.-C., D.A.D.C., F.C., A.A.M.d.O., A.M.H.d.A., T.H.J. and M.M.; resources, W.A.O.; data curation, W.A.O. and M.M.; writing—original draft preparation, D.A.D.C. and M.M.; writing—review and editing, M.I.V.-C., F.C., A.A.M.d.O., A.M.H.d.A., T.H.J. and W.A.O.; visualization, M.I.V.-C., W.A.O. and M.M.; supervision, W.A.O. and

M.M.; project administration, W.A.O. and M.M. All authors have read and agreed to the published version of the manuscript.

**Funding:** This research was funded by the grants 2007/08072-0, 2017/24786-4, and 2018/16193-6 São Paulo Research Foundation (FAPESP), by the National Council for Scientific and Technological Development (CNPq), by the Coordenação de Aperfeiçoamento de Pessoal de Nível Superior—Brasil (CAPES)—Finance Code 001.

**Institutional Review Board Statement:** Not applicable.

**Informed Consent Statement:** Not applicable.

**Data Availability Statement:** Data is contained within the article.

**Acknowledgments:** The authors would like to acknowledge Laboratório de Conformação Nanométrica (IF/UFRGS) for the Nb film growth, Laboratório de Microfabricação (LNNano/CNPq) for the film lithography, and Laboratório de Caracterização Estrutural (DEMa/UFSCar) for the structural characterization.

**Conflicts of Interest:** The authors declare no conflict of interest.

**Sample Availability:** Nb thin films are available from the authors.

## Abbreviations

The following abbreviations are used in this manuscript:

FIB	Focused ion beam
MO	Magneto-optical
AFM	Atomic force microscopy
EDS	Energy Dispersive X-ray Spectrometry
SEM	Scanning Electron Microscope
GF	Grooved Film
PF	Plain Film
S	Plain region of Grooved Film
S'	Groove region of Grooved Film
$T_c$	Superconducting critical temperature
WL	Weak-link
$T_c^{WL}$	Weak-link critical temperature
$H_{rem}$	Remnant DC magnetic field
$h$	Applied excitation field amplitude
$T$	Temperature
$\rho(T)$	Temperature-dependent resistivity
$n$	Power-law exponent in $\rho(T)$
$A_S$ ( $A_{S'}$ )	Cross-section area of the grain (groove)
$l_S$ ( $l_{S'}$ )	Length of the grain (groove)
$\rho_0$	Residual resistivity
$\rho_{S'}$	Groove resistivity
$\rho_G$	Grain resistivity
$\rho_{epi}$	Electron-phonon-impurity resistivity contribution
$\rho_{sd}$	<i>sd</i> interband scattering resistivity contribution
$\rho_{ss}$	<i>ss</i> intraband scattering resistivity contribution
$\rho_{10}$	Resistivity at 10 K
$\rho_{300}$	Resistivity at 300 K
$V_G$	Voltage measured between electrodes 2 and 3 (plain region)
$V_{SS'S}$	Voltage measured between electrodes 3 and 4 (SS'S contribution)
$B$	Electron-phonon-impurity coefficient
$\Theta_D$	Debye temperature
$T_{max}$	Upper limit of temperature to fit $\rho(T)$
$\chi_{AC}(T)$	Temperature-dependent AC susceptibility
$\chi'$	Real part of $\chi_{AC}$

$\chi''$	Imaginary part of $\chi_{AC}$
$f$	Frequency
$R$	Resistance
$RRR$	Residual resistivity ratio
$l$	Mean free path
$\xi$	Coherence length
$\lambda$	Penetration depth
$H_{c2}$	Upper critical field

## References

- Lubberts, G. Transport critical current density and electrical characterization of patterned high- $T_c$  superconducting thin films prepared by metallo-organic decomposition. *J. Appl. Phys.* **1990**, *68*, 688–694. [[CrossRef](#)]
- Harada, K.; Kamimura, O.; Kasai, H.; Matsuda, T.; Tonomura, A.; Moshchalkov, V.V. Direct observation of vortex dynamics in superconducting films with regular arrays of defects. *Science* **1996**, *274*, 1167–1170. [[CrossRef](#)]
- Welp, U.; Xiao, Z.L.; Jiang, J.S.; Vlasko-Vlasov, V.K.; Bader, S.D.; Crabtree, G.W.; Liang, J.; Chik, H.; Xu, J.M. Superconducting transition and vortex pinning in Nb films patterned with nanoscale hole arrays. *Phys. Rev. B* **2002**, *66*, 212507. [[CrossRef](#)]
- Shaw, G.; Mandal, P.; Bag, B.; Banerjee, S.; Tamegai, T.; Suderow, H. Properties of nanopatterned pins generated in a superconductor with FIB. *Appl. Surf. Sci.* **2012**, *258*, 4199–4202. [[CrossRef](#)]
- Latimer, M.L.; Berdiyrov, G.R.; Xiao, Z.L.; Peeters, F.M.; Kwok, W.K. Realization of artificial ice systems for magnetic vortices in a superconducting MoGe thin film with patterned nanostructures. *Phys. Rev. Lett.* **2013**, *111*, 067001. [[CrossRef](#)] [[PubMed](#)]
- Golod, T.; Iovan, A.; Krasnov, V.M. Single Abrikosov vortices as quantized information bits. *Nat. Commun.* **2015**, *6*, 1–5. [[CrossRef](#)] [[PubMed](#)]
- Brisbois, J.; Adami, O.A.; Avila, J.I.; Motta, M.; Ortiz, W.A.; Nguyen, N.D.; Vanderbemden, P.; Vanderheyden, B.; Kramer, R.B.G.; Silhanek, A.V. Magnetic flux penetration in Nb superconducting films with lithographically defined microindentations. *Phys. Rev. B* **2016**, *93*, 054521. [[CrossRef](#)]
- Dobrovolskiy, O.V.; Huth, M.; Shklovskij, V.A.; Vovk, R.V. Mobile fluxons as coherent probes of periodic pinning in superconductors. *Sci. Rep.* **2017**, *7*, 13740. [[CrossRef](#)] [[PubMed](#)]
- Kalcheim, Y.; Katzir, E.; Zeides, F.; Katz, N.; Paltiel, Y.; Millo, O. Dynamic Control of the Vortex Pinning Potential in a Superconductor Using Current Injection through Nanoscale Patterns. *Nano Lett.* **2017**, *17*, 2934–2939. [[CrossRef](#)]
- Golod, T.; Kapran, O.M.; Krasnov, V.M. Planar superconductor-ferromagnet-superconductor Josephson junctions as scanning-probe sensors. *Phys. Rev. Appl.* **2019**, *11*, 014062. [[CrossRef](#)]
- Trabaldo, E.; Ruffieux, S.; Andersson, E.; Arpaia, R.; Montemurro, D.; Schneiderman, J.F.; Kalaboukhov, A.; Winkler, D.; Lombardi, F.; Bauch, T. Properties of grooved Dayem bridge based YBa<sub>2</sub>Cu<sub>3</sub>O<sub>7- $\delta$</sub>  superconducting quantum interference devices and magnetometers. *Appl. Phys. Lett.* **2020**, *116*, 132601. [[CrossRef](#)]
- Singh, G.; Lesne, E.; Winkler, D.; Claeson, T.; Bauch, T.; Lombardi, F.; Caviglia, A.D.; Kalaboukhov, A. Nanopatterning of weak links in superconducting oxide interfaces. *Nanomaterials* **2021**, *11*, 398. [[CrossRef](#)] [[PubMed](#)]
- Golod, T.; Hovhannisyan, R.A.; Kapran, O.M.; Dremov, V.V.; Stolyarov, V.S.; Krasnov, V.M. Reconfigurable Josephson Phase Shifter. *Nano Lett.* **2021**, *12*, 5240–5246. [[CrossRef](#)]
- McCarthy, J.; Pei, Z.; Becker, M.; Atteridge, D. FIB micromachined submicron thickness cantilevers for the study of thin film properties. *Thin Solid Films* **2000**, *358*, 146–151. [[CrossRef](#)]
- Volkert, C.A.; Minor, A.M. Focused ion beam microscopy and micromachining. *MRS Bull.* **2007**, *32*, 389–399. [[CrossRef](#)]
- Wu, C.H.; Jhan, F.J.; Chen, J.H.; Jeng, J.T. High- $T_c$  Josephson junctions fabricated by focused ion beam direct milling. *Supercond. Sci. Technol.* **2012**, *26*, 025010. [[CrossRef](#)]
- Pautrat, A.; Scola, J.; Goupil, C.; Simon, C.; Villard, C.; Domengès, B.; Simon, Y.; Guilpin, C.; Méchin, L. Quantitative analysis of the critical current due to vortex pinning by surface corrugation. *Phys. Rev. B* **2004**, *69*, 224504. [[CrossRef](#)]
- Dobrovolskiy, O.V.; Begun, E.; Huth, M.; Shklovskij, V.A. Electrical transport and pinning properties of Nb thin films patterned with focused ion beam-milled washboard nanostructures. *New J. Phys.* **2012**, *14*, 113027. [[CrossRef](#)]
- Cybart, S.A.; Cho, E.Y.; Wong, T.J.; Wehlin, B.H.; Ma, M.K.; Huynh, C.; Dynes, R.C. Nano Josephson superconducting tunnel junctions in YBa<sub>2</sub>Cu<sub>3</sub>O<sub>7- $\delta$</sub>  directly patterned with a focused helium ion beam. *Nat. Nanotechnol.* **2015**, *10*, 598–602. [[CrossRef](#)]
- Dobrovolskiy, O.V. Abrikosov fluxonics in washboard nanolandscapes. *Physica C* **2017**, *533*, 80–90. [[CrossRef](#)]
- Mayer, J.; Giannuzzi, L.A.; Kamino, T.; Michael, J. TEM sample preparation and FIB-induced damage. *MRS Bull.* **2007**, *32*, 400–407. [[CrossRef](#)]
- De Leo, N.; Fretto, M.; Lacquaniti, V.; Cassiogo, C.; D'Ortenzi, L.; Boarino, L.; Maggi, S. Thickness modulated niobium nanoconstrictions by focused ion beam and anodization. *IEEE Trans. Appl. Supercond.* **2016**, *26*, 1–5. [[CrossRef](#)]
- Singh, M.; Chaujar, R.; Husale, S.; Grover, S.; Shah, A.P.; Deshmukh, M.M.; Gupta, A.; Singh, V.N.; Ojha, V.N.; Aswal, D.K.; Rakshit, R.K. Influence of fabrication processes on transport properties of superconducting niobium nitride nanowires. *Curr. Sci.* **2018**, *114*, 1443–1450. [[CrossRef](#)]
- Datesman, A.M.; Schultz, J.C.; Cecil, T.W.; Lyons, C.M.; Lichtenberger, A.W. Gallium ion implantation into niobium thin films using a focused-ion beam. *IEEE Trans. Appl. Supercond.* **2005**, *15*, 3524–3527. [[CrossRef](#)]

25. Heim, G.; Kay, E. Ion implantation during film growth and its effect on the superconducting properties of niobium. *J. Appl. Phys.* **1975**, *46*, 4006–4012. [[CrossRef](#)]
26. Linker, G. Superconducting properties and structure of ion bombarded Nb layers. *Radiation Effects* **1980**, *47*, 225–228. [[CrossRef](#)]
27. Camerlingo, C.; Scardi, P.; Tosello, C.; Vaglio, R. Disorder effects in ion-implanted niobium thin films. *Phys. Rev. B* **1985**, *31*, 3121. [[CrossRef](#)]
28. Ziman, J. *Electrons and Phonons: The Theory of Transport Phenomena in Solids*; International Series of Monographs on Physics, OUP: Oxford, UK, 2001.
29. Grüneisen, E. Die Abhängigkeit des elektrischen Widerstandes reiner Metalle von der Temperatur. *Ann. Phys.* **1933**, *408*, 530–540. [[CrossRef](#)]
30. Mott, N.F. A discussion of the transition metals on the basis of quantum mechanics. *Proc. Phys. Soc.* **1935**, *47*, 571. [[CrossRef](#)]
31. Wilson, A.H. The electrical conductivity of the transition metals. *Proc. R. Soc. A* **1938**, *167*, 580–593. [[CrossRef](#)]
32. Webb, G.W. Low-Temperature Electrical Resistivity of Pure Niobium. *Phys. Rev.* **1969**, *181*, 1127–1135. [[CrossRef](#)]
33. Lee, P.A.; Ramakrishnan, T.V. Disordered electronic systems. *Rev. Mod. Phys.* **1985**, *57*, 287. [[CrossRef](#)]
34. MacDonald, A.H. Electron-Phonon Enhancement of Electron-Electron Scattering in Al. *Phys. Rev. Lett.* **1980**, *44*, 489–493. [[CrossRef](#)]
35. Reizer, M.Y.; Sergeev, A. The effect of the electron-phonon interaction on the conductivity of impure metals. *Sov. Phys. JETP* **1987**, *65*, 1291–1298.
36. Altshuler, B.; Aronov, A. Electron–Electron Interaction In Disordered Conductors. In *Electron–Electron Interactions in Disordered Systems*; Modern Problems in Condensed Matter Sciences; Efros, A., Pollak, M., Eds.; Elsevier: Amsterdam, The Netherlands, 1985; Volume 10, pp. 1–153.
37. ElMassalami, M.; Neto, M.B.S. Superconductivity, Fermi-liquid transport, and universal kinematic scaling relation for metallic thin films with stabilized defect complexes. *Phys. Rev. B* **2021**, *104*, 014520. [[CrossRef](#)]
38. Likharev, K.K. Superconducting weak links. *Rev. Mod. Phys.* **1979**, *51*, 101–159. [[CrossRef](#)]
39. Caffer, A.M.; Chaves, D.A.D.; Pessoa, A.L.; Carvalho, C.L.; Ortiz, W.A.; Zadorosny, R.; Motta, M. Optimum heat treatment to enhance the weak-link response of Y123 nanowires prepared by Solution Blow Spinning. *Supercond. Sci. Technol.* **2021**, *34*, 025009. [[CrossRef](#)]
40. Babcock, S.E.; Vargas, J.L. The nature of grain boundaries in the high-Tc superconductors. *Annu. Rev. Mater. Sci.* **1995**, *25*, 193–222. [[CrossRef](#)]
41. Ortiz, W.A.; Lisboa-Filho, P.N.; Passos, W.A.C.; Araujo-Moreira, F.M. Field-induced networks of weak-links: an experimental demonstration that the paramagnetic Meissner effect is inherent to granularity. *Physica C* **2001**, *361*, 267–273. [[CrossRef](#)]
42. Clem, J.R. Granular and superconducting-glass properties of the high-temperature superconductors. *Physica C* **1988**, *153*, 50–55. [[CrossRef](#)]
43. Clarke, J.; Braginski, A.I. *The SQUID handbook: Applications of SQUIDS and SQUID Systems*; John Wiley & Sons: New York, NY, 2006.
44. Halbritter, J. RF residual losses, surface impedance, and granularity in superconducting cuprates. *J. Appl. Phys.* **1990**, *68*, 6315–6326. [[CrossRef](#)]
45. Tafuri, F.; Kirtley, J.R. Weak links in high critical temperature superconductors. *Rep. Prog. Phys.* **2005**, *68*, 2573. [[CrossRef](#)]
46. Graser, S.; Hirschfeld, P.J.; Kopp, T.; Gutser, R.; Andersen, B.M.; Mannhart, J. How grain boundaries limit supercurrents in high-temperature superconductors. *Nat. Phys.* **2010**, *6*, 609–614. [[CrossRef](#)]
47. Wang, G.; Raine, M.J.; Hampshire, D.P. How resistive must grain boundaries in polycrystalline superconductors be, to limit  $J_c$ ? *Supercond. Sci. Technol.* **2017**, *30*, 104001. [[CrossRef](#)]
48. Dimos, D.; Chaudhari, P.; Mannhart, J. Superconducting transport properties of grain boundaries in YBa<sub>2</sub>Cu<sub>3</sub>O<sub>7</sub> bicrystals. *Phys. Rev. B* **1990**, *41*, 4038. [[CrossRef](#)] [[PubMed](#)]
49. Polyanskii, A.A.; Gurevich, A.; Pashitski, A.E.; Heinig, N.F.; Redwing, R.D.; Nordman, J.E.; Larbalestier, D.C. Magneto-optical study of flux penetration and critical current densities in [001] tilt YBa<sub>2</sub>Cu<sub>3</sub>O<sub>7- $\delta$</sub>  thin-film bicrystals. *Phys. Rev. B* **1996**, *53*, 8687. [[CrossRef](#)] [[PubMed](#)]
50. Arrington, C.H., III; Deaver, B.S., Jr. Superconducting weak links formed by ion implantation. *Appl. Phys. Lett.* **1975**, *26*, 204–206. [[CrossRef](#)]
51. Goldfarb, R.B.; Lelental, M.; Thompson, C.A. Alternating-Field Susceptometry and Magnetic Susceptibility of Superconductors. In *Magnetic Susceptibility of Superconductors and Other Spin Systems*; Hein, R.A., Francavilla, T.L., Liebenberg, D.H., Eds.; Springer: Boston, MA, USA, 1991; pp. 49–80.
52. Gömöry, F. Characterization of high-temperature superconductors by AC susceptibility measurements. *Supercond. Sci. Technol.* **1997**, *10*, 523–542. [[CrossRef](#)]
53. Brandt, E.H. Ac response of thin-film superconductors at various temperatures and magnetic fields. *Philos. Mag. B* **2000**, *80*, 835–845. [[CrossRef](#)]
54. Jooss, C.; Albrecht, J.; Kuhn, H.; Leonhardt, S.; Kronmüller, H. Magneto-optical studies of current distributions in high-Tc superconductors. *Rep. Prog. Phys.* **2002**, *65*, 651. [[CrossRef](#)]
55. Colauto, F.; Motta, M.; Ortiz, W.A. Controlling magnetic flux penetration in low-Tc superconducting films and hybrids. *Supercond. Sci. Technol.* **2020**, *34*, 013002. [[CrossRef](#)]

56. Palau, A.; Puig, T.; Obradors, X.; Jooss, C. Simultaneous determination of grain and grain-boundary critical currents in  $\text{YBa}_2\text{Cu}_3\text{O}_7$ -coated conductors by magnetic measurements. *Phys. Rev. B* **2007**, *75*, 054517. [[CrossRef](#)]
57. Chen, D.X.; Sanchez, A.; Puig, T.; Martinez, L.; Muñoz, J. AC susceptibility of grains and matrix for high- $T_c$  superconductors. *Physica C* **1990**, *168*, 652–667. [[CrossRef](#)]
58. Navau, C.; Sanchez, A.; Del-Valle, N.; Chen, D.X. Alternating current susceptibility calculations for thin-film superconductors with regions of different critical-current densities. *J. Appl. Phys.* **2008**, *103*, 113907. [[CrossRef](#)]
59. Chen, D.X.; Goldfarb, R.B. Kim model for magnetization of type-II superconductors. *J. Appl. Phys.* **1989**, *66*, 2489–2500. [[CrossRef](#)]
60. Johansen, T.H.; Bratsberg, H. Critical-state magnetization of type-II superconductors in rectangular slab and cylinder geometries. *J. Appl. Phys.* **1995**, *77*, 3945–3952. [[CrossRef](#)]
61. Däumling, M.; Walker, E.; Flükiger, R. Effect of sample shape on the low-field peak in the magnetization of  $\text{YBa}_2\text{Cu}_3\text{O}_{7-\delta}$ . *Phys. Rev. B* **1994**, *50*, 13024. [[CrossRef](#)] [[PubMed](#)]
62. Shantsev, D.V.; Koblischka, M.R.; Galperin, Y.M.; Johansen, T.H.; Püst, L.; Jirsa, M. Central peak position in magnetization loops of high- $T_c$  superconductors. *Phys. Rev. Lett.* **1999**, *82*, 2947. [[CrossRef](#)]
63. Palau, A.; Puig, T.; Obradors, X.; Pardo, E.; Navau, C.; Sanchez, A.; Usoskin, A.; Freyhardt, H.C.; Fernandez, L.; Holzapfel, B.; Feenstra, R. Simultaneous inductive determination of grain and intergrain critical current densities of  $\text{YBa}_2\text{Cu}_3\text{O}_{7-x}$  coated conductors. *Appl. Phys. Lett.* **2004**, *84*, 230–232. [[CrossRef](#)]
64. Poole, C.P.; Farach, H.A.; Creswick, R.J.; Prozorov, R. *Superconductivity*, 2nd ed.; Academic Press: Amsterdam, The Netherlands, 2007; p. 670.
65. Altshuler, E.; Johansen, T.H. Colloquium: Experiments in vortex avalanches. *Rev. Mod. Phys.* **2004**, *76*, 471–487. [[CrossRef](#)]
66. Andreone, A.; Cassinese, A.; Iavarone, M.; Vaglio, R.; Kulik, I.I.; Palmieri, V. Relation between normal-state and superconductive properties of niobium sputtered films. *Phys. Rev. B* **1995**, *52*, 4473. [[CrossRef](#)]
67. Jiang, Q.D.; Xie, Y.L.; Zhang, W.B.; Gu, H.; Ye, Z.Y.; Wu, K.; Zhang, J.L.; Li, C.Y.; Yin, D.L. Superconductivity and transport properties in ultrathin epitaxial single-crystal niobium films. *J. Phys. Condens. Matter* **1990**, *2*, 3567. [[CrossRef](#)]
68. Mayadas, A.F.; Laibowitz, R.B.; Cuomo, J.J. Electrical Characteristics of rf-Sputtered Single-Crystal Niobium Films. *J. Appl. Phys.* **1972**, *43*, 1287–1289. [[CrossRef](#)]
69. Tinkham, M. *Introduction to Superconductivity*, 2nd ed.; Dover Books on Physics; Dover Publications: Mineola, NY, USA, 2004.
70. Maxfield, B.W.; McLean, W.L. Superconducting penetration depth of niobium. *Phys. Rev.* **1965**, *139*, A1515. [[CrossRef](#)]
71. Gubin, A.I.; Il'in, K.S.; Vitusevich, S.A.; Siegel, M.; Klein, N. Dependence of magnetic penetration depth on the thickness of superconducting Nb thin films. *Phys. Rev. B* **2005**, *72*, 064503. [[CrossRef](#)]
72. Allen, P.B. Boltzmann theory and resistivity of metals. In *Quantum Theory of Real Materials*; Chelikowsky, J.R., Louie, S.G., Eds.; Kluwer International Series In Engineering And Computer Science; Kluwer Academic Publishers Group: Boston, MA, USA, 1996; pp. 219–250.
73. Allen, P.B.; Butler, W.H. Electrical conduction in metals. *Phys. Today* **1978**, *31*, 44–49. [[CrossRef](#)]
74. James, A.M.; Lord, M.P. *MacMillan's Chemical and Physical Data*; MacMillan Press: Basingstoke, UK, 1992.
75. Colquitt, L. Electrical and Thermal Resistivities of the Nonmagnetic Transition Metals with a Two-Band Model. *J. Appl. Phys.* **1965**, *36*, 2454–2458. [[CrossRef](#)]
76. Ptitsina, N.G.; Chulkova, G.M.; Il'in, K.S.; Sergeev, A.V.; Pochinkov, F.S.; Gershenson, E.M.; Gershenson, M.E. Electron-phonon interaction in disordered metal films: The resistivity and electron dephasing rate. *Phys. Rev. B* **1997**, *56*, 10089–10096. [[CrossRef](#)]
77. Echternach, P.M.; Gershenson, M.E.; Bozler, H.M. Evidence of interference between electron-phonon and electron-impurity scattering on the conductivity of thin metal films. *Phys. Rev. B* **1993**, *47*, 13659–13663. [[CrossRef](#)]
78. Ptitsina, N.G.; Chulkova, G.M.; Gershenson, E.M.; Gershenson, M.E. Influence of the interference of electron-phonon and electron-impurity scattering on the conductivity of unordered Nb films. *Sov. Phys. JETP* **1995**, *80*, 960–964.
79. Chulkova, G.M.; Ptitsina, N.G.; Gershenson, E.M.; Gershenson, M.E.; Sergeev, A.V. Effect of the interference between electron-phonon and electron-impurity (boundary) scattering on resistivity Nb, Al, Be films. *Czech. J. Phys.* **1996**, *46*, 2489–2490. [[CrossRef](#)]
80. Bauriedl, W.; Heim, G.; Buckel, W. Irradiation effect on  $T_c$  of indium. *Phys. Lett. A* **1976**, *57*, 282–284. [[CrossRef](#)]
81. Bernas, H.; Nedellec, P. Structural and electronic properties of ion implanted superconductors. *Nucl. Instrum. Methods* **1981**, *182–183*, 845–864. [[CrossRef](#)]
82. Linker, G. Amorphization of niobium layers by phosphorus ion implantation. *Nucl. Instrum. Methods Phys. Res.* **1983**, *209–210*, 969–974. [[CrossRef](#)]
83. Linker, G. Amorphization of niobium films by boron ion implantation. *Mater. Sci. Eng.* **1985**, *69*, 105–110.
84. Kasaei, L.; Manichev, V.; Li, M.; Feldman, L.C.; Gustafsson, T.; Collantes, Y.; Hellstrom, E.; Demir, M.; Acharya, N.; Bhattarai, P.; et al. Normal-state and superconducting properties of Co-doped  $\text{BaFe}_2\text{As}_2$  and  $\text{MgB}_2$  thin films after focused helium ion beam irradiation. *Supercond. Sci. Technol.* **2019**, *32*, 095009. [[CrossRef](#)]

## Magnetic field induced weak-to-strong-link transformation in patterned superconducting films

Davi A. D. Chaves<sup>1,\*</sup>, M. I. Valerio-Cuadros<sup>1,†</sup>, L. Jiang<sup>2,3</sup>, E. A. Abbey<sup>1</sup>, F. Colauto<sup>1</sup>, A. A. M. Oliveira<sup>4</sup>, A. M. H. de Andrade<sup>5</sup>, L. B. L. G. Pinheiro<sup>1,4</sup>, T. H. Johansen<sup>6</sup>, C. Xue<sup>7</sup>, Y.-H. Zhou<sup>8,2</sup>, A. V. Silhanek<sup>3</sup>, W. A. Ortiz<sup>1</sup> and M. Motta<sup>1,‡</sup>

<sup>1</sup>*Departamento de Física, Universidade Federal de São Carlos, 13565-905 São Carlos, SP, Brazil*

<sup>2</sup>*School of Aeronautics, Northwestern Polytechnical University, Xi'an 710072, China*

<sup>3</sup>*Experimental Physics of Nanostructured Materials, Q-MAT, CESAM, Université de Liège, B-4000 Sart Tilman, Belgium*

<sup>4</sup>*Instituto Federal de Educação, Ciência e Tecnologia de São Paulo, Campus São Carlos, 13565-905 São Carlos, SP, Brazil*

<sup>5</sup>*Instituto de Física, Universidade Federal do Rio Grande do Sul, 91501-970 Porto Alegre, RS, Brazil*

<sup>6</sup>*Department of Physics, University of Oslo, P.O. Box 1048 Blindern, 0316 Oslo, Norway*

<sup>7</sup>*School of Mechanics, Civil Engineering and Architecture, Northwestern Polytechnical University, Xi'an 710072, China*

<sup>8</sup>*Department of Mechanics and Engineering Sciences, Lanzhou University, Key Laboratory of Mechanics on Disaster and Environment in Western China, Ministry of Education of China, Lanzhou 730000, China*



(Received 7 May 2023; revised 9 October 2023; accepted 8 November 2023; published 1 December 2023)

Ubiquitous in most superconducting materials and a common result of nanofabrication processes, weak links are known for their limiting effects on the transport of electric currents. Still, they are at the root of key features of superconducting technology. By performing quantitative magneto-optical imaging experiments and thermomagnetic model simulations, we correlate the existence of local maxima in the magnetization loops of focused ion beam (FIB)-patterned Nb films to a magnetic field induced weak-to-strong-link transformation increasing their critical current. This phenomenon arises from the nanoscale interaction between quantized magnetic flux lines and FIB-induced modifications of the device microstructure. Under an ac drive field, this leads to a rectified vortex motion along the weak link. The reported tunable effect can be exploited in the development of new superconducting electronic devices, such as flux pumps and valves, to attenuate or amplify the supercurrent through a circuit element and as a strategy to enhance the critical current in weak-link-bearing devices.

DOI: [10.1103/PhysRevB.108.214502](https://doi.org/10.1103/PhysRevB.108.214502)

### I. INTRODUCTION

Nanoscale patterning of superconducting films enables the optimization and control of distinct material properties [1–9]. Moreover, patterning allows for exploring different phenomena arising from the rich physics of superconducting weak links (WLs) [10–13]. Today, patterned superconducting structures find applications in memories [14–17], diodes [18,19], quantum batteries [20], and phase shifters [21,22], serving as the backbone of superconducting electronics.

Meanwhile, focused ion beam (FIB) milling is a prominent fabrication technique with nanometric spatial resolution [23–25]. However, FIB unavoidably introduces defects along the patterned regions, arising from ionic implantation [26–28], locally increasing vortex pinning in superconductors [3,8,29]. Recently, we investigated the effects of a single FIB-milled WL on the properties of prototypical low-critical temperature Nb films, revealing the existence of local maxima in their magnetization loops [30].

Weak links are also an important challenge in the optimization of large-scale applications of high-temperature superconductors (HTSC) [31,32]. Particularly, the overall critical current density ( $J_c$ ) of HTSC is affected by an angular-dependent deterioration of  $J_c$  along grain boundaries [33,34], motivating the development of specialized fabrication techniques [35–38]. Improving critical currents in HTSC and low-critical-temperature materials remains an active research topic [39–44].

In this study, we investigate magnetic flux penetration and shielding currents in FIB-patterned Nb films containing either a single or four artificial WLs. Our results explain the origin of local maxima in the magnetization loops, revealing a field induced transformation from a weak-link to a strong-link behavior by the enhancement of  $J_c$  across the WL.

### II. METHODS

Three 180-nm-thick Nb films were patterned with a single shallow groove using FIB doses of 0.1, 0.2, and 0.3 nC/ $\mu\text{m}^2$  (GF01, GF02, and GF03, respectively). The samples have areas of 3 mm<sup>2</sup> (3 × 1) in the case of GF01 and 2 mm<sup>2</sup> (2.5 × 0.8) for the other films. This process creates WLs comprised of thinner Nb regions pervaded by defects arising from Ga<sup>+</sup> implantation, as shown in Appendix A. The

\*davi@df.ufscar.br

†Current address: Departamento de Física, Universidade Estadual de Maringá, 87020-900 Maringá, PR, Brazil.

‡m.motta@df.ufscar.br

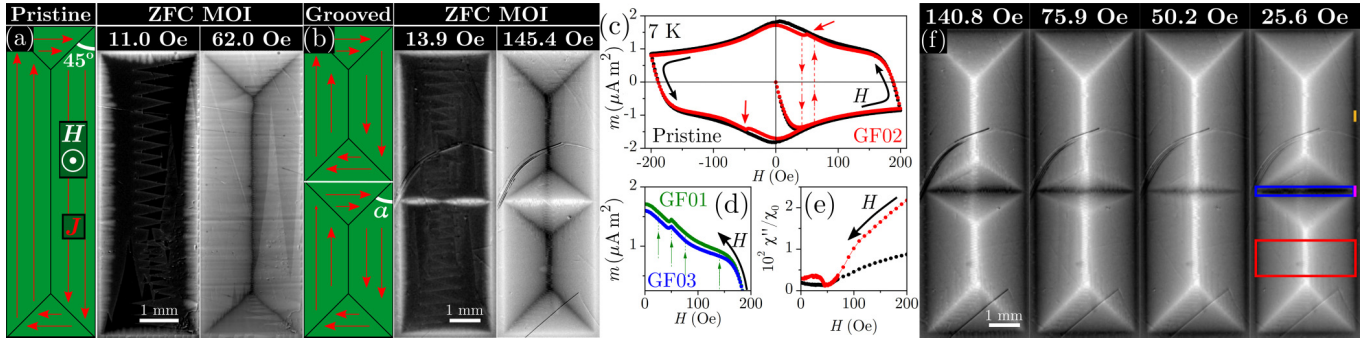


FIG. 1. Representation and MOI at 7 K of fully flux-penetrated (a) pristine and (b) grooved GF01 films under an increasing  $H$  after ZFC. Red arrows represent the direction of  $J$ ;  $\alpha$  is the angle between the  $d$  line and the edge. (c)  $m(H)$  at 7 K for the pristine and GF02 samples. (d) The positive field decreasing branch of  $m(H)$  for GF01 and GF03. (e)  $\chi''$  at 7 K as  $H$  is reduced for the pristine and GF02 samples. The probe field has an amplitude of 3 Oe and a frequency of 100 Hz. The data is normalized by the 2 K, zero-field in-phase response for each sample,  $\chi_0$ . (f) MOI of GF01 at 7 K for the decreasing values of  $H$  indicated by vertical arrows in the main panel in (d). Colored rectangles represent areas used in the investigation in Figs. 2(b)–2(d).

groove depths range from 4.2 nm to 14.6 nm. Additionally, a  $2.5 \times 2.5 \text{ mm}^2$  300-nm-thick Nb film labeled GF01+ was deposited and patterned with two perpendicular grooves using a FIB dose of  $0.1 \text{ nC}/\mu\text{m}^2$  thus exhibiting four distinct WLs in a cross pattern. A pristine film with critical temperature ( $T_c$ ) of 9.0 K is also studied. Sample preparation details are given in Ref. [30]. Global dc magnetic responses are obtained in a Quantum Design MPMS-5S in the perpendicular geometry. Quantitative magneto-optical imaging (MOI) is used to reveal the local out-of-plane magnetic flux density ( $B$ ) and current density ( $J$ ) in the films [45,46].

Furthermore, we employed the thermomagnetic model (TM) to simulate the macroscopic magnetic flux density distribution in the patterned films [47]. For that, the heat diffusion equation

$$dc \dot{T} = d\kappa \nabla^2 T - h(T - T_0) + j \cdot E \quad (1)$$

is solved considering Maxwell's equations and that the superconductor material properties are given by

$$E = \begin{cases} \rho_n(j/j_c)^{n-1} j/d & \text{if } j < j_c \text{ and } T < T_c, \\ \rho_n j/d & \text{otherwise,} \end{cases} \quad (2)$$

where  $E$  is the electric field,  $\kappa$  the thermal conductivity,  $c$  the specific heat,  $h$  the coefficient for heat removal to the substrate,  $\rho_n$  the normal state resistivity,  $d$  is the film thickness,  $j$  the sheet current,  $j_c$  the critical sheet current, and  $n$  the flux creep exponent [47]. The simulation parameters used in this work follow Ref. [48].

### III. RESULTS AND DISCUSSION

The left panel of Fig. 1(a) schematically represents a superconducting film fully penetrated by flux under a perpendicular magnetic field  $H$  after zero-field cooling (ZFC) [49,50]. We observe five dark discontinuity lines, or  $d$  lines, shielding flux more efficiently where  $J$  changes its direction. The magneto-optical (MO) image at 11.0 Oe demonstrates that flux penetrates from the edges toward the center of the pristine film as  $H$  is increased. This is manifested by bright, flux-filled regions surrounding the dark, shielded central portion of the sample. At 62.0 Oe, we observe the expected domains for

the fully penetrated film. Although the resolution of MOI reveals an apparently continuous flux front, the superconductor is in fact permeated by quantized flux lines or vortices [51,52].

In contrast, a groove across the shortest symmetry line of the film creates a WL, defining two apparently disconnected pristine regions (PR). Since the WL has a lower  $J_c$  than the PR,  $J$  needs to bend away from the groove, resulting in the central diamond-shaped domain represented in Fig. 1(b) [53–55]. In the limiting case when the depicted angle  $\alpha = 45^\circ$ , no current is able to flow through the WL, i.e.,  $J_c^{\text{WL}} = 0$ . MOI for GF01 at 13.9 Oe reveals that the WL is fully penetrated—a consequence of its weaker shielding capacity. At 145.4 Oe, the diamond-shaped domain can be clearly distinguished. Contrary to the representation, MOI shows  $\alpha > 45^\circ$  and a faded dark vertical  $d$  line appears inside the diamond. These effects happen because  $J_c^{\text{WL}} > 0$ , meaning that a fraction of  $J$  is able to flow through the WL. The dark scratches above the diamond-shaped and bottom triangular domains are defects on the MO indicator and do not interfere with the flux penetration into the sample.

Figure 1(c) shows complete magnetic moment hysteresis loops,  $m(H)$ , at 7 K for the pristine film and GF02. The pristine behavior matches that expected for a type-II superconductor presenting a flux-dependent critical current density,  $J_c(B)$  [56,57]. In contrast, GF02 exhibits local maxima in the positive and negative decreasing-field branches of  $m(H)$ . Figure 1(d) reveals the same feature around 50 Oe for GF01 and GF03. Out-of-phase ac magnetic susceptibility ( $\chi''$ ) measurements in Fig. 1(e) demonstrate that this effect is sensible to ac excitations. For sufficiently large probe fields, a dip in  $\chi''$  occurs around the same  $H$  values at which  $m(H)$  peaks for GF02. This ac experiment is equivalent to performing a minor  $m(H)$  loop, as indicated by dashed arrows in Fig. 1(c). Thus, at the upper branch of the loop, while the probe field decreases the total applied field, the sample experiences the same phenomenon giving rise to the  $m(H)$  peak.

We elect GF01 to illustrate our investigation of what leads to this phenomenon. GF01 contains a 4.2-nm-deep groove with an 800 nm width—see Appendix A. Figure 1(f) shows

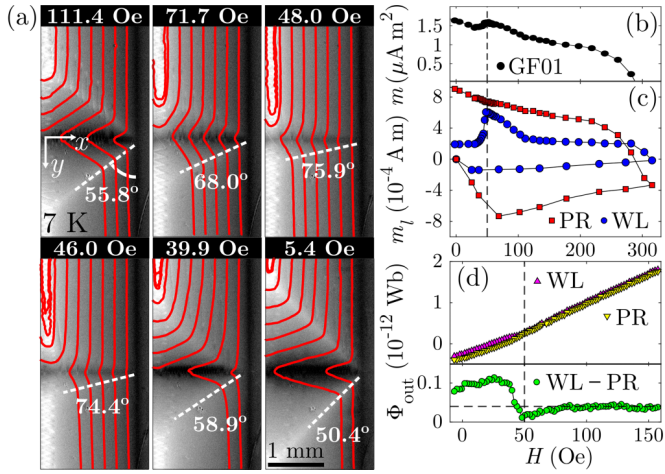


FIG. 2. (a) MOI of GF01 at 7 K as  $H$  is reduced from full penetration. The  $J$  distribution is shown as red streamlines. (b)  $m(H)$  for GF01 evaluated by MOI. (c)  $m_l(H)$  averaged over different regions of the sample. (d) Upper panel shows  $\Phi_{\text{out}}$  besides the WL and the PR. Lower panel highlights the difference in  $\Phi_{\text{out}}$  between the two regions. The quantities are obtained for the color-matched regions shown in Fig. 1(f).

a series of MO images as  $H$  is decreased from full penetration. At 140.8 Oe, flux penetration is similar to that of Fig 1(b). The WL now appears in dark contrast, because  $H$  was reduced from 315.6 Oe, and the WL shows a lower, but positive flux density due to its weaker shielding capability. However, as  $H$  approaches 50 Oe, the  $d$  lines forming the central diamond-shaped domain move toward the groove—as if they were closing. The image at 50.2 Oe resembles a pristine film, as the diamond shape practically vanishes. If  $H$  is further reduced, the  $d$  lines move away from the groove, as if they were reopening, reestablishing the diamond-shaped domain, as seen at 25.6 Oe. This analysis demonstrates that MOI is an ideal tool for this study, revealing details of the local flux penetration and current distribution that are hidden in global magnetometry.

The observed  $d$ -line movement is associated with an enhancement of the transport properties in the WL. This is demonstrated in Fig. 2(a). As the  $d$  lines close,  $\alpha$  increases, and  $J$  changes accordingly—streamlines that initially did not

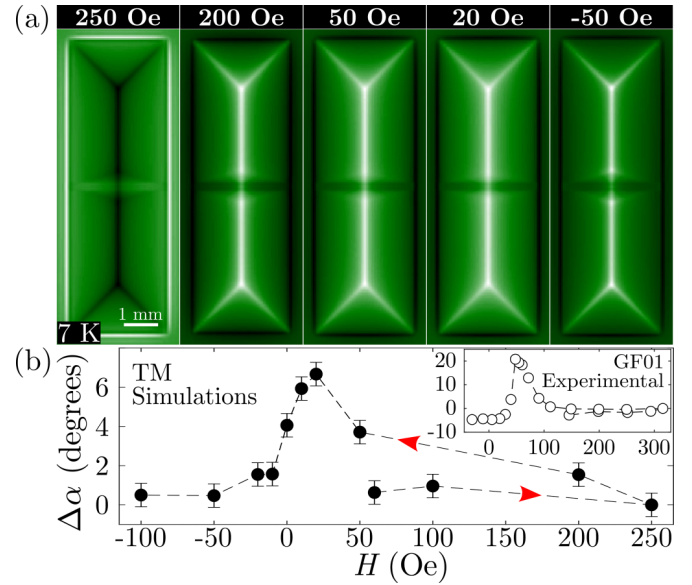


FIG. 4. (a)  $B$  distribution at 7 K captured by TM simulations as  $H$  is reduced from 250 Oe. (b)  $\Delta\alpha(H)$  for the simulated sample. Inset:  $\Delta\alpha(H)$  for GF01.

cross the WL become straighter and have a higher density across the WL. This trend is maximized at 48.0 Oe, when the diamond-shaped domain almost fades out. Thus, after the sample is fully penetrated and  $H$  is reduced to a specific value, the WL behaves as a strong link, allowing currents to flow through it largely unaffected. At 46.0 Oe and as  $H$  is further reduced, the  $d$  lines reappear, reestablishing the WL behavior. As  $J_c$  is proportional to the height of the  $m(H)$  curve [58], this notion explains the observed local peak as an increase in the overall  $J_c$  due to an increase in  $J_c^{\text{WL}}$ .

In Fig. 2(b), we evaluate the magnetic moment of GF01 via MOI as  $m = \sum_y m_l(y) l_{px} = l_{px} \sum_y 2 \int_0^{w/2} x j_y(x) dx$ , where  $m_l(y)$  is  $m$  per unit length at a position  $y$ ,  $l_{px}$  is the image pixel size,  $w$  is the film width,  $j_y = J_y d$  is the sheet current flowing perpendicular to the WL, and  $d$  is the film thickness [59,60]. The results reproduce those in Fig. 1(c). Figure 2 also presents quantitative results obtained along the four color-matched regions in Fig. 1(f). In Fig. 2(c), we average  $m_l$  over the WL (blue) and on a selected portion of the PR (red),

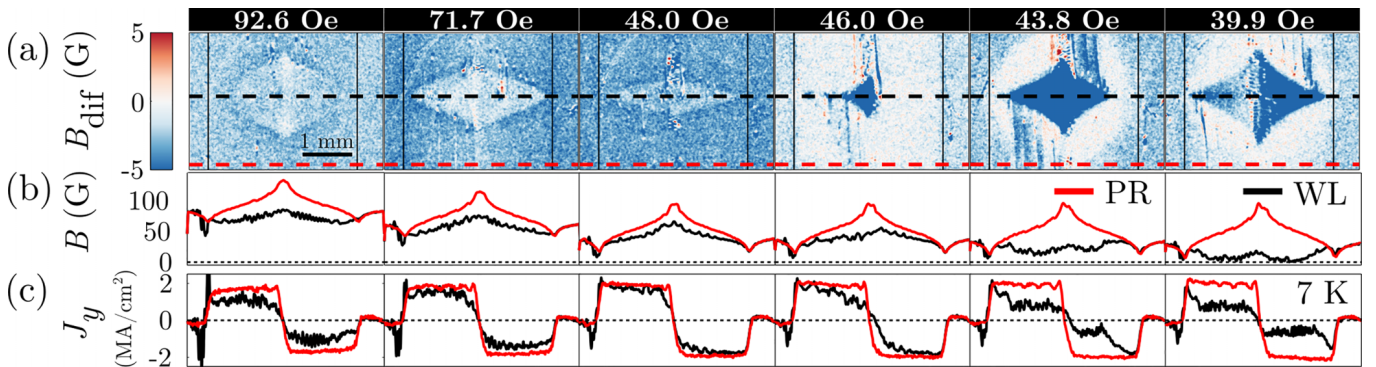


FIG. 3. (a)  $B_{\text{dif}}$  distribution around the region of  $d$ -line movement for GF01 at 7 K at different  $H$ . Thin vertical lines represent the edges of the film. (b)  $B$  and (c)  $J_y$  profiles along the WL and PR, evaluated respectively at the black and red dashed lines in panel (a).



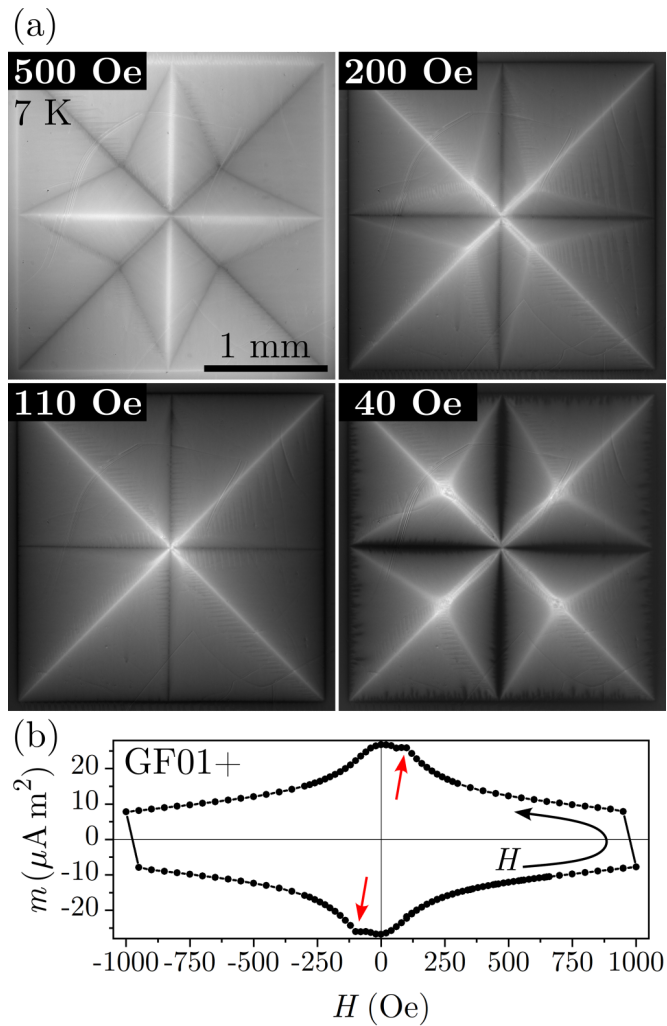


FIG. 5. (a) MOI and (b)  $m(H)$  of GF01+ at 7 K. The MO images are acquired as  $H$  is reduced from 500 Oe, at which the film is fully flux penetrated. Red arrows indicate the local maxima in  $m(H)$ .

confirming that the peak in  $m(H)$  manifests an effect tied to the WL. Moreover, we gauge the flux behavior just outside the sample,  $\Phi_{\text{out}}$ . Figure 2(d) shows that, as  $H$  is reduced,  $\Phi_{\text{out}}$  is everywhere higher just beside the WL (pink) than beside the PR (yellow) for equal areas. However, as the  $d$  lines are closing,  $\Phi_{\text{out}}$  decreases close to the WL while it is unaffected beside the PR, lessening the difference between  $\Phi_{\text{out}}$  along the two regions (green). This indicates that fewer vortices are able to escape the sample through the WL at these fields. When the  $d$  lines reopen below 50 Oe,  $\Phi_{\text{out}}$  is enhanced besides the groove, indicating a large amount of flux is expelled through the edges of the WL. In the ac experiment, if the device is properly field biased, this implies a rectified vortex motion characterized by the directed flux movement along the WL albeit vortices are subjected to a zero-mean excitation [61–65].

Figure 3 locally resolves the behavior of  $B$  and  $J$  for GF01. Figure 3(a) depicts the differential flux density,  $B_{\text{dif}}$ , for GF01. It captures the  $B$  variation due to the variation of  $H$  (kept around  $-2$  Oe) by subtracting the target MO image  $n$  by the one taken at the previous field step, i.e.,  $B_{\text{dif}} = B_n - B_{n-1}$ .

In the first three  $B_{\text{dif}}$  images, we visualize the closing of the  $d$  lines by the shrinking of a brighter diamond-shaped inner region. This indicates that  $B$  decreases less in that region than outside the  $d$  lines. Therefore, flux is pushed toward the WL as the  $d$  lines close. This agrees with the fact that flux is unable to cross  $d$  lines [49]. At 46.0 Oe, a dark-colored region confirms flux is intensely expelled from the WL. At 43.8 Oe, the bright halo centered in the groove reveals that flux is still being pushed away from the inner part of the sample. For 39.9 Oe and further, the flux pushed out of the WL is systematically reduced.

Figure 3(b) shows the evolution of  $B$  along the WL (in black) and the PR (red). From 92.6 to 48.0 Oe, the black profile decreases less and becomes increasingly similar to the red one, indicating that the flux pushed inward by the  $d$ -line movement is partially retained by the WL. This is related to an increased vortex pinning potential in the WL due to its reduced thickness and FIB-induced defects, which act as pinning centers and locally suppress  $T_c$  [3,30]—see Appendix A. The observed relative increase in  $B$  corroborates the increase in  $m_l$  across the WL seen in Fig. 2(c). Starting at 46.0 Oe, trapped flux is vigorously pushed away from the WL and the  $B$  profiles become distinct again. As  $B$  is still positive at 46.0 Oe, the maximum in  $m(H)$  is not related to a net neutral flux in the WL. Here, we argue that the increased vortex pinning in the WL reduces energy dissipation coming from flux line movement, thus increasing  $J_c^{\text{WL}}$  within that specific  $H$  range. A similar behavior exists in HTSC [60,66–71]. The fact that the associated  $d$ -line movement was not previously observed in YBCO bicrystalline films [53,71–73] may be related to the absence of the FIB-added pinning centers and the relatively higher  $H$  for which the peak occurs in HTSC, rendering  $J_c(B)$ -dependent effects less prominent [57].

Figure 3(c) presents an analysis of  $J$  perpendicular to the WL,  $J_y$ . Initially, there is a gradual increase in the current able to cross the WL. At 48.0 Oe,  $J_y$  across the WL closely matches that flowing in the PR—as GF01 behaves almost as a pristine film. This trend is reversed when the  $d$  lines reappear and a sharp decrease in  $J_y$  is observed beginning in the center of the WL. The increased current density, paired with the higher vortex concentration at the center of the WL results in a repulsive force that eventually overcomes the pinning force, thus relieving the magnetic pressure built up in the WL and inducing a strong-to-weak-link transformation. Hence  $J_c$  for a field biased grooved sample subjected to ac fields alternates between maxima and minima in intervals dictated by the drive field frequency. Appendix B depicts the behavior of  $B$  and  $J_y$  at several applied fields, corroborating their relationship to the  $d$ -line movement.

With the experimental input, we now turn to numerical simulations based on the thermomagnetic model, which allow for the comprehension of subtle distinctions in specimen behavior arising from a  $B$ -dependent  $J_c$  [48,74,75]. The simulated Nb sample shares the geometry of GF01, except for the groove width, set to  $45 \mu\text{m}$  to improve computational performance. Notably, the higher density of pinning sites introduced by Ga implantation in the WL is not considered. A reduction of  $\sim 15\%$  in the zero-field  $J_c^{\text{WL}}$  is induced by reducing  $T_c$  in the WL, as experimentally observed—see Appendix A and Ref. [30].

Figure 4 describes the TM results obtained when considering  $j_c = j_c(T, B) = j_{c0}(1 - T/T_c)[B_0/(B + B_0)]$ , with  $B_0 = \mu_0 j_{c0}/\pi$  [76]. Disorder is introduced by lowering  $j_{c0}$  for randomly selected grid points [47]. First,  $H$  is increased up to 250 Oe after ZFC to 7 K. The resulting flux distribution in Fig. 4(a) qualitatively matches that of GF01 in the full penetration state. Then,  $H$  is progressively reduced. At 50 Oe, we notice the shrinking of the diamond-shaped domain, which is maximum at 20 Oe. This is quantitatively corroborated by Fig. 4(b), which depicts  $\Delta\alpha(H) = \alpha(H) - \alpha(H = 250 \text{ Oe})$ . The inset of Fig. 4(b) confirms that the simulations reproduce the  $d$ -line movement observed experimentally. The lesser closure of the  $d$  lines is likely due to the larger width of the simulated groove. Finally, the  $d$  lines reappear, as demonstrated in Fig. 4(a) at  $-50$  Oe. TM simulations at 7 K indicate a lower threshold of  $J_{c0}^{\text{WL}}/J_{c0} \sim 64\%$  for the occurrence of the reported phenomenon. This is higher than the  $\sim 40\%$  ratio for GF01 at 7 K due to the different geometry and the irradiation-induced pinning centers. A lower bound for  $J_{c0}^{\text{WL}}/J_{c0}$  corroborates experimental observations—see Appendix A. Additional simulations, conducted for  $J_c$  independent of  $B$ , did not reproduce the  $d$ -line movement, reinforcing the  $J_c(B)$ -dependency role in the observed phenomenon.

Finally, Fig. 5(a) presents MO results for GF01+. The weak links appear in bright contrast at the image captured at the maximum applied field of 500 Oe. Enveloping the WLs, a set of four quadrilateral domains define a remarkable four-pointed starlike pattern [55]. As the field is reduced to 200 Oe, such a pattern systematically fades out, as the  $d$  lines close around the WLs—see Appendix B. At 110 Oe, the observed flux distribution matches that of a pristine square film [58], as all four WLs simultaneously behave as strong links. This coincides with a local peak in  $m(H)$ , as revealed by Fig. 5(b). Further  $H$  reduction will cause the  $d$  lines to reopen, reestablishing the weak-link behavior and the starlike pattern. Therefore, GF01+ behaves completely analogously to GF01 and provides further evidence of the phenomenon reproducibility while revealing it can be scaled up for samples containing multiple WLs.

#### IV. CONCLUSIONS

In summary, combining MOI and TM simulations, we demonstrate that the presence of local maxima in the magnetization loops of FIB-patterned Nb films is associated with a field induced transformation of the sample behavior from weak-to-strong link. This effect can be tuned by temperature [30] as well as by the amount of defects introduced along the WL. As the transformation is associated with nanoscale interactions between vortices and defects, the phenomenon should also be present in micro- and nanometric devices typically implemented in superconducting electronics. Possible applications can take advantage of the vortex rectification and tunable flux escape along the WL in flux pumps or valves. The overall  $J_c$  modulation can be explored for constant or periodic signal attenuation or amplification in selected circuit components. Additionally, the targeted inclusion of pinning centers along grain boundaries of weak-link-bearing materials may also lead to the improvement of operating conditions

for different superconducting technologies, resulting in effectively higher critical currents for HTSC devices.

#### ACKNOWLEDGMENTS

This work was partially supported by Coordenação de Aperfeiçoamento de Pessoal de Nível Superior, Brazil (CAPES), Finance Code 001, the São Paulo Research Foundation (FAPESP, Grant No. 2021/08781-8), and the National Council for Scientific and Technological Development (CNPq, Grants No. 431974/2018-7, No. 316602/2021-3, and No. 309928/2018-4). C.X. acknowledges the support by the National Natural Science Foundation of China (Grants No. 11972298 and 12011530143). L.J. was supported by the China Scholarship Council. The authors thank the Laboratory of Structural Characterization (LCE/DEMa/UFSCar) for the EDS and AFM measurements. The research was supported by LNNano, Brazilian Nanotechnology National Laboratory (CNPEM/MCTI) during the use of the Device Manufacturing open access facility.

#### APPENDIX A: MORPHOLOGY, STRUCTURE, AND SUPERCONDUCTING PROPERTIES

The Nb samples are deposited by magnetron sputtering on a  $\text{SiO}_2$  substrate, as described in Ref. [30]. The single-WL samples are schematically represented in Fig. 6(a), where the grooved region appears in dark in the center of the film, spanning the whole sample's width. The lower right corner shows a sketch of the weak-link lateral profile, representing the FIB-milled-induced defects arising from Ga implantation as red circles. SRIM simulations [77] indicate Ga ions penetrate less than 30 nm into the Nb film. As described in Refs. [26,27,30], the Ga implantation is an unavoidable consequence of FIB milling, leading to a suppression of the Nb sample superconducting properties.

Figure 6(b) presents atomic-force microscopy (AFM) results for GF01 centered around the WL, confirming the presence of the groove. The AFM measurements were conducted on a Digital Instruments Nanoscope V. The thickness values are presented with respect to the average height of the Nb film, permitting to highlight the groove depth. In Fig. 6(c), a thickness profile is plotted centered along the white dashed line in panel (b). The points are averaged for a  $1 \times 10 \mu\text{m}^2$  area. The profile reveals a maximum groove depth of 4.2 nm for GF01, as well as an 800 nm width at half depth.

Figure 6(d) confirms the Ga implantation inside the WL. This is accomplished by performing an energy dispersive x-ray spectrometry (EDS), conducted using a Philips XL-30 FEG Scanning Electron Microscope. We take EDS spectra of GF02 of both the pristine region (PR) and the WL, which are shown in red and black, respectively. For the PR, EDS reveals characteristic  $K\alpha$  emission peaks for Si (due to the substrate) and Nb. However, when the WL is gauged, an additional emission line due to the presence of Ga is observed.

Figure 6(e) demonstrates the deterioration of the superconducting properties in the WL due to the milling process. It shows the temperature dependency of both in-phase ( $\chi'$ ) and out-of-phase ( $\chi''$ ) ac-susceptibility components for GF01, in black, and the pristine sample, in red. The results were

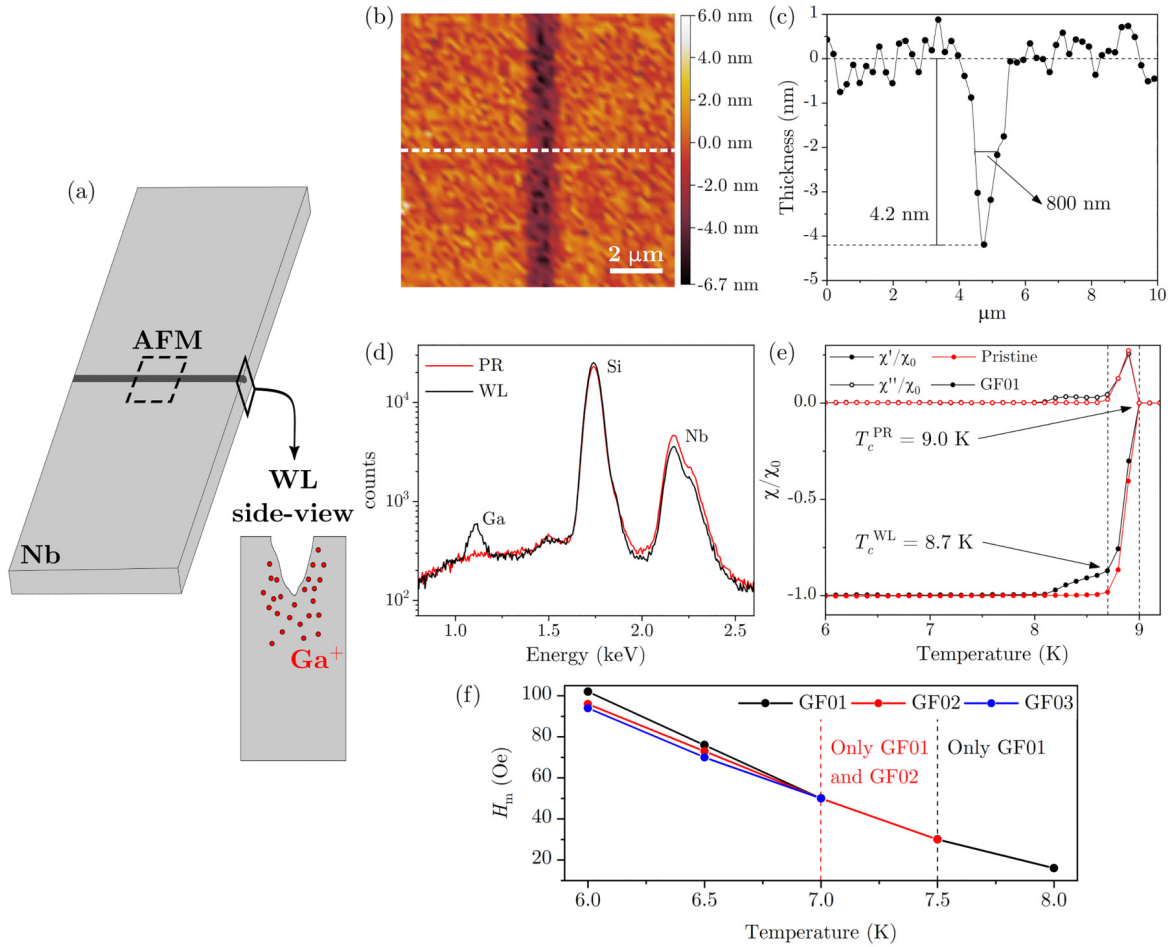


FIG. 6. (a) Schematic representation of the grooved Nb film. In detail, the lateral cross section of the sample highlights the WL profile. Red circles represent the damage caused by Ga implantation. (b) AFM of a  $10 \times 10 \mu\text{m}^2$  area around the central WL of GF01, as represented in (a). The data points are shown in comparison to the film's mean thickness. (c) Thickness profile centered along the dashed white line in (b). (d) EDS spectra of GF02 measured in the PR (in red) and the WL (in black). The results reveal the existence of a Ga  $K\alpha$  emission peak only in the WL. (e) Temperature-dependent ac susceptibility for GF01 and for the pristine sample, highlighting the different superconducting transition temperatures for the PR and the WL. (f) The variation of  $H_m$  as a function of temperature for GF01, GF02, and GF03. From left to right, the dashed lines delimit the temperature range for which the peak is only observed for GF01 and GF02 or only for GF01.

obtained on a SQUID-based Quantum Design MPMS-5S magnetometer and the curves for each sample are normalized by their respective  $\chi'$  Meissner state plateau,  $\chi_0$ . A 100 Hz probe ac-magnetic field with 0.5 Oe amplitude was used in the measurements. The results show a single sharp superconducting transition at  $T_c^{\text{PR}} = 9.0$  K for the pristine sample. However, a two-step transition is observed for GF01, revealing a second transition, related to the WL, at  $T_c^{\text{WL}} = 8.7$  K [30].

Figure 6(f) depicts the variation of the field at which the magnetization peak is observed ( $H_m$ ) as a function of temperature for GF01, GF02, and GF03. The  $H_m$  values are obtained from  $m(H)$  curves measured at different temperatures. It shows that, as temperature increases, the samples exposed to lower FIB doses still present a maximum in  $m(H)$ , whereas those exposed to higher doses do not. This is associated with a reduction of the ratio between the zero-field current able to flow through the WL in comparison to the PR,  $J_{c0}^{\text{WL}}/J_{c0}$ . Since the films patterned with a higher FIB dose present a larger concentration of defects at the WL, they experience a further

reduction of  $J_{c0}^{\text{WL}}$ . Therefore, as the emergence of the magnetization peak depends on  $J_{c0}^{\text{WL}}/J_{c0}$ , GF03 ceases to undergo the weak-to-strong-link transformation at temperatures lower than those corresponding to GF02, which, in turn, does so at lower temperatures than GF01.

## APPENDIX B: MAGNETIC FLUX PENETRATION

Figure 7 shows a snapshot of a supplemental video containing MOI results for GF01 at 47 different applied magnetic fields, both while  $H$  is increased after ZFC to 7 K and while it is decreased from a maximum applied value of 315.6 Oe. The full video is available in the Supplemental Material [78]. Besides the MO images,  $J_y$  and  $B$  profiles are shown for each of the presented  $H$  values. The profiles are evaluated on the PR (in red) and along the WL (in black), as indicated by color-matched arrows beside the MO images. A green profile is also presented and it is obtained by subtracting the  $B$  profile across the WL from that across the PR. Noticeably, there is a scratch on the MO indicator film beside the left side of the groove.

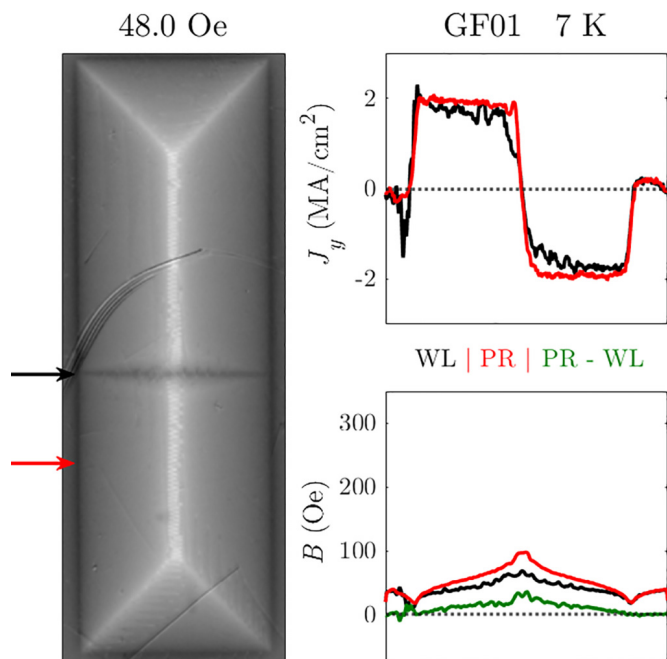


FIG. 7. Snapshot of supplemental video showing the magnetic flux and shielding current behavior in GF01 at 7 K as the applied magnetic field is first increased and then decreased. The black and red profiles highlight the behavior along the WL and the PR, respectively. The green curve shows the difference in  $B$  between the PR and the WL (see Supplemental Material [78]).

This creates rather visual discontinuities on the left side of the black profiles but does not interfere with the interpretation of the behavior inside the WL. The video corroborates the discussion presented in the main text by showing the gradual increase in  $J_y$  across the WL as  $H$  is reduced accompanied by the relative increase in  $B$  in the same region. This happens as

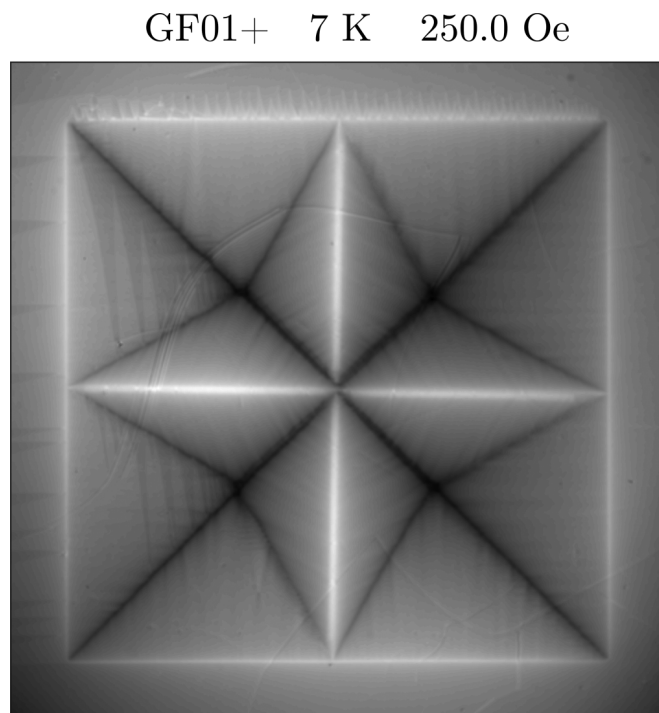


FIG. 8. Snapshot of supplemental video showing the magnetic flux penetration into GF01+ at 7 K as the applied magnetic field is first increased and then decreased (see Supplemental Material [78]).

the central discontinuity lines, visible in the MO images, close toward the groove.

Figure 8 shows a snapshot of a supplemental video depicting flux penetration patterns into sample GF01+ at 7 K after zero-field cooling as  $H$  is increased up to 500 Oe and subsequently decreased down to 0 Oe [78]. The video corroborates the simultaneous  $d$ -line movement along all four weak links as the applied field is reduced, as discussed in the main text.

- [1] K. Harada, O. Kamimura, H. Kasai, T. Matsuda, A. Tonomura, and V. V. Moshchalkov, Direct observation of vortex dynamics in superconducting films with regular arrays of defects, *Science* **274**, 1167 (1996).
- [2] A. V. Silhanek, L. Van Look, S. Raedts, R. Jonckheere, and V. V. Moshchalkov, Guided vortex motion in superconductors with a square antidot array, *Phys. Rev. B* **68**, 214504 (2003).
- [3] O. V. Dobrovolskiy, E. Begun, M. Huth, and V. A. Shklovskij, Electrical transport and pinning properties of Nb thin films patterned with focused ion beam-milled washboard nanostructures, *New J. Phys.* **14**, 113027 (2012).
- [4] G. Shaw, P. Mandal, B. Bag, S. Banerjee, T. Tamegai, and H. Suderow, Properties of nanopatterned pins generated in a superconductor with FIB, *Appl. Surf. Sci.* **258**, 4199 (2012).
- [5] Y. L. Wang, M. L. Latimer, Z. L. Xiao, R. Divan, L. E. Ocola, G. W. Crabtree, and W. K. Kwok, Enhancing the critical current of a superconducting film in a wide range of magnetic fields with a conformal array of nanoscale holes, *Phys. Rev. B* **87**, 220501(R) (2013).
- [6] O. V. Dobrovolskiy, Abrikosov fluxonics in washboard nanolandscapes, *Physica C* **533**, 80 (2017).
- [7] Y. Kalcheim, E. Katzir, F. Zeides, N. Katz, Y. Paltiel, and O. Millo, Dynamic control of the vortex pinning potential in a superconductor using current injection through nanoscale patterns, *Nano Lett.* **17**, 2934 (2017).
- [8] O. V. Dobrovolskiy, V. A. Shklovskij, M. Hanefeld, M. Zörb, L. Köhs, and M. Huth, Pinning effects on flux flow instability in epitaxial Nb thin films, *Supercond. Sci. Technol.* **30**, 085002 (2017).
- [9] F. Colauto, M. Motta, and W. A. Ortiz, Controlling magnetic flux penetration in low- $T_c$  superconducting films and hybrids, *Supercond. Sci. Technol.* **34**, 013002 (2021).
- [10] K. K. Likharev, Superconducting weak links, *Rev. Mod. Phys.* **51**, 101 (1979).
- [11] *Nanoscience and Engineering in Superconductivity*, edited by V. Moshchalkov, R. Woerdenweber, and W. Lang (Springer Berlin, Heidelberg, 2010).
- [12] A. Fornieri, A. M. Whitticar, F. Setiawan, E. Portolés, A. C. Drachmann, A. Keselman, S. Gronin, C. Thomas, T. Wang, R.

- Kallaher, G. C. Gardner, E. Berg, M. J. Manfra, A. Stern, C. M. Marcus, and F. Nichele, Evidence of topological superconductivity in planar Josephson junctions, *Nature (London)* **569**, 89 (2019).
- [13] I. Holzman and Y. Ivry, Superconducting nanowires for single-photon detection: Progress, challenges, and opportunities, *Adv. Quantum Technol.* **2**, 1800058 (2019).
- [14] A. Murphy, D. V. Averin, and A. Bezryadin, Nanoscale superconducting memory based on the kinetic inductance of asymmetric nanowire loops, *New J. Phys.* **19**, 063015 (2017).
- [15] L. Chen, L. Wu, Y. Wang, Y. Pan, D. Zhang, J. Zeng, X. Liu, L. Ma, W. Peng, Y. Wang, J. Ren, and Z. Wang, Miniaturization of the superconducting memory cell via a three-dimensional Nb nano-superconducting quantum interference device, *ACS Nano* **14**, 11002 (2020).
- [16] E. Ilin, X. Song, I. Burkova, A. Silge, Z. Guo, K. Ilin, and A. Bezryadin, Supercurrent-controlled kinetic inductance superconducting memory element, *Appl. Phys. Lett.* **118**, 112603 (2021).
- [17] D. A. D. Chaves, L. Nulens, H. Dausy, B. Raes, D. Yue, W. A. Ortiz, M. Motta, M. J. Van Bael, and J. Van de Vondel, Nanobridge SQUIDs as multilevel memory elements, *Phys. Rev. Appl.* **19**, 034091 (2023).
- [18] Y.-Y. Lyu, J. Jiang, Y.-L. Wang, Z.-L. Xiao, S. Dong, Q.-H. Chen, M. V. Milošević, H. Wang, R. Divan, J. E. Pearson, P. Wu, F. M. Peeters, and W.-K. Kwok, Superconducting diode effect via conformal-mapped nanoholes, *Nat. Commun.* **12**, 2703 (2021).
- [19] T. Golod and V. M. Krasnov, Demonstration of a superconducting diode-with-memory, operational at zero magnetic field with switchable nonreciprocity, *Nat. Commun.* **13**, 3658 (2022).
- [20] E. Strambini, A. Iorio, O. Durante, R. Citro, C. Sanz-Fernández, C. Guarcello, I. V. Tokatly, A. Braggio, M. Rocci, N. Ligato, V. Zannier, L. Sorba, F. S. Bergeret, and F. Giazotto, A Josephson phase battery, *Nat. Nanotechnol.* **15**, 656 (2020).
- [21] T. Yamashita, S. Kim, H. Kato, W. Qiu, K. Semba, A. Fujimaki, and H. Terai,  $\pi$  phase shifter based on NbN-based ferromagnetic Josephson junction on a silicon substrate, *Sci. Rep.* **10**, 1 (2020).
- [22] T. Golod, R. A. Hovhannisyanyan, O. M. Kapran, V. V. Dremov, V. S. Stolyarov, and V. M. Krasnov, Reconfigurable Josephson phase shifter, *Nano Lett.* **21**, 5240 (2021).
- [23] C. A. Volkert and A. M. Minor, Focused ion beam microscopy and micromachining, *MRS Bull.* **32**, 389 (2007).
- [24] M. Wyss, K. Bagani, D. Jetter, E. Marchiori, A. Vervelaki, B. Gross, J. Ridderbos, S. Gliga, C. Schönenberger, and M. Poggio, Magnetic, thermal, and topographic imaging with a nanometer-scale SQUID-on-lever scanning probe, *Phys. Rev. Appl.* **17**, 034002 (2022).
- [25] F. Sigloch, S. Sangiao, P. Orús, and J. M. de Teresa, Direct-write of tungsten-carbide nanoSQUIDs based on focused ion beam induced deposition, *Nanoscale Adv.* **4**, 4628 (2022).
- [26] A. M. Datesman, J. C. Schultz, T. W. Cecil, C. M. Lyons, and A. W. Lichtenberger, Gallium ion implantation into niobium thin films using a focused-ion beam, *IEEE Trans. Appl. Supercond.* **15**, 3524 (2005).
- [27] N. De Leo, M. Fretto, V. Lacquaniti, C. Cassiago, L. D'Ortenzi, L. Boarino, and S. Maggi, Thickness modulated niobium nanoconstrictions by focused ion beam and anodization, *IEEE Trans. Appl. Supercond.* **26**, 1 (2016).
- [28] M. Singh, R. Chaujar, S. Husale, S. Grover, A. P. Shah, M. M. Deshmukh, A. Gupta, V. N. Singh, V. N. Ojha, D. K. Aswal, and R. K. Rakshit, Influence of fabrication processes on transport properties of superconducting niobium nitride nanowires, *Curr. Sci.* **114**, 1443 (2018).
- [29] B. Aichner, B. Müller, M. Karrer, V. R. Misko, F. Limberger, K. L. Mletschnig, M. Dosmailov, J. D. Pedarnig, F. Nori, R. Kleiner, D. Koelle, and W. Lang, Ultradense tailored vortex pinning arrays in superconducting  $\text{YBa}_2\text{Cu}_3\text{O}_{7-\delta}$  thin films created by focused He ion beam irradiation for fluxonics applications, *ACS Appl. Nano Mater.* **2**, 5108 (2019).
- [30] M. I. Valerio-Cuadros, D. A. D. Chaves, F. Colauto, A. A. M. Oliveira, A. M. H. Andrade, T. H. Johansen, W. A. Ortiz, and M. Motta, Superconducting properties and electron scattering mechanisms in a Nb film with a single weak-link excavated by focused ion beam, *Materials* **14**, 7274 (2021).
- [31] D. Larbalestier, A. Gurevich, D. M. Feldmann, and A. Polyanskii, High- $T_c$  superconducting materials for electric power applications, *Nature (London)* **414**, 368 (2001).
- [32] S. R. Foltyn, L. Civale, J. L. MacManus-Driscoll, Q. X. Jia, B. Maiorov, H. Wang, and M. Maley, Materials science challenges for high-temperature superconducting wire, *Nat. Mater.* **6**, 631 (2007).
- [33] H. Hilgenkamp and J. Mannhart, Grain boundaries in high- $T_c$  superconductors, *Rev. Mod. Phys.* **74**, 485 (2002).
- [34] S. Graser, P. J. Hirschfeld, T. Kopp, R. Gutser, B. M. Andersen, and J. Mannhart, How grain boundaries limit supercurrents in high-temperature superconductors, *Nat. Phys.* **6**, 609 (2010).
- [35] R. P. Reade, P. Berdahl, R. E. Russo, and S. M. Garrison, Laser deposition of biaxially textured yttrium-stabilized zirconia buffer layers on polycrystalline metallic alloys for high critical current  $\text{YBaCuO}$  thin films, *Appl. Phys. Lett.* **61**, 2231 (1992).
- [36] Y. Iijima, K. Onabe, N. Futaki, N. Tanabe, N. Sadakata, O. Kohno, and Y. Ikeno, Structural and transport properties of biaxially aligned  $\text{YBa}_2\text{Cu}_3\text{O}_{7-x}$  films on polycrystalline Nibased alloy with ionbeammodified buffer layers, *J. Appl. Phys.* **74**, 1905 (1993).
- [37] X. D. Wu, S. R. Foltyn, P. N. Arendt, W. R. Blumenthal, I. H. Campbell, J. D. Cotton, J. Y. Coulter, W. L. Hults, M. P. Maley, H. F. Safar, and J. L. Smith, Properties of  $\text{YBa}_2\text{Cu}_3\text{O}_{7-\delta}$  thick films on flexible buffered metallic substrates, *Appl. Phys. Lett.* **67**, 2397 (1995).
- [38] A. Goyal, D. P. Norton, J. D. Budai, M. Paranthaman, E. D. Specht, D. M. Kroeger, D. K. Christen, Q. He, B. Saffian, F. A. List, D. F. Lee, P. M. Martin, C. E. Klabunde, E. Hartfield, and V. K. Sikka, High critical current density superconducting tapes by epitaxial deposition of  $\text{YBa}_2\text{Cu}_3\text{O}_x$  thick films on biaxially textured metals, *Appl. Phys. Lett.* **69**, 1795 (1996).
- [39] J. Díez-Sierra, P. López-Domínguez, H. Rijckaert, M. Rikel, J. Hänisch, M. Z. Khan, M. Falter, J. Bennowitz, H. Huhtinen, S. Schäfer, R. Müller, S. A. Schunk, P. Paturi, M. Bäcker, K. D. Buysse, and I. V. Driessche, High critical current density and enhanced pinning in superconducting films of  $\text{YBa}_2\text{Cu}_3\text{O}_{7-\delta}$  nanocomposites with embedded  $\text{BaZrO}_3$ ,  $\text{BaHfO}_3$ ,  $\text{BaTiO}_3$ , and  $\text{SrZrO}_3$  nanocrystals, *ACS Appl. Nano Mater.* **3**, 5542 (2020).
- [40] I. Ahmad, S. Sarangi, and P. Sarun, Enhanced critical current density and flux pinning of anthracene doped magnesium diboride superconductor, *J. Alloys Compd.* **884**, 160999 (2021).
- [41] M. Rocci, D. Suri, A. Kamra, G. Vilela, Y. Takamura, N. M. Nemes, J. L. Martinez, M. G. Hernandez, and J. S. Moodera,

- Large enhancement of critical current in superconducting devices by gate voltage, *Nano Lett.* **21**, 216 (2021).
- [42] A. M. Caffer, D. A. D. Chaves, A. L. Pessoa, C. L. Carvalho, W. A. Ortiz, R. Zadorosny, and M. Motta, Optimum heat treatment to enhance the weak-link response of Y123 nanowires prepared by solution blow spinning, *Supercond. Sci. Technol.* **34**, 025009 (2021).
- [43] R. Algarni, M. A. Almessiere, Y. Slimani, E. Hannachi, and F. B. Azzouz, Enhanced critical current density and flux pinning traits with Dy<sub>2</sub>O<sub>3</sub> nanoparticles added to YBa<sub>2</sub>Cu<sub>3</sub>O<sub>7- $\delta$</sub>  superconductor, *J. Alloys Compd.* **852**, 157019 (2021).
- [44] D. A. D. Chaves, I. M. de Araújo, D. Carmo, F. Colauto, A. A. M. Oliveira, A. M. H. Andrade, T. H. Johansen, A. V. Silhanek, W. A. Ortiz, and M. Motta, Enhancing the effective critical current density in a Nb superconducting thin film by cooling in an inhomogeneous magnetic field, *Appl. Phys. Lett.* **119**, 022602 (2021).
- [45] G. Shaw, J. Brisbois, L. B. G. L. Pinheiro, J. Müller, S. Blanco Alvarez, T. Devillers, N. M. Dempsey, J. E. Scheerder, J. Van de Vondel, S. Melinte, P. Vanderbemden, M. Motta, W. A. Ortiz, K. Hasselbach, R. B. G. Kramer, and A. V. Silhanek, Quantitative magneto-optical investigation of superconductor/ferromagnet hybrid structures, *Rev. Sci. Instrum.* **89**, 023705 (2018).
- [46] A. Y. Meltzer, E. Levin, and E. Zeldov, Direct reconstruction of two-dimensional currents in thin films from magnetic-field measurements, *Phys. Rev. Appl.* **8**, 064030 (2017).
- [47] J. I. Vestgård, D. V. Shantsev, Y. M. Galperin, and T. H. Johansen, Dynamics and morphology of dendritic flux avalanches in superconducting films, *Phys. Rev. B* **84**, 054537 (2011).
- [48] L. Jiang, C. Xue, L. Burger, B. Vanderheyden, A. V. Silhanek, and Y.-H. Zhou, Selective triggering of magnetic flux avalanches by an edge indentation, *Phys. Rev. B* **101**, 224505 (2020).
- [49] T. Schuster, M. V. Indenbom, M. R. Koblishka, H. Kuhn, and H. Kronmüller, Observation of current-discontinuity lines in type-II superconductors, *Phys. Rev. B* **49**, 3443 (1994).
- [50] T. Schuster, H. Kuhn, and M. V. Indenbom, Discontinuity lines in rectangular superconductors with intrinsic and extrinsic anisotropies, *Phys. Rev. B* **52**, 15621 (1995).
- [51] R. G. Mints and A. L. Rakhmanov, Critical state stability in type-II superconductors and superconducting-normal-metal composites, *Rev. Mod. Phys.* **53**, 551 (1981).
- [52] G. Blatter, M. V. Feigel'man, V. B. Geshkenbein, A. I. Larkin, and V. M. Vinokur, Vortices in high-temperature superconductors, *Rev. Mod. Phys.* **66**, 1125 (1994).
- [53] A. A. Polyanskii, A. Gurevich, A. E. Pashitski, N. F. Heinig, R. D. Redwing, J. E. Nordman, and D. C. Larbalestier, Magneto-optical study of flux penetration and critical current densities in [001] tilt YBa<sub>2</sub>Cu<sub>3</sub>O<sub>7- $\delta$</sub>  thin-film bicrystals, *Phys. Rev. B* **53**, 8687 (1996).
- [54] T. H. Johansen, F. Colauto, A. M. H. de Andrade, A. A. M. Oliveira, and W. A. Ortiz, Transparency of planar interfaces in superconductors: a critical-state analysis, *IEEE Trans. Appl. Supercond.* **29**, 1 (2019).
- [55] F. Colauto, D. Carmo, A. M. H. Andrade, A. A. M. Oliveira, W. A. Ortiz, Y. M. Galperin, and T. H. Johansen, Measurement of critical current flow and connectivity in systems of joined square superconducting plates, *Physica C* **589**, 1353931 (2021).
- [56] Y. B. Kim, C. F. Hempstead, and A. R. Strnad, Magnetization and critical supercurrents, *Phys. Rev.* **129**, 528 (1963).
- [57] D. V. Shantsev, Y. M. Galperin, and T. H. Johansen, Thin superconducting disk with field-dependent critical current: Magnetization and ac susceptibilities, *Phys. Rev. B* **61**, 9699 (2000).
- [58] T. H. Johansen and H. Bratsberg, Critical state magnetization of type II superconductors in rectangular slab and cylinder geometries, *J. Appl. Phys.* **77**, 3945 (1995).
- [59] E. H. Brandt and M. Indenbom, Type-II-superconductor strip with current in a perpendicular magnetic field, *Phys. Rev. B* **48**, 12893 (1993).
- [60] D. V. Shantsev, M. R. Koblishka, Y. M. Galperin, T. H. Johansen, L. Püst, and M. Jirsa, Central peak position in magnetization loops of high- $T_c$  superconductors, *Phys. Rev. Lett.* **82**, 2947 (1999).
- [61] J. F. Wambaugh, C. Reichhardt, C. J. Olson, F. Marchesoni, and F. Nori, Superconducting fluxon pumps and lenses, *Phys. Rev. Lett.* **83**, 5106 (1999).
- [62] C. J. Olson, C. Reichhardt, B. Jankó, and F. Nori, Collective interaction-driven ratchet for transporting flux quanta, *Phys. Rev. Lett.* **87**, 177002 (2001).
- [63] Y. Togawa, K. Harada, T. Akashi, H. Kasai, T. Matsuda, F. Nori, A. Maeda, and A. Tonomura, Direct observation of rectified motion of vortices in a niobium superconductor, *Phys. Rev. Lett.* **95**, 087002 (2005).
- [64] C. C. de Souza Silva, J. Van de Vondel, B. Y. Zhu, M. Morelle, and V. V. Moshchalkov, Vortex ratchet effects in films with a periodic array of antidots, *Phys. Rev. B* **73**, 014507 (2006).
- [65] C. C. de Souza Silva, J. Van de Vondel, M. Morelle, and V. V. Moshchalkov, Controlled multiple reversals of a ratchet effect, *Nature (London)* **440**, 651 (2006).
- [66] J. E. Evetts and B. A. Glowacki, Relation of critical current irreversibility to trapped flux and microstructure in polycrystalline YBa<sub>2</sub>Cu<sub>3</sub>O<sub>7</sub>, *Cryogenics* **28**, 641 (1988).
- [67] D. Dimos, P. Chaudhari, and J. Mannhart, Superconducting transport properties of grain boundaries in YBa<sub>2</sub>Cu<sub>3</sub>O<sub>7</sub> bicrystals, *Phys. Rev. B* **41**, 4038 (1990).
- [68] M. J. Hogg, F. Kahlmann, Z. H. Barber, and J. E. Evetts, Angular hysteresis in the critical current of YBa<sub>2</sub>Cu<sub>3</sub>O<sub>7</sub> low-angle grain boundaries, *Supercond. Sci. Technol.* **14**, 647 (2001).
- [69] J. R. Thompson, H. J. Kim, C. Cantoni, D. K. Christen, R. Feenstra, and D. T. Verebelyi, Self-organized current transport through low-angle grain boundaries in YBa<sub>2</sub>Cu<sub>3</sub>O<sub>7- $\delta$</sub>  thin films studied magnetometrically, *Phys. Rev. B* **69**, 104509 (2004).
- [70] A. Palau, T. Puig, X. Obradors, E. Pardo, C. Navau, A. Sanchez, A. Usoskin, H. C. Freyhardt, L. Fernández, B. Holzapfel, and R. Feenstra, Simultaneous inductive determination of grain and intergrain critical current densities of YBa<sub>2</sub>Cu<sub>3</sub>O<sub>7- $x$</sub>  coated conductors, *Appl. Phys. Lett.* **84**, 230 (2004).
- [71] A. Palau, T. Puig, X. Obradors, and C. Jooss, Simultaneous determination of grain and grain-boundary critical currents in YBa<sub>2</sub>Cu<sub>3</sub>O<sub>7</sub>-coated conductors by magnetic measurements, *Phys. Rev. B* **75**, 054517 (2007).
- [72] K. Guth, V. Born, and C. Jooss, Inhomogeneous current distribution in wide high-temperature superconducting small-angle grain boundaries, *Eur. Phys. J. B* **42**, 239 (2004).

- [73] V. Born, K. Guth, H. C. Freyhardt, and C. Jooss, Self-enhanced flux penetration into small angle grain boundaries in YBCO thin films, *Supercond. Sci. Technol.* **17**, 380 (2004).
- [74] Z. Jing, H. Yong, and Y. Zhou, Influences of non-uniformities and anisotropies on the flux avalanche behaviors of type-II superconducting films, *Supercond. Sci. Technol.* **29**, 105001 (2016).
- [75] Z. Jing, H. Yong, and Y. Zhou, Numerical simulation on the flux avalanche behaviors of microstructured superconducting thin films, *J. Appl. Phys.* **121**, 023902 (2017).
- [76] Y. B. Kim, C. F. Hempstead, and A. R. Strnad, Critical persistent currents in hard superconductors, *Phys. Rev. Lett.* **9**, 306 (1962).
- [77] J. F. Ziegler and J. P. Biersack, The stopping and range of ions in matter, in *Treatise on Heavy-Ion Science: Volume 6: Astrophysics, Chemistry, and Condensed Matter*, edited by D. A. Bromley (Springer US, Boston, MA, 1985), pp. 93–129.
- [78] See Supplemental Material at <http://link.aps.org/supplemental/10.1103/PhysRevB.108.214502> to watch the full videos capturing the flux penetration into the samples.

## Chapter 5

# A magnetic-field-assisted superconducting multilevel memory

In this Chapter, I present an investigation of the properties of a SQUID with Josephson junctions consisting of punctual and elongated constrictions of the superconducting material.<sup>21</sup> The appeal of such systems is that, by tuning the geometrical parameters of nanobridge constrictions, it is possible to alter the device's response to magnetic fields, allowing access to multiple energy states under a single applied field. In the results published on *Physical Review Applied* [148]<sup>22</sup>, we demonstrate how such a fact can be explored to obtain a multilevel memory element with a stochastic field-assisted writing protocol. The probabilistic nature of this writing scheme is shared with similar binary memories but is unwanted for realistic applications of the devices. By understanding the relationship between the SQUID's energy, magnetic fields, and bias currents, we reveal a phase-slip-based state-switching mechanism that may prove to be a path toward a deterministic writing protocol for phase-slip memory elements.

---

<sup>21</sup>This work is a result of the six-month period I spent at KU Leuven under the supervision of Prof. Joris Van de Vondel during my international internship.

<sup>22</sup>Copyright © 2023 by American Physical Society. All rights reserved.



## Nanobridge SQUIDs as Multilevel Memory Elements

Davi A.D. Chaves<sup>1,2,\*</sup> Lukas Nulens<sup>1</sup>, Heleen Dausy<sup>2</sup>, Bart Raes<sup>2</sup>, Donghua Yue<sup>2</sup>,  
Wilson A. Ortiz<sup>1</sup>, Maycon Motta<sup>1</sup>, Margriet J. Van Bael<sup>2</sup> and Joris Van de Vondel<sup>2,†</sup>

<sup>1</sup>*Departamento de Física, Universidade Federal de São Carlos, São Carlos SP 13565-905, Brazil*

<sup>2</sup>*Quantum Solid-State Physics, Department of Physics and Astronomy, KU Leuven, Celestijnenlaan 200D, Leuven B-3001, Belgium*

 (Received 15 November 2022; revised 1 February 2023; accepted 3 February 2023; published 28 March 2023)

With the development of alternative computing schemes working at cryogenic temperatures, superconducting memory elements have gained interest. In this context, superconducting quantum interference devices (SQUIDs) are promising candidates, as they may trap different discrete amounts of magnetic flux. We demonstrate that a field-assisted writing scheme allows such a device to operate as a multilevel memory by the readout of eight distinct vorticity states at zero magnetic field. We present an alternative mechanism based on single phase slips, which allows the vorticity state to be switched while preserving superconductivity. This mechanism provides a possibly deterministic channel for flux control in SQUID-based memories, under the condition that the field-dependent energy of different vorticity states are nearby.

DOI: [10.1103/PhysRevApplied.19.034091](https://doi.org/10.1103/PhysRevApplied.19.034091)

### I. INTRODUCTION

Multilevel memory systems are technologically appealing, for instance, due to an increase in storage density [1–3]. In recent years, alternative nonsemiconducting materials were proposed as nonvolatile multilevel memories in photonic [4] and antiferromagnetic [5] systems. In superconductors, a yTron current combiner can be used for nondestructive current readout and is capable of differentiating between discrete magnetic flux values trapped in superconducting loops [6], finding applications in proposed binary [7,8] and multilevel [9] memory elements.

Superconducting quantum interference devices (SQUIDs) are widely used as powerful magnetometers and are a driving force in the development of quantum technology [10–14]. In a conventional SQUID, superconductor-insulator-superconductor junctions present a sinusoidal current-phase relationship (C $\Phi$ R) leading to a periodic single-valued dependence between the device critical current  $I_c$  and the applied magnetic field  $B$ . However, if at least one of the junctions is an elongated constriction, such as a nanobridge or a nanowire, the C $\Phi$ R of the junction becomes linear [15,16]. As a result, the  $I_c(B)$  oscillations become linear as well and the four line segments of  $I_c(B)$ , two in the positive and two in the negative current side, define a so-called vorticity diamond [17,18].

Additionally, the superconducting phase across such elongated constrictions can exceed  $2\pi$  [18]. As such, different solutions exist at one magnetic field value (overlap of the vorticity diamonds), each corresponding with a different winding number,  $n_v$ , of the superconducting phase across the SQUID. Moreover, each vorticity state is characterized by a particular energy and critical-current value. Therefore, a critical-current measurement is a reliable tool to distinguish between different vorticity states. Finally, a single or series of topological fluctuations will trigger a transition to a different vorticity state or to the normal state by locally suppressing the order parameter, causing the phase across that given region to change by an integer multiple of  $2\pi$  [19–23]. These events are known as phase slips.

The SQUID vorticity may be set to a predetermined value by the establishment of proper writing protocols [24–26]. This implies that information can be stored in the SQUID's different vorticity states. Indeed, flux-based qubits and memory elements relying on phase-slip physics have already been proposed [20,26–30]. In this context, an applied magnetic field affects the SQUID energy and is a natural choice of control parameter in a flux-based memory. By providing a straightforward manner of changing the trapped flux inside a superconducting ring, it allows changing vorticities via phase slips. Recently, the role played by the field-dependent SQUID energy in the phase-slip phenomena has gained attention. It was demonstrated that applied transport currents flowing in SQUIDs subjected to constant magnetic fields can also induce a transition between different vorticity states [31]. This fact

\*davi@df.ufscar.br

†joris.vandevondel@kuleuven.be

has been explored in proposed zero-field memory elements [26,29], in which the key ingredient is the creation of an asymmetry in the superconducting properties of the SQUID junctions. For a fully superconducting device, we previously demonstrated that the kinetic induction of the junctions may be tuned via nanofabrication, allowing control over the  $I_c(B)$  characteristics of the device [18].

In this paper, we report on the feasibility of SQUIDs containing nanobridges as multilevel memory elements. We demonstrate that by defining a field-assisted writing protocol, a large number of vorticity states can be accessed and then read at zero applied field, effectively creating an eight-level memory system. However, writing to a specific state relies on a probabilistic process that requires the vorticity to be frozen in a determined state as the device transitions from the normal to the superconducting state. This process is heavily influenced by the total SQUID energy, an ingredient overlooked in previous studies. Using this information, we demonstrate that at applied fields for which adjacent vorticity states have equal energy, there is a very high probability of changing vorticity via single phase slips. By not triggering an unwanted transition out of the superconducting state, this mechanism constitutes an alternative and possibly deterministic channel for flux control.

## II. EXPERIMENTAL DETAILS

The samples investigated in this work are asymmetric Au-capped  $\text{Mo}_{78}\text{Ge}_{22}$  nanoSQUIDs comprised of one Dayem bridge (DB) and one 40-nm-wide nanobridge (NB) of lengths varying from 100 to 400 nm. Figure 1(a) shows the SEM image of a prototypical device. To illustrate our discussion, we report on three selected samples, labeled devices 250, 400a, and 400b according to the nominal length of the nanobridge. Devices 400a and 400b share the same geometry. By changing the NB length, we effectively control the superconducting properties of the junctions [18]. The devices are patterned using standard e-beam lithography. A 22-nm-thick  $\text{Mo}_{78}\text{Ge}_{22}$  layer is deposited in a high-vacuum pulsed-laser deposition chamber and the resulting structures are capped with a 3-nm-thick gold layer to prevent oxidation. Critical-current values were extracted from standard  $VI$  measurements using the four-point probe method, as shown schematically in Fig. 1(a). During experiments, samples are kept in an Oxford Instruments Heliox  $^3\text{He}$  cryostat at a base temperature of 300 mK. A room-temperature  $\pi$  filter with a cutoff frequency of 1 MHz and a Stanford Research Systems SR560 low-noise preamplifier are used in the measurements.

## III. FIELD-ASSISTED WRITING: THE SQUID AS A MULTILEVEL MEMORY ELEMENT

Initial  $I_c(B)$  characterizations for device 400a are performed as presented in Fig. 1(b). These measurements,

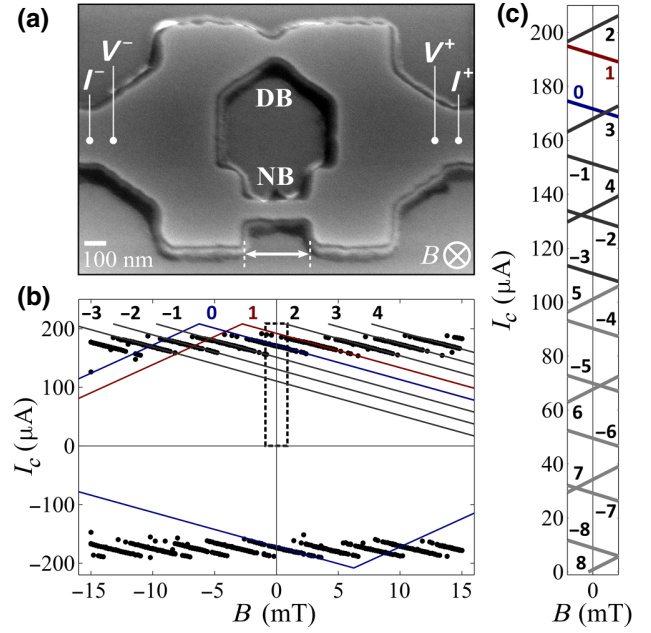


FIG. 1. (a) SEM image of a representative asymmetric  $\text{Mo}_{78}\text{Ge}_{22}/\text{Au}$  SQUID with nominal nanobridge length of 300 nm and width of 80 nm. (b) Characteristic  $I_c(B)$  distribution for device 400a at 300 mK. The points are gathered during three different sweeps for each magnetic field value and for each current direction. Numbered lines are fits of the vorticity diamond branches—the left-side branch is shown only for  $n_v = 0$  and 1 for simplicity. (c) The vorticity diamonds for  $-8 \leq n_v \leq 8$  in the region around 0 mT defined by the dashed rectangle in (b).

collected in three independent runs, allow the identification of different vorticity states based on their corresponding critical-current values. The fit of  $I_c(B)$  is performed following Eq. (A1) and is represented by the numbered lines for different  $n_v$  states in Fig. 1(b) [32]. As defined in Appendix A, the results for device 400a reveal values of  $\Delta B = 3.5 \pm 0.1$  mT,  $I_c^{NB} = 101.5 \pm 0.3$   $\mu\text{A}$ ,  $I_c^{DB} = 106.7 \pm 0.6$   $\mu\text{A}$ ,  $\varphi_c^{NB} = 31.3 \pm 0.4$  rad,  $\varphi_c^{DB} = 20.1 \pm 0.6$  rad,  $L_k^{NB} = 102 \pm 1$  pH, and  $L_k^{DB} = 62 \pm 2$  pH, indicating a significant difference in the properties of the junctions.

These parameters allow us to trace the complete vorticity diamonds for device 400a, extrapolating the regions in the  $I_c(B)$  distribution where critical-current measurements of a specific state are favored. For simplicity, Fig. 1(b) shows only the four diamond branches for  $n_v = 0$ . The choice for a very long nanobridge is based on the knowledge that such a constriction would present a large critical phase and kinetic inductance [18]. As a consequence, a large number of states is expected to be found at a given applied field. Figure 1(c) highlights the region delimited by the dashed rectangle in (b) showing the vorticity diamonds for  $-8 \leq n_v \leq 8$  around 0 mT. We observe that, although our initial experimental data reveals only two states at zero

field, 17 total vorticities are expected to exist on the positive current side of the  $I_c(B)$  distribution, supporting our design choices. To explore this rich landscape two things are paramount: the ability to write, i.e., select, the device vorticity state  $n_v$ ; and the possibility to perform a readout of that state in a determined field value.

The acquired  $I_c(B)$  information can be used to implement a writing (or preparation) protocol that allows one to actively choose the device vorticity state [17,31,33]. To illustrate this, consider Fig. 2(a). It shows the critical current obtained for device 400a after performing 1500  $I_c$  measurements at zero magnetic field. Comparing the results with the  $I_c(B)$  distribution of Fig. 1(b) we can identify only  $I_c(0)$  values representing vorticity states  $n_v = 1$  ( $I_{c,1} \sim 192 \mu\text{A}$ , with a probability of 11%) and  $n_v = 0$  ( $I_{c,0} \sim 172 \mu\text{A}$ , 89%). These probabilities are dictated by the stochastic freeze-in process that determines the SQUID vorticity after entering the superconducting state at zero field. Notice that the highest  $I_c$  state,  $n_v = 2$ , is never observed. This is associated to the fact that, for sufficiently asymmetric SQUIDs [18,26], the highest  $I_c$  state is not energetically favored when entering the superconducting state at zero magnetic field, as it presents a higher total energy than  $n_v = 0$ —see Appendix B. Figure 2(b) then shows the  $I_c(B)$  distribution around the positive peaks of  $n_v = 0$  and 1, highlighting their zero-field critical currents,  $I_{c,0}$  and  $I_{c,1}$ . Figure 2(c) shows how a bias current  $I^*$  may be used to gauge the SQUID vorticity. If  $I^* < I_{c,0}$ , as represented by the blue region, it is not possible to distinguish between  $n_v = 0$  and  $n_v = 1$ , as both are possible at such bias current and the device will remain in the superconducting state regardless. However, if  $I_{c,0} < I^* < I_{c,1}$  the device will remain superconducting if it is found in  $n_v = 1$ , but will transition to the normal state if it was previously in  $n_v = 0$ . For the latter case, if the current is then reduced to zero, re-establishing superconductivity, the resulting vorticity state is dictated by the stochastic process with probabilities revealed by Fig. 2(a). Therefore, the protocol to write device 400a in  $n_v = 1$  consists of looping the current between zero and  $I_{c,0} < I^* < I_{c,1}$  until the voltage  $V_S$  across the device reads zero at  $I^*$ , i.e., it is in the superconducting state. The same principle is used in combination with a bias magnetic field,  $B^*$ , to successfully prepare the device in different states [31].

The use of our devices as memory elements requires the ability to reliably read different prepared states at the same applied magnetic field. To illustrate this, we prepare device 400a in different vorticity states using the coordinates presented in Table I. By first reducing the bias current and then the bias field to zero, thus never leaving the constraints of the vorticity diamond, we are able to preserve the prepared states at zero magnetic field. Figure 2(d) reveals that the readout is successful at 0 mT for  $-3 \leq n_v \leq 4$ . It shows eight different histograms, each containing 100  $I_c$  measurements after preparing the device in the

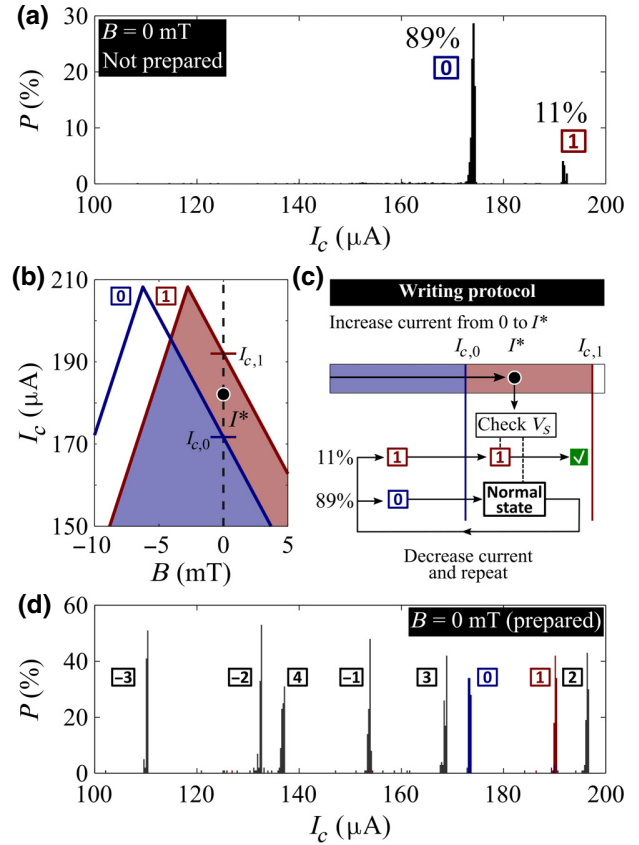


FIG. 2. (a) Critical-current distribution for device 400a after 1500 measurements at zero magnetic field when the vorticity state is frozen in during a cool down from  $+220 \mu\text{A}$ , i.e., without preparing the device in any specific state. (b) Detail of the  $I_c(B)$  distribution showing the vorticity diamond fit for  $n_v = 0$ , blue solid line, and  $n_v = 1$ , red solid line. The value of  $I^*$  is chosen such that  $I_{c,0} < I^* < I_{c,1}$ . (c) Schematic representation of the writing protocol for vorticity state  $n_v = 1$ . Repeatedly applying a current between 0 and  $I^*$  will prepare the system in  $n_v = 1$ . To gauge if the preparation is successful, the voltage  $V_S$  across the device is checked with the current set at  $I^*$ . If  $V_S$  reveals the SQUID is in the normal state, current should be reduced to zero, restoring the superconducting state, and the procedure repeated. If  $V_S = 0$ , then the SQUID is in state  $n_v = 1$  and the preparation is successful. (d)  $I_c$  distributions at zero magnetic field after preparing the device in different vorticity state. All measurements are performed at 300 mK.

corresponding state before each current sweep. The observed critical currents are as low as  $I_{c,-3} \sim 112 \mu\text{A}$  and as high as  $I_{c,2} \sim 198 \mu\text{A}$ —a variation of over 76% and an enhancement of approximately 14.8% for  $I_{c,2}$  in comparison with  $I_{c,0}$ . The measurements in Fig. 2(d) show close agreement with fits of the vorticity diamonds at zero field presented in Fig. 1(c). State  $n_v = 5$ , on its turn, could not be read at zero field, as the same 100 measurements yielded  $I_c$  readings representing states  $n_v = -3, -2, \text{ and } -1$ . This fact is related to Joule heating. For the previous eight

TABLE I. Bias current ( $I^*$ ) and magnetic field ( $B^*$ ) used in the field-assisted preparation protocol for device 400a.

$n_v$	-3	-2	-1	0	1	2	3	4	5
$B^*$ (mT)	-13	-10	-6.5	-3.7	0	3.7	6.5	10	13.5
$I^*$ ( $\mu$ A)	178	178	178	180	180	183	183	183	183

states, with higher  $I_c$ , as the current is swept across the diamond edge, the heat dissipated by phase slips is large enough so that the device could not re-establish the superconducting state. For  $n_v = 5$ , and all subsequent lower  $I_c$  states, this is not the case. As the current reaches the diamond edge, a phase slip will occur without causing a cascade transition to the dissipative state. In other words, during the readout the vorticity is altered by a nonobservable, or hidden phase slip. As such, no reliable reading is possible for these states at 0 mT. Figures 2(a)–2(d) also reveal around 5% of  $I_c$  readings that cannot be traced to any specific  $n_v$ . These are random errors related to voltage fluctuations in the measurement setup that can be reduced by better line filtration.

This analysis reveals the ability of our SQUID to behave as an eight-level memory, i.e., it presents eight different nonvolatile states that can be read at a fixed magnetic field. Differently from a recently proposed memory element that relies on the physics of a single elongated weak link [30], the writing between different states in Fig. 2(d) is not a direct process, i.e., it does not require one sole physical stimulus like one magnetic field pulse. On the other hand, it is only by embedding the nanobridge in a SQUID that the possibility of exploring the physics of the weak link to create a multilevel memory element arises. Moreover, the total number of available states depends decisively on three factors: (i) the slope of the vorticity diamond, tuned by the NB length; (ii) the device’s critical current; and (iii) the maximum current for which the device can recover from a phase slip without triggering a transition to the normal state. Therefore, it is possible to develop memory elements suited for specific needs by appropriate material and design choices. These are remarkable features that can only be accessed by the use of magnetic fields in the writing protocol and may be explored for sensing applications and in the development of nonvolatile multilevel memory elements.

#### IV. TOWARDS NONPROBABILISTIC VORTICITY STATE SWITCHING

The fact that the writing process depicted in Fig. 2(c) is probabilistic is a major downside in comparison to alternative deterministic memory systems. Although a probabilistic writing scheme has been used previously in proposed memory elements [26], it is paramount to move towards a viable vorticity state switch protocol that does not rely on the process of leaving and returning to the superconducting

state. Moreover, simply reducing the width of applied current pulses to manipulate the state does not solve the issue. As we demonstrate in Sec. III, the frozen-in vorticity when the SQUID enters the superconducting state depends decisively on the device energy. In asymmetric SQUIDs [26], as our own, the lowest energy state may not present the highest  $I_c$  at a desired applied field, hampering the writing process.

Fortunately, it is possible to influence the probability of changing states without triggering irreversible heating to the dissipative state by exploring single phase slips—if an applied magnetic field is used to favorably bias the energy [31]. Figure 3(a) presents the energy versus magnetic field behavior at zero bias current obtained from the kinetic inductance values for device 400a for  $n_v = 0$  and 1 according to Eq. (B1). The field-dependent absolute energy difference between the states, labeled as  $|\Delta E_{0,1}|$ , is highlighted in the panel. At zero field, the energy values  $E_0^{n_v}$  increase parabolically with  $n_v$ . As such,  $E_0^0 = 0$  represents the more energetically favorable configuration for the investigated SQUID, as shown in Appendix B, which helps to explain why the probability that device 400a freezes in  $n_v = 0$  is the highest when entering the superconducting state at zero field. Accordingly, the only other observed state,  $n_v = 1$ , presents the second lowest energy at 0 mT and, therefore, the second highest probability. The possibility that a metastable energy state appears in the measurements is related to random fluctuations experienced while the device enters the superconducting state [31]. Figure 3(b) shows a schematic representation of the energy landscape around vorticity states  $n_v = 0$  and 1 at selected magnetic fields. Finally, although  $E_0^{+1} = E_0^{-1}$ ,  $n_v = -1$  is not observed in Fig. 2(a). This happens because there is a dependence of the current polarity on the freeze-in probability, which is tied to the shape of the vorticity diamonds and can be attested in Fig. 1(b) by noting that, for the negative current measurements, it is  $n_v = -1$  and not  $n_v = 1$  that is observed at zero field.

Figure 3(c), meanwhile, reveals an intriguing feature. When the device is prepared in  $n_v = 0$ , there is a defined field region, highlighted by the gray shaded area, showing a predominant probability of observing a single phase slip changing the vorticity of the SQUID to  $n_v = 1$ . This is demonstrated in the main panel by one representative field-dependent  $I_c$  measurement in which device 400a is prepared in  $n_v = 0$  prior to a current sweep at each field value—solid blue points [34]. The blue and red solid lines are fits of Eq. (A1) for the vorticity diamonds for states  $n_v = 0$  and 1, respectively. Considering the blue points, for the left-most field values, the observed critical currents correspond to that of the prepared state,  $n_v = 0$ . As the field is increased towards and beyond the line at  $B = 1.74$  mT, at which  $E_B^{+1} = E_B^0$ , a current sweep may induce a single phase slip and the observed  $I_c$  now corresponds to that of  $n_v = 1$ . For measurements at even higher fields, device

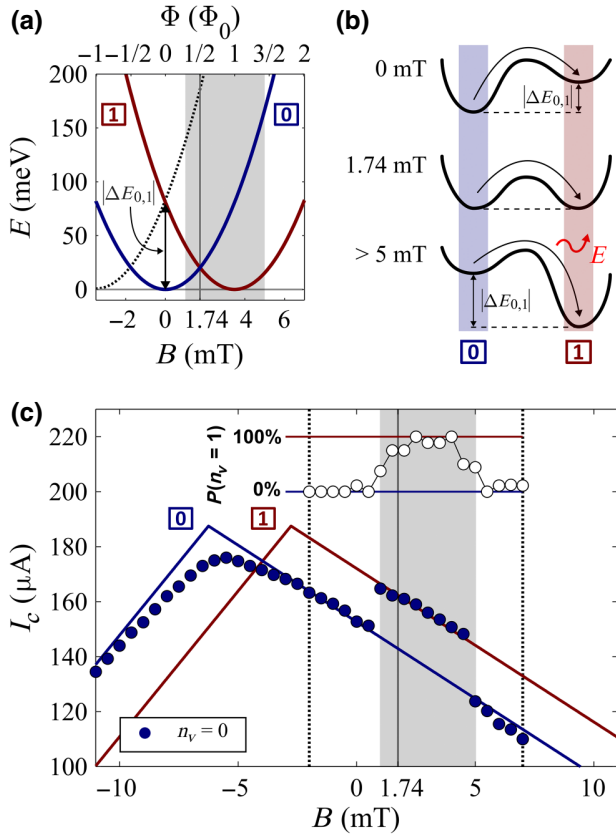


FIG. 3. (a) Energy versus magnetic field at zero current bias for  $n_v = 0$  and 1 for device 400a obtained from the kinetic inductance. The dotted curve represents the energy for  $n_v = -1$ . (b) Schematic representation of the energy landscape around the minima at  $n_v = 0$  and 1 at selected applied fields. The absolute energy difference  $\Delta E_{0,1}$  is represented along a pictorial view of the energy barrier between the states. Curved dark arrows indicate the switch from state  $n_v = 0$  to 1 and the red arrow highlights the energy dissipated by one such phase slip at high applied fields. (c) Main panel shows one representative  $I_c(B)$  measurement after preparing device 400a in  $n_v = 0$  at 300 mK. The respective vorticity diamonds for states  $n_v = 0$  and 1 are shown as solid lines. The inset shows the probability of finding the device in  $n_v = 1$  after a current sweep at particular field values as averaged for nine different measurements. In (a) and (c), a gray shaded area highlights the field values for which there is a high probability of observing single phase slips from  $n_v = 0$  to  $n_v = 1$ .

400a no longer experiences single phase slips and again the readout corresponds to the state  $n_v = 0$ . This experiment is repeated nine times in the field region between the two dotted lines in Fig. 3(c). The averaged probability of finding device 400a in state  $n_v = 1$  after the current sweep is plotted in the inset. It shows that, at particular field values, the device will mostly endure a single phase slip to  $n_v = 1$  instead of transitioning to the normal state.

Such an observation may be better understood with the help of Fig. 3(b). At zero field, there is a nonzero energy difference between states  $n_v = 0$  and  $n_v = 1$  for device 400a. On top of that, switching from  $n_v = 0$  to  $n_v = 1$  requires the SQUID to surpass a characteristic energy barrier. Then, as the current is swept across the edges of the vorticity diamond of  $n_v = 0$  at 0 mT, a phase slip to  $n_v = 1$  will not occur, as it would strongly increase the energy of the system, and the normal state would be recovered. However, as the magnetic field is increased,  $|\Delta E_{0,1}|$  decreases. At an applied field corresponding to  $\Phi_0/2$ , or 1.74 mT,  $|\Delta E_{0,1}| = 0$ . For  $B > 1.74$  mT,  $n_v = 1$  presents the lowest energy and is thus the favorable state, as seen in Fig. 3(a). Inspection of Fig. 3(c) reveals that around such an applied field, device 400a will mainly be found at  $n_v = 1$  after the current sweep. This is now the case because the energy released by a phase slip is lower than that required to switch from  $n_v = 0$  to  $n_v = 1$  at 0 mT, and the SQUID may sustain it while remaining in the superconducting state. As  $|\Delta E_{0,1}|$  becomes small, this reasoning explains why a number of energy-increasing phase slips are observed as  $B$  approaches 1.74 mT. An analogous behavior is reported by Ref. [31]. As the field is increased above 1.74 mT,  $|\Delta E_{0,1}|$  increases, ultimately causing a phase slip from  $n_v = 0$  to  $n_v = 1$  to release enough energy to again drive the device out of the superconducting state. For that reason, the observed vorticity state switch from  $n_v = 0$  to  $n_v = 1$  is not present at fields higher than 5 mT in Fig. 3(c).

A second SQUID containing a 400-nm-long NB, labeled device 400b, is studied. Completely analogous results are found and are shown in Appendix C. Moreover, for device 400b, we observe that preparation in all states between  $-2 \leq n_v \leq 2$  results in a similar behavior, i.e., there are contained field regions that favored phase slips increasing the vorticity of the SQUID by +1. This suggests an alternative, step-by-step, vorticity state switching mechanism with very high probabilities, possibly even deterministic. Based on single phase slips, such mechanism would also present the benefit of not requiring leaving the superconducting state, thus reducing dissipation during memory operation.

Of note, this mechanism appears to be unidirectional in  $n_v$ , as we are not able to observe the reverse process in phase slips that decrease the vorticity. We can understand this considering the  $I_c(B)$  distribution in Fig. 1(b). If device 400a is initially prepared in  $n_v = 0$ , one could expect a high probability to observe phase slips to  $n_v = -1$  at  $-1.74$  mT, corresponding to  $-\Phi_0/2$ —see the dotted curve in Fig. 3(a). However, around such an applied field,  $n_v = -1$  has a lower  $I_c$  than  $n_v = 0$ . It is then impossible for the vorticity to change to  $n_v = -1$  after the current is swept across the positive side of the vorticity diamond of  $n_v = 0$  and the device will transition to the dissipative state. Moreover, at zero field, such phase slips may compromise the readout of the prepared state, therefore

an optimal device design is required. As such, the exploration of the presented effect as an alternative, possibly deterministic, and tunable flux control mechanism is an enticing possibility for the development of superconducting memory elements. In this effort, we find that a long NB is a necessity. While longer NBs consistently present particular regions with high single phase-slip probabilities, measurements conducted for devices containing 250-nm (see Appendix C) and 300-nm NBs did not show such regions. Inspection of the energy versus field behavior of these samples does not reveal a significant difference in comparison with what is shown in Fig. 3(a) for device 400a. Therefore, an approach capable of resolving the dynamics of the system and the role of the characteristic energy barrier between adjacent vorticity states is needed to explain our experimental observations for shorter NBs.

## V. CONCLUSIONS

We fabricate different fully superconducting  $\text{Mo}_{78}\text{Ge}_{22}$  SQUIDs comprised of one Dayem bridge and one nanobridge. Due to the tailored properties of the junctions, multiple vorticity diamonds intersect the zero-field line in the  $I_c(B)$  distribution of our devices, which can be further influenced by the modification of the nanobridge length, an effective control parameter of the superconducting properties of the junctions. The implementation of a field-assisted writing protocol allows reliable access to eight different vorticity states with distinct macroscopic properties at zero applied magnetic field, revealing the potential of our device as a superconducting multilevel memory element. An alternative approach to effectively switch the SQUID vorticity state by one winding number is presented, as for long enough nanobridges we demonstrate the existence of particular field regions where a current sweep favorably induces a single phase slip to the next vorticity state. Our analysis points to the determinant role played by the SQUID energy in the mechanisms involved in the freeze-in and phase-slip probabilities, indicating applied magnetic fields as a vital ingredient in the effective manipulation of the vorticity states.

## ACKNOWLEDGMENTS

This work is supported by Coordenação de Aperfeiçoamento de Pessoal de Nível Superior—Brasil (CAPES)—Finance Code 001, the São Paulo Research Foundation (FAPESP, Grant No. 2021/08781-8), the National Council for Scientific and Technological Development (CNPq, Grants No. 316602/2021-3, and No. 309 928/2018-4), the China Scholarship Council (No. 202004 890002), Research Foundation Flanders (FWO, Belgium, Grants G0A0619N, G0D5619N, and 11K6523N), and by COST action SUPERQUMAP (Grant No. CA21144). D.A.D.C. acknowledges Capes-PDSE Grant No. 88881.624531/2021-01.

## APPENDIX A: VORTICITY DIAMONDS

To obtain reliable readings of the SQUID vorticity states, it is necessary to have prior knowledge of their respective critical currents for different applied fields. For the SQUIDs employed in this work, we may consider the junctions to present linear  $C\Phi$ Rs of the form  $I_c^{NB,DB} = I_c^{NB,DB} (\varphi_c^{NB,DB} / \varphi_c^{NB,DB})$ , where  $I_c^{NB,DB}$  is the supercurrent and  $\varphi_c^{NB,DB}$  the critical phase difference across the nanobridge and the Dayem bridge, respectively [18]. The left- and right-side linear segments of the positive current side of  $I_c(B)$  are then given by

$$\begin{aligned} I_c^{\text{left}}(B) &= I_c^{NB} \\ &+ \left( \frac{\Phi_0}{2\pi L_k^{DB}} \right) \left( \varphi_c^{NB} + 2\pi \frac{B}{\Delta B} \right), \\ I_c^{\text{right}}(B) &= I_c^{DB} \\ &+ \left( \frac{\Phi_0}{2\pi L_k^{NB}} \right) \left( \varphi_c^{DB} - 2\pi \frac{B}{\Delta B} \right), \end{aligned} \quad (\text{A1})$$

where  $\Phi_0$  is the magnetic flux quantum,  $L_k^{NB,DB}$  the kinetic inductance of the junction, and  $\Delta B$  is the Little-Parks oscillation period defined by the area of the SQUID loop as  $\Delta B = \Phi_0 / A_{\text{loop}}$ .

## APPENDIX B: SQUID ENERGY

The ability to write the device to a specific state is a process related to the SQUID energy, as a freeze-in from the normal to the superconducting state will favor stable (less energetic) states over metastable ones [31]. Then, by neglecting the self-inductance contribution estimated to be around 30 to 50 times smaller for a loop with the dimensions of our devices [18], the total energy stored in the SQUID depends on the the bias current  $I_{\text{bias}}$  and the magnetic field as [31]

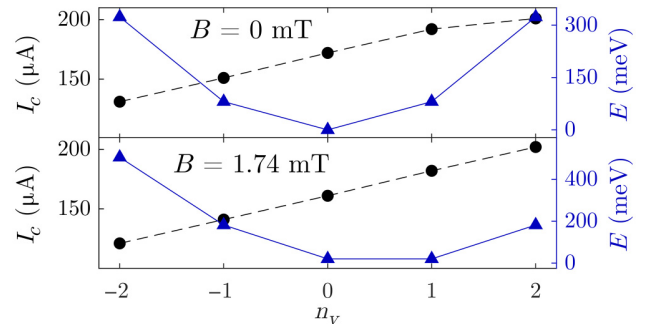


FIG. 4. Evolution of the critical current (dark circles) and total SQUID energy (blue triangles) as a function of  $n_v$  for different applied magnetic fields at 300 mK.

$$E_B^{n_v} = \frac{1}{2} \left( \frac{L_k^{NB} L_k^{DB}}{L_k^{NB} + L_k^{DB}} \right) I_{\text{bias}}^2, \\ + \frac{1}{2} \frac{1}{L_k^{NB} + L_k^{DB}} \left( \frac{B}{\Delta B} \Phi_0 - \Phi_0 n_v \right)^2, \quad (\text{B1})$$

where  $n_v$  is the vorticity state given by the relationship  $\varphi^{NB} - \varphi^{DB} + 2\pi B/\Delta B = 2\pi n_v$ , which represents the single valuedness of the superconducting order parameter [18].

For a given applied magnetic field, the lowest energy state may not be the one presenting the highest critical current. To illustrate such a situation for device 400a, Fig. 4 shows  $I_c$  and  $E$  at  $B = 0$  mT and  $B = 1.74$  mT as a function of  $n_v$ . The values represented are obtained from the fit of the vorticity diamonds and from Eq. (B1). In both cases,  $n_v = 2$  presents the highest  $I_c$  value, while  $n_v = 0$

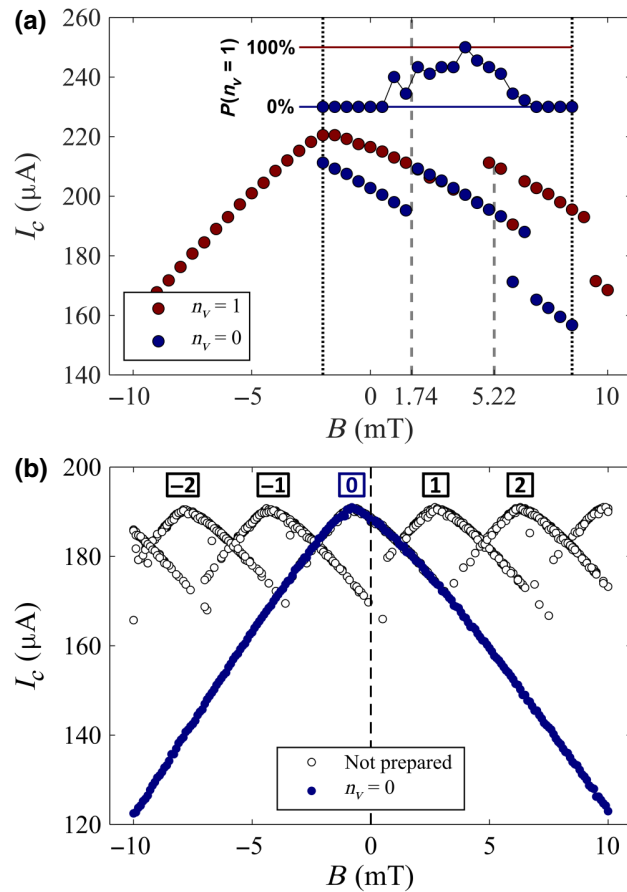


FIG. 5. (a) Main panel shows representative  $I_c(B)$  measurements after preparing device 400b in  $n_v = 0$  and  $n_v = 1$ . The inset shows the probability of finding device 400b in  $n_v = 1$  after a current sweep at particular field values after it is initially prepared in  $n_v = 0$ . The presented values are averaged from nine different measurements. (b)  $I_c(B)$  for device 250 when no preparation protocol is performed and after preparing in  $n_v = 0$  before each measurement. All measurements are performed at 300 mK.

and  $n_v = 1$  have a lower total energy and  $n_v = -1$  also has a lower energy at 0 mT. This picture can be understood following Fig. 3(a) and knowing that  $E(B)$  for  $n_v = -1$  and 2 are symmetric around 1.74 mT.

### APPENDIX C: DIFFERENT DEVICES

Figure 5 presents results obtained for devices different from the one discussed in the main text. Figure 5(a) demonstrates that, around  $\Phi_0/2$ , or 1.74 mT, device 400b shows an increased probability of experiencing single phase slips from  $n_v = 0$  to  $n_v = 1$ . This confirms the findings described in Sec. IV for device 400a. Moreover, it also shows a completely analogous behavior at  $3\Phi_0/2$ , or 5.22 mT, at which field  $|\Delta E_{1,2}| = 0$ . If device 400b is prepared in  $n_v = 1$ , it presents a high probability of experiencing a single phase slip to  $n_v = 2$ . Figure 5(b) presents data for a device containing a shorter, 250-nm NB. No phase slips are observed as the current is swept across the vorticity diamond of the prepared state  $n_v = 0$ . Therefore, we demonstrate that a long nanobridge is needed to create single-phase-slip-favorable field regions, as discussed in Sec. IV.

- [1] M. J. Rozenberg, I. H. Inoue, and M. J. Sanchez, Non-volatile Memory with Multilevel Switching: A Basic Model, *Phys. Rev. Lett.* **92**, 178302 (2004).
- [2] R. Waser, R. Dittmann, G. Staikov, and K. Szot, Redox-based resistive switching memories—nanoionic mechanisms, prospects, and challenges, *Adv. Mater.* **21**, 2632 (2009).
- [3] F. Zahoor, T. Z. Azni Zulkifli, and F. A. Khanday, Resistive random access memory (RRAM): An overview of materials, switching mechanism, performance, multilevel cell (MLC) storage, modeling, and applications, *Nanoscale Res. Lett.* **15**, 1 (2020).
- [4] C. Ríos, M. Stegmaier, P. Hosseini, D. Wang, T. Scherer, C. D. Wright, H. Bhaskaran, and W. H. P. Pernice, Integrated all-photonic non-volatile multi-level memory, *Nat. Photon.* **9**, 725 (2015).
- [5] K. Olejník, V. Schuler, X. Martí, V. Novák, Z. Kašpar, P. Wadley, R. P. Campion, K. W. Edmonds, B. L. Gallagher, J. Garcés, M. Baumgartner, P. Gambardella, and T. Jungwirth, Antiferromagnetic CuMnAs multi-level memory cell with microelectronic compatibility, *Nat. Commun.* **8**, 1 (2017).
- [6] A. N. McCaughan, N. S. Abebe, Q.-Y. Zhao, and K. K. Berggren, Using geometry to sense current, *Nano Lett.* **16**, 7626 (2016).
- [7] Q.-Y. Zhao, E. A. Toomey, B. A. Butters, A. N. McCaughan, A. E. Dane, S.-W. Nam, and K. K. Berggren, A compact superconducting nanowire memory element operated by nanowire cryotrons, *Supercond. Sci. Technol.* **31**, 035009 (2018).
- [8] A. N. McCaughan, E. Toomey, M. Schneider, K. K. Berggren, and S. W. Nam, A kinetic-inductance-based

- superconducting memory element with shunting and sub-nanosecond write times, *Supercond. Sci. Technol.* **32**, 015005 (2018).
- [9] E. Toomey, M. Onen, M. Colangelo, B. A. Butters, A. N. McCaughan, and K. K. Berggren, Bridging the Gap Between Nanowires and Josephson Junctions: A Superconducting Device Based on Controlled Fluxon Transfer, *Phys. Rev. Appl.* **11**, 034006 (2019).
- [10] M. Tinkham, *Introduction to Superconductivity* (McGraw-Hill Book Co., New York, 1996), 2nd ed.
- [11] J. Clarke, Principles and applications of SQUIDs, *Proc. IEEE* **77**, 1208 (1989).
- [12] C. P. Foley and H. Hilgenkamp, Why nanoSQUIDs are important: an introduction to the focus issue, *Supercond. Sci. Technol.* **22**, 064001 (2009).
- [13] C. Granata and A. Vettoliere, Nano superconducting quantum interference device: A powerful tool for nanoscale investigations, *Phys. Rep.* **614**, 1 (2016).
- [14] M. Kjaergaard, M. E. Schwartz, J. Braumüller, P. Krantz, J. I.-J. Wang, S. Gustavsson, and W. D. Oliver, Superconducting qubits: Current state of play, *Annu. Rev. Condens. Matter Phys.* **11**, 369 (2020).
- [15] K. Hasselbach, D. Mailly, and J. R. Kirtley, Microsuperconducting quantum interference device characteristics, *J. Appl. Phys.* **91**, 4432 (2002).
- [16] G. J. Podd, G. D. Hutchinson, D. A. Williams, and D. G. Hasko, Micro-SQUIDs with controllable asymmetry via hot-phonon controlled junctions, *Phys. Rev. B* **75**, 134501 (2007).
- [17] A. Murphy and A. Bezryadin, Asymmetric nanowire SQUID: Linear current-phase relation, stochastic switching, and symmetries, *Phys. Rev. B* **96**, 094507 (2017).
- [18] H. Dausy, L. Nulens, B. Raes, M. J. Van Bael, and J. Van de Vondel, Impact of Kinetic Inductance on the Critical-Current Oscillations of Nanobridge SQUIDs, *Phys. Rev. Appl.* **16**, 024013 (2021).
- [19] C. N. Lau, N. Markovic, M. Bockrath, A. Bezryadin, and M. Tinkham, Quantum Phase Slips in Superconducting Nanowires, *Phys. Rev. Lett.* **87**, 217003 (2001).
- [20] J. E. Mooij and Y. V. Nazarov, Superconducting nanowires as quantum phase-slip junctions, *Nat. Phys.* **2**, 169 (2006).
- [21] T. Aref, A. Levchenko, V. Vakaryuk, and A. Bezryadin, Quantitative analysis of quantum phase slips in superconducting Mo<sub>76</sub>Ge<sub>24</sub> nanowires revealed by switching-current statistics, *Phys. Rev. B* **86**, 024507 (2012).
- [22] A. Murphy, P. Weinberg, T. Aref, U. C. Coskun, V. Vakaryuk, A. Levchenko, and A. Bezryadin, Universal Features of Counting Statistics of Thermal and Quantum Phase Slips in Nanosize Superconducting Circuits, *Phys. Rev. Lett.* **110**, 247001 (2013).
- [23] A. Belkin, M. Belkin, V. Vakaryuk, S. Khlebnikov, and A. Bezryadin, Formation of Quantum Phase Slip Pairs in Superconducting Nanowires, *Phys. Rev. X* **5**, 021023 (2015).
- [24] V. Lefevre-Seguin, E. Turlot, C. Urbina, D. Esteve, and M. H. Devoret, Thermal activation of a hysteretic dc superconducting quantum interference device from its different zero-voltage states, *Phys. Rev. B* **46**, 5507 (1992).
- [25] T. A. Palomaki, S. K. Dutta, H. Paik, H. Xu, J. Matthews, R. M. Lewis, R. C. Ramos, K. Mitra, P. R. Johnson, F. W. Strauch, and A. J. Dragt, Initializing the flux state of multiwell inductively isolated Josephson junction qubits, *Phys. Rev. B* **73**, 014520 (2006).
- [26] E. Ilin, X. Song, I. Burkova, A. Silge, Z. Guo, K. Ilin, and A. Bezryadin, Supercurrent-controlled kinetic inductance superconducting memory element, *Appl. Phys. Lett.* **118**, 112603 (2021).
- [27] J. E. Mooij and C. J. P. M. Harmans, Phase-slip flux qubits, *New J. Phys.* **7**, 219 (2005).
- [28] L. Chen, L. Wu, Y. Wang, Y. Pan, D. Zhang, J. Zeng, X. Liu, L. Ma, W. Peng, Y. Wang, J. Ren, and Z. Wang, Miniaturization of the superconducting memory cell via a three-dimensional Nb nano-superconducting quantum interference device, *ACS Nano* **14**, 11002 (2020).
- [29] Y. Takeshita, F. Li, D. Hasegawa, K. Sano, M. Tanaka, T. Yamashita, and A. Fujimaki, High-speed memory driven by SFQ pulses based on 0- $\pi$  SQUID, *IEEE Trans. Appl. Supercond.* **31**, 1 (2021).
- [30] N. Ligato, E. Strambini, F. Paolucci, and F. Giazotto, Preliminary demonstration of a persistent Josephson phase-slip memory cell with topological protection, *Nat. Commun.* **12**, 1 (2021).
- [31] L. Nulens, H. Dausy, M. J. Wyszynski, B. Raes, M. J. Van Bael, M. V. Milošević, and J. Van de Vondel, Metastable states and hidden phase slips in nanobridge SQUIDs, *Phys. Rev. B* **106**, 134518 (2022).
- [32] A direct inspection of the measured  $I_c(B)$  distribution for device 400a does not reveal the full shape of the vorticity diamond used to describe the critical-current oscillation as only one of the branches appears. For this reason, we employ the preparation protocol explained in Sec. III to obtain data relative to both diamond branches for device 400a.
- [33] A. Murphy, D. V. Averin, and A. Bezryadin, Nanoscale superconducting memory based on the kinetic inductance of asymmetric nanowire loops, *New J. Phys.* **19**, 063015 (2017).
- [34] Here, the measured critical-current values differ from those presented in Fig. 1(b) because the device is removed from the experimental setup for approximately 1 month, which slightly depletes its superconducting properties.



## Chapter 6

# The interaction of a superconducting film and ac magnetic fields visualized by magneto-optical imaging

In the previous Chapters, I have presented works that directly explored the interaction of applied magnetic fields with different superconducting samples to influence their behavior in ways that may be useful for applications. In this Chapter, I will deviate from this trend. The results I present, which are deposited on arXiv [149]<sup>23</sup>, aim to expand the viability of magneto-optical imaging for quantitative studies of the behavior of superconductors under ac magnetic fields. For that, we rely on the ability to emulate the ac behavior using a dc experimental setup. As a case study, we focus on answering the question of “why the ac susceptibility of a superconducting film is independent of its thermomagnetic history.” In the process, we successfully compare MOI data to those obtained by standard SQUID-based ac magnetometry. We also explore the spatial resolution of MOI to collect quantitative information on individual flux avalanches and reveal vortex-antivortex annihilation zones in regions where an incoming flux front interacts with the pre-established flux of opposite polarity.

---

<sup>23</sup>At the date of the defense of this thesis, these results were under peer review. If the reader is unable to find the Supplemental Material of the final version of the work, they may directly request the videos from me at [daviadchaves@gmail.com](mailto:daviadchaves@gmail.com) or from Prof. Maycon Motta at [m.motta@df.ufscar.br](mailto:m.motta@df.ufscar.br).

# Using quantitative magneto-optical imaging to reveal why the ac susceptibility of superconducting films is history-independent

Davi A. D. Chaves,<sup>1,\*</sup> J. C. Corsaletti Filho,<sup>1,†</sup> E. A. Abbey,<sup>1</sup> D. Bosworth,<sup>2</sup> Z. H. Barber,<sup>2</sup> M. G. Blamire,<sup>2</sup> T. H. Johansen,<sup>3</sup> A. V. Silhanek,<sup>4</sup> W. A. Ortiz,<sup>1</sup> and M. Motta<sup>1,‡</sup>

<sup>1</sup>*Departamento de Física, Universidade Federal de São Carlos, 13565-905 São Carlos, SP, Brazil*

<sup>2</sup>*Department of Materials Science and Metallurgy, University of Cambridge, Cambridge CB3 0FS, United Kingdom*

<sup>3</sup>*Department of Physics, University of Oslo, POB 1048, Blindern, 0316 Oslo, Norway*

<sup>4</sup>*Experimental Physics of Nanostructured Materials, Q-MAT, CESAM, Université de Liège, B-4000 Sart Tilman, Belgium*

(Dated: September 18, 2023)

Measurements of the temperature-dependent ac magnetic susceptibility of superconducting films reveal reversible responses, i.e., irrespective of the magnetic and thermal history of the sample. This experimental fact is observed even in the presence of stochastic and certainly irreversible magnetic flux avalanches which, in principle, should randomly affect the results. In this work, we explain such an apparent contradiction by exploring the spatial resolution of magneto-optical imaging. To achieve this, we successfully compare standard frequency-independent first harmonic ac magnetic susceptibility results for a superconducting thin film with those obtained by ac-emulating magneto-optical imaging (acMOI). A quantitative analysis also provides information regarding flux avalanches, reveals the presence of a vortex-antivortex annihilation zone in the region in which a smooth flux front interacts with pre-established avalanches, and demonstrates that the major impact on the flux distribution within the superconductor happens during the first ac cycle. Our results establish acMOI as a reliable approach for studying frequency-independent ac field effects in superconducting thin films while capturing local aspects of flux dynamics, otherwise inaccessible via global magnetometry techniques.

## I. INTRODUCTION

The last years have seen superconducting materials be positioned as a vital part of an ongoing quantum revolution [1–5] and serving as a fertile playground for the development of several nanoscale technological applications [6–13]. Particularly, understanding, controlling, and exploring the interaction of different superconductors with distinct properties and structures with a low-frequency ac magnetic field has been an active research topic [14–22].

In a type-II superconductor, it may be energetically favorable for the sample to allow flux penetration in the form of vortices [23, 24]. For a given direction of the applied magnetic field, vortices may either be of positive or negative polarity, the latter being commonly referred to as antivortices. Whereas vortices with the same polarity interact repulsively [25], vortices and antivortices attract each other, which eventually leads to mutual annihilation when two such entities come in close proximity [26, 27].

On a mesoscopic scale, ordinary flux distributions in type-II specimens are described by critical state models [28, 29]. In this case, the magnetic field gradually penetrates toward the center of the sample as a smooth

flux front originating from the edges of the material, a consequence of vortex motion being hampered by pinning centers [30, 31]. The exact distribution profile depends on sample geometry and its magnetic history [32–34]. Moreover, the depth of the flux front penetration is tied to the sample critical current density  $J_c$ , as further penetration indicates a lower magnetic shielding capability [32]. In short, the actual flux distribution usually depends on external thermodynamic parameters such as the temperature,  $T$ , and the applied magnetic field,  $H$ , i.e.,  $J_c = J_c(T, H)$ .

The inevitable vortex displacement during flux penetration represents an energy dissipating process [24]. Then, if the superconductor is not able to swiftly assimilate the heat generated by moving vortices in order to accommodate for further vortex movement, a thermomagnetic instability may be triggered. In a given interval of magnetic fields and temperatures, these events lead to the onset of a positive feedback process in which superconducting properties are locally suppressed, allowing for abrupt flux penetration known as flux avalanches [35–37]. In thin films, flux avalanches take remarkable dendritic patterns as they propagate through the material with velocities up to the scale of hundreds of km/s [38–45].

The abrupt flux penetration during a flux avalanche event results in well-known flux jumps in the global magnetization hysteresis loop of superconductors [31, 46–49]. Another signature of avalanches in the magnetic properties of superconducting materials is a paramagnetic reentrance observed in the temperature dependence of the first harmonic ac magnetic susceptibility,  $\chi_{ac}(T) =$

\* davi@df.ufscar.br

† Present address: Laboratório Nacional de Luz Síncrotron, Centro Nacional de Pesquisa em Energia e Materiais, 13083-100 Campinas, SP, Brazil

‡ m.motta@df.ufscar.br

$\chi'_{ac}(T) + i\chi''_{ac}(T)$  [50–52]. The in-phase component  $\chi'_{ac}$  is related to an inductive response and measures the superconductor ability to shield magnetic flux [53, 54]. The so-called paramagnetic reentrance is observed as a decrease in  $|\chi'_{ac}|$  for temperatures lower than the superconducting critical temperature  $T_c$ . On its turn, the out-of-phase component  $\chi''_{ac}$  gauges the energy losses related to flux motion in type-II superconductors [53, 54]. Hence, an increase in  $\chi''_{ac}$  accompanying the decrease in  $|\chi'_{ac}|$  reveals the occurrence of flux avalanches. Although ac susceptibility studies are a ubiquitous approach for characterizing the magnetic dynamics of superconducting systems [19, 53–61], a technique with the micrometric spatial resolution of magneto-optical imaging, has remained little explored in this effort.

In this work, we investigate the effects of ac magnetic fields in a 100-nm-thick amorphous MoSi (a-MoSi) film by employing ac-emulating magneto-optical imaging (acMOI). Comparing the results with  $\chi_{ac}(T)$  measurements obtained by conventional global ac magnetometry, we demonstrate that acMOI is a reliable technique for the quantitative study of the ac magnetic susceptibility of superconductors. Moreover, as magneto-optical imaging allows to spatially resolve individual flux avalanches, acMOI is used to explain an observed thermomagnetic history-independent paramagnetic reentrance in  $\chi_{ac}(T)$  for the a-MoSi film. Quantitative acMOI also allows us to visualize how an incoming smooth flux front overrides the flux distribution of pre-established avalanches, revealing a vortex-antivortex annihilation zone separating regions permeated by magnetic flux with opposing polarities.

This paper is organized as follows: Section II details the experimental methods used to fabricate and investigate the a-MoSi thin film; Section III describes typical  $\chi_{ac}(T)$  measurements conducted in a standard ac magnetometer, demonstrating the history-independent paramagnetic reentrance in the investigated sample; Section IV qualitatively explores the nature of ac susceptibility measurements using acMOI both in the smooth penetration and avalanche regimes and quantifies the magnetic imprint of individual avalanches; Section V demonstrates how acMOI may be used to quantitatively gauge  $\chi_{ac}(T)$  for superconducting samples; Section VI further explores the spatial resolution of MOI to investigate how an incoming flux front interacts with an already established avalanche region; finally, Section VII summarizes the results and outlines perspectives on the use of acMOI.

## II. EXPERIMENTAL DETAILS

A square a-MoSi film with lateral size of 2.5 mm and thickness of 100 nm was deposited onto a silicon substrate at 77 K by dc magnetron sputtering at a pressure of 1.2 Pa in dynamical equilibrium under argon flow, similarly to the protocol described in Ref. [62]. Amorphous MoSi films typically present critical temperatures above 7 K, low intrinsic pinning, and correspondingly

low critical current densities [63, 64]. Application-wise, a-MoSi is a prominent material choice for superconducting nanowire single-photon detectors [65–67].

The complex ac magnetic susceptibility of the a-MoSi sample was investigated as a function of temperature using standard global magnetometry which captures the magnetic behavior of the sample as a whole. A SQUID-based magnetometer model MPMS-5S from Quantum Design (MPMS) was employed to measure both the in-phase ( $\chi'_{ac}$ ) and out-of-phase ( $\chi''_{ac}$ ) components of  $\chi_{ac}(T)$ . Probe ac magnetic fields of frequencies  $f = 0.05$  Hz or 1 Hz and amplitudes  $h$  varying from 0.1 Oe to 3.8 Oe were applied perpendicularly to the plane of the film during the experiments. Before measuring, the magnetic history of the dc field-generating superconducting coil of the MPMS was erased, and all measurements were performed under remanent magnetic field,  $H_{rem} \lesssim 1$  Oe. In other words, no external dc field was intentionally applied to the sample.

The magneto-optical imaging technique allows us to locally resolve the magnetic flux distribution within the sample on the micrometric scale [30]. By placing a Bi-doped yttrium iron garnet—a Faraday-active material [68]—directly on top of our superconducting film, MOI allows inspection of the deviation of the polarization angle of light in the presence of a magnetic field due to the Faraday effect. Thus, we are able to detect subtle nuances in the local field induced in the investigated material as a variation in the intensity captured by a CCD camera.

We perform a pixel-by-pixel calibration procedure implemented on MATLAB to obtain quantitative information from magneto-optical images [69]. In other words, we extract the out-of-plane magnetic flux density  $B(x, y)$  from the intensity data  $I(x, y)$ , where  $(x, y)$  defines the position of a given pixel within the image. Possible drifts in sample position relative to the sensors due to thermal dilation of the cold finger in the experimental setup are corrected within a precision of two pixels using the StackReg plugin [70] with ImageJ [71]. As a consequence of its lower  $J_c$ , a-MoSi also presents an intrinsic advantage for quantitative MO studies, as it inhibits unwanted magnetic domain wall switching in the garnet layer [72], which could otherwise compromise the  $I$ -to- $B$  transformation.

## III. AC SUSCEPTIBILITY: MPMS MEASUREMENTS

Typical temperature-dependent ac susceptibility results for superconducting films are illustrated in Fig. 1 for the 100-nm-thick a-MoSi sample. The curves depicted are obtained using the MPMS and show both  $\chi'_{ac}$  and  $\chi''_{ac}$  normalized by the Meissner state plateau  $\chi_0$  of the  $\chi'_{ac}$  measurement conducted with the lowest  $h$  and  $T$ . Figure 1(a) highlights the effects of  $h$  in  $\chi_{ac}(T)$ . In all measurements, the sample is first subjected to zero-field-

cooling (ZFC) down to 2 K. Then,  $\chi_{ac}(T)$  is measured as the temperature is increased using a probe field with  $f = 1$  Hz and varying  $h$  values from 0.1 Oe to 3.5 Oe. As we demonstrate in Appendix A, the choice of  $f$  has almost no impact on the  $\chi_{ac}(T)$  behavior in the frequency range explored in this work. For the smallest field amplitude (black points), we observe a near constant  $\chi'_{ac}$  close to  $-1$  at low temperatures. This is a signature of superconductors' perfect diamagnetism, showing that the sample initially shields its interior from magnetic flux very efficiently. Then, as the sample approaches its critical temperature ( $T_c$ ), a sharp increase in  $|\chi'_{ac}|$  is observed, as the film is no longer shielded from flux penetration. Signatures of the superconducting-normal state transition are also found in the out-of-phase component, as a peak in  $\chi''_{ac}$  accompanies the increase in  $|\chi'_{ac}|$ . Thus, the dissipative motion of vortices entering the sample is consistently captured by  $\chi''_{ac}$ , which is greatly enhanced during flux penetration. Therefore, for the a-MoSi sample, we define  $T_c = 7.30 \pm 0.05$  K as the first experimental point for which both  $\chi'_{ac}$  and  $\chi''_{ac}$  depart from zero in  $\chi_{ac}(T)$  measurements.

If  $h$  is now increased to 0.5 Oe (red points), a very similar behavior is observed in Fig. 1(a). However, flux exclusion becomes less complete as the temperature and field are increased in accordance with critical state models. Therefore, although  $T_c$  is unchanged, the onset of the superconducting-normal state transition occurs for lower temperatures, as  $T$  is increased from 2 K. This trend continues as  $h$  is further increased to 1.0 Oe and 1.5 Oe, represented in Fig. 1(a) by green and blue points, respectively. For all measurements with  $h \leq 1.5$  Oe, the a-MoSi film is in the smooth penetration regime and all flux penetration occurs gradually and uniformly from the edges toward the center of the sample, as described by critical state models. For  $h = 2.5$  Oe, however, a radically different behavior is observed: the pink points in Fig. 1(a) sharply differ from those observed in the smooth regime. For the lowest temperatures, an apparently noisy response is observed in both  $\chi_{ac}(T)$  components while shielding becomes much less effective. The purple points reveal the same trend for measurements carried out with a probe field of 3.5 Oe. As we will demonstrate in this paper using MOI, these characteristics are signs of the occurrence of magnetic flux avalanches in the film [73]. Such variations in  $|\chi'_{ac}|$  and  $\chi''_{ac}$  are then explained by a reduction of the volume of the film free from flux penetration as avalanches advance throughout the sample. Eventually, as  $T$  is increased above 4 K, the noisy behavior in  $\chi_{ac}(T)$  is no longer present for both the 2.5 Oe and 3.5 Oe curves. This occurs because the temperature is increased beyond that for which avalanches can be triggered ( $T_{th}$ ), keeping the sample in a thermomagnetically stable condition, as described by the thermomagnetic model [74]. As such, flux will now only penetrate the sample smoothly, although frozen imprints of previous avalanches may remain in the flux patterns observed in the film.

Flux avalanches are of a stochastic nature. It is there-

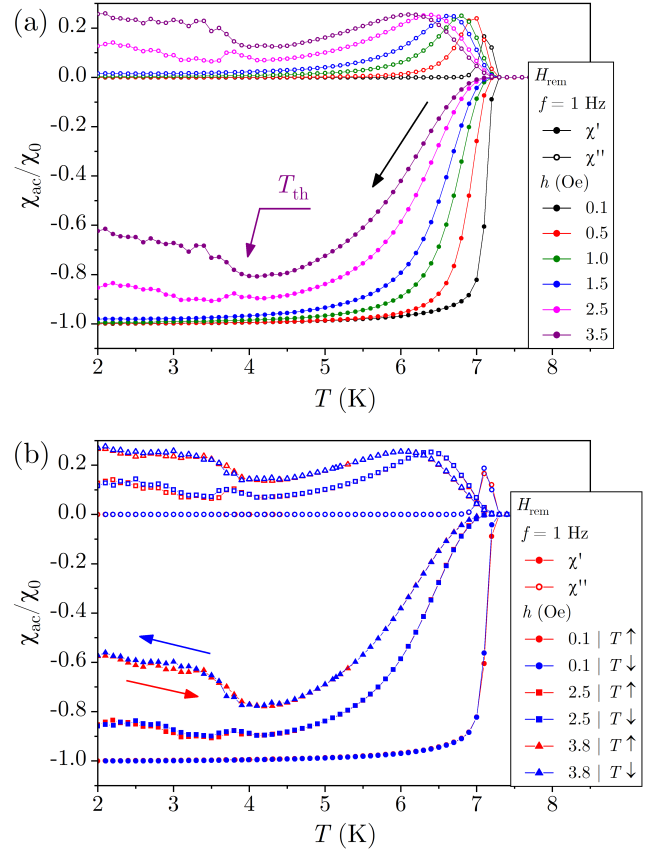


FIG. 1. Temperature-dependent ac susceptibility of a-MoSi film under  $H_{rem}$  obtained using the MPMS. (a) Data acquired as the temperature is decreased from the normal state using a probe magnetic field of  $f = 1$  Hz and amplitude varying from  $h = 0.1$  Oe to  $h = 3.5$  Oe. Purple arrow indicates the onset of flux avalanches, characterizing the paramagnetic reentrance region. (b) Data acquired both as the temperature is decreased from the normal state ( $T \downarrow$ ) and increased from the Meissner state ( $T \uparrow$ ) with  $f = 1$  Hz and  $h = 0.1$  Oe (smooth regime) and  $h = 2.5$  Oe and 3.8 Oe (avalanche regime).

fore not possible to accurately predict their shape or size, nor to precisely pinpoint the moment or the position at which an avalanche will be triggered [37, 44]. In spite of this fact, Fig. 1(b) reveals an interesting feature of  $\chi_{ac}(T)$  measurements: the results are not only largely reproducible but also independent of the thermomagnetic history both in the smooth and in the unpredictable avalanche regime. To illustrate that, we conduct  $\chi_{ac}(T)$  measurements for the a-MoSi film after ZFC to 2 K using a probe field with  $f = 1$  Hz and  $h = 0.1$  Oe. The red circles represent the results as  $T$  is gradually increased through  $T_c$  up to 9 K. Then,  $\chi_{ac}(T)$  is recorded as the temperature is lowered from the normal state back to 2 K, as shown by the blue circles. A close inspection of both curves reveals essentially no difference in  $\chi_{ac}(T)$  in the smooth regime, independently of the direction of the temperature variation. If now  $h$  is increased to 2.5 Oe and

the experiment is repeated, the sample is in the avalanche regime for  $T < T_{th} \sim 4.5$  K. In this temperature range, the red and blue squares in Fig. 1(b) are no longer indistinguishable, although they remain very close to each other. More precisely, the observed ups and downs in  $\chi_{ac}(T)$  gauged as  $T$  is increased mirror those obtained as  $T$  is decreased. The red and blue triangles in Fig. 1(b) reveal the same behavior in the avalanche regime for a higher probe field amplitude  $h = 3.8$  Oe.

#### IV. AC SUSCEPTIBILITY: MOI MEASUREMENTS

We now turn to magneto-optical imaging to explain why there appears to be to a large extent a reversible response in the noisy ac susceptibility behavior caused by stochastic avalanche events. To do so, it is instructive to first recall the working principle of how  $\chi_{ac}(T)$  is obtained in magnetometers such as the MPMS. An applied zero-mean probe ac field with an amplitude  $h$  and frequency  $f$ , such that  $h(t) = h \cos(2\pi ft)$ , induces a time-dependent magnetic moment in the investigated sample. Hence, a detectable electric current is induced in the magnetometer's superconducting pickup coils, connected to the SQUID sensor, allowing the determination of the magnetic moment  $m_{ac}$ . After averaging measurements performed for successive probe field cycles,  $m_{ac}$  is fitted to an equation of the form [75]

$$m_{ac} = C(t) + m' \cos(2\pi ft) + m'' \sin(2\pi ft), \quad (1)$$

where  $C(t)$  represents any dc offset or drift in field or temperature, and  $m'$  and  $m''$  are respectively related to  $\chi'_{ac}$  and  $\chi''_{ac}$  as

$$\chi'_{ac} = \frac{m'}{h} \quad \text{and} \quad \chi''_{ac} = \frac{m''}{h}. \quad (2)$$

Recalling that  $\chi_{ac} = \chi'_{ac} + i\chi''_{ac} = \partial M / \partial H$ , if the total applied magnetic field is  $H = H_{dc} + h$ , then  $\chi_{ac} = \partial M / \partial h$ . Hence, the above measurement protocol can be used in combination with a dc applied magnetic field to gauge the sample susceptibility in different points of the  $M(H)$  curve.

The process to emulate ac measurements using a magneto-optical imaging setup equipped with a dc magnetic field source was first introduced by Ref. [52]. Here, we refer to such measurements as acMOI. To summarize the process, the dc field is incremented in stair-like steps until it reaches a preset maximum amplitude  $h_{dc} = h_{dc}^{max}$ . After each field step, a MO image is recorded. Then, keeping the same step size, the applied field is reduced to  $-h_{dc}^{max}$  and, finally, increased to zero. This routine reproduces one ac field cycle and it is schematically presented in Fig. 2. Although the data acquisition rate of the acMOI technique is substantially slower than the MPMS ac magnetic field source, by successively repeating the above routine, we may take advantage of the frequency-independent nature of the first harmonic  $\chi_{ac}$  to capture

ac effects in the investigated sample. We are also capable of varying external parameters, such as the temperature or an additional dc field, allowing investigations of their effects on the sample. Following, we will explore this ability to qualitatively visualize how magnetic flux penetrates the superconducting a-MoSi film during typical temperature-dependent ac susceptibility measurements, both in the smooth and in the avalanche regimes.

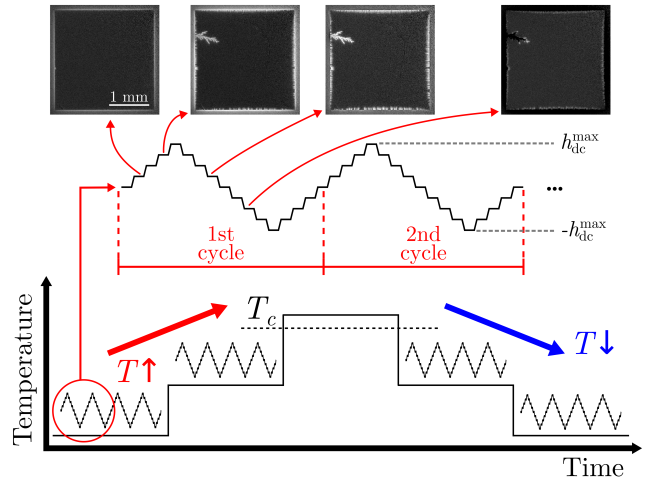


FIG. 2. Ac-emulated magneto-optical imaging (acMOI). A dc magnetic field is progressively applied in stair-like discrete steps. The dc field intensity is varied from zero to  $h_{dc}^{max}$ , then from  $h_{dc}^{max}$  to  $-h_{dc}^{max}$ , and finally from  $-h_{dc}^{max}$  to zero. Successively repeating this field cycle emulates an applied low-frequency ac magnetic field. After each field step, a MO image of the sample is recorded, as exemplified in the detail of the first field cycle. Additional parameters may be controlled, as schematically represented by an increase followed by a decrease in the temperature.

##### A. Smooth penetration regime

Figure 3 exemplifies results obtained for the a-MoSi film following the acMOI procedure. In this case,  $h_{dc}^{max} = 1.0$  Oe, corresponding to the situation in which the film remains in the smooth regime for all temperatures below  $T_c$ , as revealed by Fig. 1(a). The first row of Fig. 3(a) shows MO images as directly obtained during the first field cycle after the sample was zero-field-cooled to the base temperature of 2.9 K. A schematic representation of the point in the field cycle at which each of the four images is captured is presented at the lower left corner of Fig. 3. The first image reveals a shallow bright region surrounding the darker inner region of the square film at 1.0 Oe. As discussed previously, such a bright region represents the small flux front able to penetrate the superconductor at lower temperatures and ac field amplitudes, due to its elevated shielding capacities. As the field cycle continues, the second image, taken at 0 Oe, reveals that some positive flux remains trapped in the

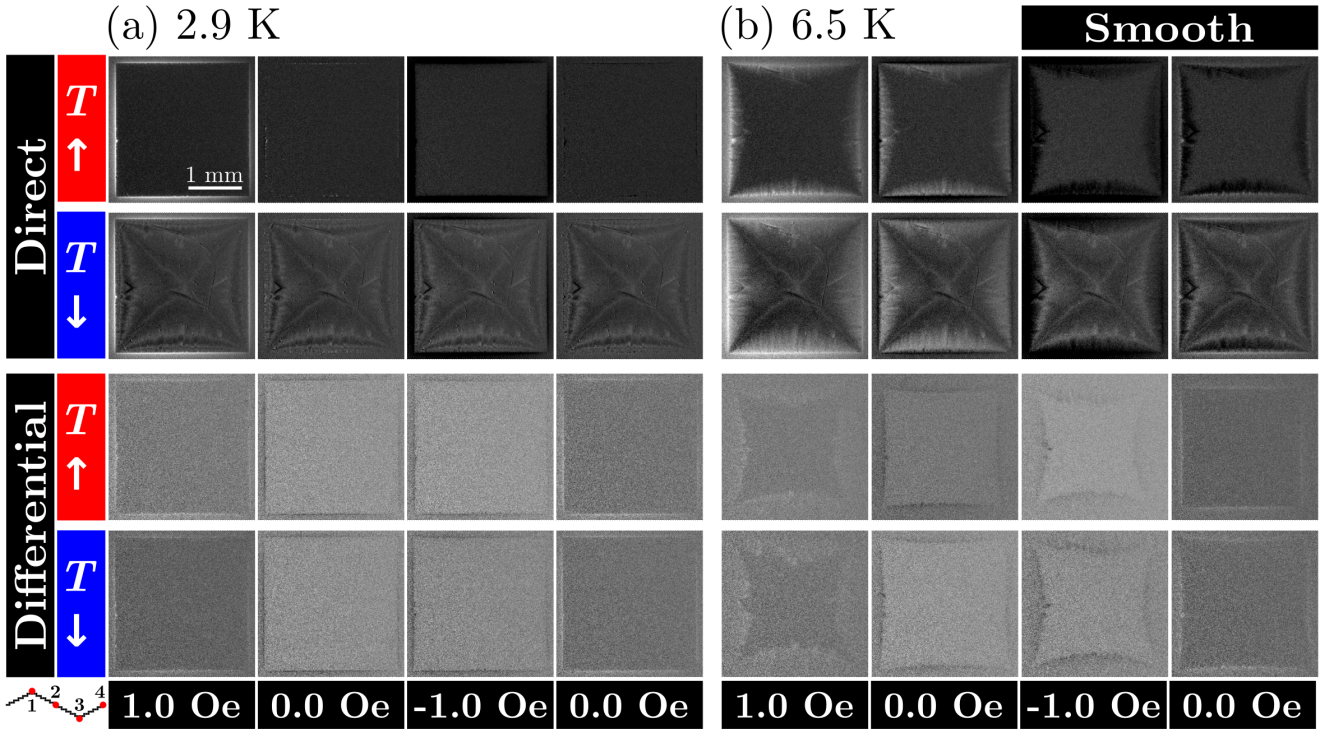


FIG. 3. Comparison between direct MO images and differential MO images of a-MoSi film taken at (a) 2.9 K and (b) 6.5 K as the temperature is increased ( $T \uparrow$ ) after ZFC to the base temperature and as it is decreased ( $T \downarrow$ ) from above  $T_c$ . Data is acquired using an ac-emulating applied field with an amplitude of 1.0 Oe, thus in the smooth regime. The contrast in each image was individually adjusted for optimal visualization of the flux penetration. The lower left corner detail represents the point of the field cycle at which each image was captured.

sample, but the edges of the film no longer appear in bright contrast as the flux polarity is being reversed in that region. In the third image, taken at  $-1.0$  Oe, the flux inside the superconductor has completely reversed its sign and appears now in dark contrast, signaling its negative intensity. Finally, the fourth image, at  $0$  Oe, reveals some trapped negative flux in the interior of the sample, but the edges again indicate the reversal of the applied field. The ac-emulated field cycle is repeated a total of four times before the temperature is increased and set to 3.5 K, 4.0 K, 4.5 K, 5.0 K, 5.5 K, 6.0 K, 6.5 K, and 7.0 K, every time repeating the field cycle four times and collecting a MO image after each field step of 0.1 Oe. We will refer to this data as the  $T \uparrow$  experiment. The first row of images of Fig. 3(b) shows results obtained at 6.5 K as the temperature is increased after ZFC. They are analogous to those obtained at 2.9 K, however, the flux front penetrates deeper into the film due to its reduced shielding capability near  $T_c$ .

Then, the temperature is risen above  $T_c$  in the absence of an applied magnetic field, erasing the magnetic history of the sample. After that,  $T$  is progressively reduced back to the base temperature while subjecting the sample to four ac-emulating field cycles at the same set temperatures listed before. This is the  $T \downarrow$  experiment. The second row in Fig. 3(a) shows the MO images recorded

at 2.9 K during this experiment, i.e., after  $T$  was reduced from above  $T_c$ . Although the temperature is the same, the flux landscapes inside the superconductor in the first and second rows of Fig. 3(a) are completely different. For the images taken during the  $T \downarrow$  experiment, the complete magnetic history of the sample due to the successive field cycles is retained by the film. This happens because higher temperatures enable further flux penetration, therefore the flux trapped in the most inner regions of the sample is not superimposed by new field cycles at lower temperatures. Accordingly, the MO images obtained at 6.5 K as  $T$  is reduced, shown in the second row of Fig. 3(b), differ from those presented in the first row. In this case, the sample was previously subjected to four ac-emulating field cycles at 7.0 K, resulting in the observed trapped flux in the interior of the film.

After these observations, it may be natural to ask why such different flux distributions lead to the indistinguishable  $\chi_{ac}(T)$  observed in the smooth regime in Fig. 1(b) for increasing and decreasing temperatures. To understand this, it is necessary to remember that ac susceptibility is a measurement of the flux variation in the material as the applied field is changed, rather than its total magnetic moment. To gauge flux variation due to the variation of an applied field using MOI, we may turn to what is called differential MOI [76]. This approach

consists of subtracting the measured flux density distribution in a given MO image from that obtained in the previous field step. In other words,  $B_n^{\text{diff}}(x, y) = B_n(x, y) - B_{n-1}(x, y)$ , where  $n$  represents the MO image number, chronologically increasing from the first to the last image obtained in a given data set.

The third and fourth rows of Figs. 3(a) and (b) show differential MO images of the same images represented in the first two rows of each figure. The results demonstrate that, although the flux distribution in the superconductor is vastly different depending on its thermomagnetic history, the flux variation within an ac field cycle does not present significant differences for measurements conducted while increasing or decreasing the sample temperature—given that the probe field amplitude and frequency are kept the same. This notion explains why  $\chi_{\text{ac}}(T)$  does not depend on the sample's thermomagnetic history in the smooth regime. In the Supplemental Material [77], a video highlights this behavior for all MO images obtained during the four field cycles at temperatures of 2.9 K, 3.8 K, 4.5 K, 5.5 K, and 6.5 K.

## B. Flux avalanches regime

Figure 4 presents results obtained by acMOI for an applied field with amplitude of  $h_{\text{dc}}^{\text{max}} = 2.4$  Oe. As revealed in Fig. 1, such a probe field will lead to the nucleation of flux avalanches in the a-MoSi film for temperatures lower than  $T_{\text{th}}$ . These abrupt, non-critical-state-like flux penetration events have a characteristic dendritic morphology observable in several MO images in Fig. 4. Such a strong flux variation leads to the paramagnetic reentrance region in  $\chi_{\text{ac}}(T)$  measurements. The acMOI results in the avalanche regime were obtained using a field step of 0.2 Oe and  $T$  values of 2.9 K, 3.5 K, 3.8 K, 4.5 K, 5.0 K, 5.5 K, 6.0 K, 6.5 K, and 7.0 K.

The interpretation of Fig. 4 is analogous to that of Fig. 3. A series of MO images are taken within the same ac-emulating field cycle both as  $T$  is increased after ZFC to 2.9 K and as  $T$  is decreased after the magnetic history of the sample is erased above  $T_c$ . Figure 4(a) shows images taken at 2.9 K and, hence, below  $T_{\text{th}}$ . In the first row, the first image reveals that a positive flux avalanche was triggered in the film, advancing further into the interior of the sample than the shallow critical-state-like bright flux front. Then, as revealed by the third image, a new, negative flux avalanche, or anti-avalanche, was triggered, reusing the flux channel created by the first positive avalanche [52, 78]. The differential MOI analysis on the third row of Fig. 4(a) allows us to conclude that the avalanches appearing in the first row were not triggered on the depicted images, but as  $h_{\text{dc}}$  was ramped from zero to 2.4 Oe and, then, from 2.4 Oe to  $-2.4$  Oe. This is the case because the differential flux distributions do not show any signs of abrupt flux intake by the sample. On the other hand, analysis of the second and fourth rows of Fig. 4(a) reveals that a positive flux avalanche was

triggered in the sample at 2.4 Oe. The differential image allows us to clearly distinguish this specific penetration event from the complex flux landscape presented by the sample.

In the case depicted in Fig. 4(b),  $T = 5.5$  K  $> T_{\text{th}}$ . Even though previously triggered avalanches are visible in the first row of images, all flux penetration at this temperature occurs smoothly from the edges of the film. Hence, the very different flux landscapes in the first and second rows lead to similar differential flux patterns, shown in the third and fourth rows of Fig. 4(b). These results are compatible with those in Fig. 1, as the sample is in the smooth regime above  $T_{\text{th}}$ . However, if we now compare the differential images below  $T_{\text{th}}$  at 2.9 K, we see that, contrary to the smooth penetration regime, there is not a match between each corresponding image due to the nucleation of flux avalanches. In the Supplemental Material, a video highlights this fact, showing distinct differential flux distributions each time an avalanche occurs in the film either as  $T$  is increased or decreased and at different temperatures.

Such a difference in behavior in the avalanche regime, coupled with the unpredictable nature of these events, seems to indicate that there should not be a match between independent  $\chi_{\text{ac}}(T)$  measurements. Nevertheless, we do observe in Fig. 1(b) very similar behaviors as  $T$  varies up or down. To understand why this happens, we will rely on the potential of MOI as a quantitative analysis tool, as its spatial resolution allows the study of individual avalanches in a manner that is not possible with standard magnetometers like the MPMS.

The first image of the forth row of Fig. 4(a) indicates how we may extract information on individual avalanches. By differentiating an image in which an avalanche event occurs, we are able to highlight it from the rest of the sample's flux landscape. To harness this possibility and study all avalanches triggered in the a-MoSi film during our measurements, we implemented an algorithm in MATLAB, schematically represented in the top row of Fig. 5. As multiple avalanches may occur simultaneously in different parts of the sample, we first select the region of the film which will be analyzed. Then, we differentiate the MO images, resulting in a  $B^{\text{diff}}(x, y)$  distribution around zero outside of the smooth flux front and the avalanches. However, avalanches result in much more intense flux variation than critical-state-like penetration. This allows the algorithm to identify every image in which an avalanche was triggered. Moreover, it is possible to clearly separate the avalanches from the rest of the image by applying an intensity threshold mask over the selected avalanche region. This mask can be used either on the directly obtained MO image or on the differential flux distribution, allowing the investigation of different quantities.

Using this algorithm, we analysed all 3474 MO images obtained using the ac-emulated field cycles with  $h_{\text{dc}}^{\text{max}} = 2.4$  Oe. In those, a total of 105 flux avalanches were triggered. Table I specifies the distribution of these

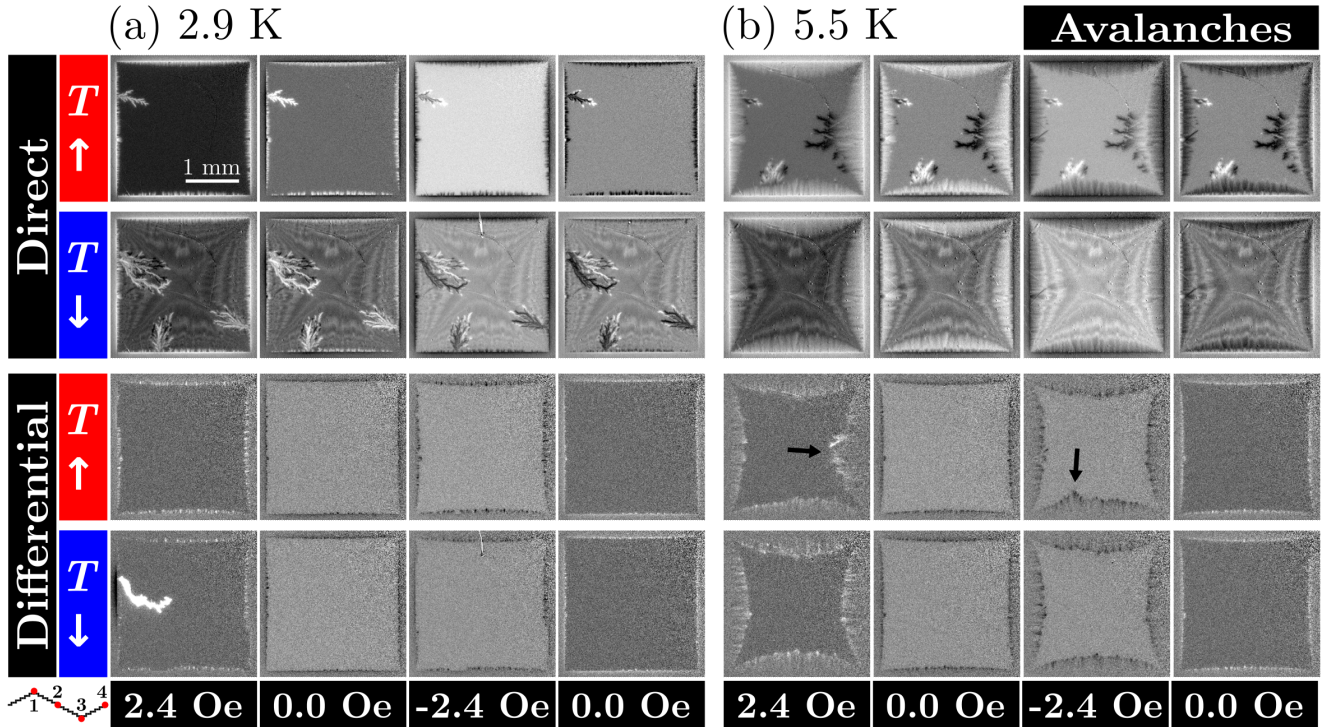


FIG. 4. Comparison between direct MO images and differential MO images of a-MoSi film taken at (a) 2.9 K and (b) 5.5 K as the temperature is increased ( $T \uparrow$ ) after ZFC to the base temperature and as it is decreased ( $T \downarrow$ ) from above  $T_c$ . Data is acquired using an ac-emulating applied field with an amplitude of 2.4 Oe, thus in the avalanche regime. The contrast in each image was individually adjusted for optimal visualization of the flux penetration. The lower left corner detail represents the point of the field cycle at which each image was captured. Black arrows indicate regions of further flux penetration that will be discussed in Section VI.

avalanches between different temperatures. It also highlights if the avalanches were triggered while increasing or decreasing  $T$  as well as if they are comprised of positive or negative flux. These statistics reveal that many more avalanches occur when the temperature is being reduced from above  $T_c$ . This difference is related to the established flux landscape within the sample, clearly visible on the second image row in Fig. 4. As the sample is fully penetrated by vortices, the probability of triggering thermomagnetic instabilities increases [79, 80].

TABLE I. Number of flux avalanches observed in the MO images obtained during the  $T \uparrow$  and  $T \downarrow$  experiments for field cycles with  $h_{dc}^{max} = 2.4$  Oe at different temperatures.

	2.9 K	3.5 K	3.8 K	4.5 K
$T \uparrow$ — Positive flux	8	3	3	0
$T \uparrow$ — Negative flux	8	6	1	0
$T \downarrow$ — Positive flux	19	9	10	1
$T \downarrow$ — Negative flux	21	10	6	0

Once all avalanches were identified, we may calculate the magnetic flux difference in the sample due to each avalanche,  $\Delta\Phi_{aval}$ , by numerically integrating  $B^{diff}(x, y)$ .

Figure 5 shows  $\Delta\Phi_{aval}$  as  $T$  is increased and decreased as a function of the avalanche area,  $A_{aval}$ . Noticeably, the data reveals a temperature-independent linear relationship between  $\Delta\Phi_{aval}$  and  $A_{aval}$ , as highlighted by the sloped guides to the eye. This may be understood considering the microscopic nature of the mixed state in type-II superconductors, in which quantized flux vortices permeate the sample. The vortex core size is proportional to the coherence length of the material,  $\xi$ , whereas the intervortex spacing is related to the penetration depth,  $\lambda$  [24]. In turn, these quantities evolve in temperature as  $(1 - T/T_c)^{-1/2}$ , which implies that they only vary significantly for temperatures close to  $T_c$ . Therefore, the density of vortices is nearly constant in the temperature range for which the film is in the avalanche regime, leading to the behavior observed in Fig. 5. The slope of the linear relationship is roughly equal to 0.75 mT, indicating fields slightly above the ones used to trigger the avalanches. This difference is explained by the higher flux concentration along the edges of the thin film due to demagnetization effects [32].

Moreover, the solid horizontal lines in Fig. 5 represent the net  $\Delta\Phi_{aval}$  calculated by summing  $\Delta\Phi_{aval}$  for all avalanches that occur at a given set temperature when  $T$  is increased (red lines) or decreased (blue lines). Al-



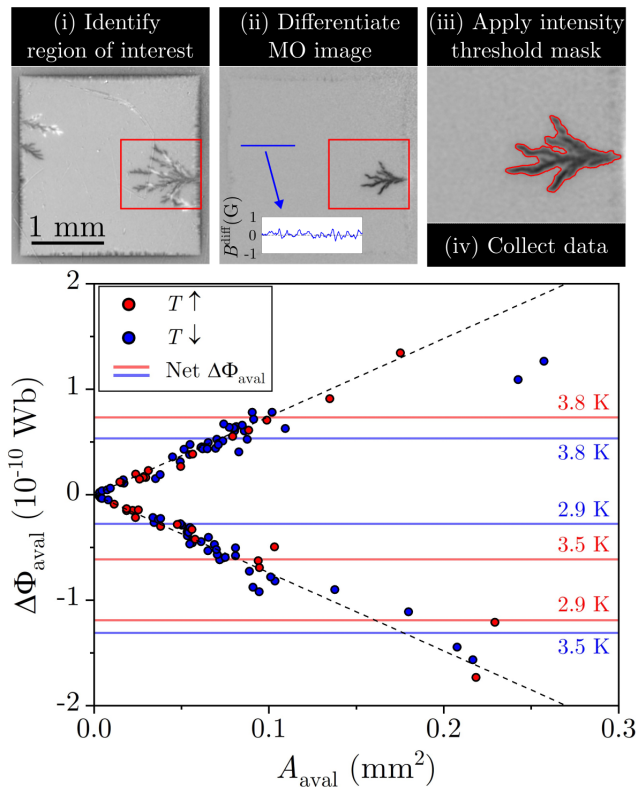


FIG. 5. Top row: demonstration of the process used to obtain quantitative data on single avalanches. See the main text for a detailed explanation. Main panel: the total magnetic flux of each individual avalanche triggered in the a-MoSi film as the temperature is increased ( $T \uparrow$ ) after ZFC to the base temperature and decreased ( $T \downarrow$ ) from above  $T_c$ . Results are plotted against the area of the respective avalanches. Solid horizontal lines represent the net  $\Delta\Phi_{\text{aval}}$  obtained by summing the flux of all avalanches triggered at the same temperature as  $T$  is increased (red) or as  $T$  is decreased (blue). Dashed lines are guides to the eye.

though many more avalanches happen during the  $T \downarrow$  experiment, the blue lines reveal that the net flux variation they cause in the sample is comparable to that caused by a single avalanche. The same is true during the temperature increase, as shown by the red lines. This fact is associated with the effects of an ac field cycle on the superconducting film. As can be observed in Fig. 4, there is a tendency for new avalanches to reuse the flux channel created by previously nucleated avalanches of opposite polarity. Note that bright and dark contrast avalanches are superimposed in the MO images. This same trend has been previously reported both experimentally [52] and numerically [78]. Such behavior is explained by the attractive nature of the interaction between vortices and antivortices, as well as by the fact that the existing avalanche creates an easy channel of locally reduced critical current density inside the film, facilitating the propagation of magnetic flux. A Supplemental Material

video demonstrates that most new avalanches reuse previously existing flux channels. Therefore, these dynamics tend to balance out positive and negative flux variations arising from abrupt penetration events. As the ac susceptibility is measured by averaging the flux variation captured throughout several ac field cycles, the avalanche contributions become very similar in both directions of temperature variation, resulting in the remarkably similar  $\chi_{\text{ac}}(T)$  measurements as  $T$  is increased and decreased, as shown in Fig. 1(b).

## V. QUANTITATIVE AC SUSCEPTIBILITY ANALYSIS FROM MOI

In Section IV, we qualitatively discussed the link between differential MO images and ac susceptibility measurements conducted in the MPMS. In this Section, we demonstrate how MOI can be further utilized as a tool for quantitatively studying ac field-induced effects on superconducting films. The in-phase and out-of-phase components of  $\chi_{\text{ac}}$  are obtained by acMOI as a function of  $T$ , which can then be compared to MPMS measurements.

To achieve that, let us first be reminded that  $\chi'_{\text{ac}}$  is associated with the superconductor inductive response to shield magnetic flux from its interior. Therefore,  $\chi'_{\text{ac}}$  captures the evolution of the sample magnetization with an applied magnetic field. On the other hand,  $\chi''_{\text{ac}}$  is associated with a resistive response arising from energy losses, caused by the dissipative flux motion within the superconductor. As discussed in Ref. [81], this energy can be gauged by evaluating the area of the  $M(h)$  loop,  $A_{\text{ac}}^{\text{loop}}$ , defined by the application of one ac field cycle. This way, we may obtain the  $\chi_{\text{ac}}(T)$  components from ac-emulating MOI cycles as [52]

$$\chi'_{\text{ac}} = \left\langle \frac{\partial \langle M_{\text{MOI}} \rangle}{\partial h_{\text{dc}}} \right\rangle \quad \text{and} \quad \chi''_{\text{ac}} = \frac{A_{\text{ac}}^{\text{loop}}}{\pi (h_{\text{dc}}^{\text{max}})^2}, \quad (3)$$

where the mean magnetization  $\langle M_{\text{MOI}} \rangle$  is obtained from the out-of-plane flux density distribution within the sample on a MO image as [52]

$$\langle M_{\text{MOI}} \rangle = \frac{1}{N_{\text{px}}} \sum_{n=1}^{N_{\text{px}}} \{B_n(x, y)/\mu_0 - h_{\text{dc}}\}, \quad (4)$$

where  $N_{\text{px}}$  is the number of pixels which correspond to the sample within the MO image. These quantities are calculated for each ac-emulating field cycle at a given temperature in SI units as exemplified in Fig. 6(a-b), which shows typical  $\langle M_{\text{MOI}} \rangle(h_{\text{dc}})$  loops. The results are then averaged for the four cycles to obtain the  $\chi_{\text{ac}}(T)$  evolution for the sample.

Figure 6(c-d) displays MPMS measurements of  $\chi_{\text{ac}}(T)$  for the a-MoSi film using probe fields with  $f = 0.05$  Hz and  $h = 1.0$  Oe and 2.4 Oe, hence in the smooth and avalanche regimes, respectively. Although the  $\chi_{\text{ac}}$  analysis is frequency-independent, this  $f$  value is chosen to

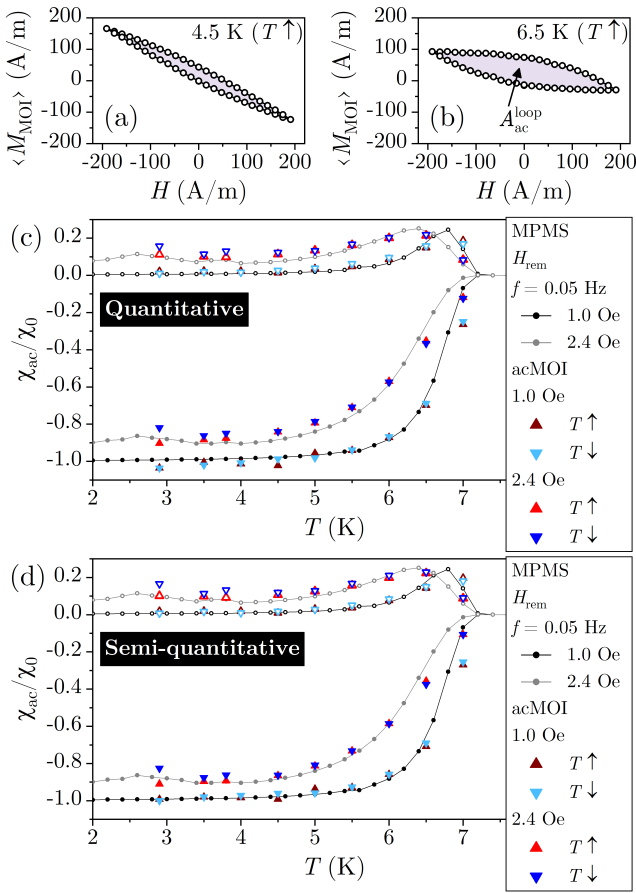


FIG. 6. Example of typical  $M_{\text{MOI}}(h_{\text{dc}})$  loops obtained for measurements as the temperature is increased ( $T \uparrow$ ) at (a) 4.5 K and (b) 6.5 K for  $h_{\text{dc}}^{\text{max}} = 2.4 \text{ Oe} \approx 191 \text{ A/m}$ . Comparison between the temperature-dependent ac susceptibility of the a-MoSi film under  $H_{\text{rem}}$  obtained using the MPMS and (c) a quantitative acMOI analysis and (d) a semi-quantitative acMOI analysis. In both panels, the MPMS measurements are carried at  $f = 0.05 \text{ Hz}$  for better correspondence with the slower MO measurements. MO images are taken as the temperature is increased ( $T \uparrow$ ) and decreased ( $T \downarrow$ ), with ac-emulated field amplitudes of 1.0 Oe and 2.4 Oe, thus in the smooth and avalanche regimes, respectively.

match an “effective” frequency estimated considering a light exposure time of 200 ms during the acMOI measurements, which, in turn, is used to optimize the image contrast. The MPMS data in Fig. 6 is averaged from eight successive field cycles [see Eqs. (1) and (2)]. Although this differs from the four cycles used in the acMOI measurements, Appendix B demonstrates that MPMS results are equivalent for measurements conducted with these numbers of field cycles. Thus, in Fig. 6(c), the MPMS measurements are compared to  $\chi'_{\text{ac}}$  and  $\chi''_{\text{ac}}$  quantitatively obtained from the acMOI measurements using Eq. (3), both as the temperature is increased after ZFC and as  $T$  is decreased from above  $T_c$ . There are two main observations in Fig. 6(c). The first is that, despite limi-

tations in the measurement resolution in comparison to SQUID magnetometers and the presence of defects on the MO indicator which could compromise the result, acMOI captures with high fidelity the behavior of both components of  $\chi_{\text{ac}}(T)$ , specially at the lower temperatures and ac field amplitudes. When  $T$  approaches  $T_c$ , however, the lower contrast of the MO images induce larger errors, therefore, the acMOI data points at 7 K are detached from those obtained using the MPMS. The second observation is that acMOI captures exceptionally well the independence of  $\chi_{\text{ac}}(T)$  on thermomagnetic history in the smooth regime, as  $\chi'_{\text{ac}}$  and  $\chi''_{\text{ac}}$  are mostly superimposed in Fig. 6(c). When the film is in the avalanche regime, acMOI also captures the paramagnetic reentrance observed in the MPMS measurements. However, it appears that the technique is more susceptible to differences in the flux landscape in the sample, as measurements conducted as the temperature was decreased resulted in slightly lower values of  $|\chi'_{\text{ac}}|$ . Nonetheless, within the natural limitations of the technique, it is possible to accurately investigate the ac susceptibility of a superconducting thin film using ac-emulating MOI.

A semi-quantitative approach can also be used to obtain  $\chi_{\text{ac}}(T)$  from acMOI. As highlighted by Eq. (3), the sample magnetization is the crucial ingredient in the calculation of  $\chi'_{\text{ac}}$  and  $\chi''_{\text{ac}}$ .  $M$ , however, is a global parameter, describing the average behavior of the sample. In Fig. 6(c), we obtained this quantity from the local flux density distribution in the film. If we remember that raw MOI data is an intensity count, we may define a mean intensity for each MO image,  $\langle I(x, y) \rangle$ . Then, using measurements performed above  $T_c$ , such that the sample magnetization does not interfere with the flux distribution, we may find a relationship between an applied magnetic field  $H$  and  $\langle I(x, y) \rangle$ . Considering that, above  $T_c$ ,  $M = 0$  and  $H = B/\mu_0$ , the mean flux density distribution  $\langle B \rangle$  can be found by fitting an empirical polynomial relationship between  $\langle B \rangle$  and  $\langle I(x, y) \rangle$  [82]. The influence of defects on the MO indicator can be minimized by subtracting the zero-field background from all images.

Once the images are calibrated, the mean sample magnetization in each MO image within an ac-emulating field cycle can be calculated as

$$\langle M \rangle = \langle B \rangle / \mu_0 - h_{\text{dc}}. \quad (5)$$

Using  $\langle M \rangle$  and Eq. (3), we obtained the  $\chi_{\text{ac}}(T)$  results shown in Fig. 6(d). The results are completely analogous and very similar to those depicted in Fig. 6(c), demonstrating the robustness of MOI as a tool to gauge  $\chi_{\text{ac}}(T)$ .

## VI. ERASING FLUX AVALANCHES

Let us now discuss a side benefit of using quantitative MO data to gain insight into the interaction between an incoming magnetic flux front and the region where an

avalanche previously took place. In Fig. 4(b), arrows indicate regions in differential images taken at 2.4 Oe and  $-2.4$  Oe in which positive and negative flux, respectively, penetrate further into the sample than elsewhere. Figure 7 sheds light on this dynamics by highlighting results obtained for the a-MoSi sample at 5 K as  $T$  is increased from the base temperature after ZFC. Panels (a) and (b) show the same MO images side-by-side, only with different color scales. This is done to evidence different aspects of the flux penetration dynamics.

The first image of Fig. 7, taken at 0 Oe, is captured before the ac-emulating magnetic field is applied to the film at 5 K. Therefore, the depicted flux landscape is a result of the 16 ac-emulating field cycles applied to the film at the four previous temperature steps. Noticeably, a number of flux avalanches took place, resulting in the characteristic dendritic flux-filled regions observed in the sample. On the second row,  $h_{dc}$  is increased to 2.4 Oe for the first time at 5 K. As previously discussed, this will result in the penetration of a positive, smooth flux front from the edges toward the center of the film. Figure 7(a) illustrates an interesting characteristic of the dynamics of how this flux front interacts with avalanches previously triggered in the film. First, notice the presence of a large negative flux avalanche on the right edge of the film framed by the dashed white rectangle. Then, we may observe that the positive flux front penetrates deeper into the sample where it interacts with the negative avalanche than elsewhere—compare, for instance, the penetration from the right edge with that from the top edge of the sample. Additionally, a medium-sized positive flux avalanche had previously occurred on the bottom-left edge of the film. Near that avalanche, the positive flux front has a shallower penetration than on the right side of the bottom edge. The explanation for such a difference in the flux penetration lies in the nature of the attractive interaction between vortices and antivortices [83], leading to the deeper penetration of the flux front coming from the right edge on the second image of Fig. 7(a). However, if the incoming flux has the same polarity as the pinned flux, it will be repelled, causing the shallower penetration of the positive flux front over the positive avalanche on the bottom edge of the sample.

Moreover, vortices and antivortices will be annihilated if they come in close contact, leaving behind a region of zero net magnetic flux on the superconductor. Figure 7(b) allows us to visualize such vortex-antivortex annihilation regions. Using again the second image of the depicted sequence as a reference, we may look at the right edge of the sample, where the positive (dark-blue) flux front penetrates over the negative (yellow) avalanche. Then, we notice the presence of a zero flux (light-blue) region between the flux front and the avalanche. As vortices penetrate the sample from the right edge, they encounter previously pinned antivortices, leading to mutual annihilation. The resulting flux-free region is then filled by new incoming vortices which, in turn, will be annihilated with further pinned antivortices, in a process that

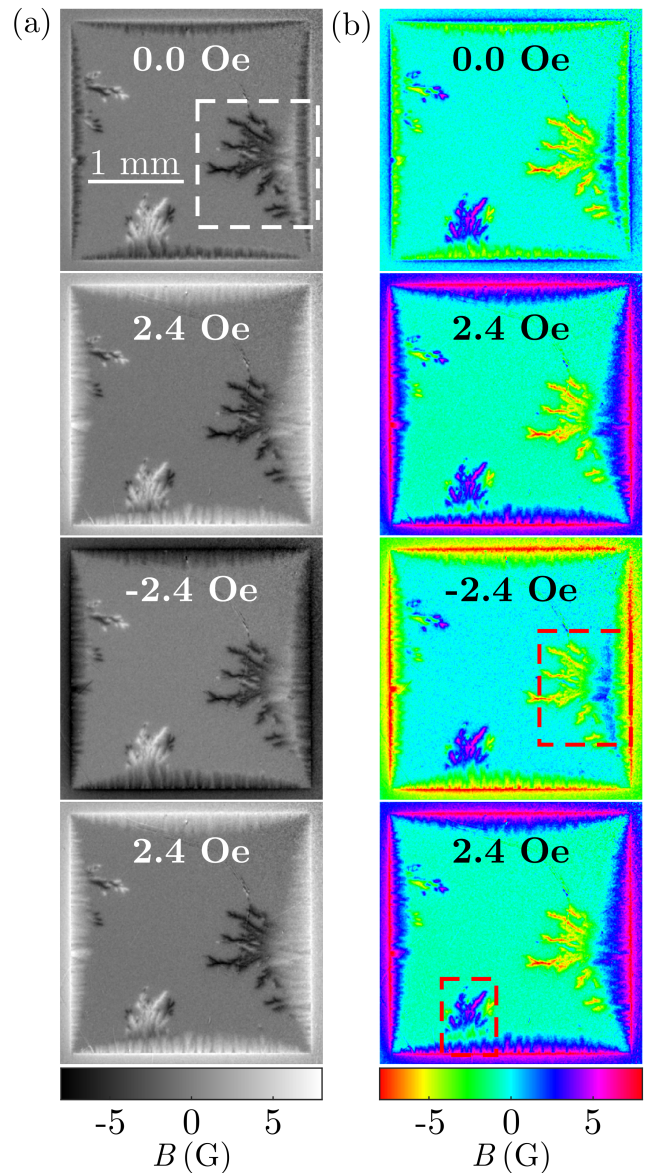


FIG. 7. MOI of a-MoSi film at 5 K as the temperature is increased after ZFC. The images were captured during ac-emulating field cycles with  $h_{dc}^{\max} = 2.4$  Oe and demonstrate how an incoming flux front interacts with previously established avalanches. Panels (a) and (b) show the same MO images with different color scales to highlight different features of the flux penetration dynamics. Dashed rectangles highlight regions in which it is possible to observe the vortex-antivortex annihilation zone.

enables the positive flux penetration as the field is increased up to  $h_{dc}^{\max}$ .

In the next step of the ac-emulating field cycle, the field is reduced to  $-h_{dc}^{\max}$ . Then, negative (yellow) flux will penetrate the sample from the edges. As observed in the third row of Fig. 7, negative flux penetrates less from the right edge of the sample than the positive flux front did. Moreover, we observe that the negative flux further pene-

trates over the positive flux avalanche that previously occurred at the bottom edge of the sample. Thus, the negative flux penetration dynamics follow the same behavior observed when a positive flux front penetrates the film. Accordingly, the third image of Fig. 7(b) reveals a vortex-antivortex annihilation zone between the incoming negative flux front and the deeper positive front. Then, inside the dashed red rectangle, we observe beginning from the edge of the sample: a negative flux region, a first annihilation zone, a positive flux region, a second annihilation zone, and, finally, the negative deeply pinned flux where the avalanche propagated through the film. In the fourth image of the depicted sequence, the applied field is once again increased to  $h_{dc}^{\max}$ , leading to positive flux penetration. Now, along the bottom edge, the incoming positive flux penetrates less than the established negative flux over the positive avalanche. This creates the region highlighted by the dashed rectangle on the fourth image of Fig. 7(b), where it is possible to observe a positive flux region, an annihilation zone, a negative flux region, another annihilation zone, and the positive flux pinned after the avalanche penetrated deep into the sample. The Supplemental Material presents a video highlighting the interaction between an incoming flux front with the pre-established avalanches in Fig. 7 at different moments of the ac-emulating field cycle.

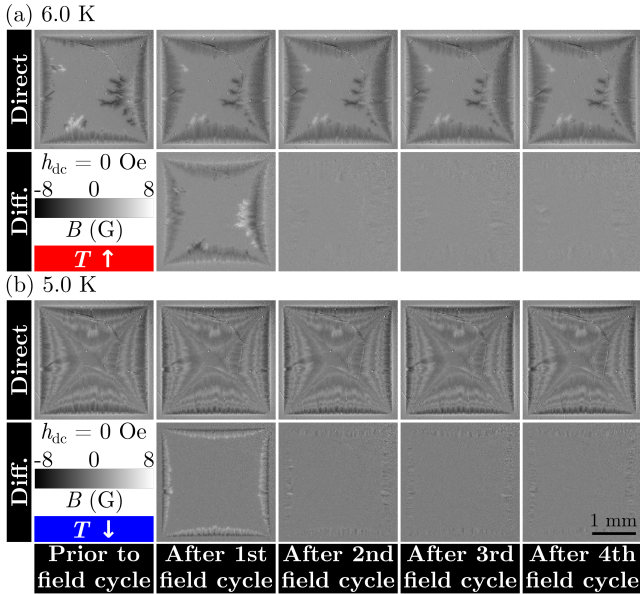


FIG. 8. MOI of a-MoSi film at (a) 6 K as  $T$  is increased after ZFC and (b) 5 K as  $T$  is decreased from above  $T_c$ . The images were captured after ac-emulating field cycles with  $h_{dc}^{\max} = 2.4$  Oe were completed, i.e., under  $h_{dc} = 0$  Oe. The first row shows direct measurements whereas the second row shows differential results. The differential images were obtained by subtracting the images after a field cycle from those obtained after the previous field cycle, i.e., the one in the previous column on the first row.

The flux penetration dynamics in the smooth pene-

tration regime revealed by Fig. 7 hints at a different aspect of ac susceptibility measurements. To wit, Fig. 7(a) shows two panels with  $h_{dc} = 2.4$  Oe where no clear differences are observed in the penetrated flux landscape. Figure 8 further explores this aspect of the results both as the temperature is increased after ZFC [Fig. 8(a), at 6 K] and as it is decreased from above  $T_c$  [Fig. 8(b), at 5 K]. The first row of both panels shows MO images obtained before the ac-emulating magnetic field is applied at the indicated temperature followed by the flux landscape captured at the end of each field cycle, when the a-MoSi is under  $h_{dc} = 0$  Oe. The second row shows differential MO images obtained by subtracting the flux landscape after field cycle  $N$  by that after cycle  $N - 1$ . As established, flux penetration differs when the field is applied at different temperatures. Thus, a different flux pattern is revealed after the first cycle when compared to the previously pinned landscape, as evidenced by the first differential image in both panels. However, as the applied field reaches  $h_{dc}^{\max}$  (or  $-h_{dc}^{\max}$ ), the penetrated positive (or negative) flux front reaches its maximum depth into the sample for those specific measurement conditions. Therefore, there is no sensitive difference between the flux landscapes observed at equivalent  $h_{dc}$  at the subsequent field cycles after the field reaches its maximum value. This is evidenced by the last three differential images in both panels. In the Supplemental Material, an accompanying video shows that these dynamics are observed in all images captured within the four field cycles for the measurements presented in Fig. 8(a). Therefore, in the smooth regime, the important dynamic aspects of flux penetration into superconducting samples are restricted to occur during the first field cycle. This naturally explains the observed independence of  $\chi_{ac}$  on the number of averaged field cycles in MPMS measurements, as reported in Appendix B.

## VII. CONCLUSIONS

We have investigated the ac magnetic susceptibility of a superconducting thin film with lateral dimensions in the millimeter range. Standard global ac magnetometry measurements of frequency-independent first harmonic  $\chi_{ac}(T)$  reveal that the sample exhibits a paramagnetic reentrance related to the abrupt magnetic flux intake experienced during a flux avalanche event. Despite the stochastic nature of these avalanches, their effect on  $\chi_{ac}(T)$  is nearly insensitive to the sample thermomagnetic history. We employ quantitative ac-emulating magneto-optical imaging to uncover the reasons behind this fact. In the smooth penetration regime, the indistinguishability of  $\chi_{ac}(T)$  measured as the temperature is increased from 2 K or decreased from above  $T_c$  is explained using differential MO images highlighting that the flux variation within the sample during an ac cycle is independent of the previously established flux landscape. The same is not true in the presence of flux avalanches. Nev-

ertheless, we demonstrate that new avalanches preferentially nucleate along previously established and frozen avalanche regions of opposite polarity. By quantifying the flux variation due to each single avalanche, we find out that this process leads to similar contributions as  $T$  is increased or decreased. We thus correlate these findings to the similar  $\chi_{ac}(T)$  behavior in the avalanche regime, independently of the thermomagnetic history of the sample. Moreover, we use acMOI to quantitatively gauge  $\chi_{ac}(T)$  in superconductors obtaining excellent agreement with standard global measurements, particularly at low temperatures and probe field amplitudes. Although the results have been obtained for an a-MoSi film, they are of total generality and, in principle, applicable to any kind of type-II superconductor, even those with high critical temperatures. We also take advantage of the technique to locally resolve regions of vortex-antivortex annihilation, explaining how an income flux front interacts with previously nucleated avalanches. This interplay also allows us to visualize that, after the ac field reaches its maximum amplitude in both field polarities, no new features are observed for subsequent field cycles, explaining the observed independence of  $\chi_{ac}$  on the number of cycles averaged to obtain the results. Therefore, by analyzing the history-independent  $\chi_{ac}(T)$  of an a-MoSi sample, we demonstrate that acMOI is an effective technique to quantitatively study frequent-independent ac magnetic field effects in superconducting materials. This was recently employed to explain the impact of flux dynamics and, in particular, avalanches, on the resonance frequency of large-area superconducting coplanar waveguide resonators [84].

### ACKNOWLEDGMENTS

This work was partially supported by Coordenação de Aperfeiçoamento de Pessoal de Nível Superior – Brasil (CAPES) – Finance Code 001, the São Paulo Research Foundation (FAPESP, Grant No. 2021/08781-8), the National Council for Scientific and Technological Development (CNPq, Grants No. 431974/2018-7 and 316602/2021-3) and by the UK EPSRC through Grant EP/I036303/1.

D.A.D.C. and J.C.C.F. contributed equally to this work.

### Appendix A: Ac susceptibility dependency on the drive frequency

Figure 9 shows  $\chi_{ac}(T)$  measurements performed in the MPMS varying the magnetic field drive frequency between 0.05 Hz and 1000 Hz. The results are normalized by  $\chi_0$  obtained from the  $f = 1000$  Hz curve. In the investigated frequency range,  $\chi_{ac}(T)$  shows no significant variations for different values of  $f$ .

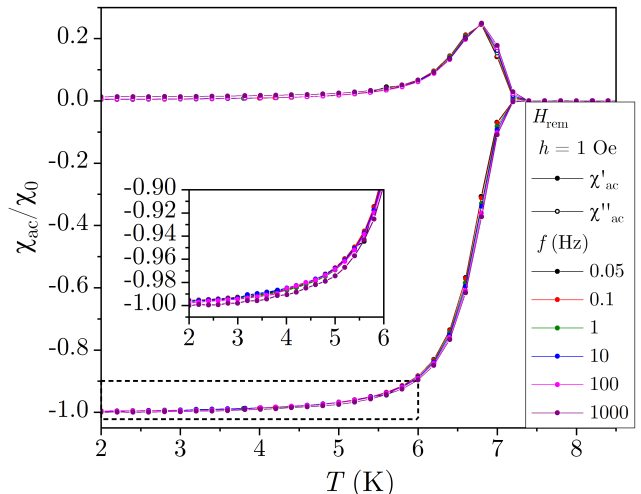


FIG. 9. Temperature-dependent ac susceptibility under  $H_{rem}$  of a-MoSi film obtained using the MPMS. The probe field amplitude is kept constant at  $h = 1$  Oe while  $f$  is varied between 0.05 Hz to 1000 Hz. Inset shows an amplification of the graph region highlighted by the dashed rectangle in the main panel.

### Appendix B: Ac susceptibility dependence on the number of field cycles

Figure 10 shows three different measurements of the ac susceptibility of the a-MoSi sample as a function of  $h$ . The data is obtained varying the number of field cycles used by the MPMS to average the magnetic moment [see Eqs. (1) and (2)]. The  $h$  range explored depicts the full limit of the MPMS. If the sample is in the smooth penetration regime, i.e.,  $h < 2.0$  Oe for  $T = 2$  K, Fig. 10 quantitatively shows that  $\chi_{ac}$  is independent of the number of field cycles. In the avalanche regime, small variations are observed due to the stochastic nature of the abrupt flux penetration events.

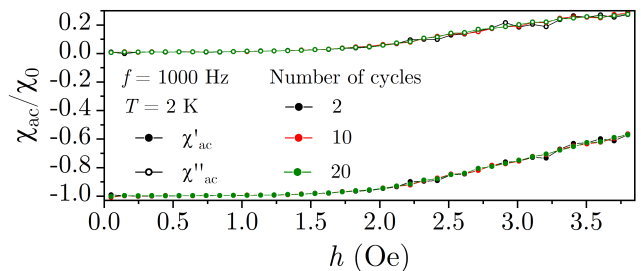


FIG. 10. Ac susceptibility of a-MoSi film under  $H_{rem}$  as a function of  $h$  obtained using the MPMS. The different measurement runs reflect results obtained by averaging different number of field cycles. All measurements were carried out at  $f = 1000$  Hz and  $T = 2$  K.

- 
- [1] A. G. J. MacFarlane, J. P. Dowling, and G. J. Milburn, Quantum technology: the second quantum revolution, *Phil. Trans. R. Soc. Lond. A* **361**, 1655 (2003).
- [2] M. H. Devoret and R. J. Schoelkopf, Superconducting circuits for quantum information: An outlook, *Science* **339**, 1169 (2013).
- [3] G. Wendin, Quantum information processing with superconducting circuits: a review, *Rep. Prog. Phys.* **80**, 025001 (2017).
- [4] M. Kjaergaard, M. E. Schwartz, J. Braumüller, P. Krantz, J. I.-J. Wang, S. Gustavsson, and W. D. Oliver, Superconducting qubits: Current state of play, *Annu. Rev. Condens. Matter Phys.* **11**, 369 (2020).
- [5] A. Blais, A. L. Grimsmo, S. M. Girvin, and A. Wallraff, Circuit quantum electrodynamics, *Rev. Mod. Phys.* **93**, 025005 (2021).
- [6] C. M. Natarajan, M. G. Tanner, and R. H. Hadfield, Superconducting nanowire single-photon detectors: physics and applications, *Supercond. Sci. Technol.* **25**, 063001 (2012).
- [7] A. N. McCaughan and K. K. Berggren, A superconducting-nanowire three-terminal electrothermal device, *Nano Lett.* **14**, 5748 (2014).
- [8] Q.-Y. Zhao, E. A. Toomey, B. A. Butters, A. N. McCaughan, A. E. Dane, S.-W. Nam, and K. K. Berggren, A compact superconducting nanowire memory element operated by nanowire cryotrons, *Supercond. Sci. Technol.* **31**, 035009 (2018).
- [9] E. Strambini *et al.*, A Josephson phase battery, *Nat. Nanotechnol.* **15**, 656 (2020).
- [10] L. Chen *et al.*, Miniaturization of the superconducting memory cell via a three-dimensional Nb nano-superconducting quantum interference device, *ACS Nano* **14**, 11002 (2020).
- [11] N. Ligato, F. Paolucci, E. Strambini, and F. Giazotto, Thermal superconducting quantum interference proximity transistor, *Nat. Phys.* , 1 (2022).
- [12] T. Golod and V. M. Krasnov, Demonstration of a superconducting diode-with-memory, operational at zero magnetic field with switchable nonreciprocity, *Nat. Commun.* **13**, 3658 (2022).
- [13] D. A. D. Chaves, L. Nulens, H. Dausy, B. Raes, D. Yue, W. A. Ortiz, M. Motta, M. J. Van Bael, and J. Van de Vondel, Nanobridge SQUIDs as multilevel memory elements, *Phys. Rev. Appl.* **19**, 034091 (2023).
- [14] J. R. Clem and A. Sanchez, Hysteretic ac losses and susceptibility of thin superconducting disks, *Phys. Rev. B* **50**, 9355 (1994).
- [15] M. Willemin, C. Rossel, J. Hofer, H. Keller, A. Erb, and E. Walker, Strong shift of the irreversibility line in high- $T_c$  superconductors upon vortex shaking with an oscillating magnetic field, *Phys. Rev. B* **58**, R5940 (1998).
- [16] E. H. Brandt and G. P. Mikitik, Why an ac magnetic field shifts the irreversibility line in type-II superconductors, *Phys. Rev. Lett.* **89**, 027002 (2002).
- [17] C. Hoffmann, D. Pooke, and A. D. Caplin, Flux pump for hts magnets, *IEEE Trans. Appl. Supercond.* **21**, 1628 (2011).
- [18] J. Geng and T. A. Coombs, Mechanism of a high- $T_c$  superconducting flux pump: Using alternating magnetic field to trigger flux flow, *Appl. Phys. Lett.* **107**, 10.1063/1.4932950 (2015).
- [19] C. C. d. S. Silva, B. Raes, J. Brisbois, L. R. E. Cabral, A. V. Silhanek, J. Van de Vondel, and V. V. Moshchalkov, Probing the low-frequency vortex dynamics in a nanostructured superconducting strip, *Phys. Rev. B* **94**, 024516 (2016).
- [20] I. Ivan, A. M. Ionescu, V. Sandu, A. Crisan, and L. Miu, Vortex dynamics driven by AC magnetic field in YBCO thin films with complex pinning structures, *Supercond. Sci. Technol.* **31**, 105012 (2018).
- [21] B. Shen, F. Grilli, and T. Coombs, Review of the AC loss computation for HTS using H formulation, *Supercond. Sci. Technol.* **33**, 033002 (2020).
- [22] G. Pasquini, M. M. Bermúdez, and V. Bekeris, AC dynamic reorganization and critical phase transitions in superconducting vortex matter, *Supercond. Sci. Technol.* **34**, 013003 (2020).
- [23] A. A. Abrikosov, On the magnetic properties of superconductors of the second group, *Sov. Phys. JETP* **5**, 1174 (1957).
- [24] G. Blatter, M. V. Feigel'man, V. B. Geshkenbein, A. I. Larkin, and V. M. Vinokur, Vortices in high-temperature superconductors, *Rev. Mod. Phys.* **66**, 1125 (1994).
- [25] E. H. Brandt, Vortex-vortex interaction in thin superconducting films, *Phys. Rev. B* **79**, 134526 (2009).
- [26] A. Chaves, F. M. Peeters, G. A. Farias, and M. V. Milošević, Vortex-vortex interaction in bulk superconductors: Ginzburg-Landau theory, *Phys. Rev. B* **83**, 054516 (2011).
- [27] E. Sardella, P. N. Lisboa Filho, C. C. de Souza Silva, L. R. Eulálio Cabral, and W. A. Ortiz, Vortex-antivortex annihilation dynamics in a square mesoscopic superconducting cylinder, *Phys. Rev. B* **80**, 012506 (2009).
- [28] C. P. Bean, Magnetization of high-field superconductors, *Rev. Mod. Phys.* **36**, 31 (1964).
- [29] Y. B. Kim, C. F. Hempstead, and A. R. Strnad, Critical persistent currents in hard superconductors, *Phys. Rev. Lett.* **9**, 306 (1962).
- [30] C. Jooss, J. Albrecht, H. Kuhn, S. Leonhardt, and H. Kronmüller, Magneto-optical studies of current distributions in high- $T_c$  superconductors, *Rep. Prog. Phys.* **65**, 651 (2002).
- [31] F. Colauto, M. Motta, and W. A. Ortiz, Controlling magnetic flux penetration in low- $t_c$  superconducting films and hybrids, *Supercond. Sci. Technol.* **34**, 013002 (2020).
- [32] E. Zeldov, J. R. Clem, M. McElfresh, and M. Darwin, Magnetization and transport currents in thin superconducting films, *Phys. Rev. B* **49**, 9802 (1994).
- [33] E. H. Brandt, Superconductor disks and cylinders in an axial magnetic field. I. flux penetration and magnetization curves, *Phys. Rev. B* **58**, 6506 (1998).
- [34] D. V. Shantsev, Y. M. Galperin, and T. H. Johansen, Thin superconducting disk with  $b$ -dependent  $J_c$ : flux and current distributions, *Phys. Rev. B* **60**, 13112 (1999).
- [35] S. L. Wipf, Review of stability in high temperature superconductors with emphasis on flux jumping, *Cryogenics* **31**, 936 (1991).
- [36] D. V. Denisov, A. L. Rakhmanov, D. V. Shantsev, Y. M. Galperin, and T. H. Johansen, Dendritic and uniform flux jumps in superconducting films, *Phys. Rev. B* **73**, 014512 (2006).

- [37] D. V. Denisov, D. V. Shantsev, Y. M. Galperin, E.-M. Choi, H.-S. Lee, S.-I. Lee, A. V. Bobyl, P. E. Goa, A. A. F. Olsen, and T. H. Johansen, Onset of dendritic flux avalanches in superconducting films, *Phys. Rev. Lett.* **97**, 077002 (2006).
- [38] P. Leiderer, J. Boneberg, P. Brüll, V. Bujok, and S. Herminghaus, Nucleation and growth of a flux instability in superconducting  $\text{YBa}_2\text{Cu}_3\text{O}_{7-x}$  films, *Phys. Rev. Lett.* **71**, 2646 (1993).
- [39] C. A. Durán, P. L. Gammel, R. E. Miller, and D. J. Bishop, Observation of magnetic-field penetration via dendritic growth in superconducting niobium films, *Phys. Rev. B* **52**, 75 (1995).
- [40] T. H. Johansen, M. Baziljevich, D. Shantsev, P. E. Goa, Y. M. Galperin, W. N. Kang, H. J. Kim, E. M. Choi, M.-S. Kim, and S. I. Lee, Dendritic flux patterns in  $\text{MgB}_2$  films, *Supercond. Sci. Technol.* **14**, 726 (2001).
- [41] U. Bolz, B. Biehler, D. Schmidt, B.-U. Runge, and P. Leiderer, Dynamics of the dendritic flux instability in  $\text{YBa}_2\text{Cu}_3\text{O}_{7-\delta}$  films, *Europhys. Lett.* **64**, 517 (2003).
- [42] I. S. Aranson, A. Gurevich, M. S. Welling, R. J. Wijngaarden, V. K. Vlasko-Vlasov, V. M. Vinokur, and U. Welp, Dendritic flux avalanches and nonlocal electrodynamics in thin superconducting films, *Phys. Rev. Lett.* **94**, 037002 (2005).
- [43] J. I. Vestgård, D. V. Shantsev, Y. M. Galperin, and T. H. Johansen, Dynamics and morphology of dendritic flux avalanches in superconducting films, *Phys. Rev. B* **84**, 054537 (2011).
- [44] F. Colauto, M. Motta, A. Palau, M. G. Blamire, T. H. Johansen, and W. A. Ortiz, First observation of flux avalanches in a-MoSi superconducting thin films, *IEEE Trans. Appl. Supercond.* **25**, 1 (2015).
- [45] J. I. Vestgård, T. H. Johansen, and Y. M. Galperin, Nucleation and propagation of thermomagnetic avalanches in thin-film superconductors (Review Article), *Low Temp. Phys.* **44**, 460 (2018).
- [46] A. L. Schawlow, Structure of the intermediate state in superconductors, *Phys. Rev.* **101**, 573 (1956).
- [47] Y. B. Kim, C. F. Hempstead, and A. R. Strnad, Magnetization and critical supercurrents, *Phys. Rev.* **129**, 528 (1963).
- [48] P. Esquinazi, A. Setzer, D. Fuchs, Y. Kopelevich, E. Zeldov, and C. Assmann, Vortex avalanches in Nb thin films: Global and local magnetization measurements, *Phys. Rev. B* **60**, 12454 (1999).
- [49] E. Altshuler and T. H. Johansen, Colloquium: Experiments in vortex avalanches, *Rev. Mod. Phys.* **76**, 471 (2004).
- [50] A. V. Silhanek, S. Raedts, and V. V. Moshchalkov, Paramagnetic reentrance of ac screening: Evidence of vortex avalanches in Pb thin films, *Phys. Rev. B* **70**, 144504 (2004).
- [51] M. Menghini, R. J. Wijngaarden, A. V. Silhanek, S. Raedts, and V. V. Moshchalkov, Dendritic flux penetration in pb films with a periodic array of antidots, *Phys. Rev. B* **71**, 104506 (2005).
- [52] M. Motta, F. Colauto, R. Zadorosny, T. H. Johansen, R. B. Dinner, M. G. Blamire, G. W. Ataklti, V. V. Moshchalkov, A. V. Silhanek, and W. A. Ortiz, Visualizing the ac magnetic susceptibility of superconducting films via magneto-optical imaging, *Phys. Rev. B* **84**, 214529 (2011).
- [53] R. B. Goldfarb, M. Lelental, and C. A. Thompson, Alternating-field susceptometry and magnetic susceptibility of superconductors, in *Magnetic Susceptibility of Superconductors and Other Spin Systems*, edited by R. A. Hein, T. L. Francavilla, and D. H. Liebenberg (Springer US, Boston, MA, 1991) pp. 49–80.
- [54] F. Gömöry, Characterization of high-temperature superconductors by AC susceptibility measurements, *Supercond. Sci. Technol.* **10**, 523 (1997).
- [55] K.-H. Müller, Ac susceptibility of high temperature superconductors in a critical state model, *Physica C* **159**, 717 (1989).
- [56] A. A. M. Oliveira, N. Hur, S.-W. Cheong, and W. A. Ortiz, Vortex glass melting in Mg-deficient  $\text{MgB}_2$ , *Phys. Rev. B* **82**, 104506 (2010).
- [57] R. B. G. Kramer, G. W. Ataklti, V. V. Moshchalkov, and A. V. Silhanek, Direct visualization of the Campbell regime in superconducting stripes, *Phys. Rev. B* **81**, 144508 (2010).
- [58] L. L. Zhao, S. Lausberg, H. Kim, M. A. Tanatar, M. Brando, R. Prozorov, and E. Morosan, Type-I superconductivity in  $\text{YbSb}_2$  single crystals, *Phys. Rev. B* **85**, 214526 (2012).
- [59] C. V. Topping and S. J. Blundell, A.C. susceptibility as a probe of low-frequency magnetic dynamics, *J. Phys.: Condens. Matter* **31**, 013001 (2018).
- [60] M. I. Erements, V. S. Minkov, A. P. Drozdov, P. P. Kong, V. Ksenofontov, S. I. Shylin, S. L. Bud'ko, R. Prozorov, F. F. Balakirev, D. Sun, S. Mozaffari, and L. Balicas, High-temperature superconductivity in hydrides: Experimental evidence and details, *J. Supercond. Novel Magn.* **35**, 965 (2022).
- [61] G. Ghigo, M. Fracasso, R. Gerbaldo, L. Gozzelino, F. Laviano, A. Napolitano, G.-H. Cao, M. J. Graf, R. Prozorov, T. Tamegai, Z. Shi, X. Xing, and D. Torsello, High-frequency ac susceptibility of iron-based superconductors, *Materials* **15**, 1079 (2022).
- [62] D. Bosworth, S.-L. Sahonta, R. H. Hadfield, and Z. H. Barber, Amorphous molybdenum silicon superconducting thin films, *AIP Advances* **5**, 087106 (2015).
- [63] S. Kubo, Superconducting properties of amorphous MoX (X=Si, Ge) alloy films for Abrikosov vortex memory, *J. Appl. Phys.* **63**, 2033 (1988).
- [64] A. Banerjee, L. J. Baker, A. Doye, M. Nord, R. M. Heath, K. Erotokritou, D. Bosworth, Z. H. Barber, I. MacLaren, and R. H. Hadfield, Characterisation of amorphous molybdenum silicide (MoSi) superconducting thin films and nanowires, *Supercond. Sci. Technol.* **30**, 084010 (2017).
- [65] V. B. Verma, B. Korzh, F. Bussièrès, R. D. Horansky, S. D. Dyer, A. E. Lita, I. Vayshenker, F. Marsili, M. D. Shaw, H. Zbinden, R. P. Mirin, and S. W. Nam, High-efficiency superconducting nanowire single-photon detectors fabricated from MoSi thin-films, *Opt. Express* **23**, 33792 (2015).
- [66] M. Caloz, M. Perrenoud, C. Autebert, B. Korzh, M. Weiss, C. Schönenberger, R. J. Warburton, H. Zbinden, and F. Bussièrès, High-detection efficiency and low-timing jitter with amorphous superconducting nanowire single-photon detectors, *Appl. Phys. Lett.* **112**, 061103 (2018).
- [67] X. Zhang, I. Charaev, H. Liu, T. X. Zhou, D. Zhu, K. K. Berggren, and A. Schilling, Physical properties of amorphous molybdenum silicide films for single-photon detec-

- tors, *Supercond. Sci. Technol.* **34**, 095003 (2021).
- [68] L. E. Helseth, R. W. Hansen, E. I. Il'yashenko, M. Bazilevich, and T. H. Johansen, Faraday rotation spectra of bismuth-substituted ferrite garnet films with in-plane magnetization, *Phys. Rev. B* **64**, 174406 (2001).
- [69] G. Shaw, J. Brisbois, L. B. G. L. Pinheiro, *et al.*, Quantitative magneto-optical investigation of superconductor/ferromagnet hybrid structures, *Rev. Sci. Instrum.* **89**, 023705 (2018).
- [70] P. Thevenaz, U. Ruttimann, and M. Unser, A pyramid approach to subpixel registration based on intensity, *IEEE Trans. Image Process.* **7**, 27 (1998).
- [71] C. A. Schneider, W. S. Rasband, and K. W. Eliceiri, NIH Image to ImageJ: 25 years of image analysis, *Nat. Methods* **9**, 671 (2012).
- [72] H. Ferrari, V. Bekkeris, and T. Johansen, Magneto-optic imaging of domain walls in ferrimagnetic garnet films, *Physica B* **398**, 476 (2007).
- [73] S. Raedts, A. V. Silhanek, M. J. Van Bael, and V. V. Moshchalkov, Flux-pinning properties of superconducting films with arrays of blind holes, *Phys. Rev. B* **70**, 024509 (2004).
- [74] V. V. Yurchenko, D. V. Shantsev, T. H. Johansen, M. R. Nevala, I. J. Maasilta, K. Senapati, and R. C. Budhani, Reentrant stability of superconducting films and the vanishing of dendritic flux instability, *Phys. Rev. B* **76**, 092504 (2007).
- [75] Quantum Design, Magnetic property measurement system: AC option user's manual, San Diego (1999); Introduction to: AC susceptibility, Available at: [qdusa.com](http://qdusa.com).
- [76] A. Soibel, E. Zeldov, M. Rappaport, Y. Myasoedov, T. Tamegai, S. Ooi, M. Konczykowski, and V. B. Geshkenbein, Imaging the vortex-lattice melting process in the presence of disorder, *Nature* **406**, 282 (2000).
- [77] See Supplemental Material at [URL\\_will\\_be\\_inserted\\_by\\_publisher](https://www.nature.com/articles/s41534-023-00241-8) for videos highlighting aspects of the flux penetration dynamics revealed in the main text.
- [78] Z. Jing and M. D. Ainslie, Numerical simulation of flux avalanches in type-II superconducting thin films under transient AC magnetic fields, *Supercond. Sci. Technol.* **33**, 084006 (2020).
- [79] A. J. Qviller, V. V. Yurchenko, K. Eliassen, J. I. Vestgård, T. H. Johansen, M. R. Nevala, I. J. Maasilta, K. Senapati, and R. C. Budhani, Irreversibility of the threshold field for dendritic flux avalanches in superconductors, *Physica C* **470**, 897 (2010).
- [80] L. B. L. G. Pinheiro, L. Jiang, E. A. Abbey, D. A. D. Chaves, A. J. Chiquito, T. H. Johansen, J. Van de Vondel, C. Xue, Y.-H. Zhou, A. V. Silhanek, W. A. Ortiz, and M. Motta, Magnetic flux penetration in nanoscale wedge-shaped superconducting thin films, *Phys. Rev. B* **106**, 224520 (2022).
- [81] J. R. Clem, AC losses in type-II superconductors, in *Magnetic Susceptibility of Superconductors and Other Spin Systems*, edited by R. A. Hein, T. L. Francavilla, and D. H. Liebenberg (Springer, New York, NY, 1991) pp. 177-211.
- [82] For the data presented in this work, we found by inspection that a third degree polynomial successfully described the behavior of the mean intensity with the applied magnetic field.
- [83] D. A. D. Chaves, I. M. de Araújo, D. Carmo, F. Colauto, A. A. M. de Oliveira, A. M. H. de Andrade, T. H. Johansen, A. V. Silhanek, W. A. Ortiz, and M. Motta, Enhancing the effective critical current density in a Nb superconducting thin film by cooling in an inhomogeneous magnetic field, *Appl. Phys. Lett.* **119**, 022602 (2021).
- [84] L. Nulens, N. Lejeune, J. Caeyers, S. Marinković, I. Cools, H. Dausy, S. Basov, B. Raes, M. J. V. Bael, A. Geresdi, A. V. Silhanek, and J. V. de Vondel, Catastrophic magnetic flux avalanches in NbTiN superconducting resonators (2023), arXiv:2305.02418 [cond-mat.supr-con].



# Final remarks and outlook

In this thesis, I have presented different studies in which the core concept is to explore the interaction of superconducting materials with applied magnetic fields to tune properties or induce effects that are potentially useful for implementations of superconducting technology.

Chapter 3 deals with the field cooling of superconducting thin films under different magnetic field configurations. To wit, a plain Nb film is field-cooled (i) without an applied field, (ii) under positive and negative homogeneous fields, and (iii) under positive and negative inhomogeneous fields, the latter generated by a superconducting ring concentric to the Nb film. The field cooling procedures result in different distributions of pinned magnetic flux entities through the film, either vortices or antivortices, depending on the field orientation. Then, using MOI, we reveal a hierarchy of the effective critical currents through the film depending on the interaction with the established flux landscape. The study demonstrates that cooling under inhomogeneous magnetic fields with a direction matching that of an incoming flux front allows for the highest effective critical current. The results are consistent if the data is analyzed by critical state models in which the critical current density depends or not on the magnetic flux. Therefore, changing the distribution of the applied magnetic field during a field cooling procedure allows for tuning, and enhancing, the amount of current a film can carry in the superconducting state without requiring any further complex nanofabrication steps, such as the inclusion of antidots.

In Chapter 4, I presented two studies investigating the effects of a single FIB-milled weak-link on the properties of Nb thin films. First, we systematically characterized the

normal state and superconducting properties, quantifying the effects of the nanofabrication process. Overall, there is a deterioration of superconductivity related to the inclusion of Ga impurities along the patterned area. We also confirmed that the reduction in the superconducting critical temperature can be directly linked to a modification in the normal state electronic transport with the emergence of a squared-in-temperature resistivity contribution by the degree of impurities included by the FIB. Another interesting observation is the emergence of a local magnetization peak in the field-decreasing branch of the magnetization hysteresis curve for the patterned samples. This effect is further studied by MOI, evidencing a transformation in the sample behavior. Magnetic fields at which the magnetization peaks cause the sample to behave as a strong-link, allowing current to flow through the patterned region largely unaffected. By quantifying the MOI data, we can understand the observed tunable effect arising from the reduced energy dissipation caused by the immobilization of vortices that tend to leave the sample through the weak-link as the applied field is reduced. Therefore, the resulting modulation of the magnetic flux can be explored in superconducting devices, such as a flux pump. Moreover, the phenomenon can be employed in the design of superconducting current attenuators and amplifiers.

Chapter 5 describes the behavior of amorphous MoGe nanobridge SQUIDs in which the elongated constriction is sufficiently long to induce metastability in the system. By first characterizing the device's vorticity diamonds, it is possible to map adequate bias magnetic field and current values enabling reliable access to any available vorticity state. Then, it is possible to read out several states at a single field value, depending on the characteristics of the device and the energy stored by the prepared states, characterizing the nanobridge SQUID as a viable superconducting multilevel memory element, increasing the density of information able to be stored in comparison to similar binary alternatives. However, selecting the states is a stochastic process, which is unwanted in practical applications of such devices. By further understanding the SQUID's energy dependence on the applied field, we demonstrated how this limitation can be overcome using a phase

slip-based mechanism to switch between consecutive vorticity states. Further investigating this hypothesis using high-frequency setups, enabling faster current pulses to be used to switch the states, may allow reliable access to a two-level quantum system, realizing a phase slip-based flux qubit.

Finally, Chapter 6 presents a study on how MOI can be used to gauge ac magnetic field effects on superconducting films. This can be achieved despite the experimental setup characteristic image acquisition times only allowing for reliable readings of dc fields. An ac-emulating field procedure circumvents this limitation and MOI results can be successfully quantitatively compared to temperature-dependent first-harmonic ac magnetic susceptibility data obtained using standard SQUID-based ac magnetometry. We employ such an acMOI technique to investigate why the thermomagnetic history of an amorphous MoSi film does not affect its susceptibility response, even in the presence of stochastic avalanche events. By exploring the spatial resolution in MOI to obtain information on individual flux avalanches, we reveal that, although the pinned flux landscape influences the triggering of new avalanches, there is an overall tendency that opposite-polarity events superpose those previously existing avalanche regions, such that the net contribution of these events within multiple ac field cycles tends to zero. The technique also demonstrates the existence of vortex-antivortex annihilation zones in regions where an incoming flux front interacts with the previously established flux of opposite polarity.

Overall, this collection of papers and manuscripts presents alternatives to motivate the study and development of new superconducting devices by providing avenues for controlling the properties of superconducting materials. It is worth mentioning that the observed effects are not believed to be directly tied to the specific samples used in the respective works and should also be observed in other type-II materials, such as in high-temperature superconductors.

# List of Publications

This list contains published papers and works under peer review at the time of the thesis defense.

◆ The following works are covered by this thesis:

1) **Davi A. D. Chaves**, I. M. de Araújo, D. Carmo, F. Colauto, A. A. M. de Oliveira, A. M. H. de Andrade, T. H. Johansen, A. V. Silhanek, W. A. Ortiz, and M. Motta, *Enhancing the effective critical current density in a Nb superconducting thin film by cooling in an inhomogeneous magnetic field*, Applied Physics Letters **119**, 022602 (2021) [Editor's Pick].

2) M. I. Valerio-Cuadros,\* **Davi A. D. Chaves**,\* F. Colauto, A. A. M. de Oliveira, A. M. H. de Andrade, T. H. Johansen, W. A. Ortiz, and M. Motta, *Superconducting properties and electron scattering mechanisms in a Nb film with a single weak-link excavated by Focused Ion Beam*, Materials **14**, 7274 (2021) [Editor's Choice].

\* Equal contributors.

3) **Davi A. D. Chaves**, M. I. Valerio-Cuadros, L. Jiang, E. A. Abbey, F. Colauto, A. A. M. Oliveira, A. M. H. Andrade, L. B. L. G. Pinheiro, T. H. Johansen, C. Xue, Y.-H. Zhou, A. V. Silhanek, W. A. Ortiz, and M. Motta, *Magnetic field induced weak-to-strong-link transformation in patterned superconducting films*, Physical Review B **108**, 214502 (2023).

4) **Davi A. D. Chaves**, L. Nulens, H. Dausy, B. Raes, D. Yue, W. A. Ortiz, M.

Motta, M. J. Van Bael, J. Van de Vondel, *Nanobridge SQUIDs as multilevel memory elements*, Physical Review Applied **19**, 034091 (2023).

5) **Davi A. D. Chaves**,\* J. C. Corsaletti Filho,\* E. A. Abbey, D. Bosworth, Z. H. Barber, M. G. Blamire, T. H. Johansen, A. V. Silhanek, W. A. Ortiz, and M. Motta, *Understanding the history-independent ac susceptibility of a superconducting thin film through quantitative magneto-optical imaging*, arXiv:2309.08062 (2023).

\* Equal contributors.

◆ The following works have also been produced during my Ph.D. studies, but have not been included in this thesis:

6) **Davi A. D. Chaves**, F. L. Zabotto, W. A. Ortiz., and A. J. Gualdi, *PMN-PT/NFO magnetoelectric characterization and the advantages of the dynamic stress magnetization model*, Ferroelectrics 582, 12-20 (2021).

7) A. M. Caffer, **Davi A. D. Chaves**, A. L. Pessoa, Claudio L. Carvalho, W. A. Ortiz, R. Zadorosny, and M. Motta, *Optimum heat treatment to enhance the weak-link response of Y123 nanowires prepared by Solution Blow Spinning*, Superconductor Science and Technology **34**, 025009 (2021).

8) L. B. L. G. Pinheiro, L. Jiang, E. A. Abbey, **Davi A. D. Chaves**, A. J. Chiquito, T. H. Johansen, J. Van de Vondel, C. Xue, Y.-H. Zhou, A. V. Silhanek, W. A. Ortiz, M. Motta, *Magnetic flux penetration in nanoscale wedge-shaped superconducting thin films*, Physical Review B **106**, 224520 (2022).

9) S. Marinković, E. A. Abbey, **Davi A. D. Chaves**, S. Collienne, E. Fourneau, L. Jiang, C. Xue, Y. H. Zhou, W. A. Ortiz, M. Motta, N. D. Nguyen, A. Volodin, J. Van de Vondel, and A. V. Silhanek, *Effect of moderated electropulsing on Nb multiterminal transport bridge*, Physical Review Applied **19**, 054009 (2023).

# Bibliography

- [1] D. Goodstein and J. Goodstein, “Richard Feynman and the history of superconductivity,” *Physics in Perspective*, vol. 2, pp. 30–47, 2000.
- [2] C. H. Lees, “The liquefaction of gases,” *Nature*, vol. 104, no. 2610, p. 247, 1919.
- [3] P. F. Dahl, “Kamerlingh onnes and the discovery of superconductivity: The Leyden years, 1911-1914,” *Historical Studies in the Physical Sciences*, vol. 15, no. 1, pp. 1–37, 1984.
- [4] D. van Delft, *Freezing Physics: Heike Kamerlingh Onnes and the Quest for Cold*. History of science and scholarship in the Netherlands, Amsterdam: Royal Netherlands Academy of Arts and Sciences, 2007.
- [5] Wikipedia contributors, “Timeline of low-temperature technology — Wikipedia, the free encyclopedia,” 2023. [https://en.wikipedia.org/w/index.php?title=Timeline\\_of\\_low-temperature\\_technology&oldid=1157917036](https://en.wikipedia.org/w/index.php?title=Timeline_of_low-temperature_technology&oldid=1157917036), [Online; accessed 12-June-2023].
- [6] P. Drude, “Zur elektronentheorie der metalle,” *Annalen der Physik*, vol. 306, no. 3, pp. 566–613, 1900.
- [7] H. K. Onnes, K. Gavroglu (ed), and Y. Goudaroulis (ed), *Through Measurement to Knowledge: The Selected Papers of Heike Kamerlingh Onnes 1853–1926*. Dordrecht: Springer Netherlands, 1991.

- [8] H. K. Onnes, K. Gavroglu (ed), and Y. Goudaroulis (ed), *Through Measurement to Knowledge: The Selected Papers of Heike Kamerlingh Onnes 1853–1926: Further experiments with liquid helium. (a) C. On the change of electric resistance of pure metals at very low temperatures etc. IV. The resistance of pure mercury at helium temperatures; (b) D. On the change of the electrical resistance of pure metals at very low temperatures, etc. V. The disappearance of the resistance of mercury; (c) G. On the electrical resistance of pure metals, etc. VI. On the sudden change in the rate at which the resistance of mercury disappears.* Dordrecht: Springer Netherlands, 1991.
- [9] H. K. Onnes, K. Gavroglu (ed), and Y. Goudaroulis (ed), *Through Measurement to Knowledge: The Selected Papers of Heike Kamerlingh Onnes 1853–1926: Further Experiments with liquid helium. H. On the electrical resistance etc. (continued). VIII. The sudden disappearance of the ordinary resistance of tin, and the super-conductive state of lead.* Dordrecht: Springer Netherlands, 1991.
- [10] H. K. Onnes, K. Gavroglu (ed), and Y. Goudaroulis (ed), *Through Measurement to Knowledge: The Selected Papers of Heike Kamerlingh Onnes 1853–1926: Further experiments with liquid helium. B. On the change in the resistance of pure metals at very low temperatures, etc. III. The resistance of platinum at helium temperatures.* Dordrecht: Springer Netherlands, 1991.
- [11] H. K. Onnes, K. Gavroglu (ed), and Y. Goudaroulis (ed), *Through Measurement to Knowledge: The Selected Papers of Heike Kamerlingh Onnes 1853–1926: Further experiments with liquid helium. (a) J. The imitation of an Ampère molecular current or of a permanent magnet by means of a supra-conductor; (b) L. The persistence of currents without electromotive force in supra-conducting circuits.* Dordrecht: Springer Netherlands, 1991.
-

- [12] P. F. Dahl, “Superconductivity after World War I and circumstances surrounding the discovery of a state  $B=0$ ,” *Historical Studies in the Physical and Biological Sciences*, vol. 16, no. 1, pp. 1–58, 1986.
- [13] F. B. Silsbee, “A note on electrical conduction in metals at low temperatures,” *Journal of the Washington Academy of Sciences*, vol. 6, no. 17, pp. 597–602, 1916.
- [14] H. K. Onnes, K. Gavroglu (ed), and Y. Goudaroulis (ed), *Through Measurement to Knowledge: The Selected Papers of Heike Kamerlingh Onnes 1853–1926: Further experiments with liquid helium. AA. The disturbance of supra-conductivity by magnetic fields and currents. The hypothesis of Silsbee*. Dordrecht: Springer Netherlands, 1991.
- [15] H. Rogalla and P. H. Kes, eds., *100 years of superconductivity*. Boca Raton: CRC Press, 2011.
- [16] J. Matricon and G. Waysand, *The cold wars: a history of superconductivity*. New Brunswick: Rutgers University Press, 2003.
- [17] L. Hoddeson, G. Baym, and M. Eckert, “The development of the quantum-mechanical electron theory of metals: 1928—1933,” *Reviews of Modern Physics*, vol. 59, pp. 287–327, Jan 1987.
- [18] P. W. Bridgman, “The discontinuity of resistance preceding supraconductivity,” *Journal of the Washington Academy of Sciences*, vol. 11, no. 19, pp. 455–459, 1921.
- [19] W. Meissner and R. Ochsenfeld, “Ein neuer effekt bei eintritt der supraleitfähigkeit,” *Naturwissenschaften*, vol. 21, no. 44, pp. 787–788, 1933.
- [20] A. M. Forrest, “Meissner and Ochsenfeld revisited,” *European Journal of Physics*, vol. 4, no. 2, p. 117, 1983.
-



- [21] C. P. Poole, H. A. Farach, R. J. Creswick, and R. Prozorov, *Superconductivity*. Amsterdam: Elsevier, 3rd ed., 2014.
- [22] C. Gorter and H. Casimir, “On supraconductivity I,” *Physica*, vol. 1, no. 1, pp. 306–320, 1934.
- [23] F. London and H. London, “The electromagnetic equations of the supraconductor,” *Proceedings of the Royal Society of London. Series A – Mathematical and Physical Sciences*, vol. 149, no. 866, pp. 71–88, 1935.
- [24] F. London, “On the problem of the molecular theory of superconductivity,” *Physical Review*, vol. 74, pp. 562–573, Sep 1948.
- [25] L. D. Landau, “On the theory of phase transitions,” *Zh. Eksp. Teor. Fiz.*, vol. 11, p. 19, 1937.
- [26] V. Ginzburg and L. D. Landau, “On the theory of superconductivity,” *Zh. Eksp. Teor. Fiz.*, vol. 20, p. 1064, 1950.
- [27] M. Suzuki and I. S. Suzuki, “Lecture note on Solid State Physics: Ginzburg-Landau theory for superconductivity,” *Department of Physics, State University of New York at Binghamton, Binghamton, New York*, 2007.
- [28] M. Milošević and R. Geurts, “The Ginzburg–Landau theory in application,” *Physica C*, vol. 470, no. 19, pp. 791–795, 2010.
- [29] A. A. Shanenko, M. V. Milošević, F. M. Peeters, and A. V. Vagov, “Extended Ginzburg-Landau formalism for two-band superconductors,” *Physical Review Letters*, vol. 106, p. 047005, Jan 2011.
- [30] M. Cyrot, “Ginzburg-Landau theory for superconductors,” *Reports on Progress in Physics*, vol. 36, p. 103, Feb 1973.

- [31] P. G. De Gennes, “Boundary effects in superconductors,” *Reviews of Modern Physics*, vol. 36, pp. 225–237, Jan 1964.
- [32] F. London, *Superfluids*, vol. 1. New York: Wiley, 1950.
- [33] B. S. Deaver and W. M. Fairbank, “Experimental evidence for quantized flux in superconducting cylinders,” *Physical Review Letters*, vol. 7, pp. 43–46, Jul 1961.
- [34] R. Doll and M. Näbauer, “Experimental proof of magnetic flux quantization in a superconducting ring,” *Physical Review Letters*, vol. 7, pp. 51–52, Jul 1961.
- [35] A. Paskin, M. Strongin, P. P. Craig, and D. G. Schweitzer, “Temperature dependence of the Ginzburg-Landau coefficient in type-I superconductors,” *Physical Review*, vol. 137, pp. A1816–A1821, Mar 1965.
- [36] A. A. Abrikosov *Doklady Akademii Nauk SSSR*, vol. 86, p. 489, 1952.
- [37] A. A. Abrikosov, “On the magnetic properties of superconductors of the second group,” *Soviet Physics JETP*, vol. 5, pp. 1174–1182, 1957.
- [38] A. A. Abrikosov, “Nobel Lecture: Type-II superconductors and the vortex lattice,” *Reviews of Modern Physics*, vol. 76, pp. 975–979, Dec 2004.
- [39] V. V. Moshchalkov, L. Gielen, C. Strunk, R. Jonckheere, X. Qiu, C. V. Haesendonck, and Y. Bruynseraede, “Effect of sample topology on the critical fields of mesoscopic superconductors,” *Nature*, vol. 373, no. 6512, pp. 319–322, 1995.
- [40] U. Essmann and H. Träuble, “The direct observation of individual flux lines in type II superconductors,” *Physics Letters A*, vol. 24, no. 10, pp. 526–527, 1967.
- [41] G. J. C. Van Baarle, A. M. Troianovski, T. Nishizaki, P. H. Kes, and J. Aarts, “Imaging of vortex configurations in thin films by scanning-tunneling microscopy,” *Applied Physics Letters*, vol. 82, no. 7, pp. 1081–1083, 2003.
-

- [42] A. Volodin, K. Temst, C. Van Haesendonck, Y. Bruynseraede, M. I. Montero, and I. K. Schuller, “Magnetic-force microscopy of vortices in thin niobium films: Correlation between the vortex distribution and the thickness-dependent film morphology,” *Europhysics Letters*, vol. 58, no. 4, p. 582, 2002.
- [43] P. E. Goa, H. Hauglin, M. Baziljevich, E. Il’yashenko, P. L. Gammel, and T. H. Johansen, “Real-time magneto-optical imaging of vortices in superconducting NbSe<sub>2</sub>,” *Superconductor Science and Technology*, vol. 14, no. 9, p. 729, 2001.
- [44] M. Motta, *Flux avalanches in patterned superconducting thin films: ac susceptibility, morphology and related studies*. Ph.D. thesis, Universidade Federal de São Carlos, 2013. São Carlos, Brazil.
- [45] E. Sardella, P. N. Lisboa Filho, C. C. de Souza Silva, L. R. Eulálio Cabral, and W. A. Ortiz, “Vortex-antivortex annihilation dynamics in a square mesoscopic superconducting cylinder,” *Phys. Rev. B*, vol. 80, p. 012506, Jul 2009.
- [46] A. Chaves, F. M. Peeters, G. A. Farias, and M. V. Milošević, “Vortex-vortex interaction in bulk superconductors: Ginzburg-Landau theory,” *Phys. Rev. B*, vol. 83, p. 054516, Feb 2011.
- [47] W. H. Kleiner, L. M. Roth, and S. H. Autler, “Bulk solution of ginzburg-landau equations for type II superconductors: Upper critical field region,” *Physical Review*, vol. 133, pp. A1226–A1227, Mar 1964.
- [48] G. Blatter, M. V. Feigel’man, V. B. Geshkenbein, A. I. Larkin, and V. M. Vinokur, “Vortices in high-temperature superconductors,” *Reviews of Modern Physics*, vol. 66, pp. 1125–1388, Oct 1994.

- [49] F. Colauto, M. Motta, and W. A. Ortiz, “Controlling magnetic flux penetration in low- $t_c$  superconducting films and hybrids,” *Superconductor Science and Technology*, vol. 34, no. 1, p. 013002, 2021.
- [50] L. Civale, A. D. Marwick, T. K. Worthington, M. A. Kirk, J. R. Thompson, L. Krusin-Elbaum, Y. Sun, J. R. Clem, and F. Holtzberg, “Vortex confinement by columnar defects in  $\text{YBa}_2\text{Cu}_3\text{O}_7$  crystals: Enhanced pinning at high fields and temperatures,” *Physical Review Letters*, vol. 67, pp. 648–651, Jul 1991.
- [51] V. V. Moshchalkov and J. Fritzsche, *Nanostructured Superconductors*. Singapore: World Scientific, 2011.
- [52] E. Altshuler and T. H. Johansen, “Colloquium: Experiments in vortex avalanches,” *Reviews of Modern Physics*, vol. 76, no. 2, p. 471, 2004.
- [53] C. P. Bean, “Magnetization of hard superconductors,” *Physical Review Letters*, vol. 8, pp. 250–253, Mar 1962.
- [54] Y. B. Kim, C. F. Hempstead, and A. R. Strnad, “Critical persistent currents in hard superconductors,” *Physical Review Letters*, vol. 9, pp. 306–309, Oct 1962.
- [55] C. P. Bean, “Magnetization of high-field superconductors,” *Reviews of Modern Physics*, vol. 36, pp. 31–39, Jan 1964.
- [56] J. Pearl, “Current distribution in superconducting films carrying quantized fluxoids,” *Applied Physics Letters*, vol. 5, no. 4, pp. 65–66, 1964.
- [57] E. Zeldov, J. R. Clem, M. McElfresh, and M. Darwin, “Magnetization and transport currents in thin superconducting films,” *Physical Review B*, vol. 49, no. 14, p. 9802, 1994.
- [58] J. McDonald and J. R. Clem, “Theory of flux penetration into thin films with field-dependent critical current,” *Physical Review B*, vol. 53, pp. 8643–8650, Apr 1996.

- [59] E. H. Brandt and M. Indenbom, “Type-II-superconductor strip with current in a perpendicular magnetic field,” *Physical Review B*, vol. 48, no. 17, p. 12893, 1993.
- [60] T. H. Johansen, M. Baziljevich, H. Bratsberg, Y. Galperin, P. E. Lindelof, Y. Shen, and P. Vase, “Direct observation of the current distribution in thin superconducting strips using magneto-optic imaging,” *Physical Review B*, vol. 54, pp. 16264–16269, Dec 1996.
- [61] J. I. Vestgården, T. H. Johansen, and Y. M. Galperin, “Nucleation and propagation of thermomagnetic avalanches in thin-film superconductors,” *Low Temperature Physics*, vol. 44, no. 6, pp. 460–476, 2018.
- [62] G. Shaw, J. Brisbois, L. Pinheiro, J. Müller, S. Blanco Alvarez, T. Devillers, N. Dempsey, J. Scheerder, J. Van de Vondel, S. Melinte, *et al.*, “Quantitative magneto-optical investigation of superconductor/ferromagnet hybrid structures,” *Review of Scientific Instruments*, vol. 89, no. 2, p. 023705, 2018.
- [63] C. Jooss, J. Albrecht, H. Kuhn, S. Leonhardt, and H. Kronmüller, “Magneto-optical studies of current distributions in high-Tc superconductors,” *Reports on Progress in Physics*, vol. 65, no. 5, p. 651, 2002.
- [64] Y. B. Kim, C. F. Hempstead, and A. R. Strnad, “Magnetization and critical supercurrents,” *Physical Review*, vol. 129, pp. 528–535, Jan 1963.
- [65] D. V. Shantsev, Y. M. Galperin, and T. H. Johansen, “Thin superconducting disk with field-dependent critical current: Magnetization and ac susceptibilities,” *Physical Review B*, vol. 61, pp. 9699–9706, Apr 2000.
- [66] R. G. Mints and A. L. Rakhmanov, “Critical state stability in type-II superconductors and superconducting-normal-metal composites,” *Reviews of Modern Physics*, vol. 53, pp. 551–592, Jul 1981.

- [67] S. L. Wipf, "Review of stability in high temperature superconductors with emphasis on flux jumping," *Cryogenics*, vol. 31, no. 11, pp. 936–948, 1991.
- [68] J. I. Vestgård, D. V. Shantsev, Y. M. Galperin, and T. H. Johansen, "Lightning in superconductors," *Scientific Reports*, vol. 2, no. 1, p. 886, 2012.
- [69] A. L. Schawlow, "Structure of the intermediate state in superconductors," *Physical Review*, vol. 101, pp. 573–579, Jan 1956.
- [70] D. V. Denisov, D. V. Shantsev, Y. M. Galperin, E.-M. Choi, H.-S. Lee, S.-I. Lee, A. V. Bobyl, P. E. Goa, A. A. F. Olsen, and T. H. Johansen, "Onset of dendritic flux avalanches in superconducting films," *Physical Review Letters*, vol. 97, p. 077002, Aug 2006.
- [71] U. Bolz, B. Biehler, D. Schmidt, B.-U. Runge, and P. Leiderer, "Dynamics of the dendritic flux instability in  $\text{YBa}_2\text{Cu}_3\text{O}_{7-\delta}$  films," *Europhysics Letters*, vol. 64, no. 4, p. 517, 2003.
- [72] V. V. Yurchenko, D. V. Shantsev, T. H. Johansen, M. R. Nevala, I. J. Maasilta, K. Senapati, and R. C. Budhani, "Reentrant stability of superconducting films and the vanishing of dendritic flux instability," *Physical Review B*, vol. 76, p. 092504, Sep 2007.
- [73] T. H. Johansen, M. Baziljevich, D. V. Shantsev, P. E. Goa, Y. M. Galperin, W. N. Kang, H. J. Kim, E. M. Choi, M. S. Kim, and S. I. Lee, "Dendritic flux patterns in  $\text{MgB}_2$  films," *Superconductor Science and Technology*, vol. 14, no. 9, p. 726, 2001.
- [74] M. Menghini, R. J. Wijngaarden, A. V. Silhanek, S. Raedts, and V. V. Moshchalkov, "Dendritic flux penetration in pb films with a periodic array of antidots," *Physical Review B*, vol. 71, p. 104506, Mar 2005.

- [75] R. Zadorosny, F. Colauto, M. Motta, T. H. Johansen, R. Dinner, M. Blamire, G. W. Ataklti, V. V. Moshchalkov, A. V. Silhanek, and W. A. Ortiz, “Morphology of flux avalanches in patterned superconducting films,” *Journal of Superconductivity and Novel Magnetism*, vol. 26, pp. 2285–2288, 2013.
- [76] M. Motta, F. Colauto, J. I. Vestgård, J. Fritzsche, M. Timmermans, J. Cuppens, C. Attanasio, C. Cirillo, V. V. Moshchalkov, J. Van de Vondel, T. H. Johansen, W. A. Ortiz, and A. V. Silhanek, “Controllable morphology of flux avalanches in microstructured superconductors,” *Physical Review B*, vol. 89, p. 134508, Apr 2014.
- [77] M. Baziljevich, A. V. Bobyl, D. V. Shantsev, E. Altshuler, T. H. Johansen, and S. I. Lee, “Origin of dendritic flux patterns in MgB<sub>2</sub> films,” *Physica C*, vol. 369, no. 1-4, pp. 93–96, 2002.
- [78] F. Colauto, E. Choi, J. Y. Lee, S. I. Lee, E. J. Patiño, M. G. Blamire, T. H. Johansen, and W. A. Ortiz, “Suppression of flux avalanches in superconducting films by electromagnetic braking,” *Applied Physics Letters*, vol. 96, no. 9, 2010.
- [79] V. V. Yurchenko, T. H. Johansen, and Y. M. Galperin, “Dendritic flux avalanches in superconducting films,” *Low Temperature Physics*, vol. 35, no. 8, pp. 619–626, 2009.
- [80] J. I. Vestgård, D. V. Shantsev, Y. M. Galperin, and T. H. Johansen, “Dynamics and morphology of dendritic flux avalanches in superconducting films,” *Physical Review B*, vol. 84, p. 054537, Aug 2011.
- [81] Z. Jing and M. D. Ainslie, “Numerical simulation of flux avalanches in type-II superconducting thin films under transient AC magnetic fields,” *Superconductor Science and Technology*, vol. 33, no. 8, p. 084006, 2020.

- [82] L. N. Cooper and D. Feldman, eds., *BCS: 50 years*. Singapore: World Scientific, 2010.
- [83] E. Maxwell, “Isotope effect in the superconductivity of mercury,” *Physical Review*, vol. 78, pp. 477–477, May 1950.
- [84] C. A. Reynolds, B. Serin, W. H. Wright, and L. B. Nesbitt, “Superconductivity of isotopes of mercury,” *Physical Review*, vol. 78, pp. 487–487, May 1950.
- [85] H. Fröhlich, “Interaction of electrons with lattice vibrations,” *Proceedings of the Royal Society of London A*, vol. 215, no. 1122, pp. 291–298, 1952.
- [86] D. Bohm and D. Pines, “A collective description of electron interactions. I. Magnetic interactions,” *Physical Review*, vol. 82, pp. 625–634, Jun 1951.
- [87] D. Pines and D. Bohm, “A collective description of electron interactions: II. Collective vs individual particle aspects of the interactions,” *Physical Review*, vol. 85, pp. 338–353, Jan 1952.
- [88] D. Bohm and D. Pines, “A collective description of electron interactions: III. Coulomb interactions in a degenerate electron gas,” *Physical Review*, vol. 92, pp. 609–625, Nov 1953.
- [89] D. Pines, “A collective description of electron interactions: IV. Electron interaction in metals,” *Physical Review*, vol. 92, pp. 626–636, Nov 1953.
- [90] J. Bardeen and D. Pines, “Electron-phonon interaction in metals,” *Physical Review*, vol. 99, pp. 1140–1150, Aug 1955.
- [91] R. M. Fernandes, “BCS theory of superconductivity,” *Lecture notes*.
- [92] C. Timm, “Theory of superconductivity, Lecture notes,” *Institute of Theoretical Physics, TU Dresden*, 2020.
-



- [93] L. N. Cooper, “Bound electron pairs in a degenerate fermi gas,” *Physical Review*, vol. 104, pp. 1189–1190, Nov 1956.
- [94] J. Bardeen, L. N. Cooper, and J. R. Schrieffer, “Microscopic theory of superconductivity,” *Physical Review*, vol. 106, pp. 162–164, Apr 1957.
- [95] J. Bardeen, L. N. Cooper, and J. R. Schrieffer, “Theory of superconductivity,” *Physical Review*, vol. 108, pp. 1175–1204, Dec 1957.
- [96] N. M. Plakida, “JETP Golden Pages: Papers on the theory of superconductivity by N. N. Bogoliubov,” 2015. <http://jetp.ras.ru/cgi-bin/index2/gf-view/en/papers-on-the-theory-of-superconductivity-by-n-n-bogoliubov>, accessed 19-07-2023.
- [97] L. P. Gor’kov, “Microscopic derivation of the Ginzburg-Landau equations in the theory of superconductivity,” *Soviet Physics JETP*, vol. 9, no. 6, pp. 1364–1367, 1959.
- [98] N. R. Werthamer, “Theory of a local superconductor in a magnetic field,” *Physical Review*, vol. 132, pp. 663–668, Oct 1963.
- [99] J. Rohlf, *Modern Physics from  $\alpha$  to  $Z^0$* . New York: Wiley, 1994.
- [100] I. Giaever, “Electron tunneling and superconductivity,” *Reviews of Modern Physics*, vol. 46, pp. 245–250, Apr 1974.
- [101] L. Esaki, “New phenomenon in narrow germanium  $p-n$  junctions,” *Physical Review*, vol. 109, pp. 603–604, Jan 1958.
- [102] I. Giaever, “Energy gap in superconductors measured by electron tunneling,” *Physical Review Letters*, vol. 5, pp. 147–148, Aug 1960.

- [103] J. Nicol, S. Shapiro, and P. H. Smith, "Direct measurement of the superconducting energy gap," *Physical Review Letters*, vol. 5, pp. 461–464, Nov 1960.
- [104] I. Giaever, "Electron tunneling between two superconductors," *Physical Review Letters*, vol. 5, pp. 464–466, Nov 1960.
- [105] P. W. Anderson, "How Josephson discovered his effect," *Physics Today*, vol. 23, no. 11, pp. 23–29, 1970.
- [106] B. Josephson, "Possible new effects in superconductive tunnelling," *Physics Letters*, vol. 1, no. 7, pp. 251–253, 1962.
- [107] B. D. Josephson, "The discovery of tunnelling supercurrents," *Reviews of Modern Physics*, vol. 46, pp. 251–254, Apr 1974.
- [108] M. H. Cohen, L. M. Falicov, and J. C. Phillips, "Superconductive tunneling," *Physical Review Letters*, vol. 8, pp. 316–318, Apr 1962.
- [109] P. W. Anderson and J. M. Rowell, "Probable observation of the Josephson superconducting tunneling effect," *Physical Review Letters*, vol. 10, pp. 230–232, Mar 1963.
- [110] S. Shapiro, "Josephson currents in superconducting tunneling: The effect of microwaves and other observations," *Physical Review Letters*, vol. 11, pp. 80–82, Jul 1963.
- [111] I. Giaever, "Detection of the ac Josephson effect," *Physical Review Letters*, vol. 14, pp. 904–906, May 1965.
- [112] R. C. Jaklevic, J. Lambe, A. H. Silver, and J. E. Mercereau, "Quantum interference effects in Josephson tunneling," *Physical Review Letters*, vol. 12, pp. 159–160, Feb 1964.

- [113] J. Clarke, “A superconducting galvanometer employing josephson tunnelling,” *Philosophical Magazine*, vol. 13, no. 121, pp. 115–127, 1966.
- [114] R. L. Fagaly, “Superconducting quantum interference device instruments and applications,” *Review of Scientific Instruments*, vol. 77, p. 101101, 2006.
- [115] K. K. Likharev, “Superconducting weak links,” *Reviews of Modern Physics*, vol. 51, pp. 101–159, Jan 1979.
- [116] A. Murphy and A. Bezryadin, “Asymmetric nanowire SQUID: Linear current-phase relation, stochastic switching, and symmetries,” *Physical Review B*, vol. 96, p. 094507, Sep 2017.
- [117] K. Hasselbach, D. Mailly, and J. R. Kirtley, “Micro-superconducting quantum interference device characteristics,” *Journal of Applied Physics*, vol. 91, no. 7, pp. 4432–4437, 2002.
- [118] H. Dausy, L. Nulens, B. Raes, M. J. Van Bael, and J. Van de Vondel, “Impact of kinetic inductance on the critical-current oscillations of nanobridge squids,” *Physical Review Applied*, vol. 16, p. 024013, Aug 2021.
- [119] L. Nulens, “Vorticity diamonds in nanobridge SQUIDs: a study of the influence of the bridge dimensions,” 2021. KU Leuven, Belgium, Master’s thesis.
- [120] P. J. Ray, “Structural investigation of  $\text{La}(2-x)\text{Sr}(x)\text{CuO}(4+y)$  - Following staging as a function of temperature,” 2016. University of Copenhagen, Denmark, Master’s thesis.
- [121] Wikipedia contributors, “Superconductivity — Wikipedia, the free encyclopedia,” 2023. <https://en.wikipedia.org/w/index.php?title=Superconductivity&oldid=1161941136>, [Online; accessed 25-July-2023].

- [122] J. G. Bednorz and K. A. Müller, “Possible high  $T_c$  superconductivity in the Ba-La-Cu-O system,” *Zeitschrift für Physik B Condensed Matter*, vol. 64, no. 2, pp. 189–193, 1986.
- [123] P. Magierski, G. Wlazłowski, and A. Bulgac, “Onset of a pseudogap regime in ultracold fermi gases,” *Physical Review Letters*, vol. 107, p. 145304, Sep 2011.
- [124] G. R. Stewart, “Unconventional superconductivity,” *Advances in Physics*, vol. 66, no. 2, pp. 75–196, 2017.
- [125] K. Seshan, *Handbook of thin film deposition techniques Principles, Methods, Equipment and Applications*. Boca Raton: CRC Press, 2nd ed., 2002.
- [126] P. Kelly and R. Arnell, “Magnetron sputtering: a review of recent developments and applications,” *Vacuum*, vol. 56, no. 3, pp. 159–172, 2000.
- [127] L. Martin, Y.-H. Chu, and R. Ramesh, “Advances in the growth and characterization of magnetic, ferroelectric, and multiferroic oxide thin films,” *Materials Science and Engineering: R: Reports*, vol. 68, no. 4, pp. 89–133, 2010.
- [128] Y. Chen, “Nanofabrication by electron beam lithography and its applications: A review,” *Microelectronic Engineering*, vol. 135, pp. 57–72, 2015.
- [129] S. Okazaki, “High resolution optical lithography or high throughput electron beam lithography: The technical struggle from the micro to the nano-fabrication evolution,” *Microelectronic Engineering*, vol. 133, pp. 23–35, 2015.
- [130] S. Reyntjens and R. Puers, “A review of focused ion beam applications in microsystem technology,” *Journal of Micromechanics and Microengineering*, vol. 11, no. 4, p. 287, 2001.

- [131] M. Y. Ali, W. Hung, and F. Yongqi, “A review of focused ion beam sputtering,” *International Journal of Precision Engineering and Manufacturing*, vol. 11, pp. 157–170, 2010.
- [132] S. J. Bending, A. Brook, J. K. Gregory, I. A. Crisan, A. Pross, A. N. Grigorenko, A. Oral, F. Laviano, and E. Mezzetti, “Comparison of magneto-optical imaging with other local magnetic probes,” in *Magneto-Optical Imaging* (T. H. Johansen and D. V. Shantsev, eds.), (Dordrecht), pp. 11–18, Springer Netherlands, 2004.
- [133] E. Marchiori, L. Ceccarelli, N. Rossi, L. Lorenzelli, C. L. Degen, and M. Poggio, “Nanoscale magnetic field imaging for 2D materials,” *Nature Reviews Physics*, vol. 4, no. 1, pp. 49–60, 2022.
- [134] E. Persky, I. Sochnikov, and B. Kalisky, “Studying quantum materials with scanning SQUID microscopy,” *Annual Review of Condensed Matter Physics*, vol. 13, no. 1, pp. 385–405, 2022.
- [135] L. B. L. G. Pinheiro, *Quantitative magneto-optical imaging in bi-layered and in nanoscaled wedge-shaped superconducting thin films*. Ph.D. thesis, Universidade Federal de São Carlos, 2019. São Carlos, Brazil.
- [136] A. Y. Meltzer, E. Levin, and E. Zeldov, “Direct reconstruction of two-dimensional currents in thin films from magnetic-field measurements,” *Physical Review Applied*, vol. 8, p. 064030, Dec 2017.
- [137] C. Jooss, R. Warthmann, A. Forkl, and H. Kronmüller, “High-resolution magneto-optical imaging of critical currents in YBa<sub>2</sub>Cu<sub>3</sub>O<sub>7- $\delta$</sub>  thin films,” *Physica C*, vol. 299, no. 3, pp. 215–230, 1998.
- [138] J. Brisbois, M. Motta, J. I. Avila, G. Shaw, T. Devillers, N. M. Dempsey, S. K. Veerapandian, P. Colson, B. Vanderheyden, P. Vanderbemden, W. A. Ortiz, N. D.

- Nguyen, R. B. G. Kramer, and A. V. Silhanek, “Imprinting superconducting vortex footsteps in a magnetic layer,” *Scientific Reports*, vol. 6, no. 1, p. 27159, 2016.
- [139] Quantum Design, 10307 Pacific Center Court, San Diego, CA 92121, USA. <https://www.qdusa.com/>.
- [140] R. L. Fagaly, “Superconducting quantum interference device instruments and applications,” *Review of Scientific Instruments*, vol. 77, no. 10, p. 101101, 2006.
- [141] M. McElfresh, “Fundamentals of magnetism and magnetic measurements featuring Quantum Design’s magnetic property measurement system,” *Quantum Design*, 1994.
- [142] Oxford Instruments, Tubney Woods, Abingdon, Oxfordshire OX13 5QX, UK. <https://www.oxinst.com/>.
- [143] R. M. Menezes and C. C. d. S. Silva, “Conformal vortex crystals,” *Scientific Reports*, vol. 7, p. 12766, 2017.
- [144] R. M. Menezes, E. Sardella, L. R. E. Cabral, and C. C. de Souza Silva, “Self-assembled vortex crystals induced by inhomogeneous magnetic textures,” *Journal of Physics: Condensed Matter*, vol. 31, no. 17, p. 175402, 2019.
- [145] D. A. D. Chaves, I. M. de Araújo, D. Carmo, F. Colauto, A. A. M. de Oliveira, A. M. H. de Andrade, T. H. Johansen, A. V. Silhanek, W. A. Ortiz, and M. Motta, “Enhancing the effective critical current density in a Nb superconducting thin film by cooling in an inhomogeneous magnetic field,” *Applied Physics Letters*, vol. 119, no. 2, p. 022602, 2021.
- [146] M. I. Valerio-Cuadros, D. A. D. Chaves, F. Colauto, A. A. M. d. Oliveira, A. M. H. d. Andrade, T. H. Johansen, W. A. Ortiz, and M. Motta, “Superconducting

- properties and electron scattering mechanisms in a Nb film with a single weak-link excavated by focused ion beam,” *Materials*, vol. 14, no. 23, 2021.
- [147] D. A. D. Chaves, M. I. Valerio-Cuadros, L. Jiang, E. A. Abbey, F. Colauto, A. A. M. Oliveira, A. M. H. de Andrade, L. B. L. G. Pinheiro, T. H. Johansen, C. Xue, Y.-H. Zhou, A. V. Silhanek, W. A. Ortiz, and M. Motta, “Magnetic field induced weak-to-strong-link transformation in patterned superconducting films,” *Physical Review B*, vol. 108, p. 214502, 2023.
- [148] D. A. D. Chaves, L. Nulens, H. Dausy, B. Raes, D. Yue, W. A. Ortiz, M. Motta, M. J. Van Bael, and J. Van de Vondel, “Nanobridge SQUIDs as multilevel memory elements,” *Physical Review Applied*, vol. 19, p. 034091, 2023.
- [149] D. A. D. Chaves, J. C. C. Filho, E. A. Abbey, D. Bosworth, Z. H. Barber, M. G. Blamire, T. H. Johansen, A. V. Silhanek, W. A. Ortiz, and M. Motta, “Using quantitative magneto-optical imaging to reveal why the ac susceptibility of superconducting films is history-independent,” *arXiv*, p. 2309.08062, 2023.